Applications of parallel radiofrequency transmission to ultra-high-field magnetic resonance imaging



Yan Tong

University College Oxford, and

Wellcome Centre for Integrative Neuroimaging, FMRIB Division,

Nuffield Department of Clinical Neurosciences

University of Oxford

A thesis submitted for the degree of Doctor of Philosophy

Supervisors: Professor Peter Jezzard, Dr William Clarke

Trinity Term 2020

Abstract

Increasing the static magnetic field (B_0) strength of magnetic resonance imaging (MRI) scanners improves the signal-to-noise ratio (SNR). Higher SNR may be used for more sensitive, faster, and higher resolution imaging.

Despite its potential, the biggest challenges for ultra-high field MRI is inhomogeneity in the radio-frequency field (B_1^+), which causes spatially varying flip angles when using fixed-frequency pulses, leading to undesirable perturbations in signal and contrast. The most flexible solution to B_1^+ inhomogeneity at UHF is parallel transmission (pTx). A pTx enabled system consisting of more than one RF transmit channels which may be independently driven.

This thesis seeks to extend the methodology and applications of pTx magnetic resonance imaging (MRI) in the brain at 7 tesla. Specifically, this thesis focuses on two spin labelling techniques: arterial spin labelling (ASL) that measures cerebral perfusion and T_2-Relaxation-Under-Spin-Tagging (TRUST) that measures venous oxygenation.

The ASL study demonstrates that labelling efficiency can be improved by the incorporation of pTx static shimming in the labelling pulses, but indicates that the temporal SNR does not yet exceed optimised 3 tesla protocols in the absence of further developments. The TRUST study investigates the use of spatially-selective pTx pulses in a modified TRUST sequence to measure regional oxygen extraction fraction (OEF) in the brain. Results show that localised saturation was achieved by repeatedly exciting (using pTx pulses) and saturating spins outside the region-of-interest.

Declaration of the Contributions of Others

The processing pipeline for the B_1^+ and B_0 maps described in Chapter 3 was developed by Dr William Clarke. The sequence used in Chapter 4 was based a sequence previously developed by Dr Thomas Okell. The sequence used in Chapter 5 is based a sequence previously developed by Professor Peter Jezzard and Dr Caitlin O'Brien .

List of Publications Arising from this Thesis

Journal article:

Tong, Y., Jezzard, P., Okell, T. W., & Clarke, W. T. (2020). Improving PCASL at ultra-high field using a VERSE-guided parallel transmission strategy. *Magnetic Resonance in Medicine*, *84*(2), 777-786.

Conference proceedings:

Tong, Y., Jezzard, P., Okell, T. W., & Clarke, W. T., Improving arterial spin labelling at ultra-high field using parallel transmission: a simulation study, *Annual Meeting of the International Society of Magnetic Resonance in Medicine*, *Paris*, p. 3399, 2018

Tong, Y., Jezzard, P., Okell, T. W., & Clarke, W. T., Improving pseudo-continuous arterial spin labelling at ultra-high field using a VERSE-guided parallel transmission strategy, *Annual Meeting of the International Society of Magnetic Resonance in Medicine*, *Montreal*, p. 4637, 2019

Tong, Y., Jezzard, P., O'Brien, C., & Clarke, W. T., Mapping oxygen extraction fraction using a tailored parallel transmission RF pulse at 7 T, *Annual Meeting of the International Society of Magnetic Resonance in Medicine*, *Online*, p. 3690, 2020

Acknowledgments

I would like to dedicate this thesis to my grandmother, who passed away this March because of cancer. Unfortunately, I was unable to see her due to the pandemic. She was a kind, considerate, loving, and patient grandmother who could cook the most delicious food in the world. May you rest in peace.

I would like to first thank my parents for their continued support for me. I could not have been where I am today without you. Thanks for allowing me to pursue my dream. I would also like to thank Weiyi, for bringing so much love and joy in my life. Meeting you is the best thing that happened to me since coming to Oxford. To quote Coldplay here, you are "my mirror, my sword and shield".

Since many people mentioned here hold doctorates, I will save some space and omit their titles. I would like to extend my appreciation for my supervisors Peter Jezzard and William Clarke. I could not have dreamed of better supervision before coming to FMRIB. Both of them are incredibly knowledgeable, intelligent, dedicated, and responsible, and have spent tremendous amount of their time teaching, helping, and guiding me. Despite being an incredibly busy person with many titles (dean of graduates at Univ, MRM editor-in-chief, ONBI director, and a father), Peter always tries to make time for his students. A living encyclopaedia of MRI, Peter provides penetrating insights, and is always more keen to do research than his other administrative duties. Will, on the other hand, has given me an enormous amount of help on the day-to-day and practical aspects of my research such as programming on IDEA and MATLAB, scanning, using the pTx system, and getting data from the scanner. Both of you are extremely demanding in the texts and figures I ever produce, which helps me grow as a scientist.

Thanks to Karla for championing a series of initiatives to create a more inclusive working environment. Thanks to Hanna who helped me with my application to Oxford. It is truly a miracle that were working in the same office since we met each other in Switzerland in 2014. Thanks to Tom, Joe, and Caitlin for helping me in my project. Thanks to my desk mates Jack, Hongbae, Thijs, and Sophie. Thanks to everyone else in the Physics Group:

Uzay, Adam, Yuhang, Ti, Nadine, Michiel K, Olivia, Johanna, Fritz, Daniel P, Seb, Stuart, Matt, Nic, Rob, Wenchuan, Alex, Harry, Istvan, Amy, Fritz, Yuriko, Mohammed, Paula, Aurea, Ben, Chaoyue, Xi, Daniel K, Mo, Cristiana. Thanks to friends from other groups like Yingqiu, Weikang, Jiewon, Hossein, Liz, Han, Nicola, Fidel, Slava, Michiel C, Rick, Usama, Saad, Yazhuo, Jesper, Renée, Jonathan, Emma, Jon, Michael, Arjun, Zobair, and David. Finally big thanks to Sue and Nancy. FMRIB cannot function without you.

Staying at home during the lockdown was challenging for everyone. However, living through this time with William Prescott made everything much easier. I will miss the daily walks to interesting spots in Oxford we had. Thanks to my neighbours Mitch and Jess, for the conversations from the balcony, and the bakeries you made for us. I would have had a much tougher time in lockdown without these three lovely Australians. I would also like to thank all of my other housemates Aaron, Cameron, Dan, Rellie, Yanki, and the late Johnathan, who will be dearly missed.

I would also like to thank everyone who stimulated my interest in MRI. Thank you to my supervisors in Switzerland Sandrine Muller and Ferath Kherif for giving me tremendous help when I was a clueless undergraduate student working on an fMRI project. Thank you to Steven Wright and Mary McDougall for teaching the best undergraduate course I had at Texas A&M, BMEN 427 *Magnetic Resonance Engineering*. Thank you to my teaching assistants for BMEN 427, Jiaming Cui and Matt Wilcox, and my partner David Cavazos. I could not have done any of the experiments without your help.

Thanks to my colleagues at the computing lab in the physics department, especially Elizabeth Gallas. Thanks to Wednesday football friends like Kyoko, Hicham, Mohammad, Amin, Moisés, Licio, Adrienne, and Habib. Thanks to other friends like Yuli, Amanda, Richard and Phoebe.

Table of Contents

Chapter 1 Motivation and thesis outline *1*

1.1. Introduction **1**

1.2. Motivation **2**

1.3. Aims **3**

1.4. Thesis outline **3**

Chapter 2 Background *5*

2.1. Ultra-high field magnetic resonance imaging **5**

2.2. B_0 and B_1^+ mapping **9**

2.3. Mitigating the problem of inhomogeneous B_1^+ at UHF **11**

2.4. Specific absorption rate (SAR) **19**

2.5. Incorporation of pTx pulses in conventional sequences **27**

2.6. Recent developments **28**

2.7. Non-conventional use of pTx-enabled systems **31**

Chapter 3 Implementation *34*

3.1. The Bloch equations and RF excitation **34**

3.2. Discretisation and the system matrix **37**

3.3. Selective excitation using a single-channel system **40**

3.4. pTx System overview **44**

3.5. Description of online pulse design process **45**

Chapter 4 Improving pseudo-continuous arterial spin labelling at 7 T *52*

4.1. Arterial Spin Labelling: General Principles **52**

4.2. Improving PCASL labelling at UHF using a VERSE guided pTx strategy **59**

4.3. Future Improvements to PCASL labelling at UHF using a VERSE-guided pTx strategy **84**

Chapter 5 Measuring regional oxygen extraction fraction (OEF) using pTx *87*

5.1. T2-Relaxation-Under- Spin-Tagging (TRUST) **87**

5.2. Regional measurement of OEF using TRUST **96**

5.3. Discussion **131**

Chapter 6 Summary and future work ***149***

6.1. Summary **149**

6.2. Widening the adoption of pTx **150**

6.3. Future work **152**

6.4. Final remarks **156**

References ***158***

Chapter 1 Motivation and thesis outline

1.1. Introduction

Magnetic resonance imaging (MRI) is a non-invasive medical imaging method that relies on the detection of hydrogen nuclei in the human body via the manipulation of nuclear spin states. MRI can provide images of soft tissue with high spatial resolution, and does not involve ionising radiation. Furthermore, MRI is a highly versatile technique that can image anatomy, vasculature flow, molecular diffusion, tissue perfusion and metabolite concentration. With regards to tissue perfusion, defined as the passage of fluid to a tissue, a prominent contrast-free method that has been developed over the past two decades is the technique of arterial spin labelling (ASL). In ASL water spins in arterial blood are magnetically labelled as an endogenous contrast agent. Signal arising from these labelled water molecules can then be detected in the downstream tissue. A companion approach, T_2-Relaxation-Under-Spin-Tagging (TRUST), used to measure venous oxygen saturation, utilises ASL principles, but detects labelled water on the venous side of the vasculature.

As MRI hardware technology has developed, MRI scanners with higher main magnetic field strengths have become available. Increasing the static magnetic field strength of MRI scanners improves the signal-to-noise ratio (SNR). Higher SNR may be used to reduce scan time, or to increase spatial resolution. MR scanners with a field strength that is equal to or higher than 7 tesla are commonly referred to as ultra-high field (UHF) scanners. According to theory higher field strengths bring additional benefits to ASL and TRUST. Longer blood T_1 relaxation times at higher field strengths prolong lifetime of the label imparted on the blood.

Despite the increased SNR, there are a number of major challenges brought by higher field strength. The two most significant challenges are increased inhomogeneity of: 1) the radio-frequency (RF) field due to the shortened wavelength of the on-resonance RF radiation; and 2) the main static magnetic field due to increased effect of magnetic

susceptibility. RF field inhomogeneity leads to spatially varying flip-angles and a loss of image contrast. Inhomogeneity in the main magnetic field typically leads to signal loss artefacts and geometric distortion.

Parallel transmission (pTx) is a technique that can be used to mitigate RF field inhomogeneity. As opposed to most MRI scanners which only have a single RF channel for the purpose of RF excitation, a parallel transmission system has multiple RF transmit channels. Each channel in a pTx system has independent waveform generators and amplifiers. Therefore each channel can generate independent RF waveforms with arbitrary pulse envelope, amplitude and phase. By combining RF pulses across channels, excitation uniformity can be improved, or excitation of an arbitrary target magnetisation profile can be achieved.

1.2. Motivation

ASL and TRUST are both low-SNR techniques, due to the overall low amount of water molecules in the labelled blood compared the whole imaged volume (i.e. blood and static tissue). Therefore, moving to 7 T allows both sequences to take advantage of the increase in intrinsic SNR at higher field strengths. Moreover, longer blood T_1 relaxation time at 7 T slows down the attenuation of signal in the labelled blood.

The TRUST sequence also lacks spatial specificity, and implementing spatially-selective labelling pulses is one way to address this disadvantage. To facilitate this spatial selection is easier to achieve using a pTx system. In addition, one major challenge for ASL at 7 T is the poor labelling efficiency is due to low B_1^+ homogeneity and amplitude at the labelling plane, which can be mitigated by pTx approaches.

Mitigating B_1^+ homogeneity or achieving spatial selection by designing tailored RF pulses on a single transmit channel is impractical since RF pulses of a very long duration (10s of milliseconds) are often required. In a pTx system, however, each transmit channel has a distinct B_1^+ profile. This creates additional degrees of freedom that can be utilised to produce spatially-varying B_1^+ distribution using accelerated pulses, similar to how

different B_1^- (RF receive) profiles can be used to accelerate image acquisition in parallel imaging.

1.3. Aims

Achieving the above motivations requires designing and integrating tailored RF pulses on a pTx enabled system. Designing pTx pulses requires an extensive and integrated pipeline. First B_0 and B_1^+ fields must be mapped using appropriate sequences. Then the maps must be interpreted and pre-processed for use in the pulse design process. The pulse can then be designed, often on separate computing hardware, before being written back to the scanner for use. Finally, a specially modified sequence includes the designed RF pulses at runtime.

Two applications of pTx RF pulses, the ASL sequence and the TRUST sequence are the focus of this thesis. Specifically, the train of Gaussian labelling pulses in the pseudo-continuous ASL sequence were improved by RF shimming, i.e., the optimisation of amplitude and phase of the RF waveform in each channel. For the TRUST sequence, spatial localisation was achieved by designing arbitrary pulses based a shells trajectory.

The successful implementation of the proposed methods will be demonstrated in the following ways: ASL by the improvement of SNR of perfusion-weighted images; TRUST by verification of spatially-selective saturation by acquiring an image covering the ROI.

1.4. Thesis outline

This thesis seeks to extend the methodology and applications of pTx on magnetic resonance imaging in the brain at 7 tesla. Specifically, this thesis focuses on two spin labelling techniques: ASL, which measures cerebral perfusion, and TRUST, which measures venous oxygenation.

Chapter 2 introduces the benefits and challenges of UHF MRI. It then explains the concept of pTx, and discusses common pTx RF pulse design approaches. It also examines different

methods to mitigate increased specific absorption rate (SAR) at UHF, and reviews various radio-frequency field (B_1^+) mapping schemes.

Chapter 3 offers a mathematical formulation of spatially-selective RF pulse design, describes a pTx system, and details a practical implementation of applying pTx techniques on a Siemens 7 T whole-body Magnetom system.

Chapter 4 focuses on a study that aims to improve the labelling efficiency of pseudo-continuous ASL (PCASL) at 7 tesla using parallel transmit RF shimming and the technique of variable-rate selective excitation (VERSE). It demonstrates that the labelling efficiency can be improved by the incorporation of pTx static shimming in the labelling pulses, but indicates that the perfusion contrast-to-noise ratio does not yet exceed optimised 3 tesla protocols in the absence of further developments.

Chapter 5 investigates the use of 3D spatially-selective pTx pulses in a modified TRUST sequence to measure regional oxygen extraction fraction (OEF) in the brain. The localisation of the OEF estimation was achieved by repeatedly exciting (using pTx pulses) and saturating spins outside the ROI.

Chapter 6 considers future research directions and concludes the thesis.

Chapter 2 Background

This chapter introduces the benefits and challenges of ultra-high-field (UHF) MRI. It then explains the concept of parallel transmission (pTx) and discusses common pTx RF pulse design approaches. It also reviews various B_1^+ mapping schemes, and examines different methods to mitigate increased specific absorption rate (SAR) at UHF.

2.1. Ultra-high field magnetic resonance imaging

For a nuclear magnetic resonance (NMR) experiment, the signal-to-noise ratio (SNR) can be written as the following based on the principle of reciprocity [1]:

Equation 2.1

$$SNR \propto \frac{\omega^2}{\sqrt{R}} \propto \omega^{3/2}\sqrt{Q}$$

where ω is the Larmor frequency, R is the total resistance, and Q is the coil quality factor [2]. Q can be written as:

Equation 2.2

$$Q = \frac{\omega L}{R_{coil} + R_{sample}}$$

where L is the inductance of the sample, R_{coil} is the coil resistance and R_{sample} is the sample resistance [2]. In MRI of humans at clinical field strengths, conductivity-related eddy currents induced within the sample are the dominant source of noise. In the context of the quality factor Q, this is equivalent to ignoring R_{coil} while only considering R_{sample}, which is proportional to ω^2. Therefore, the overall SNR is roughly proportional to ω (ignoring other effects such as T_1). Thus, since ω is proportional to B_0, SNR scales linearly with B_0 as well.

As described above, increasing the static magnetic field (B_0) strength of magnetic resonance imaging (MRI) scanners improves the SNR [3]. Higher SNR allows more sensitive, faster, and higher resolution imaging. Ultra-high field (UHF, here ≥7 tesla) MRI scanners have been introduced for research purposes, and recently for clinical use. The first 7 T human MR system was installed at the Centre of Magnetic Resonance Research (CMRR) in the University of Minnesota in 1999. In the 2000s, three major MR vendors provided commercially available 7 T systems [4]. The development of actively shielded 7 T scanners also places less demand on the installation site compared to passively shielded scanners [4]. Lately, MRI scanners with even higher field strength (9.4 T and 10.5 T) have been developed. Recently, the 10.5 T scanner produced the first *in vivo* human images at this field strength [5], and the magnet of an 11.7 T scanner (Neurospin CEA, Saclay, France) was ramped up to field. The possibility of designing scanners with a field strength of 14 T to 20 T has also been discussed [6].

Many MR applications benefit from higher static field strength. In general, imaging can be made faster; more complex receive profiles in different receive coil elements at UHF are valuable for parallel imaging [7, 8] as they can help suppress noise amplification [9]. The reduction in SNR by the square root of the acceleration factor in parallel imaging is also compensated by the gain in intrinsic SNR at UHF [10].

Blood oxygenation level dependent functional MRI (BOLD fMRI) has been the principal method to investigate brain function since it was proposed [11]. Haemoglobin, the oxygen-carrying protein in red blood cells, is diamagnetic when oxygenated but paramagnetic when deoxygenated. The BOLD contrast relies on this susceptibility difference between the oxygenation states of haemoglobin, which is increased at higher field strengths. Therefore, BOLD fMRI benefits from the increase in both susceptibility and intrinsic SNR at UHF.

^{1}H magnetic resonance spectroscopy (MRS) is able to provide vital information about human metabolism. Low concentration of metabolites compared to water (approximately 10^5 times lower) limits the spatial resolution and lengthens the MRS acquisition. UHF is beneficial to MRS in two ways. First, increased intrinsic SNR increases measurement precision and allows for reduced voxel sizes. Second, the increased

chemical shift dispersion between metabolite peaks facilitates peak assignment and quantification. Whereas single-voxel MRS is often used at lower field strengths, these advantages at UHF make spectroscopic imaging (MRSI) more accessible. Hangel *et al.* demonstrated the feasibility of achieving MR imaging resolution (1.7×1.7 mm^2 in-plane) in a clinically feasible scan time [12].

Magnetic resonance of X-nuclei (non-proton nuclei such as ^{23}Na and ^{31}P) can be used to study human physiology and metabolism. However, at lower field strength, X-nuclei MR is severely limited by the significantly lower natural abundance in the human body. Unlike ^{1}H, X-nuclei experience shortened T_1 due to chemical shift anisotropy. Moreover, since X-nuclei have much lower Larmor frequencies for a given field strength, SNR increases almost quadratically with increased field strength.

Despite its successes, major challenges remain for UHF MRI. Since the resonant frequency of an MR-sensitive nucleus is proportional to field strength ($\nu = \gamma B_0$), the on-resonance RF wavelength decreases at UHF. The RF wavelength at UHF for the ^{1}H nucleus (roughly 12 cm at 7 T) is comparable to the size of the human body. Consequently, interference occurs, causing an inhomogeneous RF transmit (B_1^+) [and receive (B_1^-)] field [13]. Conductivity is primarily responsible for the characteristic asymmetries in B_1^+ and B_1^- maps, with some dependence on permittivity [13]. Inhomogeneity in B_1^+ causes spatially varying flip angles when using fixed-frequency pulses, causing undesirable perturbations in signal and contrast. Specifically for neuroimaging, a strong "centre brightening effect" is observed for UHF MRI in the brain [14].

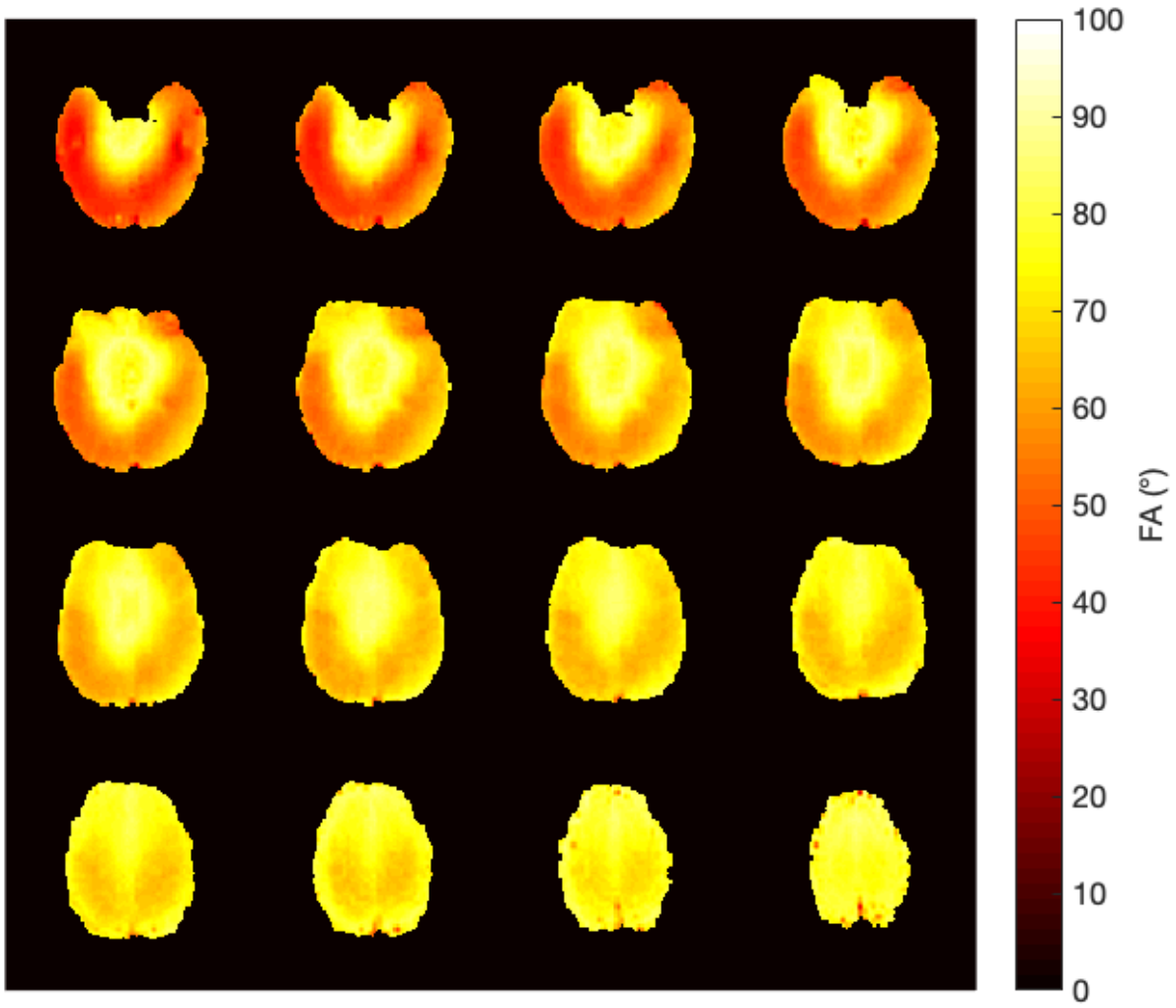


Figure 2.1: A typical flip-angle (FA) map in the brain at 7 T for an RF pulse with a nominal flip-angle of 90 degrees.

Although the increased effect of magnetic susceptibility at UHF is beneficial to susceptibility-based contrasts (e.g. BOLD fMRI), susceptibility-induced artefacts are detrimental to image quality. These artefacts manifest in images as intravoxel signal loss and geometric distortion [4]. These artefacts are conventionally mitigated by B_0 shimming, but the typically installed 2nd order spherical harmonics shims are not sufficient to correct the increased B_0 inhomogeneity at UHF. A possible technological solution at UHF [15] is dynamic shimming [16], also known as dynamic shim updating, where shim parameters are updated when acquiring each slice. However, to accomplish this specialist shim hardware which allows fast current switching is required.

Specific absorption rate (SAR), defined as the power absorbed per-unit-mass of tissue, is used as a surrogate measurement of tissue heating for patient safety [17]. SAR is approximately proportional to the square of the resonant frequency [3]. Therefore, for a

given pulse sequence the likelihood of reaching SAR limits at UHF is greater than at lower field strengths. More detailed discussion on SAR can be found in Section 2.4.

2.2. B_0 and B_1^+ mapping

Successful pTx applications require knowledge of the static field (B_0) distribution and B_1^+ field of each of the RF transmit channels.

The B_0 distribution is conventionally mapped by acquiring two gradient-echo images with different echo times. The phase difference between the two images is linearly dependent on the difference of local precession frequency. Knowledge of the echo time difference allows the calculation of the B_0 field offset. Traditionally, this phase difference is obtained by calculating the phase of the complex division of the two echoes. However, since the range of a phase image will always be [-π, π], phase unwrapping must be performed, so that phase wraps do no not appear in the final frequency map.

Mapping the B_1^+ field at UHF is challenging due to the large dynamic range (approximately 40-90 degrees in Figure 2.1). B_1^+ mapping techniques can be broadly divided into two categories: one where B_1^+ information is encoded in image magnitude, and the other where B_1^+ information is encoded in image phase. Common B_1^+ mapping methods include the following:

2.2.1. Actual flip-angle imaging

Actual flip-angle (AFI) imaging is a widely used B_1^+ mapping method for UHF MRI [18]. In an AFI sequence, two identical RF pulses are played out with different TRs. The ratio of the signal intensity of GRE images following these two RF pulses, *r*, is calculated. The ratio between the two TRs, *n,* is also computed. The flip-angle can then be calculated based on *r* and *n*.

Methods like AFI [18] are often time-consuming, as a steady-state spoiled 3D sequence with two TRs must be used for the imaging. For example, B_1^+ maps of 8 slices through the liver took 18 s using the AFI sequence, whereas they took 1.1 s using the DREAM

sequence [19]. Based on the experimental results, the working range of measured FA was 20°–70° [18]. However, tissues with long T_1 will have oversaturated signals in the raw images, thus leading to increased noise in the *r* map and FA map [18]. Furthermore, in the context of pTx, B_1^+ maps of individual channels have to be acquired sequentially, further increasing the acquisition time.

2.2.2. Bloch-Siegert shift

Bloch-Siegert shift mapping [20] is a phase-based B_1^+ mapping sequence. The Bloch-Siegert shift refers to the effect when the resonance frequency of a nucleus shifts in the presence of a strong off-resonance RF field [21]. This frequency shift is proportional to the square of the off resonance B_1^+ magnitude that is applied. Therefore, B_1^+ can be encoded in the image phase, since the Bloch-Siegert frequency shift results in accumulated phase during the pulse, observed as a change in image phase.

In a Bloch-Siegert shift B_1^+ mapping sequence, the off-resonance RF pulse is applied after an excitation pulse. The pulse shape and frequency of the off-resonance pulse are designed such that no direct excitation should occur at the sample resonant frequency. Bloch-Siegert shift mapping is a difference method, which requires two scans with positive and negative offsets. However, it is SAR intensive, as the off-resonance pulse amplitude must be high if it is to have a measurable effect at a sufficiently distant off-resonant frequency. It is therefore not commonly used at 7 T.

2.2.3. DREAM Fast B_1^+ mapping:

The dual refocusing echo acquisition mode (DREAM) sequence is a fast magnitude-based B_1^+ mapping method. In the DREAM sequence [19], a STEAM preparation module is placed before a low flip-angle (β) gradient-echo acquisition. The STEAM preparation module consists of two identical RF pulses of flip-angle α, a dephasing gradient and a spoiling gradient. The excitation pulse (with a flip-angle of β) produces signal from a stimulated echo of longitudinal magnetisation from the STEAM preparation, and a signal from the free induction decay (FID) of the unprepared longitudinal magnetisation.

DREAM is relatively robust against T_1 and T_2 variations, and is efficient since the two images required for B_1^+ sensitivity are acquired in the same TR.

Most B_1^+ sequences are normally applied on each transmit channel sequentially in the context of pTx. Therefore, the acquisition time of these methods needs to be increased by the number of transmit channels. Tse *et al*. proposed an encoding scheme to gain SNR per unit time in B_1^+ mapping at UHF [22], similar to methods proposed by Brunner and Pruessmann [23], Malik *et al.* [24], and Nehrke and Börnert [25]. In this method, Fourier phase encoding is applied to the transmit channels, whereby a regular but different phase step is applied to each channel per repetition. As a result, images acquired in each repetition include information from all channels, and per-channel B_1^+ maps are decoded as a post-processing step based on the complex encoding matrix. The relative phase maps can be obtained using a phase-preserving sum-of-magnitude reconstruction [19].

In the implementation by Tse *et al.*, the number of encoding steps in this method can be arbitrarily changed to allow for the trade-off between acquisition time and B_1^+ map resolution and/or accuracy. Moreover, since there is no restriction on phase settings, an encoding matrix using arbitrary phase settings can always be reconstructed as long as the number of measurements is larger than the number of coils [22]. When the number of measurements is larger than the number of coils, the encoding matrix is overdetermined, thus allowing suppression of unreliable measurements [22].

B_1^+ mapping techniques based on 2D slice-selective acquisitions may suffer from non-uniform excitation across the slice profile, which introduces significant errors to flip-angle based B_1^+ maps [26]. Effects due to a poor slice profile can be corrected by simulating the excitation profile based on the pulse shape [18]. However, the true excitation profile might differ from that produced by simulation due to factors such as variable relaxation properties and imperfect gradient pulses [18].

2.3. Mitigating the problem of inhomogeneous B_1^+ at UHF

2.3.1. Single channel solutions

2.3.1.1. Dielectric pads

Flexible “dielectric pads” filled with materials with high permittivity and placed between subject and RF coil have been used to mitigate B_1^+ inhomogeneity at 7 T by changing the distribution of the electro-magnetic (EM) field. Teeuwisse *et al*. quantified the performance of two dielectric pads placed on the sides of the head of the subjects [27]. *In-vivo* results showed pronounced (>100%) increase in transmit efficiency in brain regions close to the pads and moderate decrease (~10%) in the centre of the brain [27]. In addition, B_0 maps acquired with and without dielectric pads showed minimal differences [27].

Dielectric pads have also been used in combination with other B_1^+ strategies at UHF. O’Brien *et al*. combined dielectric pads and low-B_1^+ adiabatic pulses to T_1-weighted MPRAGE scans at 7 T [28]. Results showed that dielectric pads improved B_1^+ by ~50% in the cerebellum, and applying time resampled frequency offset compensated inversion (TR-FOCI) pulses in conjunction with dielectric pads produced reliable whole-brain T_1w structural images [28].

As a passive shimming method that can be easily implemented, dielectric pads have been incorporated in large-scale imaging projects such as the Human Connectome Project at UHF as well [29, 30]. Despite the benefits shown, dielectric padding offers limited degrees of freedom to mitigate B_1^+ inhomogeneity and to directly improve B_1^-. Dielectric pads are able to improve SNR in some brain regions, but such improvements are not spatially uniform. Furthermore, it is difficult to place the dielectric pads reliably using only visible anatomical features, and impractical to optimise their position once the subject is in the scanner.

2.3.1.2. Coil design and fixed phase shimming

In early studies, phase shimming was enabled in the absence of multiple independent RF power amplifiers [31]. In the implementation by Metzger *et al*., a single RF amplifier is used in conjunction with an eight-way splitter [31]. A phase shifter is then inserted between the splitter and the transmit/receive switch for each transmit channel to allow phase shimming [31].

A computational study by Lattanzi *et al.* showed that electric dipole-like current patterns could provide high SNR and low SAR while achieving a homogenous excitation profile using RF shimming at UHF [32]. Dipole antennae have then been used for body imaging [33], cardiac imaging [34], and brain imaging [35]. Ertürk *et al.* recently developed a 16-channel combined loop-dipole transceiver array at 7 T [36]. The combination of loop and dipole arrays allowed for higher channel count and density than could be achieved by using loop arrays alone [36]. A larger number of coils with distinct spatial profiles will benefit pTx strategies for mitigating B_1^+ inhomogeneity.

2.3.1.3. RF pulse design

Spatially selective excitation can be achieved by depositing RF energy at various locations in spatial frequency space, and by building up spatial patterns via spatial Fourier modulation. Therefore, RF pulses can be designed with an appropriately spatially-varying target magnetisation to mitigate the B_1^+ inhomogeneity present when applying basic slice-selective and non-selective RF pulses.

Tailored RF pulse design can be used to mitigate B_1^+ inhomogeneity on a single channel system. Spokes pulses were used to improve simple slice-selective pulses [37] and simultaneous multislice excitation pulses [38]. k_T-points were used to improve T_2-weighted imaging [39, 40]. Although these methods can reduce B_1^+ inhomogeneity, the same methods would have enhanced effects when applied on a pTx system. More details of these approaches will be covered in the next section.

The use of adiabatic pulses [41] is another option to manage B_1^+ inhomogeneity at UHF since they are relatively insensitive to B_1^+ variations. The flip-angle achieved by an adiabatic pulse is not simply proportional the pulse amplitude or pulse length. Rather, it depends on how the B_1^+ amplitude and phase vary during the RF pulse. Adiabatic pulses were optimised for excitation [42] and refocusing [43] at 7 T, and they are widely used in magnetic resonance spectroscopy [44-46]. However, adiabatic pulses are normally longer in duration than constant-frequency pulses, and deposit higher SAR. Moreover, sufficient B_1^+ strength (and hence deposited power) must be available for the adiabatic condition to be met.

2.3.1.4. Sequence design

Gradient-echo (GRE) sequences still show adequate contrast and minimal centre-brightening, even with relatively large deviations in flip-angle at UHF. However, they are T_2* sensitive, and have lower SNR compared to steady-state free precession (SSFP) sequences. In addition, although T_1- or T_2-weighted scans could be acquired using GRE sequences, B_1^+ inhomogeneity has to be solved for quantitative imaging or sequences involving sensitization modules (e.g. tagging, inversion recovery, T_2 preparation). Therefore, a better solution that covers a broader range of MRI pulse sequences (with higher flip angles) is needed.

2.3.2. Parallel transmission (pTx) schemes

The most flexible solution to B_1^+ inhomogeneity at UHF is via the use of parallel transmission (pTx). A pTx-enabled system has more than one RF transmit channel which may be independently driven [3]. The operator has full control of the amplitude and phase modulation of each channel, furthermore independent pulse waveforms may be transmitted on each channel. Katscher and Zhu first introduced the concept of pTx by applying the principles of receive parallel imaging to RF transmission, dramatically decreasing the RF pulse duration of complex spatially-selective pulses [47, 48]. This is because each transmit channel has a distinct transmit profile that can be exploited to produce spatially varying B_1^+ distribution, similar to the benefits of multiple receive coils in parallel imaging. pTx has been used to create homogeneous excitation across a slice, a slab, or a volume, as well as for local excitation and reduced field-of-view (FOV) imaging [3].

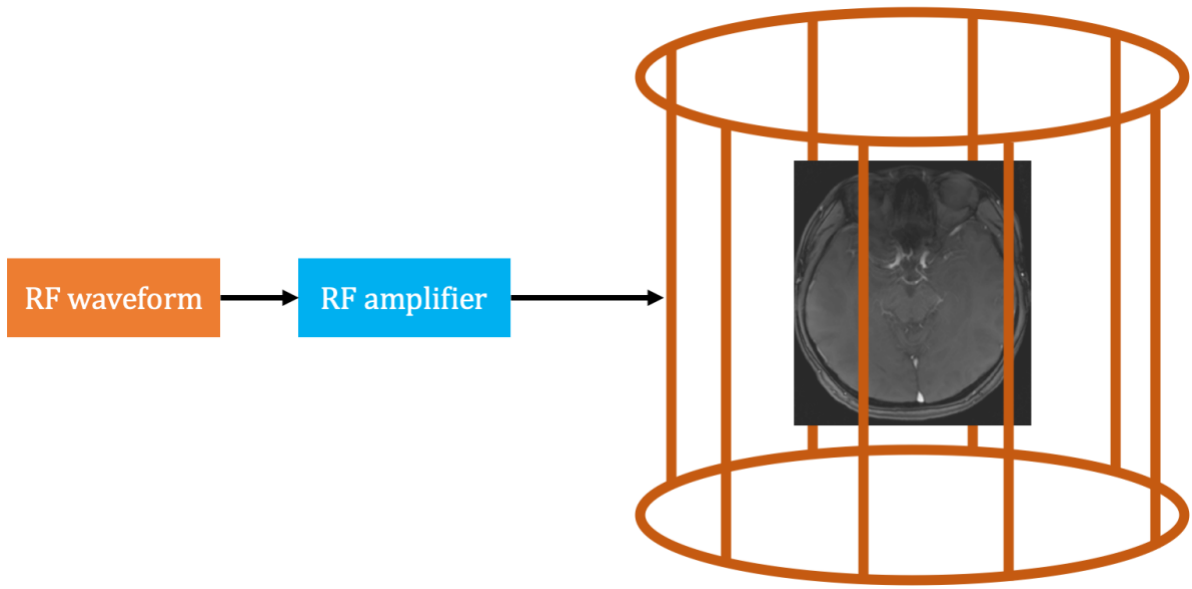


Figure 2.2: Schematic of the transmit chain of a single channel system. In a single channel system, there is only one RF amplifier that produces the same RF waveform to be transmitted in each transmit coil element. Fixed phase shifts might be applied to each channel.

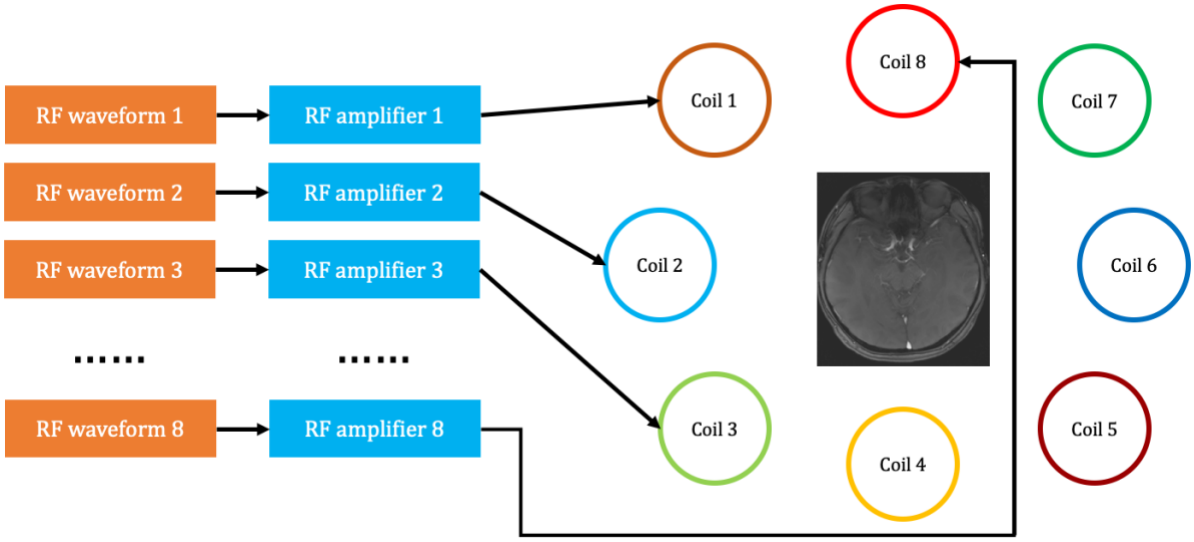


Figure 2.3: Schematic of the transmit chain of parallel transmission (pTx) system. In a pTx system, there is several RF amplifiers that produce the different RF waveforms to be transmitted in different transmit coil elements.

The simplest formulation of pTx is "static pTx", also commonly referred to as RF or B_1^+ shimming. In this case, different RF channels share the same pulse envelope and timings, but are driven with different complex weights to achieve a homogenisation of the flip-angle in a target region-of-interest (ROI). The shim may be applied to all the RF pulses in a sequence, or only to selected pulses. RF shimming has been used to image the heart [49], the brain [50], and the prostate [31]. Phase shimming, a sub-type of RF-shimming where only the phases of the complex weights are allowed to change, has also been used [51].

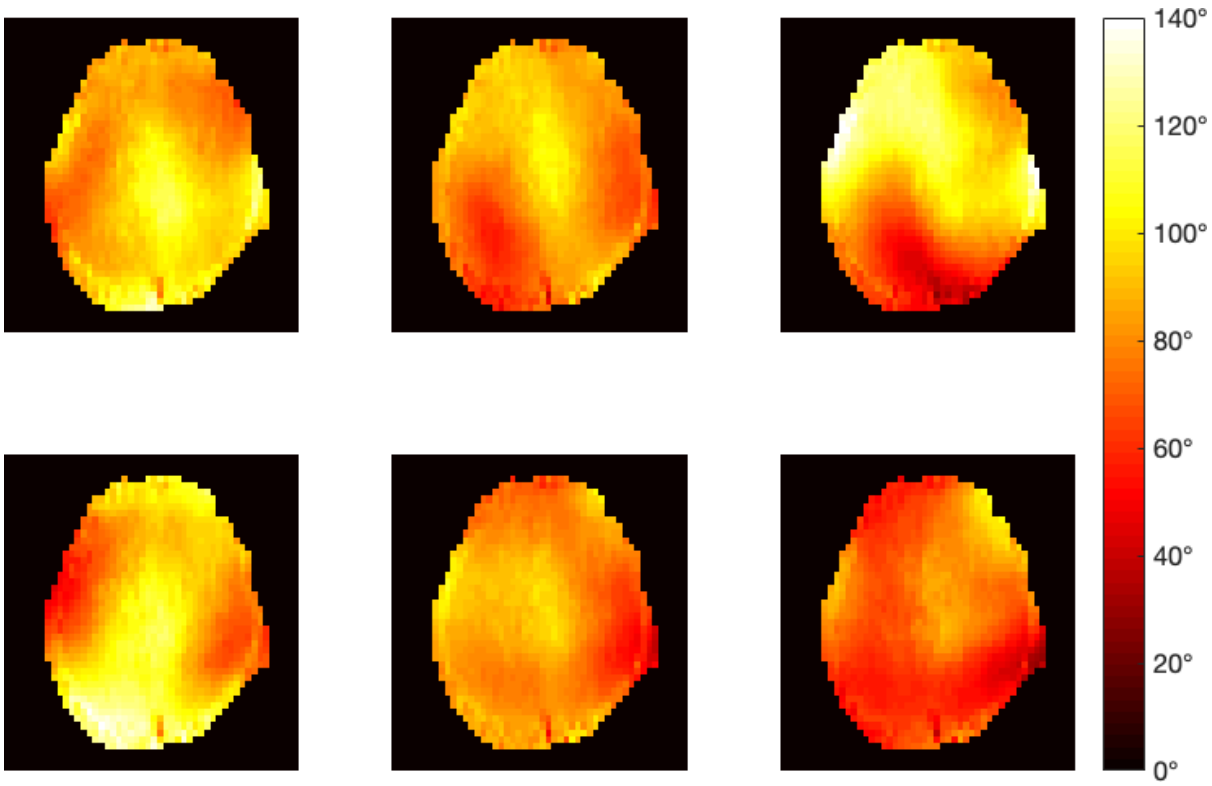


Figure 2.4: Simulated FA maps based on acquired B_1^+ maps. Six randomly generated RF shims were applied on a hard RF pulse for the simulation.

Static pTx is insufficient to mitigate B_1^+ inhomogeneity over a large ROI due to its limited flexibility: it is merely a linear combination of the coil sensitivities, with high correlation between voxels. Achieving a homogeneous magnetisation profile over a 3D volume covering a whole organ or a large ROI requires additional degrees of freedom. "Dynamic pTx" attempts to accomplish this by directly optimising arbitrary RF, optionally with gradient-blipped pulse schemes conceived using the "excitation k-space" formulation [52]. Many gradient trajectories have been implemented for dynamic pTx including: spokes [53] for homogenous slice selection, and spiral non-selective (SPINS) [54] and k_T-points [55] for homogenised volume pulses.

Setsompop *et al*. applied spokes pulses [56] with a pTx system at 7 T based on a magnitude least-square optimisation algorithm [57]. Like conventional slice selection, within each spoke, a sinc (or other frequency selective) pulse is played out in the presence of a constant gradient. In excitation k-space this can be viewed as a straight line (spoke) traversing through k-space in the k_z direction. But unlike conventional slice selection, the complex weight of each RF channel is modulated to achieve a homogenous B_1^+

distribution. Between the spokes, a gradient blip moves the subsequent spoke to a different k_x-k_y location. The number of spokes can be chosen based on the variation of B_1^+ and the size of the target ROI. Results showed that the standard deviation of the FA within a brain slice was 16.7% for conventional excitation, 13.3% for RF shimming, and 7.6% for spokes pulses across 6 subjects [57].

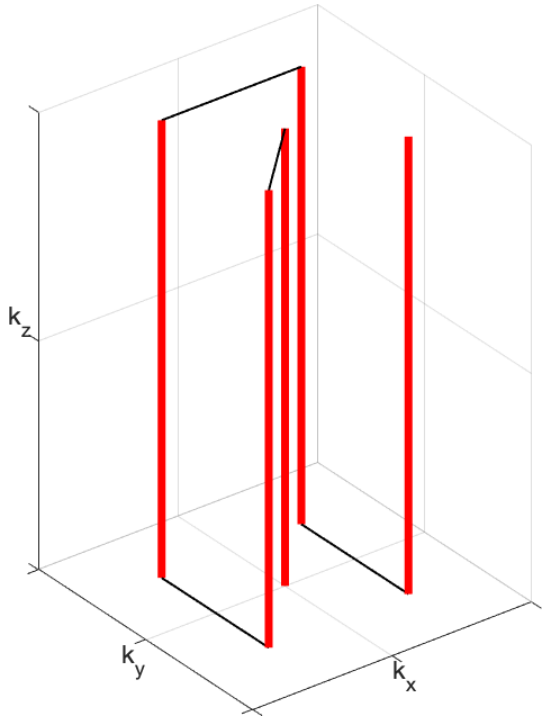


Figure 2.5: Excitation k-space trajectory of spokes excitation (5-spoke) pulses in 3D. Red lines indicate when RF is being played out. Black lines connect the individual spokes and indicate gradient only periods.

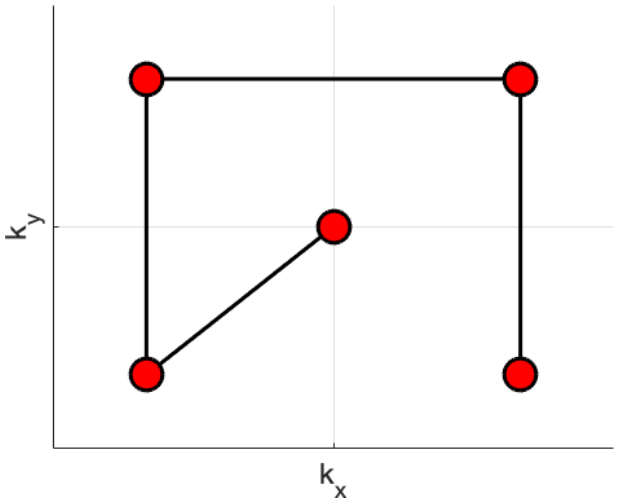


Figure 2.6: Excitation k-space trajectory of spokes (5-spoke) excitation pulses projected on the k_x-k_y plane.

Cloos *et al*. introduced k_T-points, where non-selective subpulses are played out at various specified k-space locations and time points, or k_T-points, in order throughout 3D

excitation k-space [55]. Results showed that k_T-points pulses were able to achieve a flip-angle variation of only 8% (standard deviation over mean) in the whole brain at 7 T, compared to 33% for circularly-polarised mode excitation [55]. The simple and low area gradient trajectories of k_T-points do not rely upon high-performance gradient systems. In addition, although the concept of k_T-points was first demonstrated in the context of pTx, it could similarly be applied on a single channel system to mitigate B_1^+ in homogeneity [40].

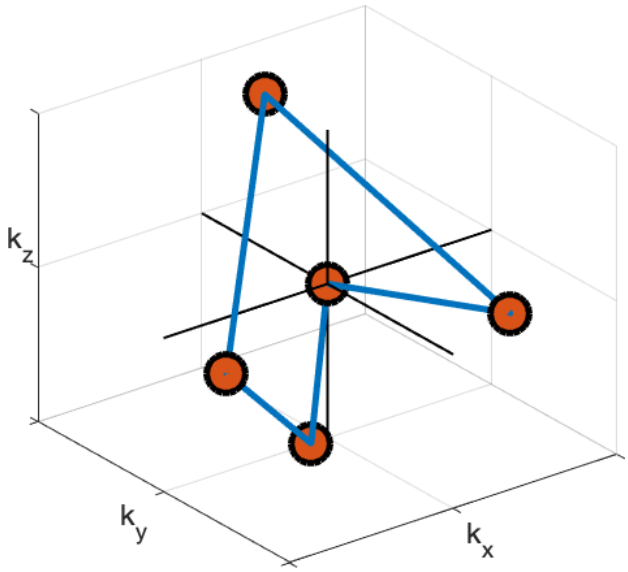


Figure 2.7: Excitation k-space trajectory of k_T-points.

2.3.3. pTx pulse design

To effectively use pTx to mitigate subject-specific B_1^+ inhomogeneity an estimate of the subject-specific B_1^+ and B_0-fields is required. These "field maps" may be either measured using dedicated mapping sequences (see Section 2.2), estimated from other contrast scans or assumed from prior knowledge or data. Subsequently, pulses may be designed using the Bloch equations to describe the behaviour of magnetisation under the effect of the designed pulse and gradient scheme at each spatial location simulated [58]. The Bloch equations may be simplified using the "small-tip-angle" (STA) simplification when the flip-angle is small (< 90 degrees) [52]. Under the STA approximation pulse design may be sped up using a system matrix approach [59]. A target ROI can also be readily introduced

in the pulse design within the total field of excitation [59]. Detailed discussions of the pulse design problem can be found in Chapter 3.

The pulse calculation is usually formulated as an optimisation problem that minimises the error between the target and achieved magnetisation state, within the target ROI. The complexity of the optimisation problem varies depending on the chosen pTx strategy. In approaches such as RF shimming, spokes and k_T-points, the shape of the sub-pulse is pre-defined. Therefore, only the complex weights of individual sub-pulses are calculated. In methods such as SPINS, the RF amplitude of each channel at each time point can be modulated arbitrarily. Regularisation terms or hard limits on RF power (as a surrogate for SAR) or SAR can also be added to the cost function or optimisation. More discussion of SAR in regard to pTx pulse design can be found in the next section.

2.4. Specific absorption rate (SAR)

2.4.1. SAR monitoring in MRI

2.4.1.1. Monitoring local power deposition by monitoring global power

RF power deposition in the human body causes tissue heating. However, measuring tissue temperature directly during an MRI scan is not trivial. Since real-time EM simulations are not possible, a pre-simulated EM model based on a realistic body model and the electrical properties of the coil is generally used in practice. Before scanning, a look-ahead prediction is done by retrieving information on RF power and patient weight from the sequence files and the console. Additional hardware monitoring stops the sequence in real time if global SAR is exceeded.

2.4.1.2. Power monitor

The mechanism of heat dissipation is complex in the human body and cannot be easily modelled. Therefore, SAR is often used as a surrogate measurement of tissue temperature increase. The SAR in a sample is defined by the following equation:

Equation 2.3

$$SAR = \frac{\sigma \parallel \boldsymbol{E} \parallel^2}{2\rho}$$

where σ is the sample conductivity, E is the electric field, and ρ is the mass density. Average SAR of a given volume can be written as:

Equation 2.4

$$SAR = \frac{1}{V}\int_{volume} \frac{\sigma(\mathbf{r})|\boldsymbol{E}(\mathbf{r})|^2}{2\rho(\mathbf{r})} d(\mathbf{r})$$

where V is the volume and $\mathbf{r}$ is the 3D position vector.

The International Electrotechnical Commission (IEC) set requirements for SAR deposition. The limit in the head is 3.2 W/kg for global SAR, and 10 W/kg for local 10 g SAR [60]. The 10g SAR is defined as the SAR averaged over any 10g of tissue [60]. SAR is often averaged over time, typically over periods of 10 seconds and 6 minutes.

Furthermore, the IEC guidelines define three modes of operation: normal operating mode, first level controlled operating mode, and second level operating mode. The normal operating mode is defined as: "mode of operation of the MR equipment in which none of the outputs have a value that may cause physiological stress to patients". First level controlled operating mode is defined as: "mode of operation of the MR equipment in which one or more outputs reach a value that may cause physiological stress to patients which needs to be controlled by medical supervision". Second level operating mode is defined as: "mode of operation of the MR equipment in which one or more outputs reach a value that may produce significant risk for patients, for which explicit ethical approval is required (i.e. a human studies protocol approved to local requirements)".

SAR monitoring on a single-channel system can be achieved by combining one-time electromagnetic field simulations of body voxel models for a specific coil with a single point power measurement of forward (and reflected) RF power. The same RF waveform is played out on every transmit coil element and is subject to fixed power attenuation and

phase relationships (i.e. there is a fixed and known relationship between all the coil elements). Therefore, the spatial E-field profile is invariant. Rather, it only scales in magnitude with coil loading (dependent on the subject) and the instantaneous RF power. Given this, a single simulation may be performed to determine the instantaneous SAR per unit power. This can further be expressed as a single transmit-coil-dependent SAR parameter. This parameter is then used to provide a time-averaged SAR once suitably scaled by power monitor inputs, and once coil loading is taken into account by measuring the forward and reflected RF power for each subject.

A power monitor on a single transmit channel system measures the forward and reflected power of the RF transmission, which is then translated to a power deposition figure in the body using a single pre-calibrated number from a simulation of a body in the coil.

2.4.1.3. Electromagnetic Field Simulations for MRI

To predict the spatial distribution of SAR, electromagnetic (EM) field simulations of the transmit coil are needed to generate estimates of the E-field distribution in a representative virtual human (or virtual human population). Predicting the SAR using EM simulations requires solving Maxwell's equations. A number of software packages are available for biophysical EM simulation and either use FDTD (finite difference time domain), FEM (finite element modelling) or IE (integral equations) to solve Maxwell's equations numerically. These are Sim4Life [61] and Remcom [62] (FDTD), Ansys Electronics [63] and CST Microwave [64] (FEM), and MARIE [65] (IE). FDTD requires a realistic and detailed tissue model in voxel form. FEM allows a varying mesh size: from ~1m outside of tissue, to ~100 μm around fine anatomical details. IE methods are extremely fast to compute and have use for fast coil prototyping [65].

Despite recent advances in EM simulation for MRI, generating tailored EM models for individual subjects is not realistic during a scan session. Faster segmentation, simplified tissue model and the adoption of GPUs might further accelerate tailored EM simulation in the future.

Simulations must be carried out on virtual models representative of the population to be scanned. The body models must both be realistic (and accurate) and encompass a range of anatomical variation (e.g. gender dimorphism, age, and weight ranges). The Virtual Population from Sim4Life provides 10 different high-resolution body models for individuals of different age, gender and size. On a single channel system, a population of models can be merged into a single measurement by taking the worst case of all models. Virtual models must also capture changes in anatomy associated with pathology or clinical treatments. For example, safety assessment for patients with implanted medical devices for MR scans has become a pressing issue in the MR safety community with the increasing prevalence of implants in the population. A "virtual DBS population" has recently been proposed to allow EM simulation of deep brain stimulation patients [66].

2.4.1.4. Estimation of power deposition in the body as a surrogate of tissue heating

Even though SAR monitoring is implemented on MR scanners, it is only a surrogate measurement of tissue heating. The IEC impose SAR limits (a head average limit of 3.2 W/kg and a 10-g average limit of 10 W/kg) with the intention of limiting temperature increase [60]. In addition, the IEC stipulates that local temperature in the head should not exceed 38°C, and that the temperature rise in body core should be limited to 1°C in the first level controlled mode [60]. Modelling temperature increase due to RF power deposition might be inaccurate, as heat production (such as via metabolism) and heat loss (such as via perfusion and conduction) cannot be easily measured/estimated. MRI methods that measure cerebral perfusion such as arterial spin labelling might aid the modelling of temperature change in the brain. However, specific anatomy, namely the non-perfused cornea and vitreous humour of the eyes, are commonly found to be the most limiting tissue [67].

Massire *et al*. performed thermal simulation for a 16-channel coil at 10.5 T using temperature-dependent formulations for sweat, perfusion and metabolism, and showed that a peak 10-g SAR could result in a large range of temperature increases [68]. The study found that although temperature increase was minimal in the well-perfused brain under a 10 W/kg 10-g SAR limit, the maximum temperature increase was more than 1°C

in the eye. The temperature change in the subject should ideally be monitored during an MRI scan, but performing such calculations in real time is impractical. Therefore, RF pulses could in principle be designed with a spatially varying local SAR limit. This SAR limit could be more relaxed for the brain but should be more conservative for the eyes. Moreover, Massire *et al*. suggested that averaging SAR over a long period of time might not be appropriate. This is because the trajectory of maximal local temperature simulated from individual SAR maps did not match that calculated from a time-averaged SAR map. Further *in-vitro* studies or MR thermometry [69] experiments might be needed for validation of this approach.

2.4.2. SAR monitoring in pTx

pTx presents additional complexity to SAR estimation. On single-channel systems, total power delivered to the coil (global SAR) is monitored, with local SAR estimated using a scaling calculated from one-time field simulations. In pTx, where each channel's *B* and *E*-fields may be combined with arbitrary phase and magnitude, this approach fails, as no unique local maximum exists for all combinations [70]. Therefore, there is no fixed relationship between global monitored power and peak local SAR.

Spatially resolved SAR monitoring for pTx requires the calculation of the E-field in all spatial locations over time based on the individual arbitrary RF waveforms from all the transmit channels, which are measured by power monitors on each channel with readings sampled using directional couplers on the Siemens system.

However, such an exhaustive search across all spatial locations in real time during a pTx scan is impractical due to the high computational cost [70]. Fortunately, the recently developed virtual observation points method could greatly accelerate such calculations.

2.4.2.1. Virtual observation points (VOPs)

Eichfelder *et al*. introduced the concept of virtual observation points (VOPs) to significantly compress the number of points needed to evaluate local SAR [70]. Empirically, "hot spots" are located in only in a few regions of the body. Thus, the authors

attempted to cluster local SAR subvolumes into so-called VOPs, such that the maximal local SAR of all subvolumes was upper bounded by the maximum local SAR of the VOPs. Instead of categorising subvolumes based on their locations and tissue compositions, the formulation of this proposed method was purely mathematical. The objectives for the classification were to minimise the number of VOPs (to minimise computation time), and to estimate local SAR without underestimation and with controlled overestimation.

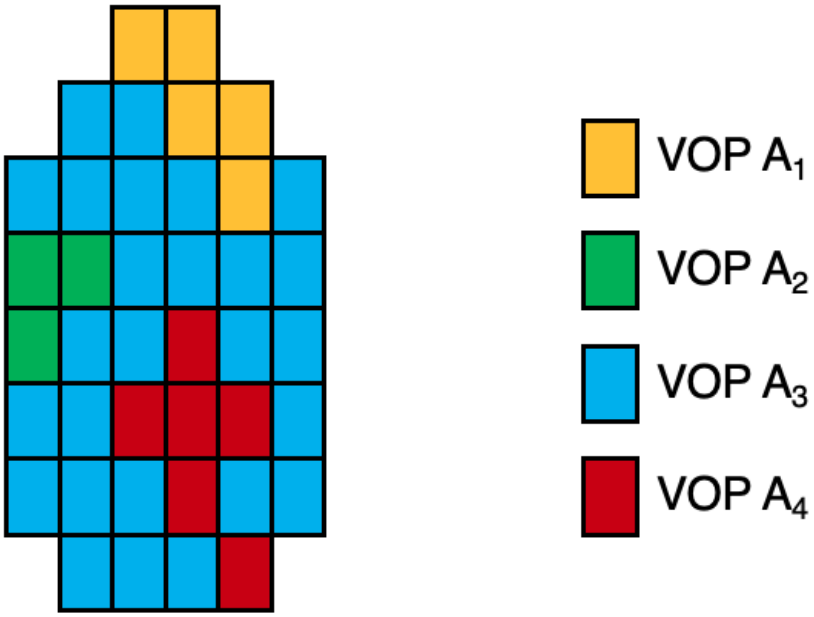


Figure 2.8: A 2D illustration of the concept of VOPs shown on a brain slice in axial view. In this example, the voxels in the slice are categorised into 4 VOPs. This figure is adapted from Fig. 1 of the work by Eichfelder et al. (doi: 10.1002/mrm.22927).

The approach proposed by Eichfelder *et al*. has had a profound impact on SAR supervision and RF pulse design at UHF. An exhaustive search of maximum local SAR over all subvolumes can be reduced to the consideration of roughly several hundred VOPs, providing a compression factor of between 1,000 to 13,000. Computation time reductions of such magnitude allows the possibility of incorporating local SAR into real time online monitoring, into RF pulse design, and even designing RF pulses with a target of minimising local SAR.

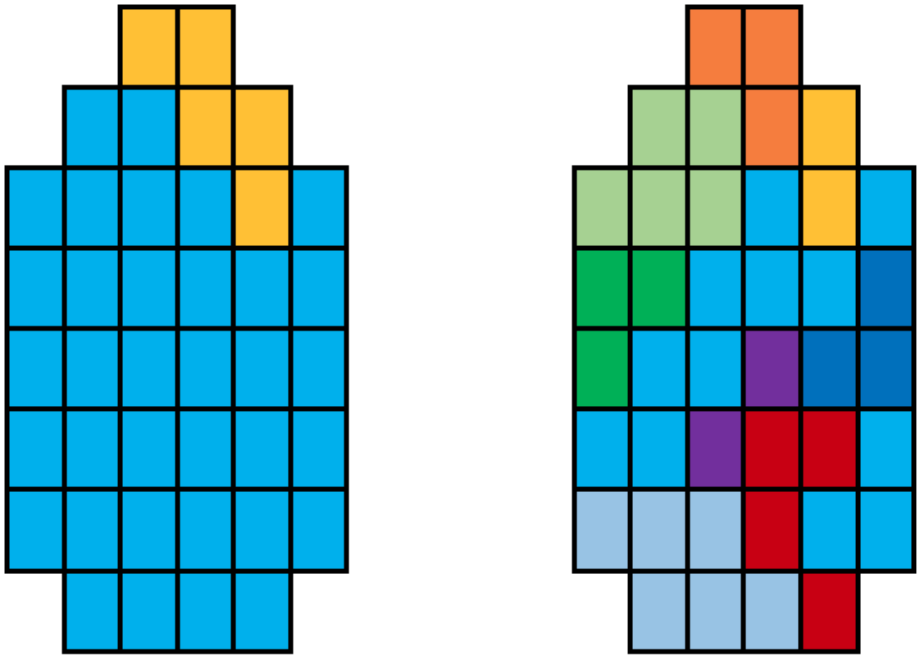


Figure 2.9: A 2D illustration of 2 (left) and 8 (right) VOPs of a brain slice in axial view. Having a large number of VOPs will reduce the amount of SAR overestimation but lengthens the calculation time. This figure is adapted from Fig. 2 of the work by Eichfelder et al. (doi: 10.1002/mrm.22927).

RF pulses specifically designed for pTx could provide a solution to SAR increase at UHF by generating spatially varying RF fields to dynamically adjust the locations of hot spots [3]. SAR could also be treated as an optimisation target, and direct global or local SAR constraints have later been applied during pTx pulse calculation [71-80]. More sophisticated approaches have taken direct estimation of tissue temperature into account [81, 82].

While VOPs offer a potential solution to the issue of online monitoring, they do not validate the EM simulation results. Since the virtual models used for the simulation are always different from the actual subject in a particular scan, additional safety margins have to be included. Subject-specific online monitoring requires rapid EM simulations based on segmented tissue maps from structural images, which cannot be done during a scan at the moment due to computational costs and difficulty in estimating body composition on an individual level.

2.4.3. Specific limits for the 8Tx32Rx Nova head coil on the Magnetom 7 T

Throughout this work the Nova Medical Inc (Wilmington, MA, USA) 8Tx32Rx head coil was used in the vendor-defined "protected mode". In this mode local SAR is not monitored directly. Rather, this mode implements SAR limits as global and per-channel power limits. These limits assume the worst case heating from simulations (the shim which produces the most heating), or imposes some very stringent safety margins. Specifically, the 6 min and 10 s average sum of channels power limit are set to 12.39 W and 24.78 W (as measured by the Power Absorption Limiter Multi Channel, PALI MC), respectively. The power limits, provided by the coil vendor (Nova Medical) in agreement with the scanner vendor (Siemens), are based on a limit at the coil plug (20 W/10 W for 10 s/6 min for the sum of all channels, respectively) and include a calibration factor for cable losses. In addition, there is a per-channel limit on average power (3 W/1.5 W for 10 s/6 min, respectively) and the instantaneous forward power (1250W). In practice, it is usually the sum-of-channel power limit that is exceeded first.

On the single-channel system (Combined Mode), the 6 min and 10 s average power limit are set to 23 W and 46 W. As such, the "protected mode" represents a very restrictive mode to work under for pTx use, since even in an equivalent circularly polarised (effectively single-channel) mode the SAR limits are reached much more quickly for the pTx coil than for the single-channel coil.

When operating under the conservative "protected mode", the responsibility of ensuring patient safety is assumed by the coil and scanner vendors. However, that responsibility falls onto the institution when operating under "experimental mode", whose RF power limit is double compared to "protected mode". Under "experimental mode", local power monitoring is performed (utilising the VOP framework to perform real time monitoring), and local SAR limits are applied, which could be more restrictive than the (more permissive) global limit. The decision of whether to adopt "experimental mode" is made at each Siemens Magnetom 7 T site. The 7 T scanner at the Wellcome Centre for Integrative Neuroimaging, where the work of the thesis was carried out, was not approved to operate under "experimental mode" at the time of submission. Extensive

work on the validation of the EM simulations is needed before the adoption of "experimental mode" is permitted. Such work should, for example, include: 1) thermometric measurements on a meat phantom; 2) a comparison between predicted vs measured B_1^+ maps; and 3) an investigation into whether simulations cover the full range of potential subjects to be scanned with pTx.

2.5. Incorporation of pTx pulses in conventional sequences

Early pTx studies focused on B_1^+ inhomogeneity mitigation [83] or reduced FOV imaging [59], as well as optimisation strategies of RF waveforms [84] and k-space trajectories [85]. More recently, pTx approaches have been incorporated into magnetic resonance fingerprinting (MRF) [86], diffusion MRI [87], functional MRI (fMRI) [88], and chemical exchange saturation transfer (CEST) [89]. Simultaneous multislice (SMS) pulses have been recently combined with pTx to produce uniform excitation of several slices [87, 90-94].

Magnetic resonance fingerprinting (MRF) is a quantitative MRI method that measures tissue parameters by applying a pseudo-random acquisition and then matching the resulting signal to a dictionary of signal evolutions from different T_1, T_2, and B_0 values [95]. A pattern recognition algorithm is used to match the acquired signal to a specific dictionary entry [95]. However, at UHF, severe B_1^+ inhomogeneity presents additional sources of signal variation. Cloos *et al*. introduced a method called "Plug-and-Play MR Fingerprinting (PnP-MRF)" that plays out two modes of excitation and encodes the B_1^+ distribution into the fingerprints [86]. Rather than treating the B_1^+ inhomogeneity as a source of error, PnP-MRF views it as a feature of the signal evolution, similar to T_1, and T_2. Unlike conventional pTx methods, no calibration scan or pulse calculations were needed in PnP-MRF. Results showed that multi-parametric mapping was possible even in the presence of B_1^+ inhomogeneity using the proposed method.

Time-of-flight (TOF) imaging is a non-contrast-enhanced angiography technique that benefits from higher intrinsic SNR and longer T_1 at UHF. Longer T_1 at UHF allows for better background suppression, but increased B_1^+ inhomogeneity produces variations in contrast. Schmitter *et al*. adopted RF phase shimming (B_1^+ phase shimming) for both the

slab-selective excitation pulse and the slab-selective saturation pulse at 7 T [51]. A trade-off between B_1^+ uniformity and B_1^+ efficiency can be made in the optimisation algorithm, and B_1^+ uniformity was improved by a factor of 2.2-2.6 for different shim settings [51]. In another study, Schmitter *el al*. further improved the excitation uniformity by applying a two-spoke pulse design, resulting in improved contrast [96]. Saib *et al*. extended the two-spoke approach to Tilted Optimised Non-saturating Excitation (TONE) pulses in TOF angiography [97].

Wu *et al*. applied multi-band pTx pulses on a Human Connectome Project (HCP)-style diffusion sequence [87]. Improved B_1^+ uniformity allowed for both more accurate estimation of multiple fibre orientation and a higher multiband factor to be achieved [87].

2.6. Recent developments

2.6.1. Designing multiple pTx pulses

While most pTx pulse design strategies involve designing one RF pulse at a time, typical MRI sequences consist of many pulses that interact with each other to determine the overall signal [3]. Instead of treating each RF pulse in isolation, Malik *et al*. proposed the direct signal control (DSC) approach to directly manipulate received signal through an entire imaging sequence [98]. The DSC method could be thought of as signal shimming, as opposed to flip angle shimming, optimising the complex weights of every RF pulse, on each channel, in one optimisation [3].

2.6.2. Universal pulses

Several preparation steps must take place before running a pTx scan: acquisition of B_0 and B_1^+ maps, data extraction, data processing, and pulse calculation. The pulse calculation time could be further prolonged when optimising for a large flip-angle, since the small tip-angle approximation is no longer reliable, and a full Bloch equation is needed for each iteration of the optimisation. Although pulse calculation can be sped up by using increased computing resources (particularly when using graphics processing units), acquisition times of B_1^+ and B_0 mapping sequences may not be. Therefore, despite

the improvement in image SNR and CNR when adopting pTx approaches, the calibration time required, which can be in the region of 10-20 minutes, remains a major obstacle for wider adoption.

Recently, Gras *et al*. proposed the concept of "universal pulses" to circumvent the preparation steps altogether [99]. B_0 and B_1^+ measurements were acquired from six subjects to be used in the design of the universal pulses. k_T-points pulses were then designed for a small FA (9°) and large FA (180 °) that would be optimal for all six subjects. Six other subjects were subsequently scanned using an MPRAGE sequence incorporating the universal pulses, without any knowledge of B_0 and B_1^+ field distribution. Universal pulses outperformed circularly polarised (CP) mode and RF shimming for both excitation and inversion pulses in excitation normalised root-mean-square error (NRMSE) and image quality, with a slight degradation compared to subject-specific design.

Gras *et al.* explored the generality of universal pulses by applying this concept on two commercial coils (Rapid-Biomed and Nova Medical) at two sites [100]. Universal pulses were incorporated into MPRAGE and 2D GRE protocols, and overall signal and contrast uniformity was improved compared to CP mode [100]. FA deviation was less than 11% for universal pulses in all subjects at both sites, whereas FA deviation exceeded 25% for CP mode [100].

Gras *et al.* also introduced a T_2 preparation module using universal pulses for a 3D FLAIR sequence [101]. This approach eliminated the need for adiabatic inversion pulses, thus reducing SAR by 6 fold [101]. Universal pulses have recently been integrated into a Human Connectome Project (HCP) style resting-state fMRI (rs-fMRI) sequence [102]. Compared to single channel excitation, the proposed method achieved a tSNR improvement of a factor of 2 in the temporal lobes .

Although universal pulses proved to be a powerful calibration-free method of mitigating B_1^+ inhomogeneity at UHF for non-selective pulses, applying the same principle to slice selection or inner volume excitation is more difficult. This is because although overall B_1^+ patterns in the brain are similar across subjects, B_1^+ distribution at a particular slice or slab might be very different depending on the exact position and the size of the subject.

2.6.3. Machine learning in pTx pulse design

An alternative to overcoming the challenge presented by the calibration time of designing tailored pTx pulses is to apply machine learning for shorter calculation time. Machine learning approaches could learn the procedures of the of pulse design in the training stage, and produce results extremely quickly in the prediction stage.

Ianni *et al.* proposed an alternative approach based on machine learning to avoid the long preparation time in conventional pTx scans [103]. Ianni *et al.* claimed that "universal pulses" traded homogeneity for simplicity (by eliminating the calibration steps), as pTx pulses cannot be universal and tailored at the same time [103]. The Ella and Duke head phantoms were scaled to produce 100 "subjects", and a vector containing features related to each subject's B_1^+ map, position, shape and their cross terms was calculated for each simulated brain slice [103]. Prediction by Iteratively Projected Ridge Regression (PIPRR) was proposed to predict the RF shims by learning a weight vector that relates to each feature through a training dataset [103]. Results showed that PIPRR shims achieved similar homogeneity to "direct design" shims, and the prediction only took 4.92 ms on average [103].

Tomi-Tricot *et al*. introduced a machine learning approach called SmartPulse to mitigate B_1^+ inhomogeneity in body imaging at 3 T [104]. Abdominal B_1^+ maps were acquired from 50 subjects, which were divided into three groups based on the similarity between their tailored k_T-points pulses. An optimal pulse was calculated for each group. A machine learning classifier was then constructed to categorise a new subject into one of the three groups based on the localiser image. The SmartPulse algorithm was tested on 53 additional subjects, and SmartPulse outperformed both the vendor's calibration-free dual excitation and tailored static B_1 shimming.

2.6.4. Correction of RF and gradient system imperfections

Tailored pTx pulses used for either spatially selective excitation or mitigation of B_1^+ inhomogeneity are sensitive to system imperfections. The accuracy of such pulses relies

hugely on the spatial and temporal fidelity of magnetic fields produced by both the gradient system and the RF chain [105]. Sources for gradient system imperfections include limited bandwidth of the gradient amplifier, eddy currents [106, 107], and field drifts due to mechanical vibrations and thermal changes [108, 109] [105]. The main source for transmit chain imperfection is the RF power amplifier [105]. pTx pulses are also susceptible to timing imperfections. Not only must the gradient system and RF chain be consistent among themselves, they need to be synchronised with each other as well [105].

Çavuşoğlu *et al*. attempted to improve pTx pulse performance by correcting the aforementioned hardware inaccuracies [105]. By employing a dynamic field camera to monitor gradient and RF fields in real time with high temporal resolution, Çavuşoğlu *et al*. turned the challenge of hardware imperfections into a measurement and control problem with excellent results [105].

2.7. Non-conventional use of pTx-enabled systems

2.7.1. Overcoming duty cycle limits

pTx systems can also be used to overcome RF amplifier duty cycle limitations. In amide proton transfer (APT) CEST MRI, a long saturation RF pulse (longer than 2 sec) is ideally required [110]. RF amplifier specifications on maximum pulse duration and duty-cycle limit the duration of the saturation to well below two seconds (tens to hundreds of ms). Keupp *et al*. proposed to prolong the saturation pulse by operating the transmit channels in a time-interleaved fashion [110]. Eight RF transmit coils were divided into two subsets of four, and each subset was driven by one RF amplifier [110]. Only one subset was switched on at a time, thus ensuring a long quasi-continuous RF saturation despite a duty cycle limit of 50% for the RF amplifiers [110].

2.7.2. Motion correction

Hess *et al*. demonstrated that a pTx coil could also be used to capture motion by leveraging the fact that RF coil coupling is sensitive to alterations in the conductivity of

surrounding tissues [111]. During RF excitation, directional couplers (DICOs) measure forward and reflected voltages of each channel, which are related to each other by the scattering matrix. Movement of tissue when the subject breathes can induce changes in the scattering matrix, thus allowing retrospective diaphragm position tracking [111] and cardiac gating [112]. Since many MRI systems use DICOs to measure transmit currents for safety monitoring, no additional equipment is required. Jaeschke *et al.* further expanded this concept by designing pTx RF pulses to measure the scattering matrix during excitation, and achieved prospective dual-gating [113].

2.8. Saturation pulses

This section aims to give a brief introduction to saturation pulses, which are used in a number of occasions throughout this thesis. Saturation pulses are often applied to suppress unwanted magnetisation before each excitation portion of the main MR imaging sequence. They are usually followed by spoiler gradients to suppress any remaining transverse magnetisation from the magnetisation that is intended to be saturated. Saturation pulses can be used for spatial saturation (e.g. for spatial localisation in single-voxel spectroscopy), flow saturation (e.g. for the removal of flow artefacts), or spectral saturation (e.g. for fat saturation by applying frequency-selective pulses followed by spoiling).

Specifically, the WET saturation scheme (*w*ater suppression *e*nhanced thorough T_1 effects) [114] is used in Chapter 4. Although a simple slice-selective pulse followed by spoiler gradients is able to achieve spatial saturation, its efficacy is influenced by T_1 relaxation and B_1^+ inhomogeneity, thus resulting a spatially-nonuniform saturation profile. Ogg *et al.* demonstrated that water suppression in MRS experiments could be made substantially insensitive to T_1 and B_1^+ variations by repeating the saturation pulses n times with different nominal flip angles [114]. Such an insensitivity was achieved by optimising for the combination of nominal flip-angles for each n that minimises the remaining transverse magnetisation at the end of the pulse train over a range of plausible T_1 and B_1^+ values. The formulation used in the WET scheme neglected the finite width of the RF pulse and assumed a complete dephasing.

The principle of achieving good saturation in the presence of variations in T_1 and B_1^+ using a pulse train has been explored in a number of other studies. Luo *et al.* proposed the BISTRO (*B*$_1$-*ins*ensitive *tr*ain to *o*bliterate signal) pulse train consisting of 32 hyperbolic secant pulses interleaved with dephasing gradients to achieve outer-volume suppression [115]. Sung *et al.* designed a pulse train consisting of hard pulses of different durations (and therefore nominal flip-angles) for uniform saturation of myocardium [116]. Kim *et al.* then introduced a hybrid pulse train consisting of two hard pulses and a nonselective adiabatic half-passage (AHP) pulse [117]. Tao *et al.* proposed a pulse train consisting of full-passage hyperbolic-secant (HS8) pulses [118].

Chapter 3 Implementation

This chapter details the practical steps of designing selective RF pulses and integrating them into pulse sequences on a Siemens Magnetom 7 T system. Sections 3.1 and 3.2 introduces the mathematical formulation of selective RF pulse design. Section 3.3 describes a proof-of-concept phantom study for spatially-selective RF pulses. Section 3.4 gives a brief overview of the pTx system. Section 3.5 illustrates the processing steps of B_1^+ and B_0 maps for RF pulse design.

3.1. The Bloch equations and RF excitation

The Bloch equations describe the classical behaviour of nuclear spins in the presence of static and radiofrequency magnetic fields [21]. During RF excitation, a gradient pulse $\mathbf{G}(t)$ and an RF pulse $\mathbf{b_1}(t)$, are typically played out. If relaxation effects are ignored during RF excitation, the Bloch equations can be written as:

Equation 3.1

$$\frac{d\mathbf{m}(\mathbf{x},t)}{dt} = \gamma \begin{pmatrix} 0 & \mathbf{G}(t)\cdot\mathbf{x} & -b_{1,y}(t) \\ -\mathbf{G}(t)\cdot\mathbf{x} & 0 & b_{1,x}(t) \\ b_{1,y}(t) & -b_{1,x}(t) & 0 \end{pmatrix} \mathbf{m}(\mathbf{x},t),$$

where $\mathbf{m}(\mathbf{x}, t)$ is the magnetisation at position $\mathbf{x}$ and time t and γ is the gyromagnetic ratio. In the formulation, the RF field is assumed to be uniform, although nonuniformity can be introduced by incorporating a transmit sensitivity term. Equation 3.1 can then be used to determine the magnetisation $\mathbf{m}$ after an RF excitation for a given initial state of magnetisation. However, in most RF pulse design problems, the goal is to find the most suitable $\mathbf{b_1}(t)$ and $\mathbf{G}(t)$ that produce the desired magnetisation $\mathbf{m}$ at the end of the pulse.

For arbitrary RF the above differential equations can only be solved numerically, which is time-consuming. When the flip-angle is small and the B_1^+ amplitude is low, the small tip-angle (STA) approximation can be used. Pauly *et al.* proposed the STA to simplify the

Bloch equations by assuming $m_z \approx m_0$ = constant [119] . Under this assumption the Bloch equations can be rewritten as:

Equation 3.2

$$\frac{d\mathbf{m}(\mathbf{x},t)}{dt} \approx \gamma \begin{pmatrix} 0 & \mathbf{G}(t)\cdot\mathbf{x} & -b_{1,y}(t) \\ -\mathbf{G}(t)\cdot\mathbf{x} & 0 & b_{1,x}(t) \\ b_{1,y}(t) & -b_{1,x}(t) & 0 \end{pmatrix} \begin{pmatrix} m_x(\mathbf{x},t) \\ m_y(\mathbf{x},t) \\ m_0(\mathbf{x}) \end{pmatrix}.$$

If we expand the matrix multiplication in Equation 3.2 in *x* and *y*, we get:

Equation 3.3

$$\frac{dm_x(\mathbf{x},t)}{dt} \approx \gamma \mathbf{G}(t)\cdot\mathbf{x} m_y(\mathrm{x},t) - \gamma b_{1,y}(t)\cdot m_0,$$

Equation 3.4

$$\frac{dm_y(\mathbf{x},t)}{dt} \approx -\gamma \mathbf{G}(t)\cdot\mathbf{x} m_x(\mathbf{x},t) - \gamma b_{1,x}(t)\cdot m_0.$$

We can then construct a representation of the transverse magnetisation in the complex domain:

Equation 3.5

$$m_\perp(\mathbf{x},t) = m_x(\mathbf{x},t) + i m_y(\mathbf{x},t)$$

Equation 3.6

$$b_1(t) = b_{1,x}(t) + i b_{1,y}(t)$$

Equations 3.3 and 3.4 can now be written in the complex representation:

Equation 3.7

$$\frac{dm_\perp(\mathbf{x},t)}{dt} \approx -i\gamma \mathbf{G}(t)\cdot\mathbf{x} m_\perp(\mathbf{x},t) + i\gamma b_1(t)\cdot m_0.$$

Equation 3.7 is a first order differential equation and therefore has a simple analytical solution. For an RF excitation pulse of duration *T*, the transverse magnetisation at the end of the RF pulse can be written as:

Equation 3.8

$$m_{\perp}(\mathbf{x}) = i\gamma m_0(\mathbf{x}) \int_0^T b_1(t) e^{-i\gamma \mathbf{x} \cdot \int_t^T \mathbf{G}(\tau) d\tau}\, dt.$$

Equation 3.8 can be simplified by introducing the concept of excitation *k*-space. We can define a variable *k* to represent the spatial frequency using the following equation:

Equation 3.9

$$\mathbf{k}(t) = -\gamma \int_t^T \mathbf{G}\,(\tau) d\tau.$$

Similarly in MRI image acquisition, the acquisition k-space (or imaging k-space) is defined as $\mathbf{k}(t) = \gamma \int_0^t \mathbf{G}\,(\tau) d\tau$. In both cases, a higher value in k-space represents a higher spatial frequency. Equation 3.8 can be now simplified as:

Equation 3.10

$$m_{\perp}(\mathbf{x}) = i\gamma m_0 \int_0^T b_1(t) e^{i\mathbf{x} \cdot \mathbf{k}(t)}\, dt.$$

We can then incorporate B_1^+ inhomogeneity by introducing a spatially varying transmit sensitivity term. For a single-channel transmit system, there is one unique transmit sensitivity $s(\mathbf{x})$ at each location **x**. The expression for transverse magnetisation can then be rewritten as:

Equation 3.11

$$m_{\perp}(\mathbf{x}) = i\gamma m_0 s(\mathbf{x}) \int_0^T b_1(t) e^{i\mathbf{x} \cdot \mathbf{k}(t)}\, dt.$$

In addition to B_1^+ inhomogeneity, static (B_0) field off-resonance influences the performance of the RF excitation as well. This can be easily included in the signal equation by adding a term for the phase accrual due to local field inhomogeneity $\Delta B_0(\mathbf{x})$ at position **x**.

Equation 3.12

$$m_{\perp}(\mathbf{x}) = i\gamma m_0 s(\mathbf{x}) \int_0^T b_1(t) e^{i\gamma \Delta B_0(\mathbf{x})(t-T)} e^{i\mathbf{x}\cdot\mathbf{k}(t)}\, dt.$$

In the context of pTx, each individual transmit channel has a different spatially varying transmit sensitivity. The B_1^+ field experienced at each location is therefore the summation of the B_1^+ field imposed by each transmit channel. Thus, the signal equation can be modified by summing coil sensitivities $s_r(\mathbf{x})$ from channel 1 to channel *R*. Furthermore, the RF pulse in each transmit channel can vary independently since there are *n* RF amplifiers. If we use b_r to represent the RF pulse played out on channel *r*, the signal equation can now be rewritten as:

Equation 3.13

$$m_{\perp}(\mathbf{x}) = i\gamma m_0 \sum_{r=1}^{R} s_r(\mathbf{x}) \int_0^T b_r(t) e^{i\gamma \Delta B_0(\mathrm{x})(t-T)} e^{i\mathbf{x}\cdot\mathbf{k}(t)}\, dt.$$

3.2. Discretisation and the system matrix

Grissom *et al.* formulated the parallel transmission problem in the spatial domain based on a STA regime [59]. The continuous function (Equation 3.13) linking B_1^+ sensitivity and magnetization is transformed into a matrix form, which is easily expressed in high-level programming languages (e.g. MATLAB). Moreover, a mask can be incorporated in the pulse design steps to exclude regions of no interest. Under the STA regime, the transverse magnetisation can be written as:

Equation 3.14

$$\mathbf{m} = \sum_{r=1}^{R} \mathbf{D}_r \mathbf{A} \mathbf{b}_r,$$

where $\mathbf{m}$ is the transverse magnetisation, *R* is the number of transmit coils, $\mathbf{D_r}$ is a diagonal matrix containing the spatial transmit sensitivities of each coil, and $\mathbf{b_r}$ is the RF pulse time domain waveform of each coil. $\mathbf{A}$ is an N_s by N_t matrix where N_s is the number

of spatial locations and N_t is the number of time steps. For channel r, the equation can be written as:

Equation 3.15

$$\mathbf{m}_r = \mathbf{D}_r \cdot \mathbf{A} \cdot \mathbf{b}_r.$$

The overall excitation pattern is then the sum of the excitation patterns due to all R transmit channels:

Equation 3.16

$$\mathbf{m} = \sum_{r=1}^{R} \mathbf{D}_r \cdot \mathbf{A} \cdot \mathbf{b}_r$$

As mentioned previously, $\mathbf{D_r}$ is a diagonal matrix containing transmit sensitivities of each coil. If we represent the transmit sensitivity of the rth transmit channel at position i by $s_r(\mathbf{x}(i))$, then $\mathbf{D_r}$ can be written as:

Equation 3.17

$$\mathbf{D}_r = \begin{bmatrix} s_r(\mathbf{x}(1)) & & & \\ & s_r(\mathbf{x}(2)) & & \\ & & \ddots & \\ & & & s_r(\mathbf{x}(N_s)) \end{bmatrix}.$$

$\mathbf{A}$ is an N_s by N_t matrix and the (i, j)-th element of A is written as:

Equation 3.18

$$a_{ij} = i\gamma m_0 \Delta t e^{i\gamma \Delta B_0(\mathbf{x}_i)(t_j - T)} e^{i\mathbf{x}_i \cdot \mathbf{k}(t_j)},$$

where m_0 is the equilibrium magnetisation, ΔB_0 is off-resonance at the relevant voxel, T is the pulse duration, $\mathbf{x}$ is a collection of spatial locations, and k is the excitation k-space trajectory. Equation 3.18 is the discretised version of Equation 3.12.

$\mathbf{b_r}$ is column vector whose elements represent the RF waveform of each coil. $\mathbf{b_r}$ can be written as:

Equation 3.19

$$\mathbf{b}_r = \begin{bmatrix} b_{r,1} \\ b_{r,2} \\ \cdots \\ b_{r,N_t} \end{bmatrix}.$$

The summation in Equation 3.14 replaced by horizontal concatenation of $\mathbf{D}_r\mathbf{A}$ and vertical concatenation of $\mathbf{b}_r$:

Equation 3.20

$$\mathbf{m} = [\mathbf{D_1 A} \quad \mathbf{D_2 A} \quad \cdots \quad \mathbf{D}_R\mathbf{A}] \begin{bmatrix} \mathbf{b}_1 \\ \mathbf{b}_2 \\ \cdots \\ \mathbf{b}_R \end{bmatrix} = \mathbf{A}_{full}\mathbf{b}_{full},$$

where $\mathbf{A}_{\text{full}}$ and $\mathbf{b}_{\text{full}}$ are the concatenated versions or $\mathbf{D}r\mathbf{A}$ and $\mathbf{b}_r$, respectively.

Therefore, the RF pulse design problem can be formulated as an optimisation problem to find a suitable $\mathbf{b}$ that minimises the difference between $\mathbf{m}$ and $\mathbf{Ab}$ for a given system matrix $\mathbf{A}$ and desired magnetisation $\mathbf{m}$.

The optimisation problem can be written using the arguments for minima (arg min) formulation:

Equation 3.21

$$\hat{\mathbf{b}}_{full} = \arg\min(\|\mathbf{A}_{full}\mathbf{b}_{full} - \mathbf{m}_{target}\|^2),$$

where $\mathbf{m}_{\text{target}}$ is the target excitation pattern and $\hat{\mathbf{b}}_{\text{full}}$ is the solution to the optimisation problem.

The optimisation problem in Equation 3.21 as written is unconstrained. As a result, any optimisation might find a solution $\hat{\mathbf{b}}_{\text{full}}$ with a high magnitude (equivalent to RF voltage) that cannot be achieved on the scanner given SAR or RFPA limits. Therefore, a regularisation term is usually required to generate sensible results. Commonly, a regularisation term is included in the RF pulse design to constrain the RF power or SAR,

because the RF system cannot generate arbitrarily large RF voltage due to hardware limits and safety regulations. Therefore, in Equation 3.21, we can add an additional generic regularisation term to limit RF power. The optimisation problem can then be rewritten as:

Equation 3.22

$$\hat{\mathbf{b}}_{full} = \arg\min(\|\mathbf{A}_{full}\mathbf{b}_{full} - \mathbf{m}_{target}\|_{\mathrm{w}}^2 + R(\mathbf{b}_{full})).$$

Equation 3.22 penalises solutions that result in a high value in the function R. One of the most common ways to control RF power is to include a Tikhonov regularisation term which can be written as:

Equation 3.23

$$R(\mathbf{b}_{full}) = \lambda \mathbf{b}'_{full}\mathbf{b}_{full},$$

where λ is the Tikhonov regularisation parameter. The tuning of λ allows for the trade-off between excitation accuracy (fitting the data) and RF power (reducing the norm of the solution).

3.3. Selective excitation using a single-channel system

In an initial demonstration of spatially-selective pulse design on a single-channel transmit system a simple spatial profile was defined in an oil phantom. The pulse design problem was formulated as described in Sections 3.1 and 3.2. An off-centre rectangular shape was chosen as the target pattern. The excitation pattern was smoothed by a 2D Hamming filter to reduce the sharpness of the edges of the excitation target.

From a frequency domain perspective, the power of the excitation pattern is concentrated in the centre of k-space because of its simple geometry. A variable-density spiral (VDS) was adopted as the gradient trajectory to ensure better coverage of the centre of k-space. The extent of the trajectory was chosen so that it covered 80% of the energy of the k-space representation of the desired excitation pattern.

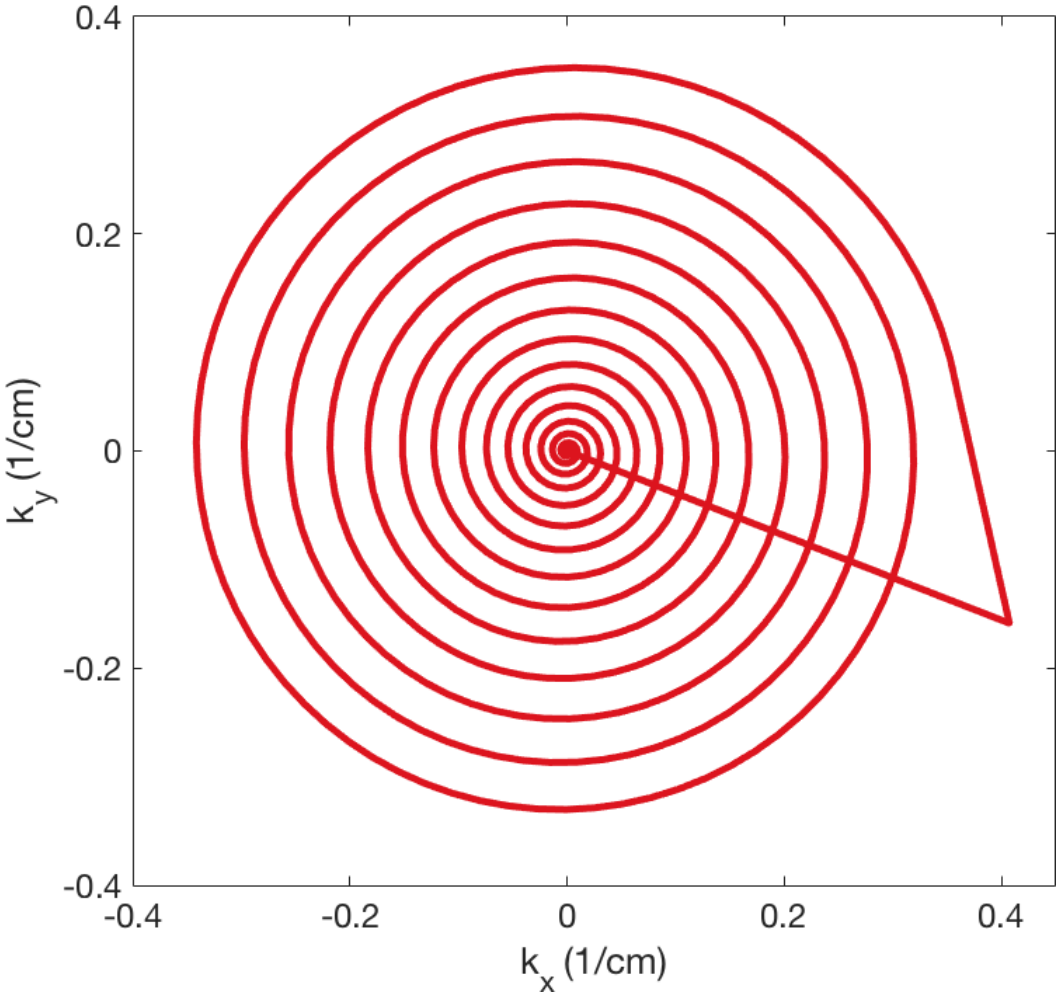


Figure 3.1: A variable-density spiral-in trajectory

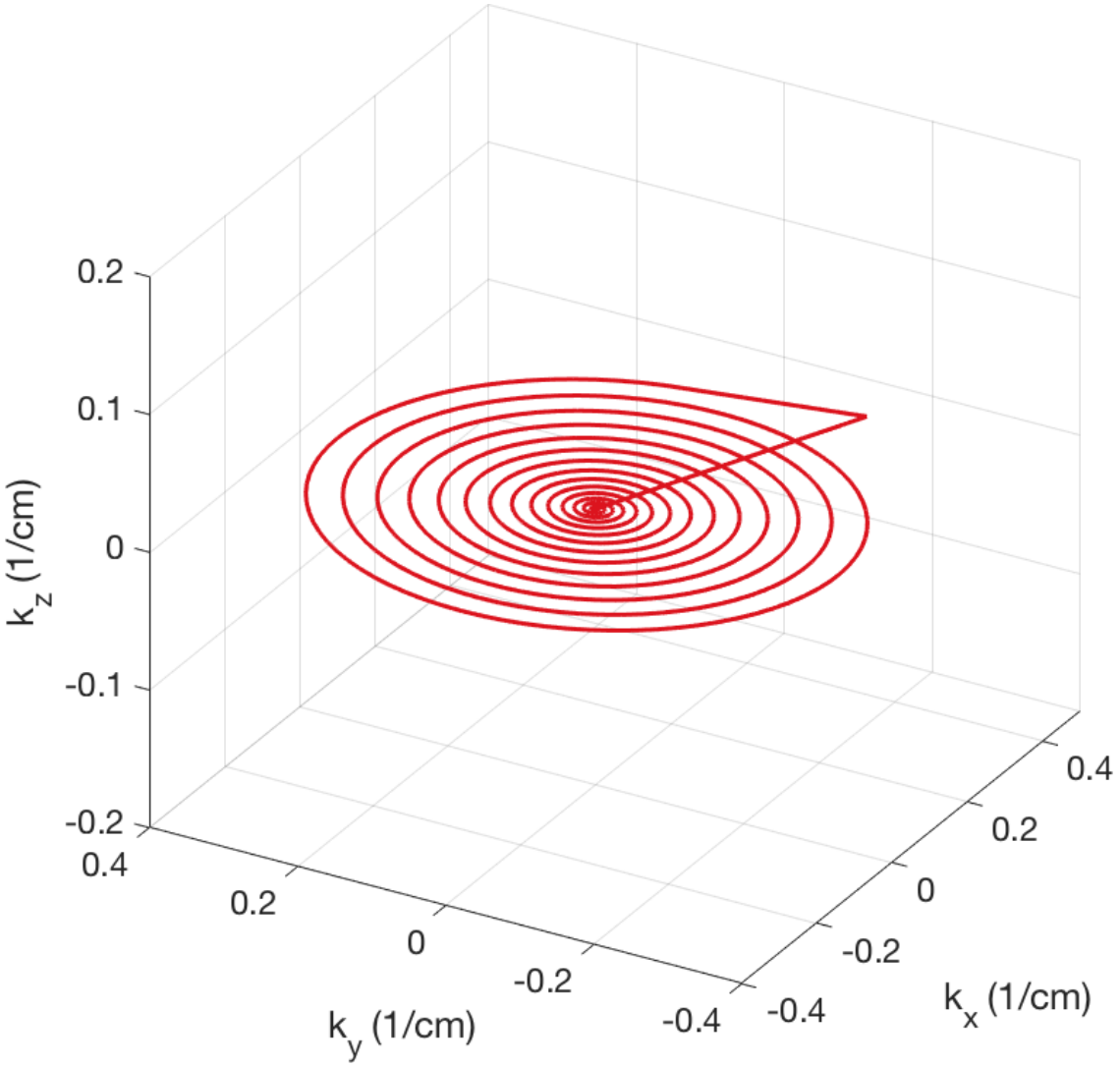


Figure 3.2: A variable-density spiral-in trajectory shown in 3D.

The slice at the iso-centre was chosen to be the slice-of-interest. B_0 and B_1^+ maps were acquired, sorted and interpolated (described in detail in Section 3.5). The B_0 map was acquired using a dual-echo GRE sequence, and the B_1^+ map was acquired using a 3D DREAM sequence [120]. A mask was generated by a simple thresholding method, and B_0 (in Hz), B_1^+ (in Hz/V), and position (in cm) in the masked region were extracted and vectored. A system matrix was then constructed based on the formulation described in Section 3.2.

The least-squares problem was solved via the variable-exchange method [72]. The calculation was run using MATLAB 2016b (MathWorks, Inc., Natick, MA, USA). The Tikhonov regularisation parameter λ was heuristically chosen to be 1e-7. Such a choice of the regularisation parameter yielded a good excitation quality without needing

prohibitively high RF pulse voltage. Although the pulse design was implemented under STA assumptions, the expected magnetisation was verified using a Bloch equations simulation [58], which showed similar results.

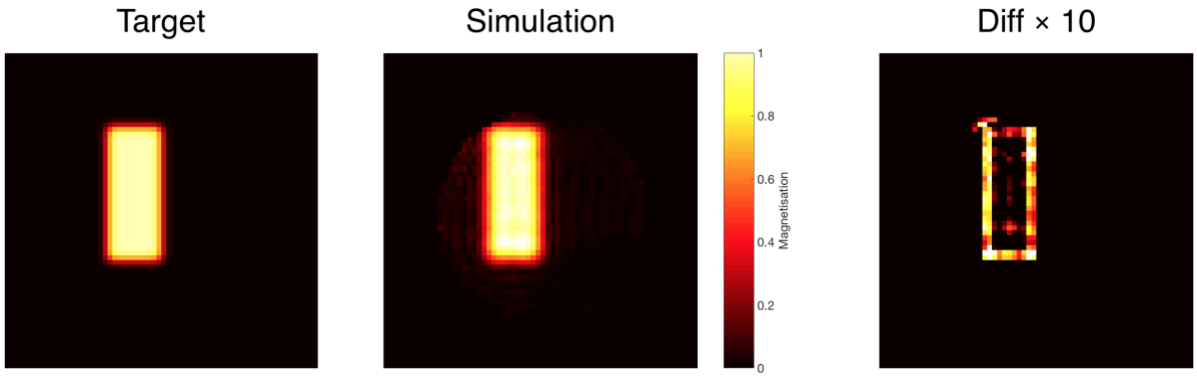


Figure 3.3: Target pattern and the expected transverse magnetisation achieved by the designed spatially-selective RF pulses are shown in the left and middle panels. The magnitude error between target and simulation is shown in the right panel with the differences magnified by 10.

The optimisation solution, comprising complex RF waveform and two-axis gradient waveforms were written into a C++ header (.h file) to be compiled into the sequence code. The pulse was therefore hardcoded into the sequence at compile-time in this demonstration implementation. This method is inflexible and time-consuming, as the sequence code needs to be recompiled and transferred to the scanner host PC each time the RF or gradient waveform is altered. Subsequent studies carried out in this thesis implemented a framework to allow for dynamically loaded RF pulses, typically defined in human readable ASCII text files and read in at run time by the sequence code. This latter approach removed the need for recompilation of the sequence source code.

A spin-echo sequence was used to image the excited pattern in an oil phantom, in which the slice-selective excitation RF pulse and gradient were replaced by the tailored spatially-selective pulses and a VDS gradient trajectory. The slice selection in this sequence was achieved by the refocusing pulse, which remained unchanged from the standard spin-echo sequence. The spiral excitation pulses did not aim to control for the magnetisation outside the imaging slice, which might contribute to the artefacts seen in Figure 3.4. Errors due to imperfections in the gradient trajectory might also be the cause of the artefacts. Furthermore, the excitation errors might be due to nonlinearity and

memory effects of RF power amplifiers as well, which are particularly pronounced in rapidly varying RF pulses [121].

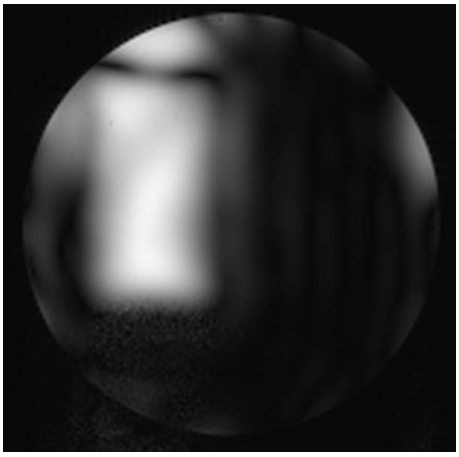


Figure 3.4: Experimental result of spatially-selective RF pulses from an oil phantom.

3.4. pTx System overview

The pTx system of the Siemens MAGNETOM 7 T MRI scanner has two dedicated console PCs (the master and the slave). The single-channel system has a single (separate) console PC (the combined host), and the scanner can be switched between the single channel system and the pTx system by following a manual process.

An external network is present to enable communication between the slave PC and the master PC. Scanner hardware is driven by real-time processing units "MPCUs" (measurement and physiological control units). On the pTx system each MPCU controls a single RF channel, comprising an independent waveform generator feeding its associated channel in an integrated 8-channel RF power amplifier (RFPA). When a sequence is started by the operator on the master console, a copy of the sequence run-time parameters is downloaded to the MPCUs. The master console directly controls a single MPCU, whilst instructions are duplicated on the slave console to the seven other MPCUs (for a total of 8 MPCUs and RF channels). The MPCUs then drive the relevant scanner hardware (master: 1xTx, gradients and other scanner sub systems, slave: 7xTx) based on based on console-derived protocol and instruction set derived from the MPCU binaries .

The global power is monitored via the PALI MC (power absorption limiter multi-channel) sub-system, which is a field-programmable gate array (FPGA) that calculates the sum of RF power over all transmit channels. The PALI MC is connected to the RFPA, and can terminate the RF transmission from the RFPA if the RF power limit is reached. PALI MC calculates global absorbed power by summing forward power and subtracting reflected power. The PALI will also terminate the RFPA if a small amount of RF power is detected when RF is not turned on in the sequence.

Local SAR monitoring is enforced by PALI MC, and relies on 8 directional couplers (DICOs) inserted into the 8 Tx channels after the RFPA and before the coil plugs, which sample both the forward and reflected voltage on each transmit path. Voltage monitors then measure the instantaneous complex (phase and amplitude) RF voltage in each channel. The data measured using the DICO system is recorded by the MR signal receive boards as a coded ADC event. The local SAR calculation is done on the "Imager" (the reconstruction sub-system of the scanner) based on the VOP model and the data measured by the system on the MR receivers. This calculation is coil-specific and patient-specific. As long as the local SAR limit is not exceeded, the Imager sends an affirmative signal to the PALI MC. However, if this signal is missing, the PALI MC will then stop the RFPA.

3.5. Description of online pulse design process

Although B_1^+ and B_0 mapping sequences can be found on most MR scanners, additional processing steps need to take place before the RF pulse calculation. First, the unprocessed DICOM images from the scanner on the 7 T Magnetom are scaled from 0 to 4095, whereas B_1^+ and B_0 maps need to be quantified in physical units (for example Hz/V and Hz respectively). Therefore, an additional conversion step is needed. Second, the B_1^+, B_0 maps, and any structural images, need to be transformed to the same coordinate system to allow harmonised use in pulse calculation. However, they normally do not have the same spatial resolution or field-of-view. This section introduces the practical steps of preparing B_1^+ and B_0 maps for RF design on a Siemens 7 T Magnetom system.

3.5.1. The overall workflow

The following is the overall workflow of pre-processing steps for RF pulse design:

1) Load the following unprocessed DICOM images into memory: localiser, B_0 maps and B_1^+ maps.

2) Convert unprocessed B_0 and B_1^+ images into maps with physical units (Hz for B_0 and Hz/V for B_1^+).

3) Choose the interpolation target (localiser, B_0, or B_1^+).

4) Apply the interpolation to the images so that the localiser, B_0 maps and B_1^+ maps are in the same coordinate system.

5) Create a mask using a dedicated masking function. This could be a brain mask, or for specific ROIs: a slice, a slab, blood vessels, or a brain region. The default masking option is a simple threshold mask applied on the localiser.

6) Apply the mask to the B_0 maps and B_1^+ maps.

7) Construct the system matrix.

8) RF pulse design via numerical optimisation.

9) Write out the designed RF pulse to the scanner (in Siemens supported ASCII format).

10) The pulse file is loaded by the pulse sequence on the scanner at runtime.

3.5.2. Pulse sequence implementation strategy

This section details the steps described in the Section 3.5.1. Note that additional care was taken to ensure that the correct orientations were implemented in the pTx system. All pulses were run using a fixed orientation and position in sequence code, separate from any orientations prescribed for any other sequence modules. The orientation matrix is initialised as an identity matrix at isocentre. Then this is related to a known transform to the DICOM coordinate system (given the same patient orientation, in this work always assumed to be head first supine), as the x-axis and y-axis of the scanner gradient coordinate system are anti-parallel to the DICOM patient anterior-posterior and left-right coordinates. By doing this, only a one-time calibration is needed to establish the relationship between the DICOM coordinate system to the fixed orientation in the scanner code.

3.5.2.1. Processing DREAM B_1^+ maps

The DREAM sequence outputs four DICOM series: the magnitude of flip-angle maps, the phase of flip-angle maps, the magnitude of B_1^+ maps and the phase of B_1^+ maps. The maps are concatenated first by different transmit channels and then by slices. For instance, if there are 30 slices and 8 channels, the first 8 images are B_1^+ maps of all 8 channels of slice 1. However, simply knowing the B_1^+ transmitted in a particular mapping sequence is not sufficient for RF pulse design. Information regarding the pulse voltage is needed to generate B_1^+ maps per unit of input RF voltage. Therefore, the following steps were implemented to generate per-Volt B_1^+ maps used for pulse design in this thesis:

1) Locate the DICOM series of the B_1^+ maps (magnitude and phase). This can be achieved by entering series number and/or the instance number of the DICOM series, or by entering a string that is contained in the name of the series. The magnitude image is in units of Hz.

2) Get the RF pulse voltage from the header of the DICOM files.

3) Get the positions of the voxels in the image (to be used in later interpolations).

4) Convert the phase image from range [0,4095] to range [-π, π].

5) Create a complex image by combining the magnitude image and scaled phase image.

6) Divide the complex B_1^+ maps by the pulse voltage, and get per-volt units B_1^+ maps in Hz/V.

7) When operating on the pTx system, reshape the B_1^+ maps from 3D matrices to 4D matrices where the additional dimension represents the transmit channels.

3.5.2.2. Processing B_0 maps

The processing of B_0 maps is relatively straightforward compared to the B_1^+ maps. The dual-echo GRE sequence outputs three DICOM series: two wrapped phase images corresponding to the two echoes, and an additional processed B_0 map in units of Hz, but scaled to be between 0 and 4095. Therefore, a simple subtraction by 2047 would scale the B_0 map in Hz correctly.

3.5.2.3. Additional images for ROI selection

In addition to B_0 maps and B_1^+ maps, another image is often used in RF pulse design for better visualisation and the generation of masks. This is because B_0 maps and B_1^+ maps typically have coarse spatial resolution, and lack anatomical detail. Such an image can be the localiser scan acquired at the beginning of the session, a T_1- or T_2-weighted structural image, or an angiogram (depending on the application).

In the arterial spin labelling study detailed in Chapter 4, a time-of-flight angiogram was used as the "localiser", which was then used to manually select the four main feeding vessels to the brain at the jaw line level as the ROI for RF pulse design.

3.5.2.4. Interpolation of the maps

In order to construct the system matrix used for RF pulse design, B_1^+ and B_0 maps, along with the localiser image, need to be in the same coordinate system. This can be achieved by interpolating the maps in the following steps:

1) Identify the interpolation target (B_0, B_1^+, or localiser).

2) Retrieve the position matrices of the corresponding DICOM images of interest.

3) Calculate the coordinates of the centres of the voxels in the DICOM coordinate system for the specified slice.

4) Calculate affine transformation based on the coordinates calculated from step 2.

5) Apply the affine transformation.

3.5.2.5. Masking and prescribing the excitation target

Masking is almost always required for RF pulse design, as the magnetisation in regions of no interest does not need to be controlled. This could be a mask for the whole brain (or phantom), or for specific ROIs: a slice, a slab, blood vessels, or a brain region.

In addition, an excitation target needs to be specified. In the ASL study detailed in Chapter 4, all the voxels in the mask (four feeding arteries) had an excitation target of 20°. In the TRUST study detailed in Chapter 5 the ROI had an excitation target of 0°, and regions outside the ROI had an excitation target of 90°.

After the mask and excitation target have been created, the 2D or 3D maps can now be vectorised by concatenating the voxels within the mask, and excluding the regions outside the mask.

3.5.2.6. Constructing the system matrix

A system matrix can then be constructed following the steps in Section 3.2. The RF pulse design is then converted to a generic optimisation problem to produce an RF waveform that minimises the difference between the target and predicted magnetisation (see Equation 3.21). A regularisation term can be added to allow the trade-off between RF power and the excitation accuracy. More complicated explicit constraints on per-channel and/or sum-of-channel power, local SAR, or temperature change can be included as well.

3.5.3. Object-oriented programming

In order to reliably perform the operations mentioned above, a class named DicomFM was developed by Dr William Clarke in MATLAB. Such an object-oriented programming approach has a few key advantages. First, it enables the user to classify certain variables and functions as either private or public, thus preventing unintentional contamination of loaded data. Second, it allows for a certain degree of flexibility through polymorphism. For instance, DicomFM has two different forms, one for the single channel system, and one for the pTx system with the ability to handle an extra dimension (the dimension for coils). Finally, the modularity of this approach makes troubleshooting easier. This section provides some details of the method, and describes the overall workflow of sorting B_1^+ and B_0 maps using DicomFM.

The unprocessed and processed maps are protected in the DicomFM class. Therefore, the user needs to use a "get" function to retrieve data in DicomFM. The available options are: get localiser (in original or interpolated coordinates); get mask; get positions; get B_1^+ (in original or interpolated coordinates, in absolute B_1^+, per-V B_1^+ or per-W B_1^+), get B_0 (in original or interpolated coordinates). Note that all of the "get" methods require the user to specify one of the masking approaches.

The DicomFM class can handle and convert between the following units: mm, cm, and m for distance; Hz, T, mT, μT, nT, Gauss for magnetic field strength. In addition, the B_1^+ map can be retrieved either in absolute units, or in the form of per-V or per-W B_1^+.

Apart from the DREAM sequence that was used as the primary B_1^+ mapping technique in this thesis, processing steps for alternative methods can be included into the framework of DicomFM as well. One only needs to provide a processing function that converts the unprocessed DICOM images to B_1^+ maps in one of the allowed units. Currently, DicomFM supports the 2D and 3D version of the DREAM sequence, and the AFI sequence.

Chapter 4 Improving pseudo-continuous arterial spin labelling at 7 T

4.1. Arterial Spin Labelling: General Principles

Arterial spin labelling (ASL) is a non-invasive technique to image cerebral blood flow [122-124]. ASL has various clinical applications such as acute stroke, dementia, and chronic vascular diseases. During an ASL scan, spins in blood vessels upstream of the imaging plane are inverted or saturated (labelled). Typically for brain imaging, the blood is labelled in the four main brain-feeding arteries: the right internal carotid artery (RICA), right vertebral artery (RVA), left internal carotid artery (LICA), and left vertebral artery (LVA). After a post-labelling delay of 1-2 s, a proton-density weighted image is acquired. Another image with no labelling is also acquired, and the subtraction of the two produces a perfusion-weighted image. Pre-saturation background suppression is usually run in the imaging region to remove signal from static tissue.

4.1.1. Labelling strategies

ASL labelling techniques can be divided into three categories: continuous ASL (CASL), pulsed ASL (PASL), and pseudo-continuous ASL (PCASL). A schematic of these approaches is shown in Figure 4.1, and corresponding pulse sequences are shown in Figure 4.2.

4.1.1.1. Pulsed Arterial Spin Labelling (PASL)

Inversion of blood spins in PASL is achieved by playing out a slab-selective 180° inversion pulse below the brain. Several variations of PASL have been developed. In FAIR (Flow-sensitive Alternating Inversion Recovery), the control condition is a slice-selective inversion, and the label condition is achieved by a non-selective inversion [125]. In

PICORE (Proximal Inversion with Control of Off-Resonance Effects), the control is achieved by an off-resonance pulse [126].

Compared to (pseudo-) continuous ASL, PASL has much lower RF power deposition. However, one major drawback of PASL is that the labelled bolus duration is poorly defined. QUIPSS II (Quantitative imaging of perfusion using a single subtraction, second version) was proposed to provide a well-defined temporal duration by playing out an additional saturation pulse at the labelling slab location for both the labelled and control conditions [127]. As a result, the tail-end of the labelled bolus is removed, and quantitative perfusion images can be obtained using a single post label delay (PLD). In addition, PASL has low SNR compared to (P)CASL. This is first because of its short temporal duration, which translates into fewer labelled spins. Moreover, the labelled bolus in PASL experiences T_1 decay for the entire time between inversion and read-out, whereas the blood spins in (P)CASL are continuously labelled, and thus are on average labelled "later" than those in PASL. As a result, blood spins in (P)CASL experience less T_1 decay and have higher ASL signal.

4.1.1.2. Continuous Arterial Spin Labelling (CASL)

CASL achieves the inversion of blood spins using flow-driven adiabatic inversion. A constant RF pulse and a constant gradient pulse in the *z* direction are played out concurrently for a long period of time. As a result, a labelling plane is defined by the plane at which the spins are on-resonance. Blood spins experience an effective magnetic field that varies over time. Spins that are far upstream of the labelling plane, and hence off-resonance, experience little effect of the RF pulse. However, as the spins move closer to the labelling plane, the contribution of the B_1^+ field to the effective field B_{eff} becomes larger. The B_{eff} that the blood spins experience slowly shifts from $+z$ to $-z$. Thus, the adiabatic condition is satisfied, and the magnetisation of the moving blood follows the B_{eff}, leading to inversion.

However, CASL does not have a wide clinical use because of its notable disadvantages. First, the RF amplifiers of most scanners are unable to deliver a continuous RF pulse, even for a low amplitude, without modification. Second, significant saturation of brain tissue

occurs during CASL due to magnetisation transfer effects, thus causing errors between the labelled and control images at all locations except a single imaging slice, unless explicitly addressed in the acquisition.

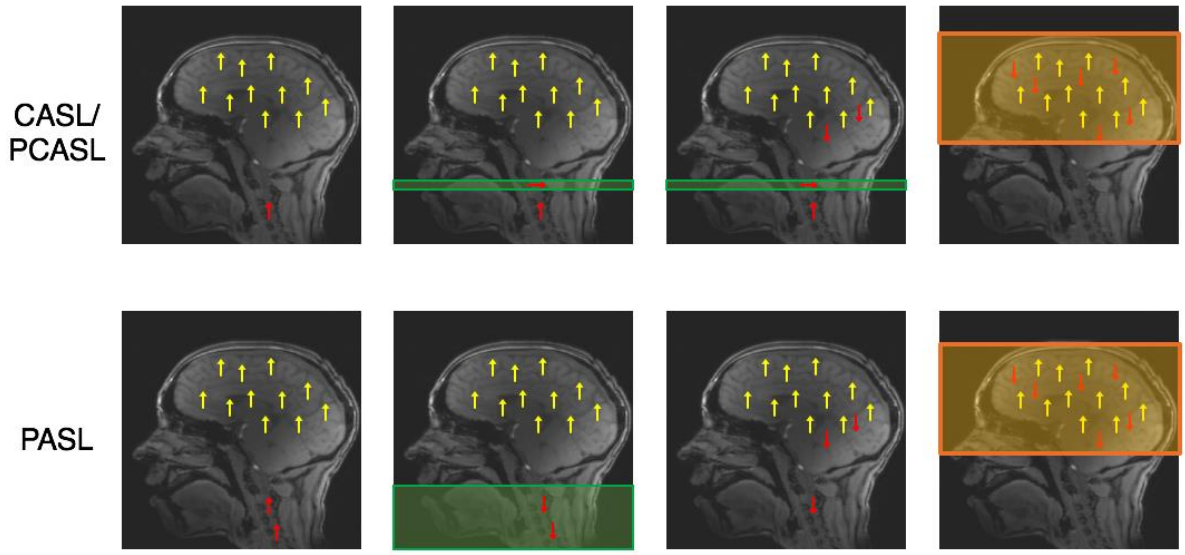


Figure 4.1: The process of various labelling strategies. Shown in yellow are spins in the static tissue, and shown in red are spins from labelled blood. Green regions indicate the labelling planes (for CASL/PCASL) or slab (for PASL). Orange regions are the image slices.

4.1.1.3. Pseudo-continuous Arterial Spin Labelling (PCASL)

Similar to CASL, PCASL relies on flow-driven adiabatic inversion to invert the blood as well. However, instead of using a constant RF pulse and a constant gradient, PCASL employs a train of short slice-selective RF pulses accompanied by z gradients with a small but non-zero mean value. The labelling pulse train usually includes more than 1000 RF pulses, the separation between which is roughly 1 ms. In the label state, each RF pulse has a low flip-angle and zero phase. In the control state, however, the amplitude of the RF pulses is constant, but the phase alternates between 0° and 180°. Compared to CASL, PCASL overcomes the clinical impracticality of CASL by effectively reducing the RF duty cycle.

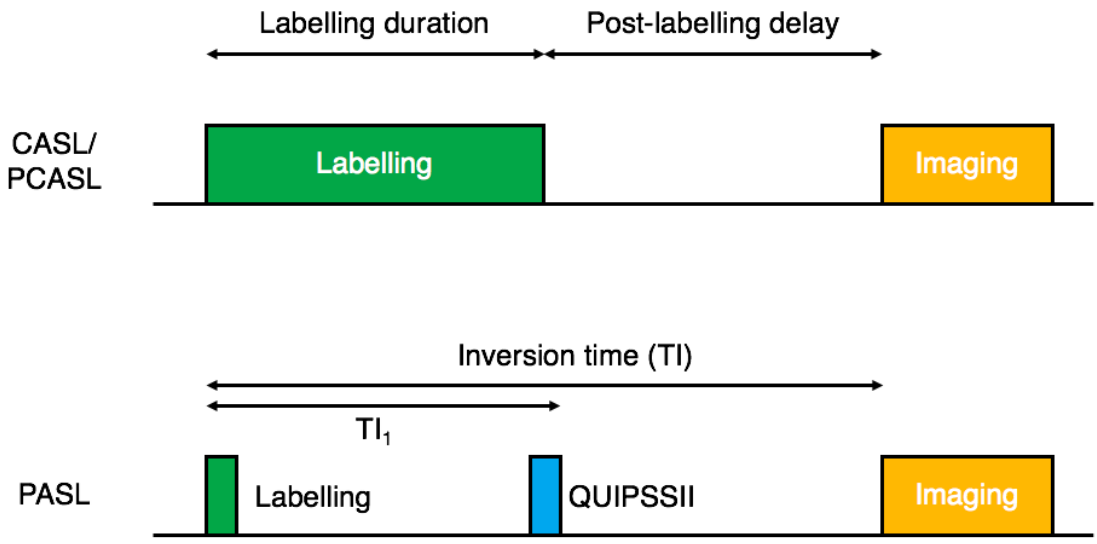


Figure 4.2: Schematic of ASL pulse sequences. The labelling module is shown in green and the imaging module is shown in yellow. For PASL, the optional QUIPSSII pulse is shown in blue.

4.1.2. Background suppression

As mentioned previously, ASL is a technique whereby signal from static tissue is cancelled by subtracting the label image from the control image. Although in theory only the signal from labelled blood should be present in the subtraction image, this may not be the case in reality. Any changes in the static tissue between the label and control images will be interpreted as perfusion signal. These changes could arise from physiological fluctuations from the respiratory and cardiac cycles, or gross subject motion. Since the signal from labelled blood is relatively small compared to the static tissue, these variations could be substantial compared with the perfusion signal. Therefore, it is desirable to suppress the signal from the static tissue during ASL acquisitions.

Background suppression in ASL is usually done by applying spatially selective saturation and inversion pulses. A spatially selective pulse (pre-sat) is first applied in the imaging region followed by a spoiling gradient, thereby saturating the signal in the imaging region while leaving spins in the labelling plane intact. Two carefully timed inversion pulses (double inversion) are then played out so that spins from the static tissue would go through a signal null at the time of image acquisition. Blood spins traveling from the labelling plane are unaffected by the saturation pulse, but experience the double

inversion pulses. If the inversion is perfectly achieved, only the sign of the magnetisation of blood spins (in both the control and labelled cases) is changed during each pulse. Therefore, the magnetisation of blood spins, and thus the signal difference between control and labelled cases is unperturbed.

4.1.3. Post-processing

4.1.3.1. Motion correction

As with most MRI scans, ASL is susceptible to subject motion. Perfusion-weighted images are generated by subtracting the label image from the control image. Since both the label and control images are acquired multiple times to enhance SNR, any motion between different repetitions corrupts the perfusion signal. This is because any imperfect subtraction between control and label images will be attributed to perfusion.

Motion correction in ASL can be done by applying rigid-body registration of the raw control and label images. A reference volume, usually the middle volume in the time series, is first chosen. Then all the volumes in the time series are registered to the reference volume. It is worth noting that motion correction is better performed before the subtraction of label and control images.

The issue of motion can be mitigated by effective background suppression. However, although background suppression removes artefacts originating from the static tissue, it inevitably makes motion correction more difficult. When the signal intensity in the raw images is too low, some key anatomical features will be missing, thus making it challenging to align the individual volumes. Therefore, a good background suppression scheme should leave some signal from static tissue to allow robust motion correction.

4.1.3.2. Distortion correction

Many ASL sequences utilise an echo planar imaging (EPI) read-out to acquire brain volumes in quick succession. Thus, ASL is susceptible to geometric distortions caused by B_0 inhomogeneity, similar to all other EPI sequences. Such a correction can be done when an additional field map (B_0) is acquired. Alternatively, the field map can be estimated if

the EPI images are acquired twice with two opposite phase-encode directions [128]. Since it is time-consuming to acquire the entire sequence twice, the acquisition of the opposite phase-encode direction is normally applied only to the M_0 calibration image (where only a single volume is acquired).

4.1.3.3. Calibration of arterial blood magnetisation

So far, only perfusion-weighted images have been described. Although they contain perfusion contrast, they are in arbitrary units. As a result, comparisons between subjects scanned in different sessions, or studies using different scanners are difficult. Ideally, one would like to have a quantitative measurement of perfusion that is independent of the scanner and the parameters set in the protocol.

A crucial step of the quantification is to estimate the equilibrium magnetisation of water in the arterial blood. This can be achieved in two ways, but both methods rely on the estimation of equilibrium magnetisation in the static tissue. Additionally, the ratio between water magnetisation in the blood and the brain tissue, the partition coefficient, must be assumed from the literature.

First, the arterial blood water magnetisation can be estimated on a voxel-wise basis. This method involves acquiring a proton-density-weighted reference image, which is primarily sensitive to the concentration of water. The proton-density-weighted image should be acquired without background suppression and should have a long TR. One advantage of the voxel-wise method is its ability to correct for receive-coil sensitivity. Modern MRI scanners are usually equipped with local receive coils. The receive sensitivity of these coil elements varies across space, and they are more sensitive to the tissue in close proximity to the coil. Dividing the perfusion-weighted image by the (typically smoothed) proton-density-weighted image eliminates the influence of such a bias, since both images are affected by the same receive sensitivity.

Second, the arterial blood water magnetisation can be estimated by generating a reference region. The most commonly used reference region is the cerebrospinal fluid (CSF) in the lateral ventricles. The selection of the reference region is usually achieved by

segmenting a high-resolution structural image, and then transforming the partial volume estimates to the ASL space. It is worth noting that including voxels that are not purely CSF in the method leads to inaccuracies in perfusion quantification. Therefore, it is recommended to choose a high threshold when creating a mask using CSF partial volume estimates, so that only voxels of pure CSF are selected. When using this method it is necessary to separately account for receive bias using a separate measurement.

4.1.4. Quantification of Cerebral Blood Flow

CBF for PCASL can be calculated using a method proposed by Buxton *et al.* [124]

Equation 4.1

$$CBF = \frac{6000 \cdot \lambda \cdot (SI_{control} - SI_{label}) \cdot e^{\frac{PLD}{T_{1,blood}}}}{2 \cdot \alpha \cdot T_{1,blood} \cdot SI_{PD} \cdot (1 - e^{-\frac{\tau}{T_{1,blood}}})} [ml/100g/min],$$

and for QUIPSS II PASL using a method proposed by Wong *et al.* [127]

Equation 4.2

$$CBF = \frac{6000 \cdot \lambda \cdot (SI_{control} - SI_{label}) \cdot e^{\frac{TI}{T_{1,blood}}}}{2 \cdot \alpha \cdot TI_1 \cdot SI_{PD}} [ml/100g/min].$$

In both equations, λ is the partition coefficient of water between blood and brain, $SI_{control}$ is the signal intensity of the control images, SI_{label} is the signal intensity of the label images, α is the labelling efficiency, SI_{PD} is the signal intensity of the proton-density-weighted image, and $T_{1,\,blood}$ is the longitudinal relaxation time of blood in seconds. For PCASL, PLD is the post-labelling delay in seconds, τ is the labelling duration in seconds. For PASL, TI is the inversion time, and TI_1 is the timing of the QUIPSS II pulse.

4.1.5. The ASL white paper

A consensus paper published by the ISMRM Perfusion Study Group and the European Consortium for ASL in Dementia [129] recommends the following for ASL acquisition and analysis:

Labelling: PCASL labelling with a duration of 1.8 s.

Post-labelling delay: A single PLD of 1.8s for healthy subjects under 70.

Background suppression: Pre-saturation and double inversion.

Calibration and quantification: The voxel-wise calibration method that corrects for receive-coil sensitivity.

4.2. Improving PCASL labelling at UHF using a VERSE guided pTx strategy

4.2.1. Introduction

ASL has intrinsically low signal-to-noise ratio (SNR) due to the relatively low amount of perturbed water magnetization delivered via blood flow versus the signal from static tissue. Thus, ASL can benefit from ultra-high field strengths due to the increase in overall SNR, and the increase of blood longitudinal relaxation time (T_1) [130]. These benefits of 7 T have been used to explore ASL applications that are challenging at lower field strength, such as to measure perfusion signal from white matter [131] and to enable investigation of the subtle metabolic consequences of mitochondrial DNA mutations [132].

Despite these theoretical advantages, the implementation of ASL at UHF is not trivial [130]. An increase of B_1^+ and B_0 inhomogeneity and reduced B_1^+ efficiency below the brain at higher field strength degrade the performance of the labelling RF pulse(s), leading to poor labelling efficiency which, in turn, diminishes the perfusion signal [130]. Also, for a given B_1^+ field strength, the specific absorption rate (SAR) scales roughly quadratically with B_0 field strength, reducing the permitted labelling pulse train duration (for PCASL) and/or amplitude. Various strategies have been proposed to address the B_1^+ challenges of ASL at UHF. Zuo *et al*. placed the labelling plane at the level of the base of the cerebrum due to deteriorating B_1^+ and B_0 inhomogeneity in more inferior positions,

but this approach limits the size of the imaging volume [133]. Wang *et al*. used dielectric pads to improve B_1^+ efficiency of the tagging pulses [134]. Stafford *et al*. introduced an actively decoupled dual transceiver coil system which consists of an eight-channel transceiver head coil and a three-channel transceiver labelling coil [135]. Zimmer *et al*. [136] presented a B_1^+-optimised adiabatic inversion pulse in conjunction with the "PICORE" labelling scheme [126] to improve the perfusion signal.

At UHF, among the labelling strategies, CASL has limited applicability since RF amplifiers in most clinical scanners cannot produce a continuous RF pulse [137]. A head-only transmit coil is often used to image the brain at UHF due to challenges in designing whole-body transmit coils. As a result, PASL approaches are somewhat limited, since a large region that extends further away from the brain is ideally required to be labelled, where B_1^+ efficiency decreases significantly. Thus, PCASL is particularly appealing at UHF. However, PCASL, shown in Figure 4.3, is sensitive to B_1^+ and B_0 inhomogeneity, which reduce its efficiency, and by SAR restrictions that limit the ability to use larger flip angles at higher field strengths. These issues are addressed by the proposed method in this work.

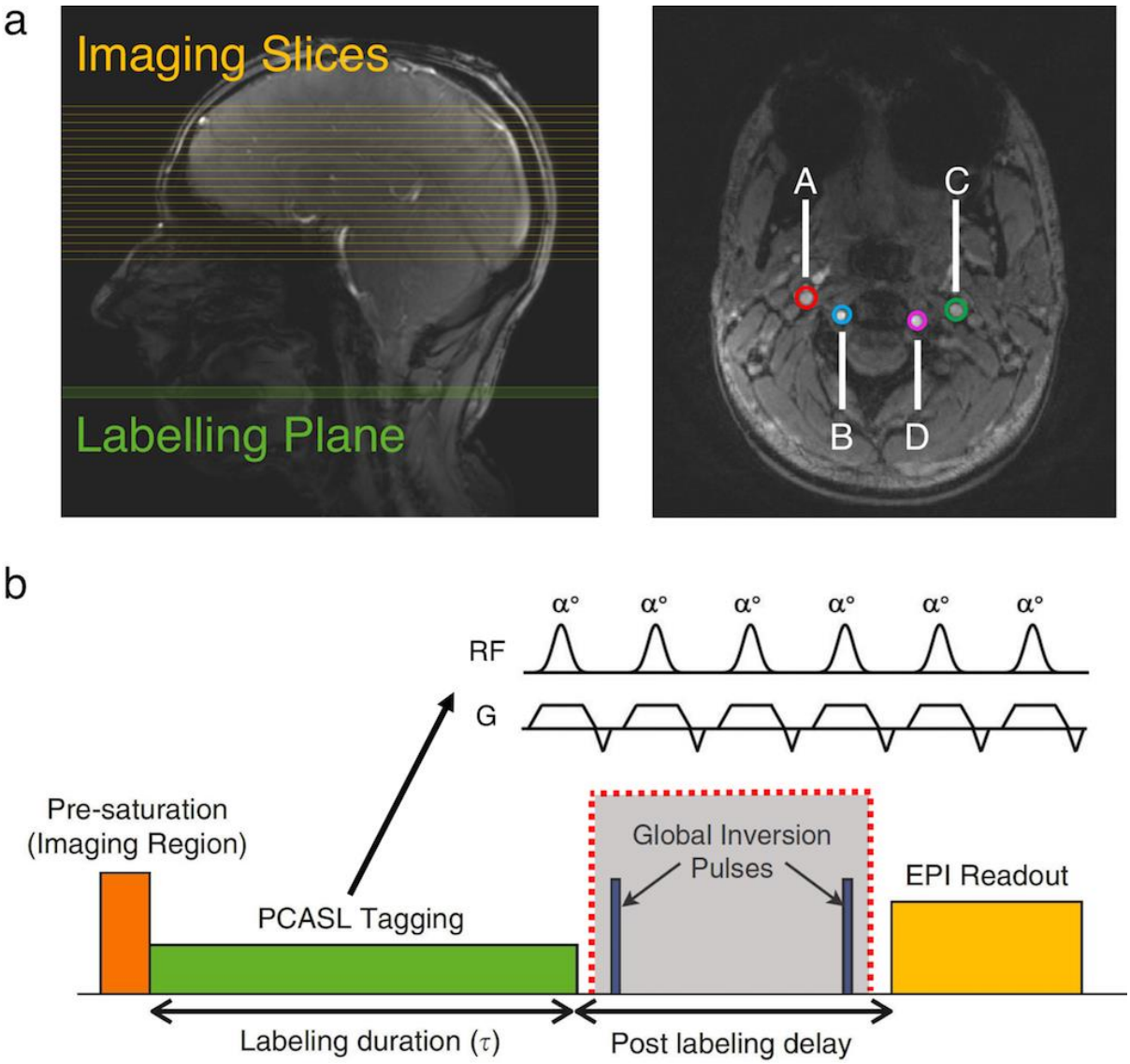


Figure 4.3: a: Labelling plane (green) and imaging slices (yellow) for PCASL on a sagittal localiser (left), and time-of-flight image of the labelling plane through the neck (right). The four main brain-feeding arteries are circled in colour: A (red): right internal carotid artery (RICA), B (blue): right vertebral artery (RVA), C (magenta): left vertebral artery (LVA) and D (green): left internal carotid artery (LICA). b. Schematic of the PCASL sequence. The global inversion pulses (greyed) were discarded at 7 T due to SAR constraints.

Parallel transmission (pTx) provides additional degrees of freedom that allow for constructive and destructive interference of different radio-frequency (RF) transmit channels to mitigate the B_1^+ inhomogeneity. RF shimming (or "static pTx"), aims to produce a more homogeneous and more accurate flip-angle distribution within the labelling region of interest (ROI) by adjusting the complex weights (phase and amplitude) of each available RF channel. In order to mitigate the challenges of SAR constraints a

Variable-Rate Selective Excitation (VERSE) RF pulse approach [138] was used in this study, without compromising the overall PCASL inter-pulse duration or slice profile.

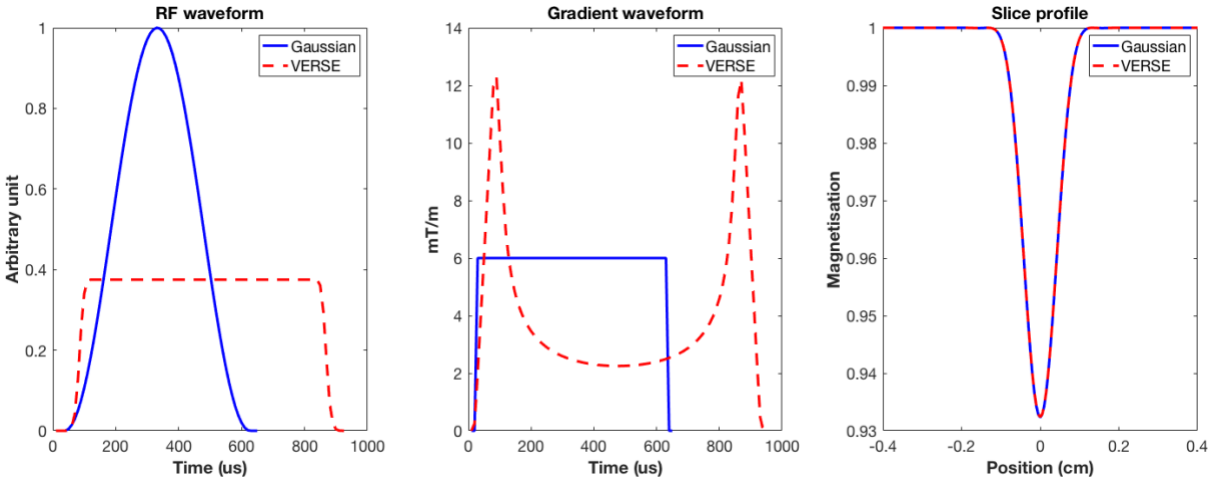


Figure 4.4: RF waveforms, gradient waveforms, and slice profiles of a Gaussian pulse and its corresponding VERSE pulse.

Variable-Rate Selective Excitation (VERSE), shown in Figure 4.4, was proposed by Conolly *et al*. to reduce the SAR of spatially selective RF pulses without compromising their duration and slice profile [138]. VERSE is refabrication technique rather than a pulse design technique, since it calculates a new pulse and a time-varying gradient waveform from a previously designed pulse [138]. Since most RF pulses are peaked in the middle, one should aim for a uniform redistribution of the pulse area by flattening the middle of the pulse, while amplifying the side lobes [138]. The same angle of precession can be achieved by exciting spins for twice as long with a field strength that is half as strong [138]. As a result, the desired SAR reduction can be achieved by extending the middle of the pulse, and expediting the side lobes using a time-varying gradient waveform [138]. More recently, VERSE has been incorporated into pTx pulse design [139]. In this study, we present a VERSE-guided RF shimming strategy to further improve PCASL labelling under explicit power constraints. The schematic of the proposed method is shown in Figure 4.5. This study builds on work presented in a previous conference proceeding showing that RF shimming improves the labelling efficiency of PCASL at 7 T [140].

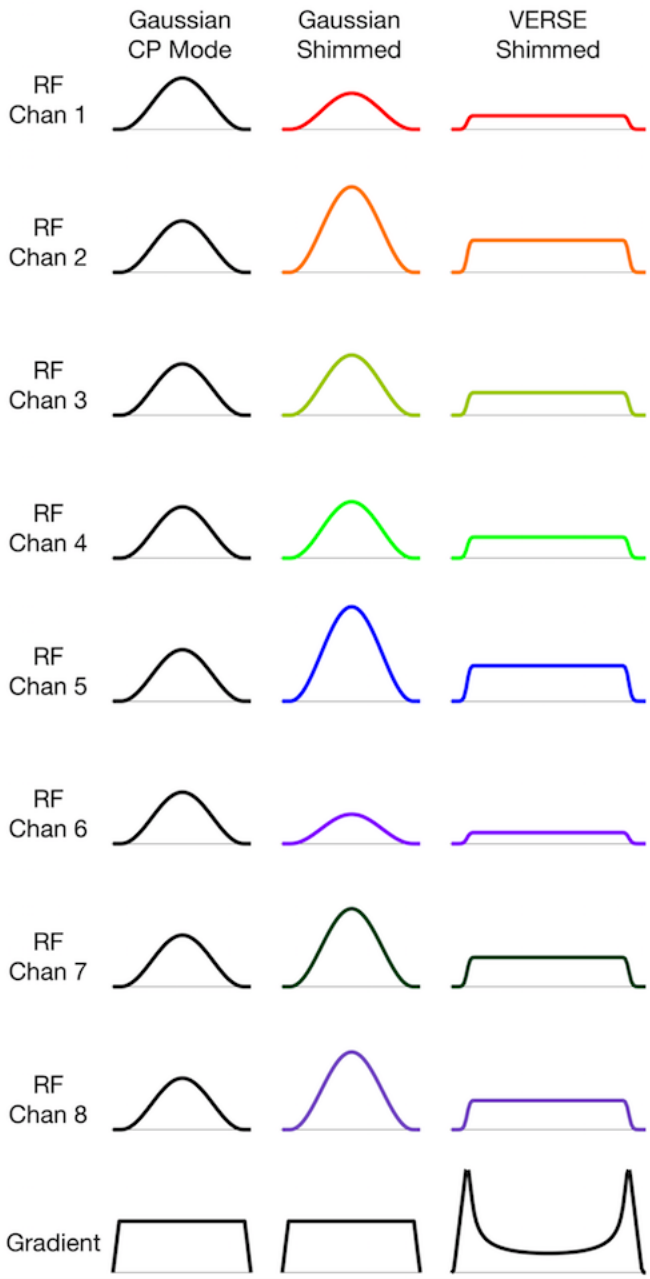


Figure 4.5: RF and gradient pulses of the three labelling schemes.

4.2.2. Methods

Five subjects (male, mean age 33.8, range 27 to 52) were scanned using a Siemens Magnetom 7 T scanner (Erlangen, Germany) equipped with an 8 channel pTx capability. A Nova Medical Inc. (Wilmington MA, USA) 8Tx32Rx head coil was used. All experiments were performed under an agreed technical development protocol approved by the Oxford University Clinical Trials and Research Governance office, in accordance with International Electrotechnical Commission and United Kingdom Health Protection

Agency guidelines. To ensure subject safety, the pTx system was operated under the Siemens-defined "protected mode". In this mode, the 6 min and 10 s average power limits are set to 12.39W and 24.78W (as measured by the Power Absorption Limiter Multi Channel, PALI MC), respectively. The power limits, provided by the coil vendor (Nova Medical) in agreement with the scanner vendor (Siemens), are based on a limit at the coil plug (10 W/20 W for 6 min/10 s, respectively) and include a calibration factor for cable losses.

B_1^+ maps were acquired using a 2D "STE first" phase-cycled DREAM sequence [19, 22]. B_0 maps were acquired using a dual-echo gradient-echo sequence. A time-of-flight (TOF) sequence was used to select a transverse labelling plane location (through the V3 segment of the vertebral arteries) and to identify the four main brain-feeding arteries within this plane (RICA, RVA, LICA, and LVA, Figure 6a). Four elliptic ROIs on the labelling plane (thickness = 2.5 mm) were then manually selected around the four arteries from the TOF image (average size = 76.4 mm^2). The PCASL sequence parameters were based on a study by Okell *et al*. [141] and are listed in Table 4-1. Pre-saturation of the imaging region was achieved via a four-pulse variable angle WET (*w*ater suppression *e*nhanced thorough T_1 effects) scheme [114]. Additional inversion pulses for background suppression [142] were not used due to the high RF power deposition of these adiabatic pulses.

Table 4-1: 7 T experiment PCASL sequence parameters

Parameter	*Value*
Gaussian RF pulse duration	600 μs
VERSE RF/gradient pulse duration	950 μs
RF labelling pulse separation	1.2 ms
Mean tagging gradient	0.8 mT/m
Tagging gradient during Gaussian pulses	6 mT/m
Maximum VERSE gradient	12.27 mT/m
Target flip-angle	20°
Labelling duration (τ)	1 s
Post-labelling delay (PLD)	1 s
6-min average RF power limit	12.39 W
10-s average RF power limit	24.78 W
Voxel size	2 × 2 × 4 mm
Matrix size	110 × 110
Partial Fourier factor	6/8
GRAPPA factor	2
Number of slices	19
Echo time (TE)	13 ms
Volume repetition time (TR)	6 s
Measurements	32 (16 pairs)
Acquisition time	3.5 min

The RF shimming calculation was carried out on a single Gaussian or VERSE pulse, producing a single shim which was applied to the whole labelling train. The VERSE pulse was obtained using an approach proposed by Hargreaves *et al*. with a targeted RF power reduction factor of 2, [143] and VERSE was applied before optimization of the weights. This reduction factor permitted the inter-pulse separation to be preserved, since a longer RF pulse is needed for a larger reduction factor. An RF pulse longer than 950 μs makes preserving the mean tagging gradient impossible without increasing the inter-pulse separation, due to slew rate limits on the gradient system. The labelling pulse flip-angle optimisation strategy was based on an algorithm by Dupas *et al*. [144], and was formulated in the small tip angle approximation and in 2D. This is because the B_1^+ map resolution is relatively coarse (4 mm isotropic) and the B_1^+ field does not change with high spatial frequency in the vicinity of the labelling plane. The pulse calculation was performed on a MacBook Pro laptop (Apple Inc. Cupertino, CA, USA) with a 2.7 GHz Intel Core i5 processer (Intel Corporation, Santa Clara, CA, USA) and 16 GB memory.

A spin dynamics matrix, **A**, was constructed the same way as described by Equation 1 of Reference [144], with inputs that included off-resonance measurements taken from the

B_0 maps, transmit sensitivities taken from the B_1^+ maps, each voxel's position, and the gradient waveforms and RF pulse shape for the Gaussian and the VERSE pulse. Note that this formulation is slightly different from the one presented in Chapter 3: It calculates the flip-angle of the RF pulse (in this case Gaussian or VERSE) of a unit amplitude first, which is then included in the construction of the system matrix. The RF shimming problem is then presented as one that minimizes $|||\mathbf{Ab}| - \boldsymbol{\theta}||^2$, subject to explicit per-channel and sum-of-channels average and absolute power limits, where $\mathbf{b}$ is the complex weight of each RF channel in Volts, and $\boldsymbol{\theta}$ is the desired flip-angle in each voxel in the ROI [145]. The RF power limit was explicitly incorporated into the optimisation algorithm. Therefore, this limit was relaxed to investigate how much gain in flip-angle could be achieved if future vendor updates were to allow for a less conservative RF power limit. A relaxation factor of two corresponds to twice the locally adopted RF power being allowed. Such RF power relaxations are achieved by changing the constraint of the fmincon function. The RF shims were only applied to the labelling pulses, and no pTx strategy was used to mitigate the readout-plane excitation B_1^+ inhomogeneity in this study.

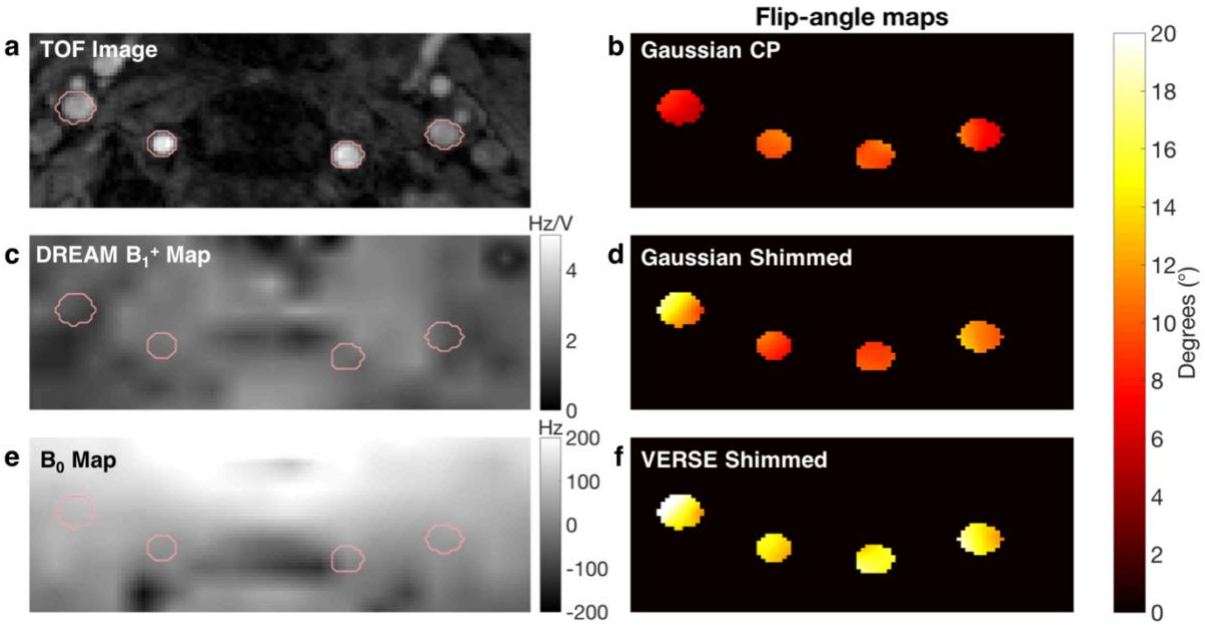


Figure 4.6: a, c, e: Time-of-flight image, γB_1^+ map in Hz/V and B_0 map in Hz with reduced field-of-view of the labelling plane. b, d, f: Flip-angle maps achieved for the three labelling schemes under identical power limits.

Similar to the approach by Dupas *et al*., the optimisation algorithm consists of two steps: the variable-exchange (V-E) method and the active-set (A-S) method [144]. Since the A-S

algorithm is a nonlinear method, the starting point is crucial to the final result. Therefore, the V-E method was used to generate candidate RF shims for the A-S method. The Tikhonov regularisation constant lambda used in the V-E method indirectly controls for the RF power, and the cost function was adjusted to $|||\mathbf{Ab}|-\boldsymbol{\theta}||^2+\lambda||\mathbf{b}||^2$ for the V-E method. A larger λ produces an RF pulse with lower power. To increase the probability of finding a good local minimum, the V-E method, with an initial phase defined to be that from the CP mode B_1^+ phase map, was run with different Tikhonov regularisation constants "λ" (λ = 10^{-6}, 10^{-5}, 10^{-4}, 10^{-3}, 10^{-2}, 10^{-1}) to generate candidate RF shims of distinct energy contents [72]. The λ values were chosen heuristically to produce acceptable results in FA with a feasible RF voltage. The exact steps of the V-E method are detailed below:

The original problem to minimise $\| \, |\mathbf{Ab}| - \boldsymbol{\theta} \, \|^2 + \lambda|\mathbf{b}|^2$ is substituted by a formulation that does not involve the absolute value function by separating the amplitude and phase components of the vector $\boldsymbol{\theta}$. A diagonal matrix (diag($\boldsymbol{\theta}$)) whose elements are the amplitude of $\boldsymbol{\theta}$, and a vector u whose elements are the phase of $\boldsymbol{\theta}$ are constructed: $\boldsymbol{\theta} = diag(\boldsymbol{\theta})\mathbf{u}$, with $\mathbf{u}$ satisfying the constraint of unity modulus $|u_i| = 1$. The optimisation problem can then be written as:

Equation 4.3

$$min(\| \, \mathbf{Ab} - diag(\boldsymbol{\theta})\mathbf{u} \, \|^2 + \lambda|\mathbf{b}|^2)$$

The V-E algorithm iterates between b and u. For a given u, b can be solved by:

Equation 4.4

$$\mathbf{b} = \tilde{\mathbf{A}}_\lambda diag(\boldsymbol{\theta})\mathbf{u}$$

The phase term $\mathbf{u}$ is initialised by the CP mode phase. $\tilde{\mathbf{A}}_\lambda$ was computed using the following equation:

Equation 4.5

$$\tilde{\mathbf{A}}_\lambda = (\mathbf{A}^H\mathbf{A} + \lambda\mathbf{I})^{-1}\mathbf{A}^H$$

where H is the Hermitian transpose operator and **I** is the identity matrix. The phase term **u** is then updated to the phase of Ax. The algorithm above is repeated until certain convergence criteria are satisfied.

The shims generated by the V-E method were then used to initialise the A-S method, and the resulting shim that minimises the cost function ($|||\mathbf{Ab}|-\boldsymbol{\theta}||^2$) under constraint was chosen as the final solution. The Tikhonov regularisation constant was removed and the RF power ($||\mathbf{b}||^2/50\Omega$) limit was explicitly incorporated into the A-S optimisation algorithm. The optimisation problem for the A-S method was as follows: minimise $||\ |\mathbf{Ab}| - \boldsymbol{\theta}\ ||^2$, subject to the limits that the 6 min and 10 s average RF power limits are less than 12.39W and 24.78W, respectively. The iterative A-S method reduces the complexity of the original problem by first generating a set of active constraints. These constraints are a set of linear constraints what would satisfy the original (nonlinear) constraints. The optimisation problem is then solved in a smaller subspace with the set of active constraints. The set of linear constraints is then updated in each iteration, and the linear constraints that are not active are removed. The optimisation algorithm mentioned above was implemented using the fmincon function in MATLAB (The MathWorks, Natick, MA, USA) [146]. A schematic detailing the steps of the RF pulse design is shown in Figure 4.7.

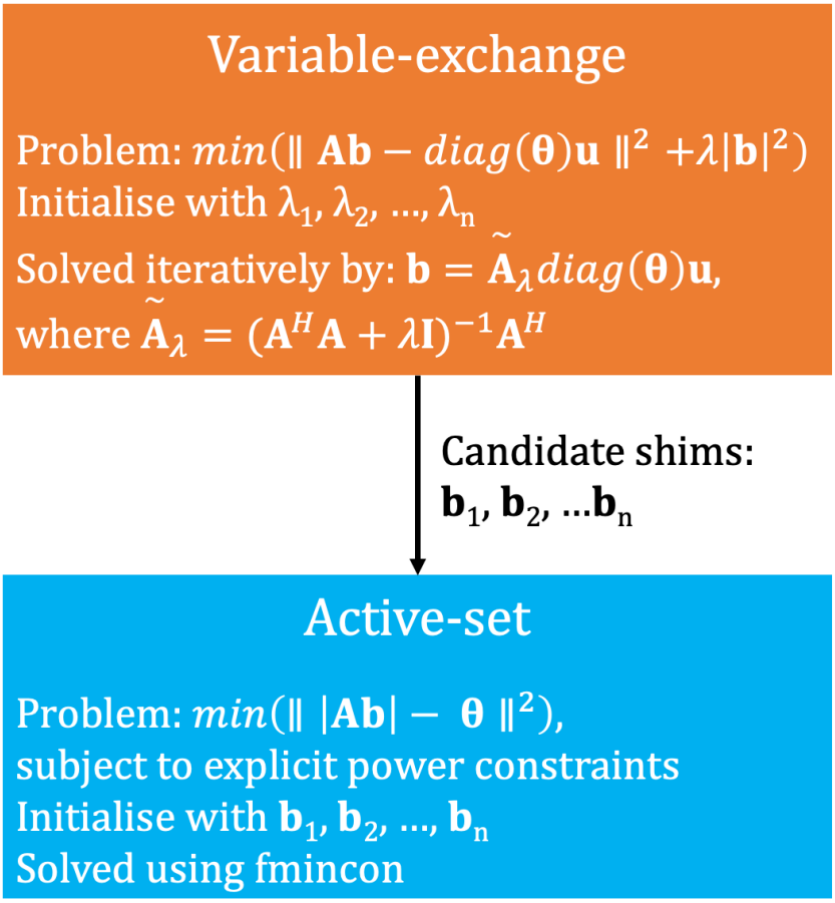


Figure 4.7: Schematic of the pulse design steps. In the first step using the variable-exchange method, RF power is controlled implicitly by changing different regularization parameter. In the second step using the active-set method, the RF power is controlled explicitly by including it as a constraint in the optimization problem.

The same subjects were scanned using a Siemens Prisma 3 T scanner (Erlangen, Germany) for comparison with the 7 T data. Four PCASL sequences were applied during the 3 T session: 1. A matched sequence with a matched labelling pulse flip-angle (7 T FA defined as the mean FA achieved in the four feeding vessels in the RF shimming simulation); 2. A matched sequence, but with a labelling pulse flip-angle of 20°; 3. A matched sequence with an optimised labelling scheme (20° FA, labelling pulse duration = 500 µs, RF separation = 1000 µs, labelling pulse train duration = 1.8 s); 4. A fully optimised 3 T sequence with the same scan time (20° FA, labelling pulse duration = 500 µs, RF separation = 1000 µs, labelling pulse train duration = 1.8 s, TR = 3.7 s, background suppression double inversion on). An M_0 image was acquired at 3 T and 7 T for the quantification of cerebral blood flow.

The data analysis pipeline is shown in Figure 4.8. All analyses were performed using tools from the FMRIB Software Library (FSL) [147]: BET [148] (brain extraction), MCFLIRT

[149] (motion correction), FLIRT [149, 150] (linear registration), BASIL [151] (CBF quantification) tools were used. Geometric distortion correction was performed on the 7 T data due to more pronounced EPI-induced image distortion. Motion correction was applied to the label and control images. Segmentation of grey matter, white matter, and cerebrospinal fluid (CSF) was performed on a T_1-weighted structural image that was also acquired using an MPRAGE sequence [152]. The sequence parameters were: TE = 3.97 ms, TR = 1900 ms, resolution: 1 mm isotropic, acquisition time = 5 min 30s. The GM partial volume was then transformed into the ASL space, and a GM mask was generated using a GM partial volume fraction threshold of 0.4. The labelling efficiency of each labelling scheme was calculated using Bloch simulation of the labelling pulse train with an assumed blood velocity in the feeding artery of 0.3 m/s. Cerebral blood flow (CBF) was calculated using an analysis method proposed by Buxton *et al*. [124] with an assumed 3 T arterial blood T_1 value of 1650 ms [153] and a 7 T arterial blood T_1 value of 2587 ms [154]. Voxel-wise temporal signal-to-noise ratio (tSNR) of the pairwise-subtracted ASL images in the central slice was calculated as the mean divided by the standard deviation of the perfusion signal across measurements. tSNR of the raw EPI series was calculated by dividing pixel-wise the M_0 image by the temporal standard deviation of control images. The mean of the control images was not used as signal in this case because pre-saturation was applied.

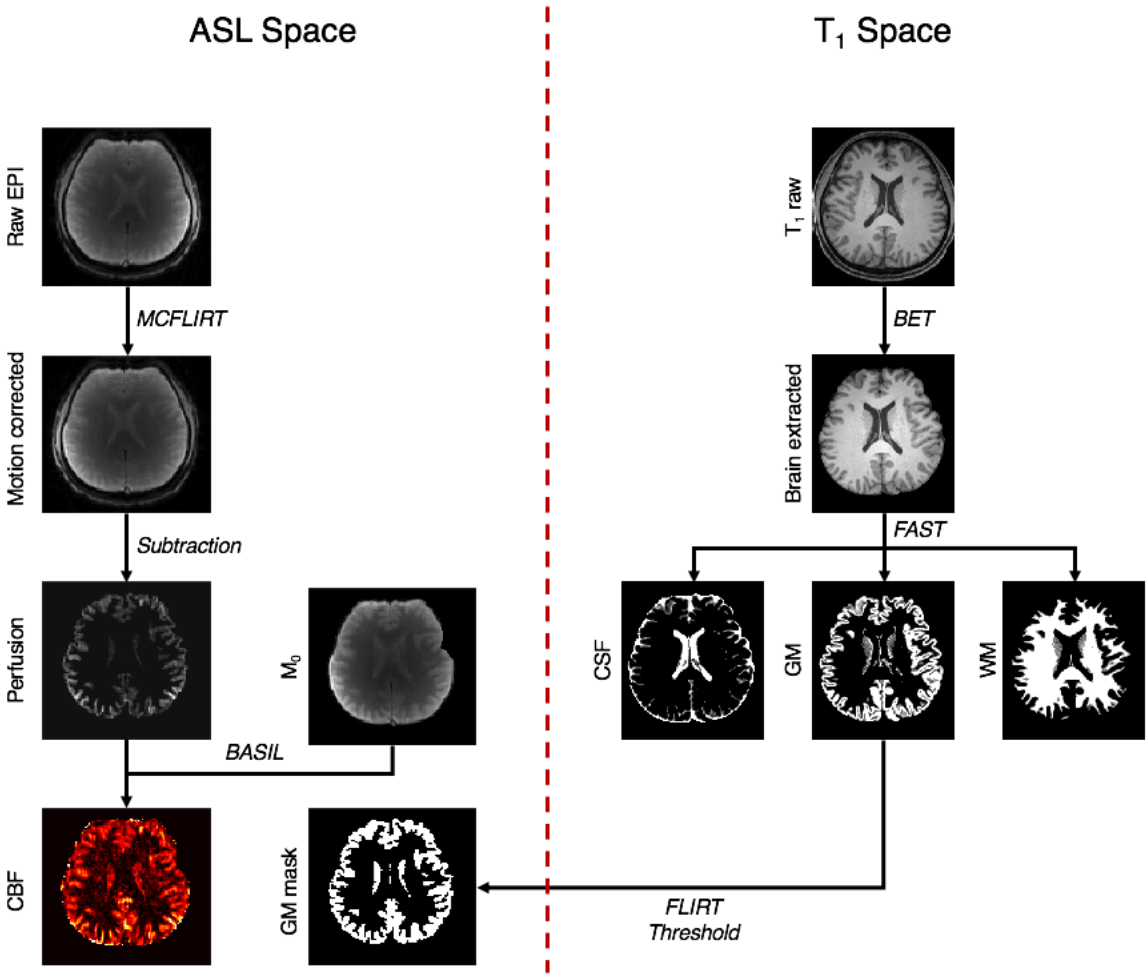


Figure 4.8: Processing pipeline of ASL data.

FA maps of the imaging volume were calculated based on the excitation pulse voltage and per-Volt B_1^+ maps interpolated to the resolution of the imaging slices. Signal loss due to B_1^+ inhomogeneity in the grey matter mask was calculated by comparing the achieved signal and the expected signal that would result from a uniform 90° excitation, using the following equation: signal loss = $1 - \frac{S}{S_0} = 1 - \frac{sin(FA)}{\sin(90°)}$.

4.2.3. Results

The slice profile of the VERSE pulses was simulated in the presence of different off-resonance values. Shown in Figure 4.9, simulation results predicted that there would be minimal contamination of slice profile from off-resonance, but that small changes in the slice position would occur.

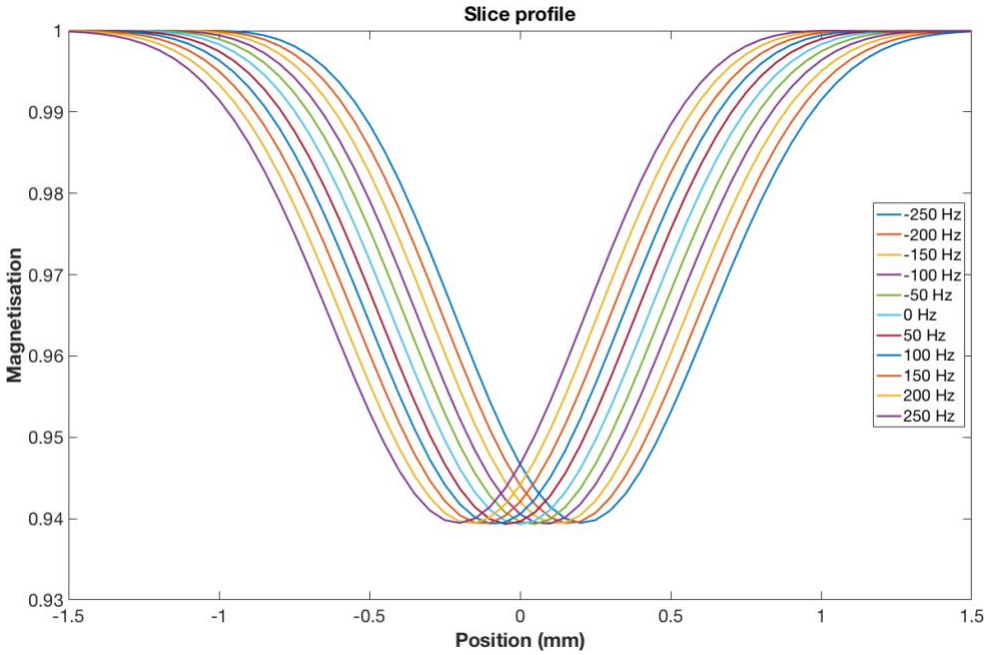


Figure 4.9: Slice profile of VERSE pulses in the presence of different off-resonance values.

The static-pTx RF pulse computation time was approximately 24 s. Simulation results predicted that RF shimming using a Gaussian pulse would improve the mean flip-angle in the ROIs across all subjects by 37% (from 7.45° to 10.17°) compared to CP mode, and that VERSE shimming would improve the mean flip-angle by 90% (from 7.45° to 14.19°) (Figure 4.6 Right, Figure 4.10). Relaxing the RF power constraint by a factor of 2 (Figure 4.11) would allow for a further increase of 39% in the mean flip-angle for the Gaussian pulse, and 31% for the VERSE pulse. A factor of 3 would enable a further increase of 67% (Gaussian pulse), and 40% (VERSE pulse). Any greater relaxation of the limits would only bring a marginal increase in the mean flip-angle, but would further homogenise the flip-angle in the ROI, resulting in a smaller standard deviation.

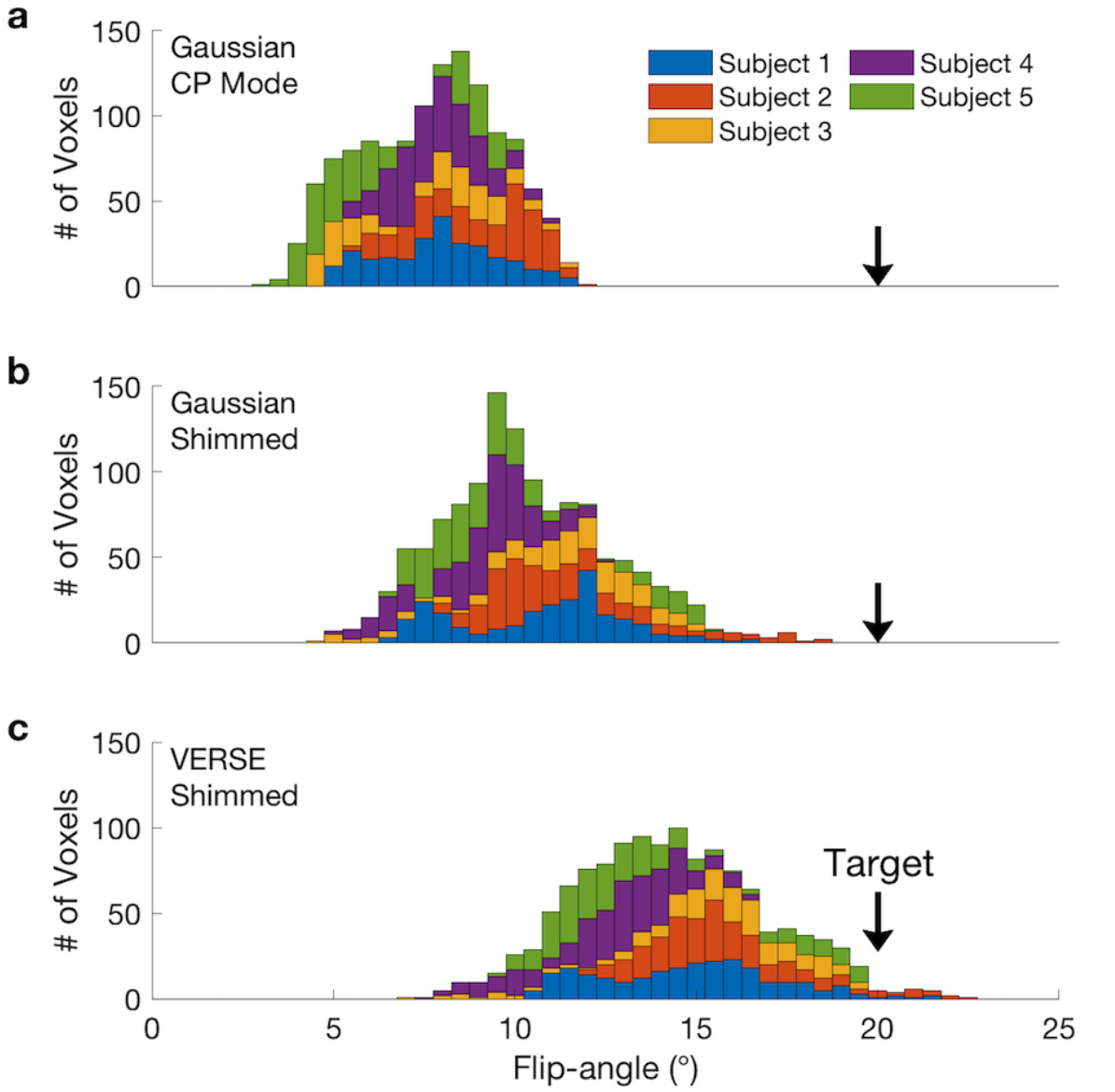


Figure 4.10: Stacked histograms of simulated flip-angles achieved in the ROI of five subjects for each labelling scheme.

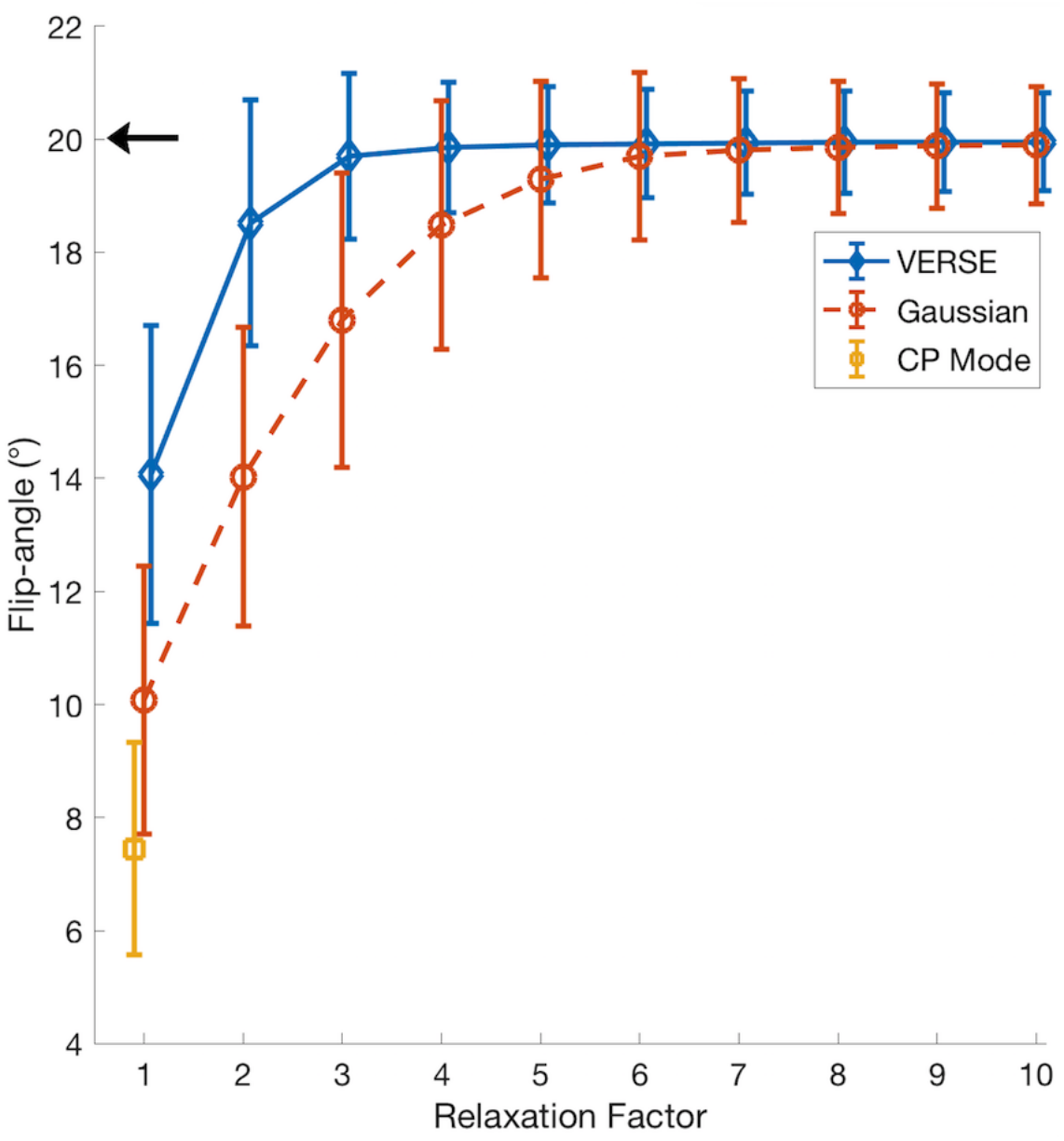


Figure 4.11: Simulated mean and standard deviation of the flip-angles achieved in the ROI if the RF power constraint is relaxed.

The quality of perfusion-weighted images was visually improved when adopting pTx approaches over CP pulses for the labelling pulses at 7 T (Figure 4.12). Compared to Gaussian CP mode, Gaussian pTx shimming improved the mean GM tSNR by 256% ± 316% with a peak of 697% in one subject. VERSE pTx shimming improved the mean GM tSNR by 375% ± 439% with a peak improvement of 1052%. The high absolute value and wide standard deviations were driven by large improvements (697.4% and 487.8%) in two subjects who had very low perfusion contrast under Gaussian CP mode. tSNR of the EPI series in the grey matter was 102.34 ± 57.38 for VERSE shimming at 7 T, 125.22 ± 60.75

for the matched sequence with matched FA at 3 T, and 200.91±74.77 for the optimised 3 T sequence. CBF maps generated from VERSE shimming are comparable qualitatively to those from an optimised 3 T sequence (Figure 4.12). A whole-brain perfusion-weighted dataset is shown in Figure 4.13.

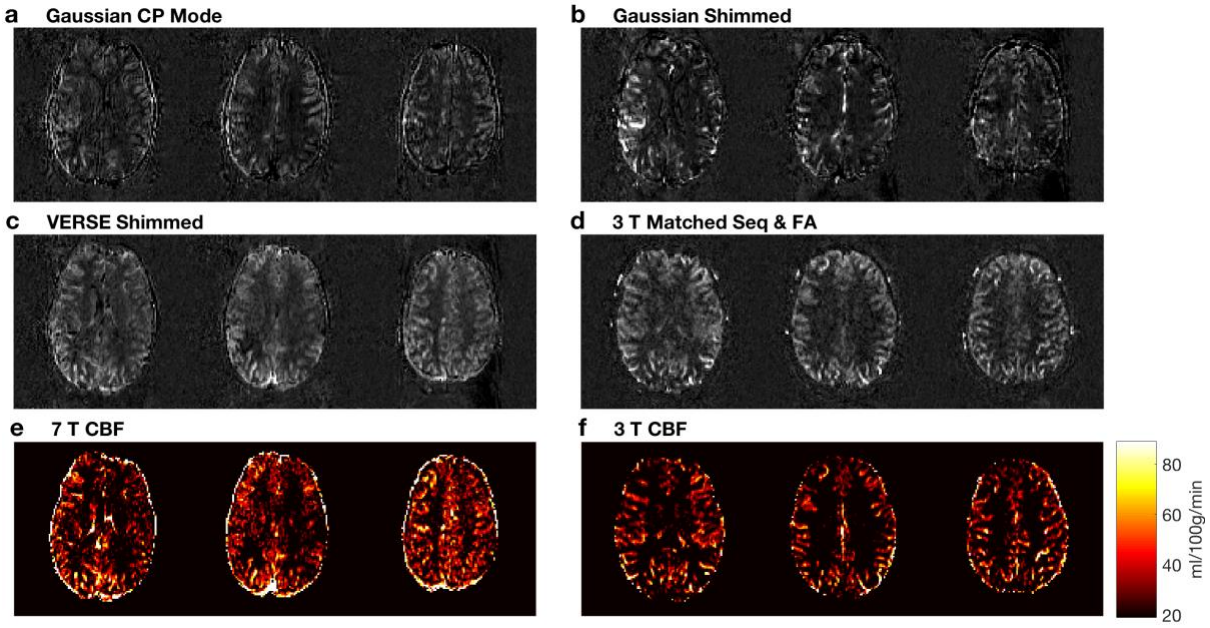


Figure 4.12: Perfusion-weighted images and CBF maps of a representative subject. CBF maps (in ml/100g/min) are derived from VERSE-shimmed images at 7 T. The 3 T CBF map is from an optimised 3 T sequence with 1.8 s of labelling, reduced TR of 3.2 s and double-inversion background suppression.

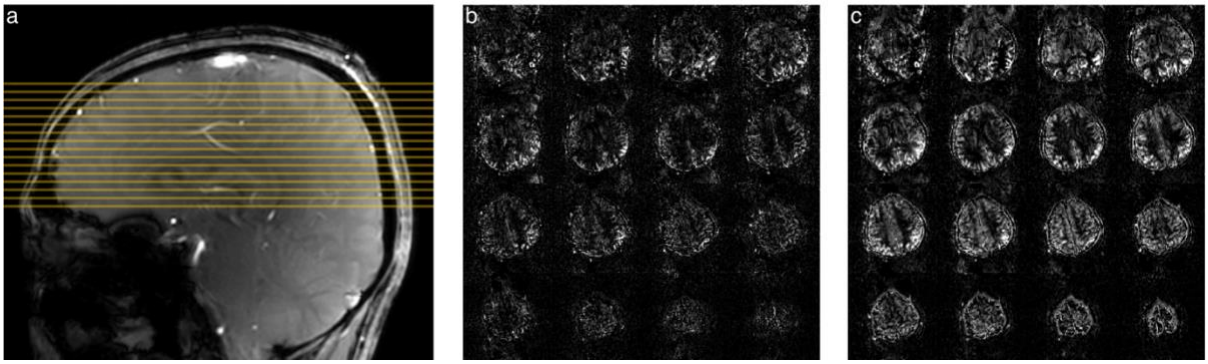


Figure 4.13: a: A sagittal localiser of subject 5 showing the slice positions of parts b and c in yellow. b: Perfusion-weighted images using the Gaussian CP mode from Subject 5. c: Perfusion-weighted images using VERSE shimming from Subject 5.

7 T FA maps for the readout portion of the PCASL sequence within the imaging volume are shown in Figure 4.14. The mean FAs of the readout excitation pulse in the GM of the five subjects are 64.12 ± 9.55°, 63.51 ± 10.52°, 67.03 ± 10.38°, 66.77 ± 10.00° and 63.69

± 10.00°, respectively. Such a variation leads to an average image SNR loss for the 7 T data of approximately 11% in the cortical grey-matter.

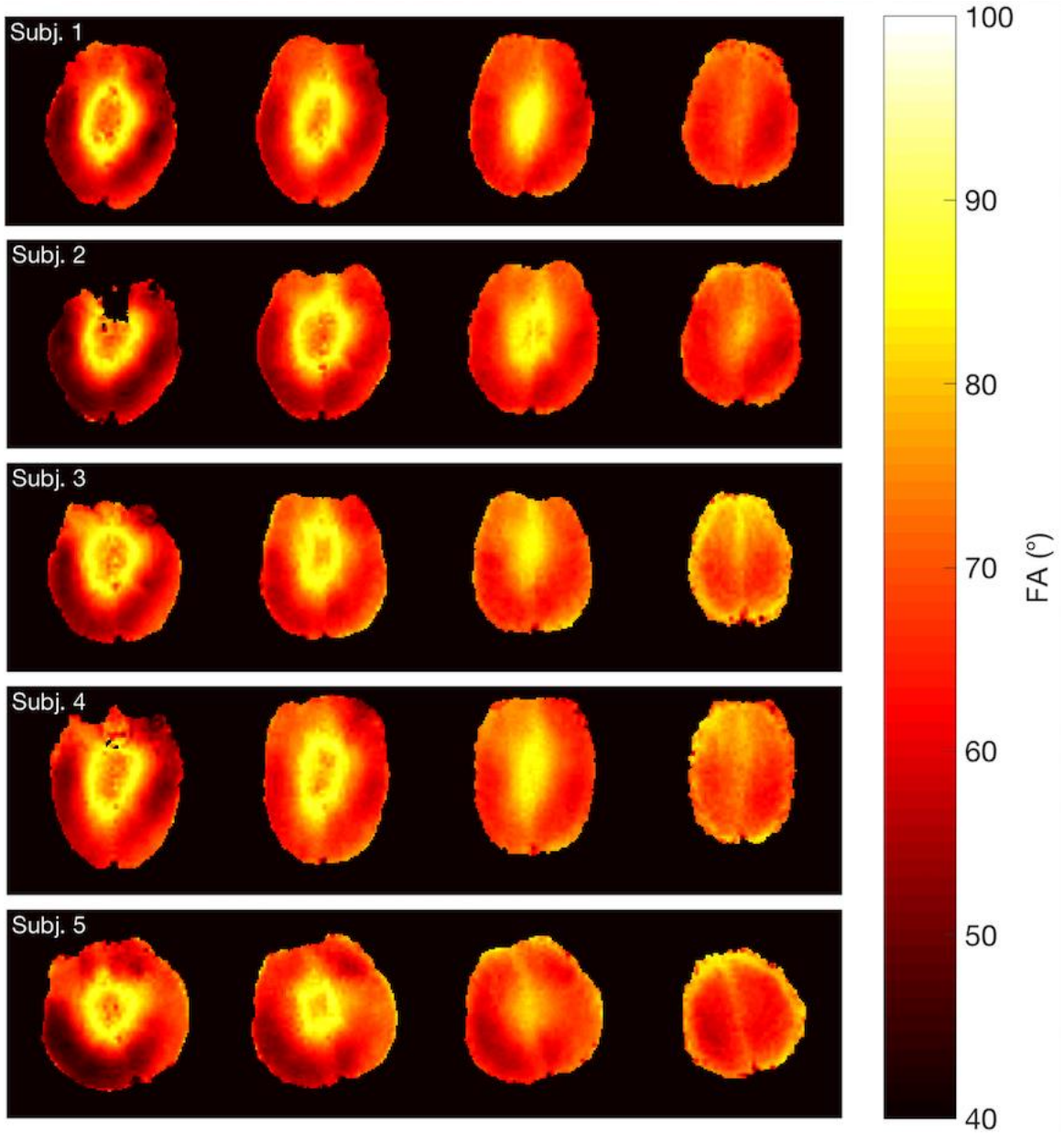


Figure 4.14: Expected 7 T FA maps of the imaging slices (slices 5, 8, 11, 14) from five subjects produced by the 90° readout excitation pulse. The FA maps were calculated based on the excitation pulse voltage and interpolated per Volt B_1^+ maps.

Disappointingly, VERSE shimming at 7 T did not outperform a matched 3 T sequence with a matched flip-angle in tSNR (Table 4-2, Figure 4.15). Compared to VERSE shimming at 7 T, a matched 3 T sequence with a matched flip-angle had a tSNR 5% higher; a matched 3 T sequence with 20° flip-angle 38% higher; a 3 T sequence with optimised labelling 82% higher; and a fully optimised 3 T sequence 110% higher.

Table 4-2: tSNR of various ASL sequences in different subjects.

B_0	7 T			3 T			
	Gaussian CP	Gaussian Shimmed	VERSE Shimmed	7T matched	7T matched (20° FA)	Optimal Labelling	3T Optimised
S1	0.12±0.24	0.16±0.31	0.29±0.21	0.33±0024	0.38±0.26	0.44±0.26	0.52±0.26
S2	0.19±0.24	0.24±0.27	0.25±0.24	0.27±0.26	0.36±0.26	0.48±0.26	0.55±0.24
S3	0.02±0.22	0.19±0.20	0.16±0.20	0.16±0.20	0.24±0.23	0.37±0.23	0.43±0.22
S4	0.13±0.23	0.19±0.28	0.24±0.28	0.27±0.25	0.35±0.29	0.44±0.26	0.55±0.27
S5	0.03±0.23	0.17±0.26	0.34±0.23	0.30±0.25	0.43±0.26	0.56±0.26	0.55±0.25

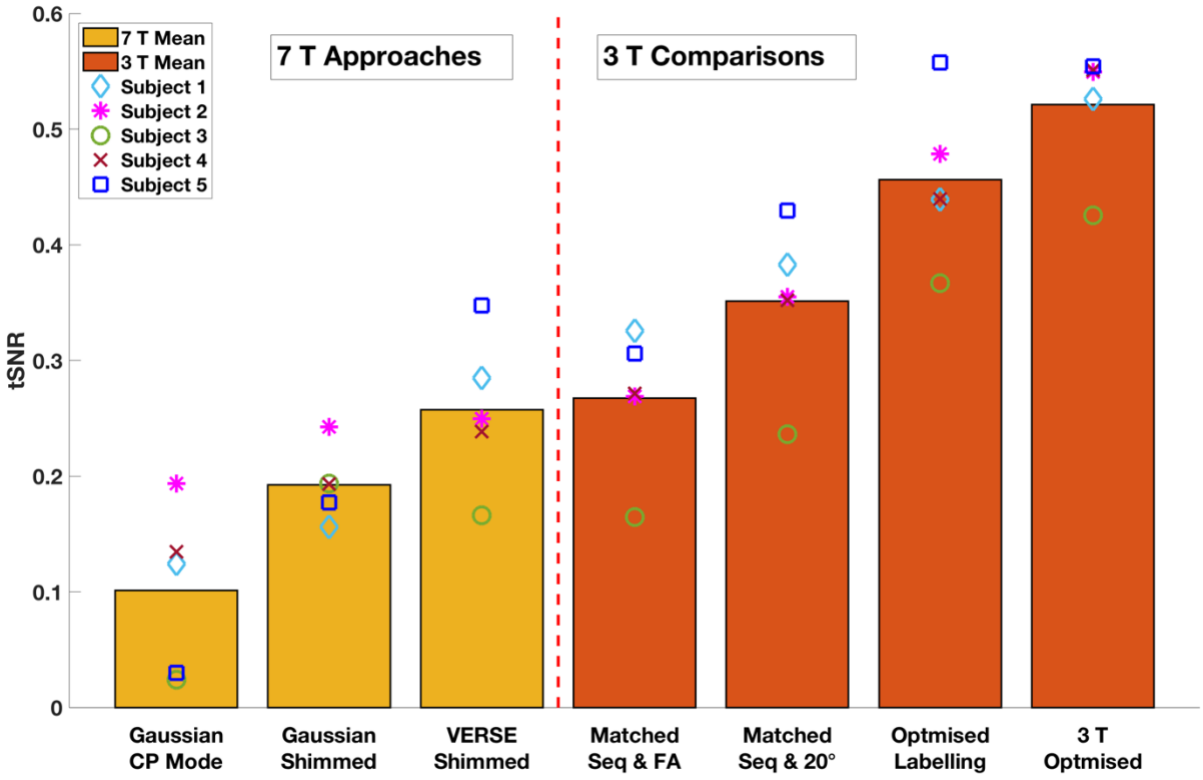


Figure 4.15: Mean GM tSNR of the perfusion-weighted images acquired from different PCASL sequences.

4.2.4. Discussion

Perfusion-weighted images acquired at 7 T using VERSE-guided RF pTx-shimming showed significant improvement in signal-to-noise ratio compared with those acquired using CP mode. This is primarily due to increased flip-angles being achieved in the labelling plane that result in a greater labelling efficiency. Since the RF power limit was included in the RF shimming calculation and all 7 T approaches were power-matched, the

proposed method corrected for both B_1^+ inhomogeneity while taking B_0 variations into account, simultaneously, compared to CP mode under the same RF power constraint, thus greatly improving the B_1^+ efficiency (B_1^+ per unit of RF voltage). Information on B_0 was incorporated into the spin dynamics matrix *A*. Therefore, the proposed approach does not aim to optimise the B_0 performance of the pulses over a range of off-resonance values. Rather, it attempts to solve for the optimal set of shims under the off-resonance value measured by the B_0 map in each voxel. However, phase accrual between the PCASL labelling pulses due to B_0 inhomogeneity was not accounted for in the proposed method. This can lead to decreased labelling efficiency, independent of whether an adequate flip angle is achieved. The off-resonance correction method proposed by Berry *et al.* [155] could provide a complementary approach to correct for phase accrual between pulses. The increased B_1^+ efficiency allows for a lower labelling plane, which in turn permits a larger imaging volume. Unlike dynamic pTx, 'static' RF shimming does not involve calculation of a full RF waveform, nor optimisation of the gradient trajectory. Although it is challenging to achieve a homogeneous B_1^+ distribution over a large field-of-view, static RF shimming is able to achieve more homogenous B_1^+ in the small ROIs used in this study with a short calculation time. Similar approaches have been introduced to improve PCASL at 7 T by using either RF shimming or VERSE. Li *et al*. proposed to improve PCASL labelling at 7 T using phase-only shimming of 8 channels [156]. Boland *et al*. applied VERSE on PCASL labelling pulses at 7 T to reduce SAR, but no pTx strategy was adopted [157]. Serrai *et al*. reduced SAR by changing the sinc saturation pulses to VERSE pulses in the Q2TIPS block of a PASL sequence at 7 T [158]. Compared to PCASL, PASL at UHF suffers from a poorly defined label bolus and a non-uniform labelling efficiency profile across the labelling slab. However, optimising adiabatic inversion pulses at 7 T might overcome such nonuniformity. A thorough comparison between optimised PCASL and PASL at 7 T is needed to evaluate whether statements established at lower fields hold true at UHF.

Despite significant improvement of tSNR for pTx-shimming versus CP mode, VERSE pTx-shimming at 7 T did not outperform the tSNR of a matched 3 T protocol with matched average flip-angle. There are several contributing factors. First, shorter T_2^* decay at 7 T can lead to lower signal in the readout image [130]. Second, our work focuses on mitigating the severe B_1^+ reduction that is observed at the location of the labelling plane

for the type of head-only coils typically used in UHF imaging, but significant B_1^+ inhomogeneity may also remain in the imaging slices. Simulation results indicated that B_1^+ inhomogeneity accounted for roughly an 11% loss in image SNR. Third, although the proposed method attempted to mitigate B_0 inhomogeneity in the design of the RF pulses when the RF pulse was played out, phase accrual due to off-resonance between neighbouring RF pulses in the PCASL pulse train was not accounted for. Such phase accrual would lead to imperfect label and control conditions, thus reducing the perfusion signal. Fourth, although the proposed method improved the mean flip-angle in the four feeding vessels, the improvement might not be uniform across the vessels. Thus, perfusion signal might differ based on the precise labelling efficiency achieved in the individual vessel from which the spins have travelled. A spatial homogeneity term could be introduced into the cost function of the RF shimming optimisation. Finally, tSNR of the raw EPI series for VERSE shimming at 7 T was not significantly different to a matched sequence with a matched FA at 3 T. This may be due to more pronounced effects of physiological noise at 7 T. Work by Triantafyllou *et al*. showed that in fMRI time series, tSNR reaches a plateau at high image SNR in the regime where physiological noise dominates [159]. Therefore, acquiring PCASL images with higher spatial resolution might help better utilise the image SNR gain at UHF.

Adopting more complex pTx strategies for the labelling pulse train might be difficult due to the small gap between one labelling RF pulse and the next (1.2ms in this study). Applying a 2-spokes pulse is likely to produce a more homogeneous FA distribution in the ROI, but we do not expect the mean FA to improve significantly. This is because the tagging performance is primarily constrained by the low B_1^+ experienced in the labelling plane. Furthermore, the inversion of blood spins relies on a flow-sensitive inversion process. Changing the sub-pulse bandwidth by reducing the pulse length to adopt spokes pulses might have undesirable effects on the labelling efficiency.

All perfusion-weighted images were acquired using the vendor's "protected mode" SAR regime, the RF power limits of which are based on conservative local SAR estimations provided by the coil manufacturer and scanner vendor. The goal of this study was to maximise labelling efficiency under a reasonable scan time (3.5 min, TR = 6 s) and an acceptable labelling duration (1 s), although the TR could be further increased and the

labelling duration further shortened to allow for a higher labelling flip-angle to be achieved. According to the simulation results, the targeted flip-angle of 20° across the feeding arteries in the labelling was not achieved in all subjects, primarily due to the low RF power limits. Many of the limitations of this study could be overcome by a less stringent RF power/SAR constraint. Relaxed SAR limits enabled by accurate personal electromagnetic simulations would also allow for higher labelling pulse amplitude, which could lead to further improvement in labelling efficiency. A relaxation factor of two in the power limit could be quickly realised by switching to a local SAR monitoring approach if relevant and validated electromagnetic simulations were available for the RF coil. Further relaxation by reducing vendor-defined safety factors applied to the power measurement hardware can be expected as well. Simulations indicate that a relaxation of the RF power limit by a factor of 2 would allow a mean flip-angle of 18.5°, whereas relaxation by a factor of 3 would allow for a mean flip-angle of 19.7°. In addition, a longer labelling duration could also be achieved, increasing the ASL signal strength further. Moreover, additional inversion pulses for background suppression were discarded due to high SAR in this study. Under more relaxed power constraints, additional inversion pulses could be incorporated into the pulse sequence in conjunction with pre-saturation, potentially providing considerable improvement of background suppression to reduce physiological noise from the static tissue signal. Finally, more advanced pTx approaches could eliminate the need for adiabatic inversion pulses, thus reducing overall SAR [101].

An explorative comparison study conducted in collaboration with a colleague at the University of Cambridge might provide some insight to how conservative the limits currently placed on the pTx system are. In the study, a FID sequence was applied on two scanners, Siemens Magnetom 7 T at Oxford and Siemens Magnetom Terra at Cambridge. The “protected mode” was used on the Oxford scanner, and the “first level controlled” mode was used on the Cambridge scanner. For the same phantom, TR, flip-angle, and the number of measurements, RF pulses with a reference voltage that was twice as high was able to be played out at the Cambridge scanner compared to the Oxford scanner. This result suggests a potential four times relaxation in allowed RF power. However, additional factors such as per volt B_1^+ need to be compared to draw an objective conclusion. It is worth noting that only RF power limits were placed on the Oxford scanner, whereas SAR limits were placed on the Cambridge scanner. In summary, more

in-depth comparisons are required to estimate a realistic and practical relaxation factor that would comply with the IEC guidelines.

A dedicated labelling coil [135, 160] could avoid B_1^+ attenuation in the neck seen in commercial head coils, but additional hardware would then be required. Moving the labelling plane towards a more superior location would increase the flip-angle achieved in the feeding vessels due to better B_1^+ performance of the head coil. However, a higher labelling plane limits the coverage of the perfusion-weighted images. Furthermore, more complex vessel geometry (morphology and tortuosity) occurs when the vessels approach the circle of Willis, which may reduce the labelling efficiency. This is because an oblique labelling plane can lead to reduced labelling efficiency [161]. In more extreme cases, pronounced tortuosity can cause the vessel to cross the labelling plane multiple times, resulting in the spins in the blood water experiencing multiple inversions [161]. More advanced pTx strategies, such as spokes pulses [72, 162] for imaging excitation, would be expected to further improve the overall perfusion image quality. However, the greatest improvements would be expected from further increased labelling efficiency/duration and an increase in the available SAR for tagging and the inclusion of a viable 7T-compatible method for background magnetisation suppression, made possible by relaxed SAR constraints.

4.2.5. 7 T vs. 3 T

Given the results from this chapter, it is worth summarising the contributions from different factors that influence the SNR in the PCASL sequence. Five factors that could be evaluated based on experimental data in this chapter or the literature are discussed below.

1) The image SNR scales linearly with the labelling efficiency, since a higher labelling efficiency implies a larger amount of bolus being labelled. The labelling efficiency can be estimated by performing Bloch equations simulations based the achieved flip-angle in experiments in the chapter (averaged over 5 subjects) and a flow velocity. When assuming an arterial flow velocity of 0.3 m/s, the labelling efficiency was 0.29 for CP mode (for a mean flip-angle of 7.45°) and 0.70 for VERSE

shimming (for a mean flip-angle of 14.19°). The ASL consensus paper by Alsop *et al.* [129] recommended a flip-angle of 20°, which corresponded to a labelling efficiency of 0.9 in simulation. Therefore, the image SNR ratio (7 T vs. 3 T) is 0.32 for CP mode, and 0.78 for VERSE shimming.

2) Shorter T_2^* at higher field strengths decreases the image SNR since more signal would have decayed away at the time of image acquisition. When assuming a T_2^* value of 55 ms at 3 T and 32 ms at 7 T based on a study van der Zwaag *et al.* [163], a TE of 13 ms used in this chapter would lead to an image SNR ratio of 0.84 (7 T vs. 3 T).

3) More pronounced B_1^+ inhomogeneity of the RF pulses used for image acquisition at higher field strength decreases the image SNR due to a lower flip-angle in the grey matter. As reported in earlier parts of this chapter, although the prescribed flip-angle was 90° for the imaging RF pulse, the mean achieved flip-angle in the grey matter was 65° for the five subjects in this study based on acquired B_1^+ maps. Such a reduction corresponded to an image SNR ratio of 0.89 (7 T vs. 3 T), if assuming a perfectly uniform excitation at 3 T.

4) Longer T_1 at higher field strengths increases the SNR, as a higher amount of magnetisation is preserved after the post labelling delay. If assuming arterial T_1 values of 1649 ms and 2087 ms for 3 T and 7 T, respectively, based on a study by Zhang *et al.* [164], a PLD of 1800 ms, as recommended by Alsop *et al.* [129] would result in an image SNR ratio of 1.28 (7 T vs. 3 T).

5) As demonstrated in Chapter 2, intrinsic SNR in an MR experiment scales with the main magnetic field strength. Therefore, moving from 3 T to 7 T would result in an image SNR ratio of 2.33 (7 T vs. 3 T).

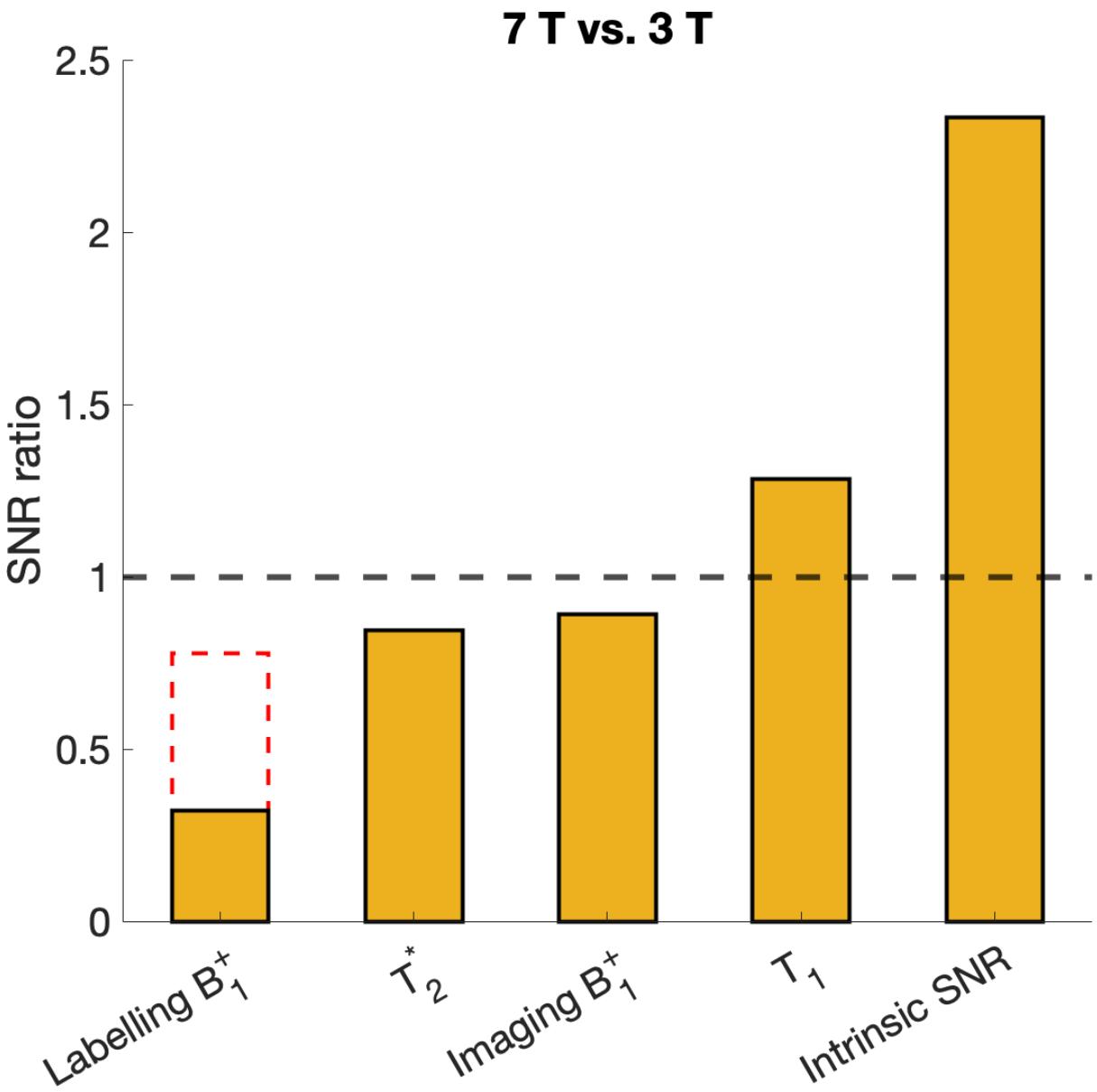


Figure 4.16: SNR gain of the perfusion signal when moving from 3 T to 7 T. The bar enclosed by white dashed lines in the first column shows the additional SNR gain achieved by adopting VERSE shimming compared to using CP mode.

The diagram showing the SNR ratios mentioned above is shown in Figure 4.16. In summary, when only considering the five factors detailed above, using the CP mode at 7 T should lead to an image SNR decrease of 28% compared to at 3 T, whereas adopting the VERSE shimming should lead to an image SNR increase of 75%.

However, the overall potential benefit of higher field strength in the context of ASL is more difficult to assess. First, as discussed in earlier sections, tSNR reaches a plateau with increasing image SNR when physiological noise dominates, as demonstrated by Triantafyllou *et al*. [159]. This finding suggests that the gain in image SNR at 7 T might

not be fully exploited. However, the "diminishing returns" in tSNR can be mitigated by adopting a higher spatial resolution or suppressing the signal from the background static tissue. Second, the current implementation of the 7 T PCASL sequence is SAR constrained, while SAR is generally not an issue at 3 T. The labelling duration and TR were decreased in 7 T experiments in this chapter, and the background suppression module was turned off as well. Therefore, experimental results in this study showed that optimised 3 T sequences outperformed 7 T sequences with the same acquisition time. Furthermore, when and if the SAR/RF power constraint can be relaxed via more sophisticated EM simulations and validation studies, there is the question of how to best "spend" the available SAR. Such considerations require more in-depth experiments and analysis.

4.2.6. Conclusion

We have demonstrated the feasibility of improving PCASL at 7 T using VERSE shimming on a commercial multi-transmit head coil under conservative SAR estimations. The tSNR achieved using VERSE shimming is comparable to that of a matched protocol at 3 T. Further relaxation of SAR constraints should enable the full benefit of 7 T to be realised.

4.3. Future Improvements to PCASL labelling at UHF using a VERSE-guided pTx strategy

The main objective of this chapter is to improve PCASL labelling efficiency by applying VERSE-based RF shimming on the labelling pulses. Therefore, pTx strategies were only applied to the labelling pulses. However, all relevant RF pulses in the sequence could be "pTx-fied". Slice-selective imaging pulses and slab-selective pre-saturation and double inversion pulses can be replaced with spokes pulses. However, since the ROI for each set of RF pulses is different, masking and manipulation of B_1^+ and B_0 maps have to be carried out separately. In PCASL, the labelling pulses typically act on the labelling plane at the jawline level, the pre-saturation and double inversion pulses act on the imaging region in the cerebrum, and the image pulses act on individual brain slices. Furthermore, for the double inversion pulses, the small-tip-angle approximation no longer holds, and a full

Bloch equation simulation is needed for each iteration of the pulse calculation. Thus, the total calibration time inevitably will need to be further extended.

Double inversion pulses were discarded in the experiments in this chapter due to high SAR. However, similar to the strategies applied to the labelling pulses, the VERSE algorithm can be applied to the double inversion pulses as well. Frequency offset corrected inversion (FOCI) pulses [165] were implemented in the sequence for the study, which improves the slice profile of the inversion without increasing peak RF amplitude by modulating the RF and gradient pulses in a way that is similar to VERSE. However, the RF power of these inversion pulses could be further reduced at the potential cost of the corruption of the slice profile. In addition, a more careful study to identify the gain in SNR at UHF by applying the double inversion pulses (in conjunction with the pre-saturation pulse) is needed. This is because in a RF power-limited regime, the same proportion of power can be used to lengthen the PCASL labelling train, or to allow a higher RF amplitude to be played out so that a higher labelling flip-angle could be achieved. Whereas the SNR scales roughly linearly with the labelling duration, increasing the amplitude of the labelling pulses yields diminishing returns in SNR, as shown earlier in this chapter. Therefore, to optimise the overall PCASL sequence, the selection of the best way to "spend" the available RF power has to be established based on quantitative measurement of SNR improvement in each strategy.

Currently, the options for commercially available pTx head coils at UHF are limited. Although tailored RF coils have been built to improve B_1^+ of the labelling pulses in ASL at UHF, the applications of these customised coils were limited. Moreover, it might not be commercially viable for a coil vendor to manufacture a coil with dedicated transmit elements around the desired ASL labelling region/plane due to its narrow applicability. However, given a growing interest in spinal cord imaging at 7 T, it might make commercial sense to manufacture coils with larger coverage around the neck. Such a coil would undoubtedly improve the B_1^+ efficiency of the labelling pulses, measured by the B_1^+ produced by a unit power of input voltage.

The ASL white paper recommends PCASL as the preferred labelling method [129]. However, the superiority in labelling performance of PCASL might not hold at UHF when

SAR is usually a major limiting factor. More comprehensive comparisons need to be performed at UHF for the same RF power or SAR limit to establish the overall superiority among the different labelling strategies. If such comparison studies can be carefully conducted, the ASL community might reach a consensus on the best practices of acquiring ASL images at UHF. Similar to the ASL consensus paper which primarily addresses applications at 1.5 T and 3 T, a UHF white paper could be presented to recommend the following key aspects of ASL acquisitions at UHF with different RF power/SAR constraints (such as Siemens "protected mode" and "experimental mode"):

a. The optimal labelling strategy.
b. The optimal labelling duration (for PCASL).
c. The optimal labelling pulse type (for PASL).
d. The optimal labelling position.
e. Whether and how to apply background suppression.

pTx approaches can also be used for vessel selection in vessel-encoded PCASL. Similar approaches have been proposed prior to the development of pTx technologies [166]. Existing vessel-selective ASL approaches rely on additional transverse gradients and phase cycling to modulate the tag or control state of each vessel of interest [167, 168]. However, this approach could be time-consuming if only a single vessel above the circle of Willis is of interest. Since the labelling pulses have to be applied with more cycles than the number of vessels present in the labelling plane, the larger number of arteries present higher up in the brain inevitably prolongs the scan time. Spatially selective pTx pulses might prove to be advantageous in this scenario, since a tailored pulse can be designed to label the vessel of interest while nulling all other vessels.

Chapter 5 Measuring regional oxygen extraction fraction (OEF) using pTx

5.1. T2-Relaxation-Under- Spin-Tagging (TRUST)

5.1.1. The TRUST sequence

Oxygen extraction fraction (OEF), defined as the ratio of blood oxygen that a tissue takes from the blood flow, is an important parameter for the understanding of normal [169] and abnormal [170] physiology in the brain. Lu and Ge [171] introduced an MR-based method named T_2-relaxation-under-spin-tagging (TRUST) to measure blood oxygenation by labelling spins in the venous blood in the brain and performing pair-wise subtraction of acquired images through the sagittal sinus, the major draining vein through which blood exits the brain. OEF is then inferred based on the known relationship between blood T_2 and blood oxygenation levels [171].

Similar to ASL, the TRUST sequence uses a difference method to isolate blood magnetisation from the background and requires a label image and a control image. However, unlike ASL, the labelling is performed in the cerebrum and imaging is performed in the downstream vasculature: the imaging slice is placed inferior to the labelling region covering the sagittal sinus. The duration between the inversion/control pulse and the image acquisition is denoted as the inversion time (TI).

In order to exploit the known relationship between blood T_2 and blood oxygenation levels the blood magnetisation must be T_2 encoded. Therefore, a T_2 encoding module is incorporated into the TRUST sequence before readout. The T_2 encoding is achieved by an MLEV pulse train [172, 173]. An MLEV pulse train consists of:

1. A 90° pulse that tips the magnetisation to the transverse plane.

2. A series of equally spaced 180° refocusing pulses. The pulses refocus T_2^* decay whilst the magnetisation in the transverse plane experiences the effect of spin-spin relaxation according to the T_2 time constant.
3. The refocussed spins are returned to the longitudinal plane by applying a second 90° pulse.

After the MLEV pulse train module T_2-weighting is encoded in the longitudinal magnetisation. The duration of the T_2 encoding module is called the effective echo time (eTE) and determines the amount of T_2 weighting. The module can be extended by including more refocusing pulses to increase the eTE and the T_2 weighting.

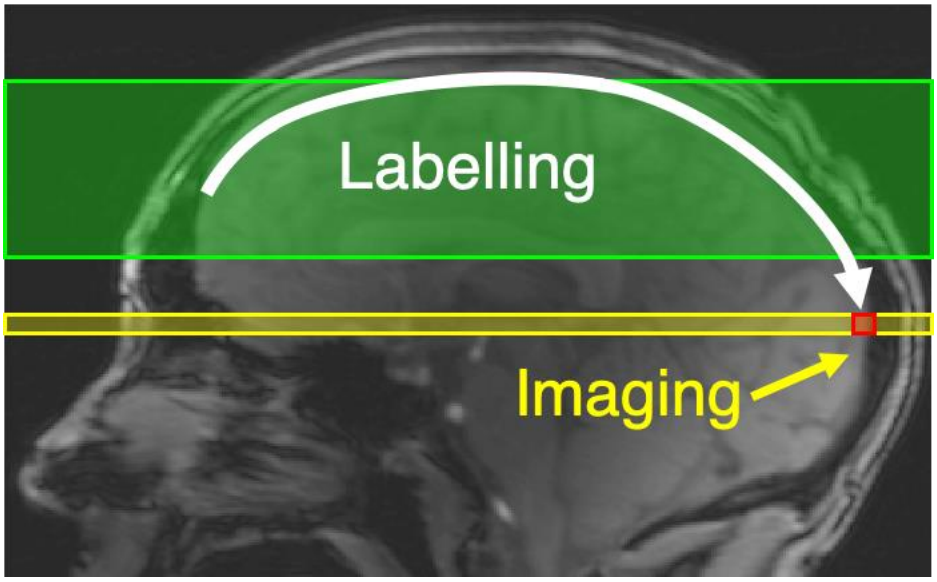


Figure 5.1: Schematic of the TRUST sequence. The labelling slab is shown in green and the imaging slice is show in yellow. The red box indicates the position of the sagittal sinus and the white arrow indicates the draining direction in the sagittal sinus.

TRUST is an intrinsically low-SNR method due to the low volume fraction of blood compared to the static tissue, though this is mitigated by the concentration of labelled blood in the single draining vein. It is therefore beneficial to null the signal from the static tissue using background suppression techniques, similar to ASL. One common background suppression approach is a combination of pre-saturation and double inversion RF pulses.

5.1.2. TRUST signal model

The blood signal from labelled and control conditions can be represented using the following equations, respectively:

Equation 5.1

$$S_{\text{blood,label}} = (1 - 2 \cdot e^{-(TI-eTE)/T_{1b}}) \cdot e^{-eTE/T_{2b}} \cdot e^{-TE/T^*_{2b}},$$

Equation 5.2

$$S_{blood,control} = 1 \cdot e^{-eTE/T_{2b}} \cdot e^{-TE/T^*_{2b}},$$

where TE is the echo time, TI is the inversion time, eTE is the effective echo time, T_{1b}, T_{2b} and T^*_{2b} are T_1, T_2 and T^*_2 of blood. These sequence times are also indicated in the sequence diagram below (Figure 5.2).

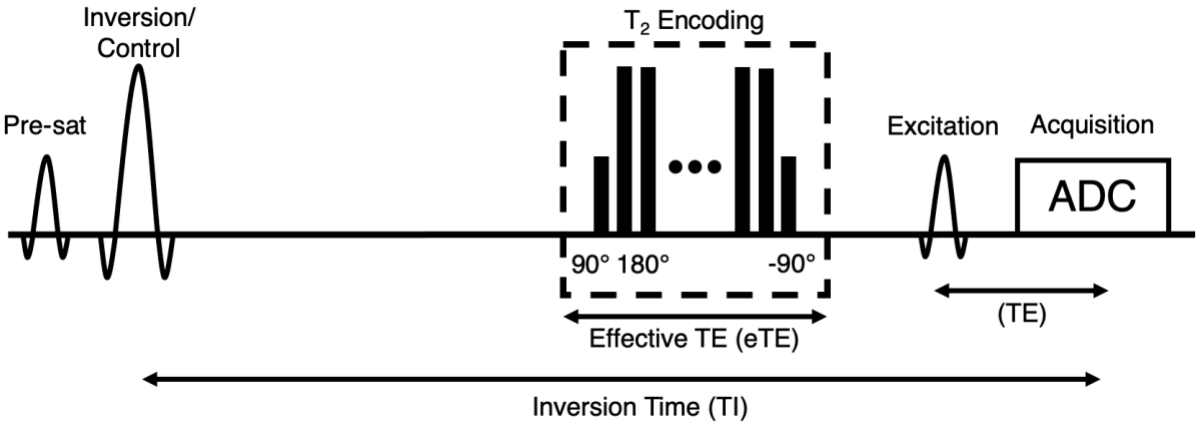


Figure 5.2: Sequence diagram of the original TRUST sequence adapted from Figure 1 of the work by Lu and Ge (doi: 10.1002/mrm.21627).

Therefore, the signal difference between the label image and control image ΔS can be written as:

Equation 5.3

$$\begin{aligned}\Delta S &= S_{control} - S_{label} = S_{control,blood} - S_{label,blood} \\ &= 2 \cdot e^{-(T_1-eTE)/T_{1b}} \cdot e^{-eTE/T_{2b}} \cdot e^{-TE/T^*_{2b}} \\ &= 2 \cdot e^{-TI/T_{1b}-TE/T^*_{2b}} \cdot e^{-eTE/(1/T_{1b}-1/T_{2b})}\end{aligned}$$

$$= S_0 \cdot e^{eTE \cdot C}$$

where $S_0 = 2 \cdot e^{-TI/T_{1b} - TE/T^*_{2b}}$, and $C = 1/T_{1b} - 1/T_{2b}$. S_0 and C are independent of eTE, and do not vary for the same subject under the same physiological conditions. Therefore, we can vary eTE in an experiment, measure the corresponding signal difference between control and label images ΔS. The relationship between ΔS and eTE can then be fitted by a mono-exponential curve to produce the coefficient C. Once C is obtained, the blood T_2 can be calculated as:

Equation 5.4

$$T_{2,b} = \frac{1}{1/T_{1,b} - C}$$

Lu *et al.* assumed that blood T_1 is not strongly dependent on blood oxygenation level [171]. Furthermore, measurement of blood T_2 in the TRUST method is insensitive to changes in blood T_1 [171].

Blood T_2 is typically obtained from a TRUST experiment by curve fitting. From blood T_2 the oxygen saturation fraction can then be calculated based on a known, empirically measured relationship. Blood oxygen saturation fraction refers to the fraction of oxygen-saturated haemoglobin relative to total haemoglobin, and is often denoted by Y.

5.1.3. Measuring physiological parameters with TRUST

Oxygen extraction fraction is the ratio between oxygen consumed by the brain tissue and oxygen delivered by the arterial blood supply. If we use Y_a and Y_v to represent arterial and venous oxygenation saturation fraction, respectively, then the oxygen extraction fraction can be written as:

Equation 5.5

$$OEF = \frac{Y_a - Y_v}{Y_a}$$

The arterial blood is normally fully saturated, and therefore Y_a is generally assumed to be 100%. Thus, under this assumption, OEF can be simplified as:

Equation 5.6

$$OEF = 1 - Y_v$$

The cerebral metabolic rate of oxygen ($CMRO_2$) is the rate of oxygen consumption in the brain taking the unit of μmol O_2/100 g/min, and is another important physiological parameter that is conventionally estimated using positron emission tomography (PET). Xu *et al.* proposed a TRUST-based method to calculate $CMRO_2$ based on the Fick principle of arteriovenous difference in oxygen content [174]. The relationship can be written as:

Equation 5.7

$$CMRO_2 = CBF \cdot (Y_a - Y_v) \cdot C_a$$

where CBF is cerebral blood flow, and C_a is a constant that specifies the amount of oxygen carried per unit volume of blood. C_a is a well-established constant in healthy humans, and was estimated at 833.7 μmol O_2/100ml blood by Xu *et al.* [174]. Therefore, measuring both OEF in the sagittal sinus by TRUST and CBF in brain tissue by ASL allowed Xu *et al.* to estimate whole brain $CMRO_2$ [174].

The scan time of the original TRUST sequence was approximately 4 minutes for a single global measurement, which might limit its wider clinical applicability [171]. Xu *et al.* reduced the scan time of the TRUST sequence while maintaining the precision of OEF estimation by introducing a post-saturation RF pulse and modifying the echo time [175].

In the original TRUST method, the influence of haematocrit (Hct) on blood T_2 was not accounted for. Lu *et al.* performed a calibration study, both on *ex vivo* blood samples and human subjects, to establish the dependence of blood T_2 on Hct and Y [176]. Based on a two-compartment model proposed by Wright *et al.* [177] and Golay *et al.* [178], the

relationship between blood oxygenation Y and blood T_2 was described in the following equation [176]:

Equation 5.8

$$\frac{1}{T_2} = A + B \cdot (1 - Y) + C \cdot (1 - Y)^2$$

where A, B, and C are coefficients that depend on Hct. A, B, and C are related to Hct in the following manner:

Equation 5.9

$$A = a_1 + a_2 \cdot Hct + a_3 \cdot Hct^2$$

Equation 5.10

$$B = b_1 \cdot Hct + b_2 \cdot Hct^2$$

Equation 5.11

$$C = c_1 \cdot Hct \cdot (1 - Hct)$$

where a_1, a_1, a_2, a_3, b_1, b_2, c_1, and c_2 are additional field-strength-dependent and T_2-encoding-sequence-dependent coefficients can that be fitted using data acquired from *in-situ* experiments. Results showed that TRUST-based arterial oxygenation measurement was in agreement with that using pulse oximetry [176].

Liu *et al*. established test-retest reproducibility of TRUST-based $CMRO_2$ measurements [179], concluding that intrasession and intersession variability was smaller than or comparable to that of ^{15}O PET [179]. Further work established robustness in multi-centre studies.[180]. However, Stout *et al.* showed motion could cause an overestimate of T_2 [181].

Various studies have applied the TRUST sequence to different patient groups: Peng *et al.* showed an age-related increase in $CMRO_2$ [182]; Jordan *et al.* found that both OEF and

CBF were elevated in patients with sickle cell disease [183]; Thomas *et al.* found a reduction in OEF in patients with amnestic mild cognitive impairment (MCI) [184].

5.1.4. Motivation for measuring regional OEF

Measuring regional OEF can be of great value in a number of clinical situations. For instance, elevated OEF values were linked with a higher risk of stroke in patients with occlusive carotid artery disease in a PET study by Hokari *et al*. [185]. Therefore, when an occlusion in a specific artery, e.g. the middle cerebral artery (MCA), is present in a patient, it is useful to measure the OEF in the MCA territory using MRI. An ROI within the MCA territory can therefore be selected. When conventional saturation pulses are used to isolate the ROI, such as using the method detailed in Section 5.1.5, the ROI is normally a cube or a cuboid. When spatially-selective RF pulses are used to define the ROI, such as using the method detailed in Section 5.2, the ROI can be a sphere, a cylinder, a cube, or any other shape that can be achieved by the RF excitation pattern. The exact size of the ROI will depend on the specific vascular territory of interest, as the ROI needs to be large enough to provide sufficient signal in the TRUST experiment, and yet should be confined within the vascular territory.

In addition, blood oxygenation levels have been shown to be important for assessing tumour development and aggressiveness [186], as well as for surgical and radiotherapy planning [187]. As an example, a Gadolinium-enhanced T_1-weighted image of a patient with glioblastoma is shown in Figure 5.3 from a study by Blanchet *et al.* [188]. It is meaningful to obtain regional measurement of blood oxygenation in the tumour region, However, the exact size and location of the ROI would depend on the tumour size and location of each patient.

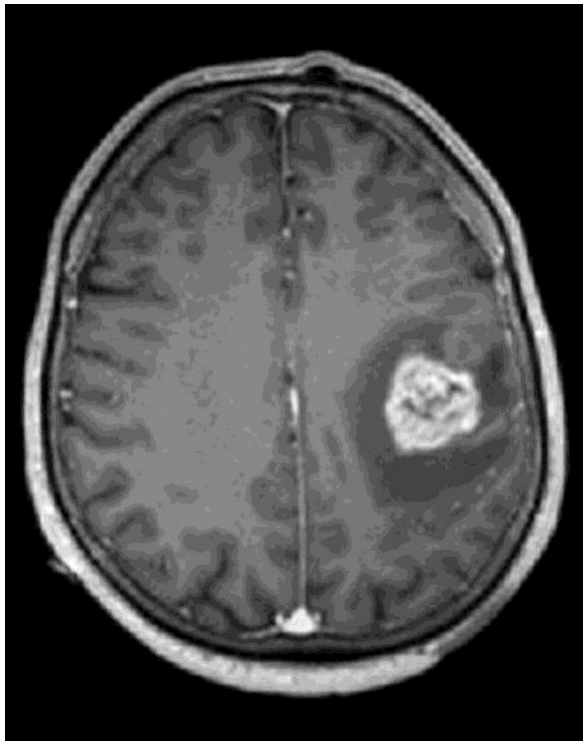


Figure 5.3: A Gadolinium-enhanced T_1-weighted image of a patient with glioblastoma. The figure is adapted from Figure 5 from the work by Blanchet et al. *(doi: 10.3174/ajnr.A2269), and is reproduced with permission.*

5.1.5. Spatially-selective TRUST

Although shown to be a robust non-invasive technique to measure cerebral OEF, TRUST has one key limitation; it does not provide spatial specificity. O'Brien *et al.* applied a train of WET (water suppression enhanced through T_1 effects) outer-volume saturation (OVS) pulses [114] in the labelling volume to measure regional OEF using selective localised-TRUST (SL-TRUST) [189].

O'Brien *et al.* moved the T_2 encoding module to the start of the sequence (shown in Figure 5.4) [189]. This allowed spatial saturation pulses to be placed immediately after T_2 encoding and spin labelling. After the spatial saturation T_2 encoding only remains in regions that have not experienced OVS pulses. The T_2 encoding and spatial saturation are immediately followed by the labelling or control pulses, similar to 'conventional' TRUST. OEF measured at the sagittal sinus therefore only comes from the labelled, unsaturated area, rather than the whole cerebrum as in conventional TRUST. Note that when no spatial saturation RF pulses are applied the modified sequence module order produces estimates of OEF close to those from the original TRUST sequence.

For spatial saturation O'Brien *et al.* used WET spatial saturation pulses [114] to saturate regions outside the target in the labelling slab. The WET saturation scheme was chosen because of its superior saturation efficiency compared to a combination of two repeated 90° pulses. Only four saturation bands are needed to localise a rectangular cuboid ROI: two saturation bands are needed in both the posterior-anterior direction and the left-right direction, with the third dimension localised by the slab-selective labelling pulse. However, since the WET scheme consists of four RF pulses, achieving 2D spatial localisation with WET is time-consuming and SAR intensive, given a total of 16 RF pulses will need to be played out.

In order to overcome this challenge, O'Brien *et al.* incorporated cosine modulation in the RF pulse design to produce a multi-band pulse [189]. Each modulated WET module produces two parallel saturation bands simultaneously. The two sub-pulses for each spatial direction were independently designed and summed.

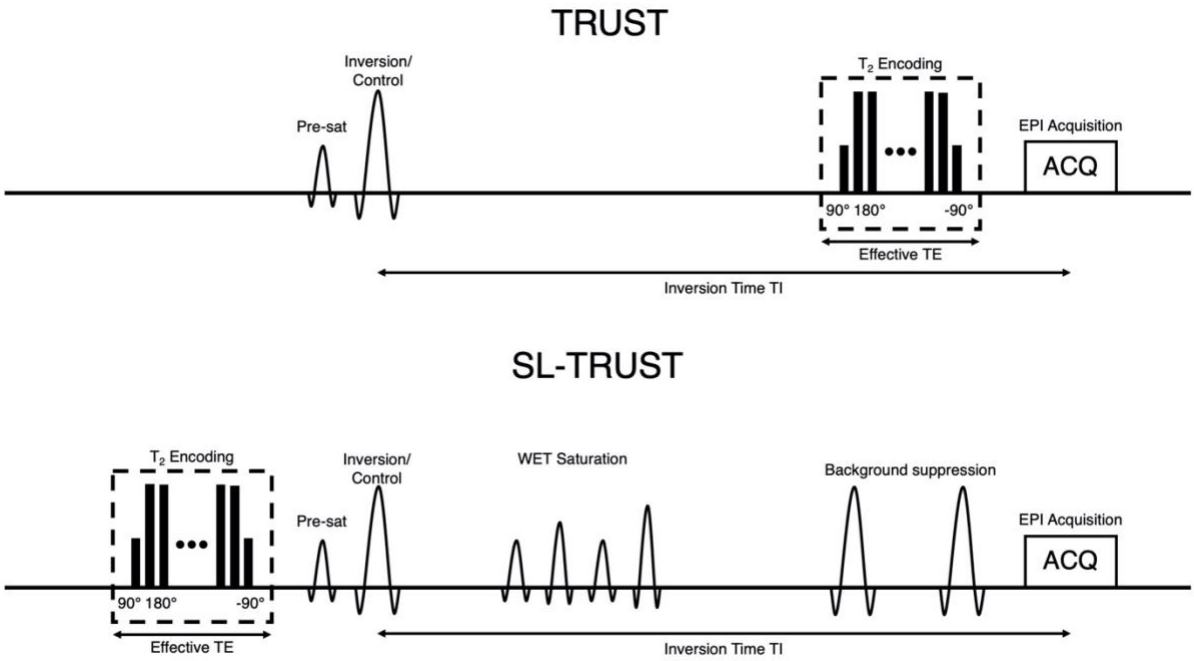


Figure 5.4: Sequence diagrams of the original TRUST sequence and the modified SL-TRUST sequence. T_2 encoding is moved before the labelling module and WET saturation (for spatial selection) is added between labelling and read out.

The modified TRUST sequence, SL-TRUST, was applied at 3 T to measure blood T_2 and OEF in 6 healthy subjects in the following locations: global (no spatial saturation pulses

applied), the right hemisphere (RHS), and middle cerebral artery (MCA) territory. Results showed that OEF values estimated from SL-TRUST (global, RHS and MCA) are similar to whole-brain OEF estimated from the original TRUST sequence in healthy subjects. Inter-session, intra-session, and inter-subject variabilities were evaluated. The coefficients of variability (CoV) were comparable to those measured in a conventional TRUST sequence. Moreover, OEF measurements of two contralateral regions could be achieved with a CoV less than 5% under 5 minutes.

In the next section, an alternative method to measure regional OEF based on pTx will be developed and evaluated.

5.2. Regional measurement of OEF using TRUST

5.2.1. Theory

Since their early developments, pTx pulses have been used for spatially-selective excitation [47, 48]. Although the principle of spatially-selective excitation, or multi-dimensional excitation, applies generally to RF pulses played out on single-channel systems as well, operating on a pTx system can greatly reduce the required pulse duration. This is because each transmit channel has a distinct B_1^+ profile, which can be exploited in pTx pulse design, similar to how the distinct B_1^- profiles of different receive channels can be exploited in standard parallel imaging.

As mentioned in the previous section, O'Brien *et al.* proposed SL-TRUST to add spatial specificity in the TRUST sequence [189]. However, using this method the shape of the ROI is somewhat restricted. Only cuboid-shaped ROIs can be selected because the localisation in SL-TRUST was achieved using pairs of slab-selective saturation pulses. Thus, the

flexibility afforded by pTx provides an alternative to measuring blood oxygenation in more arbitrary spatially selected regions using the TRUST sequence.

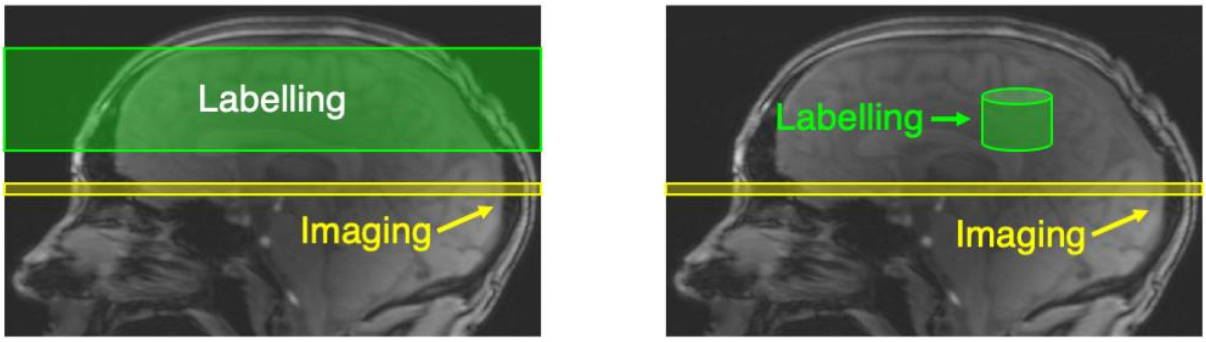


Figure 5.5: The labelling region and the imaging slice of the original TRUST method and the proposed method. .

A spatially-selective inversion (applied in the label condition) would be the logical to localise the TRUST signal, but it is difficult to achieve due to the large flip angle (180°). Therefore, an alternative was proposed to achieve localisation of the TRUST signal by selectively saturate spins outside the ROI.

The new labelling strategy consists of the following steps. First, a spatially selective pTx pulse excites a 2D profile across a column that *excludes* the region-of-interest (ROI), followed by saturation of the outer volume by a spoiler gradient. Second, a slab-selective inversion pulse is played out immediately after the saturation to invert the remaining longitudinal magnetisation within the ROI. This preparation creates the localised tag.

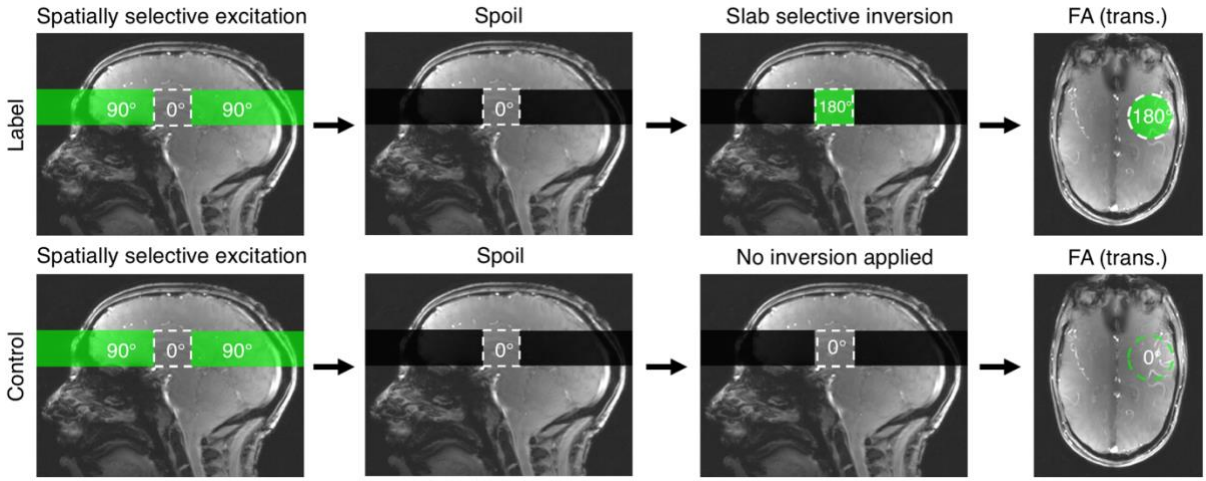


Figure 5.6: Schematic of the labelling strategies for the proposed method. A cylindrical ROI is chosen.

In the control case, the same spatially selective pulse is used, but without a subsequent inversion pulse, thereby creating a signal difference solely from the venous blood within the ROI (see Figure 5.5 and Figure 5.6). The T_2 encoding is moved to the front of the sequence (see Figure 5.7), unlike the conventional TRUST where it is at the end. This is because the blood that needs to be T_2 encoded is the blood within the ROI (created at the start of the TR period) rather than the globally-derived blood that arrives in the sagittal sinus at the time of image readout. Note that T_2-encoding the blood at this latter time would not result in a regionally localised blood oxygenation measurement, but would instead be a (low-SNR) global measurement of blood oxygenation (i.e. the same as measured by conventional TRUST).

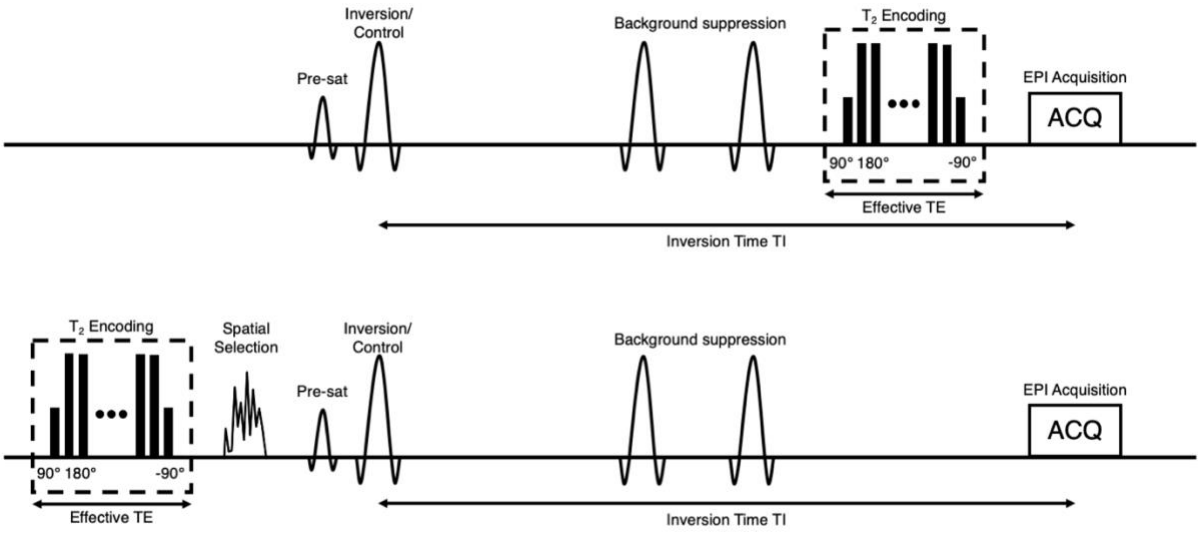


Figure 5.7: The sequence diagrams of the original TRUST sequence (top) and the proposed method (bottom).

5.2.2. Excitation k-space trajectory

A shells trajectory proposed by Davids *et al.* was used for the pulse design [190] (see Figure 5.8) of the selective pulse. One key contribution in the work by Davids *et al.* is the parameterisation of the excitation k-space trajectory using a small number of shape parameters. Three different trajectories were explored in their study: 3D shells; stack-of-spirals; and cross. However, no gradient trajectory optimisation was performed in our study due to computational constraints.

The maximum gradient amplitude and slew rate were set to 22 mT/m and 200 mT/m/s, respectively. The shells excitation k-space trajectory is parametrised using seven parameters φ_1, φ_2, φ_3, φ_4, φ_5, φ_6, and φ_7. These seven parameters represent k_x extent, k_y extent, k_z extent, number of shells, number of revolutions, non-uniform number of revolutions, and the non-uniformity of the shell radii, respectively. The φ parameters in this chapter were heuristically chosen to be 40, 40, 20, 7, 6, 1, 1, and 1.

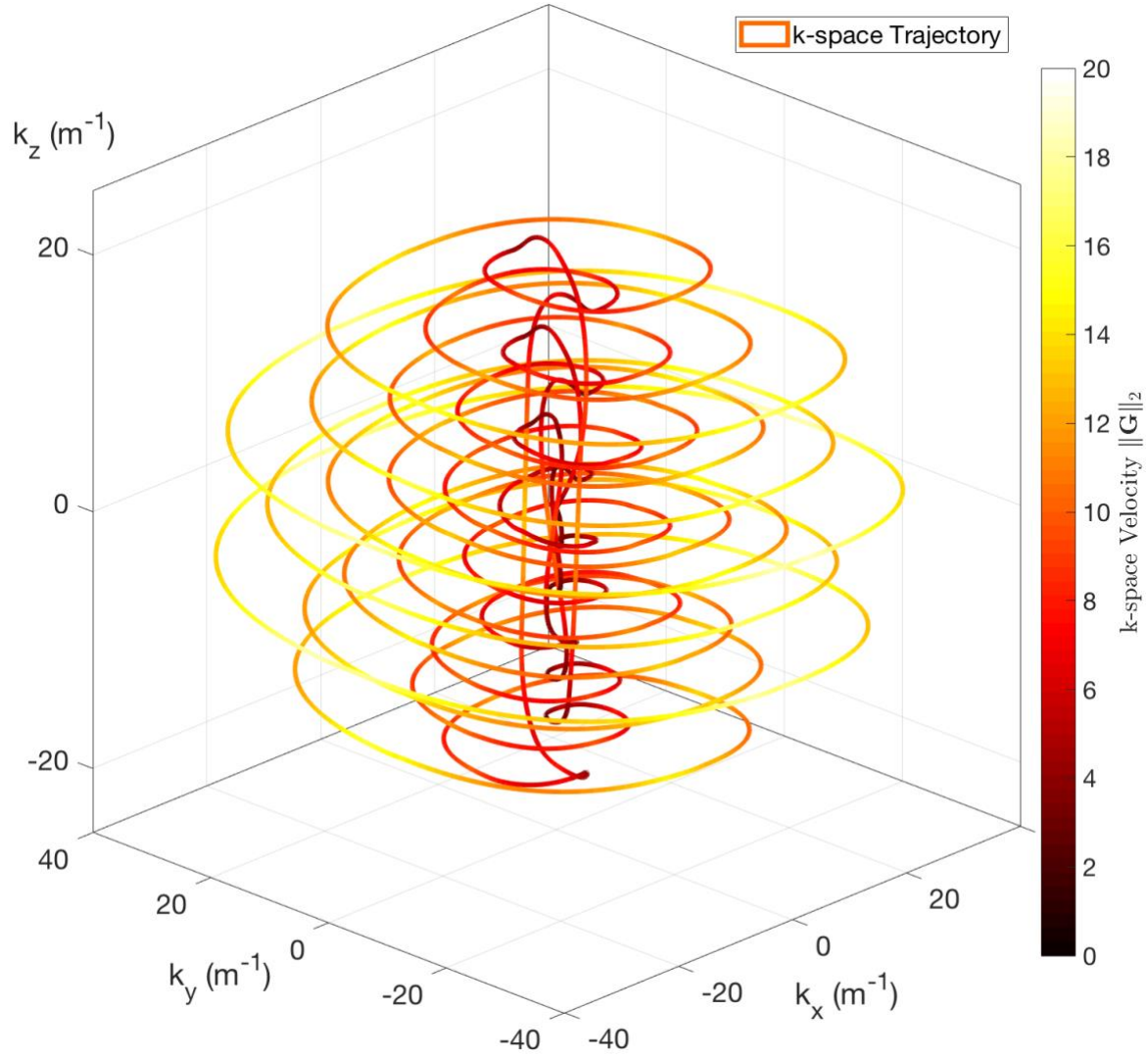


Figure 5.8: Excitation k-space trajectory of the proposed method. The colour at each location of the trajectory represents the velocity of traversing through k-space.

5.2.3. RF pulse design

B_1^+ and B_0 maps were acquired from a single subject (25 years, male) on a Siemens (Erlangen, Germany) Magnetom 7 T scanner equipped with an 8 channel pTx system, and

a Nova Medical Inc. (Wilmington, MA, USA) 8Tx/32Rx head coil. B_1^+ maps were acquired using a 2D "STE first" phase-cycled DREAM sequence [19, 22]. B_0 maps were acquired using a dual-echo gradient-echo sequence. A brain mask was generated from the raw magnitude images in the B_0 mapping sequence using BET [148].

A cylindrical ROI with a height of 30 mm was chosen. The pulse design employed the variable-exchange algorithm, which was based on a method proposed by Dupas *et al*. [144]. The regularisation constant λ values were chosen empirically to produce an acceptable balance between flip-angle and RF power. The optimisation algorithm was implemented in MATLAB (The MathWorks, Natick, MA, USA) [146].

The designed RF pulse was then incorporated into the TRUST sequence to evaluate its performance. T_2 encoding, pre-saturation and double inversion pulses were turned off to isolate the effects proposed RF pulse. Five slices in the were acquired in the target region of RF pulse design (the inversion slab) using an EPI readout.

Simulation results are shown in Fig 5.9. A root mean square error (RMSE) of 6.71% from the defined target profile was achieved in simulation. For the experimental evaluation, raw EPI images were masked and shown in Fig 5.10. A circular pattern for the intended ROI could be observed in each slice, but the boundary of the pattern varied across slices. Moreover, saturation of signal outside the ROI was not achieved with great accuracy. The sum of pixel values in the ROI accounted for an average of 27.1% of the sum of pixel values in the whole masked brain slice.

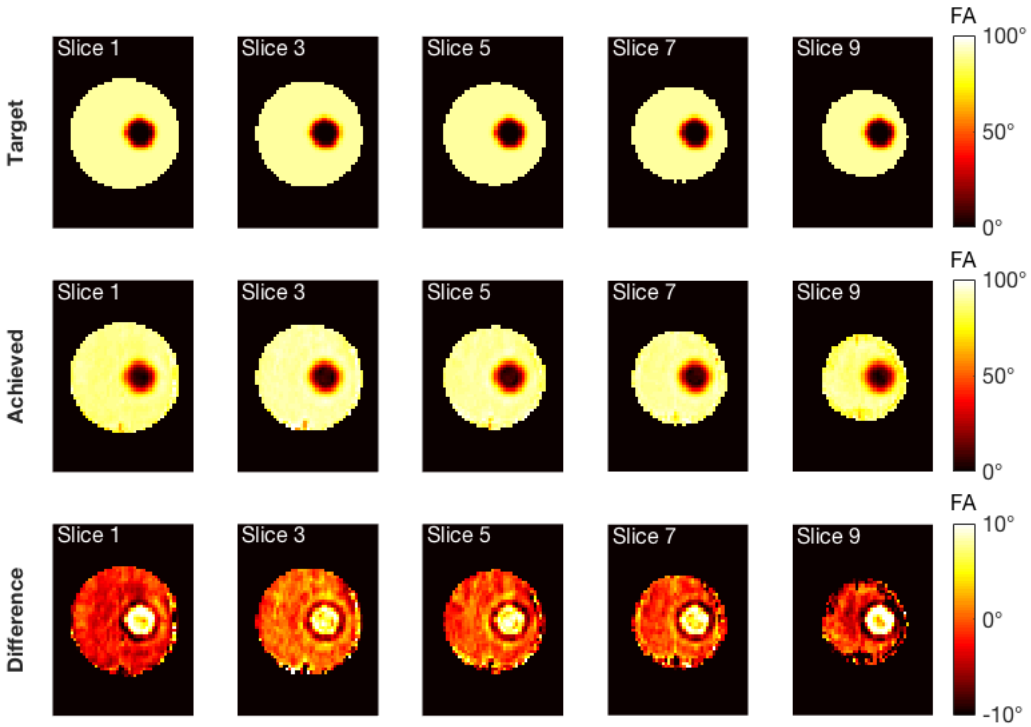


Figure 5.9: Simulation results of the proposed RF pulse. Only slices 1, 3, 5, 7, and 9 were shown for simplicity.

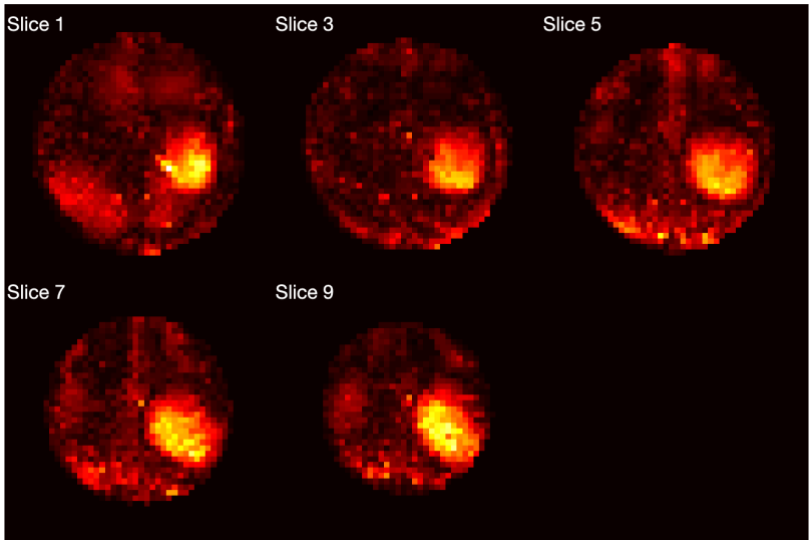


Figure 5.10: Brain masked raw EPI images acquired after the proposed RF pulse was applied in a single subject. T_2 encoding, pre-saturation and double inversion pulses were turned off to evaluate the performance of the proposed selective RF pulse. Slices are centred on the target region, not the sagittal sinus.

5.2.4. Phantom study using three saturation modules

5.2.4.1. Experimental details

The disappointing results shown in the previous subsection indicated that the saturation outside the ROI was not sufficient. The crusher gradient amplitude was modified (by varying the amplitude from -50mT to 50mT with an increment of 5mT) to investigate the efficacy of gradient spoiling, but the acquired image did not show any qualitative difference with increased spoiler moment.

Therefore, it was concluded that the imperfect saturation was primarily due to remaining magnetisation in the longitudinal axis, as opposed to unspoiled magnetisation in the transverse plane. It was hypothesised that the proposed method might benefit from repeating the saturation module (consisting of the spatially-selective pulse and a crusher gradient). Such a method would further excite and then spoil the remaining longitudinal magnetisation outside of the ROI, leaving magnetisation within the ROI largely intact. This technique is common among saturation strategies. For instance, the WET saturation module [114] contains four RF pulses with different flip-angles and interleaved spoiler gradients.

A phantom experiment was therefore conducted to examine the potential benefits of repeating the saturation module. B_0 and B_1^+ maps were acquired on an oil phantom, and the pulse design algorithm used in this subsection was identical to that used in the *in vivo* study. The simulation results of the pulse design is shown in Figure 5.11.

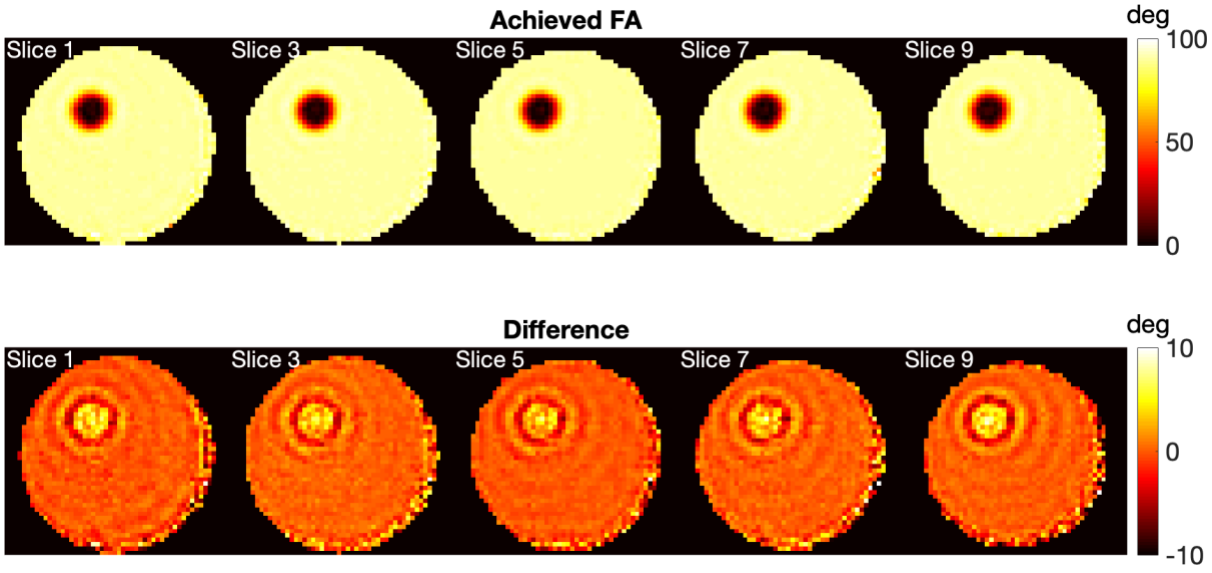


Figure 5.11: Simulated excitation profile of the spatially-selective pulse and its difference to the excitation target

EPI images were then acquired with different numbers of saturation modules with a pulse voltage of 223V. The imaging slice was placed at the bottom, in the middle, and at the top of the inversion slab (target region for RF pulse design) to explore efficacy of the proposed method in different locations (shown in Figure 5.12). The bottom, middle and top of the slab refer to the position of the imaging slice when it is placed at the lower end, the centre, and upper end of the target region. The directions of the spoiler gradients were permuted as they were repeated to avoid refocusing of the magnetisation by spoilers with the same moment. For the case with three saturation pulses, the axes along which the spoiler gradient were played out were: x and y (after the 1st pulse), y and z (after the 2nd pulse), x and z (after the 3rd pulse). Note that all images acquired in the phantom study are plotted with the same scale in this section.

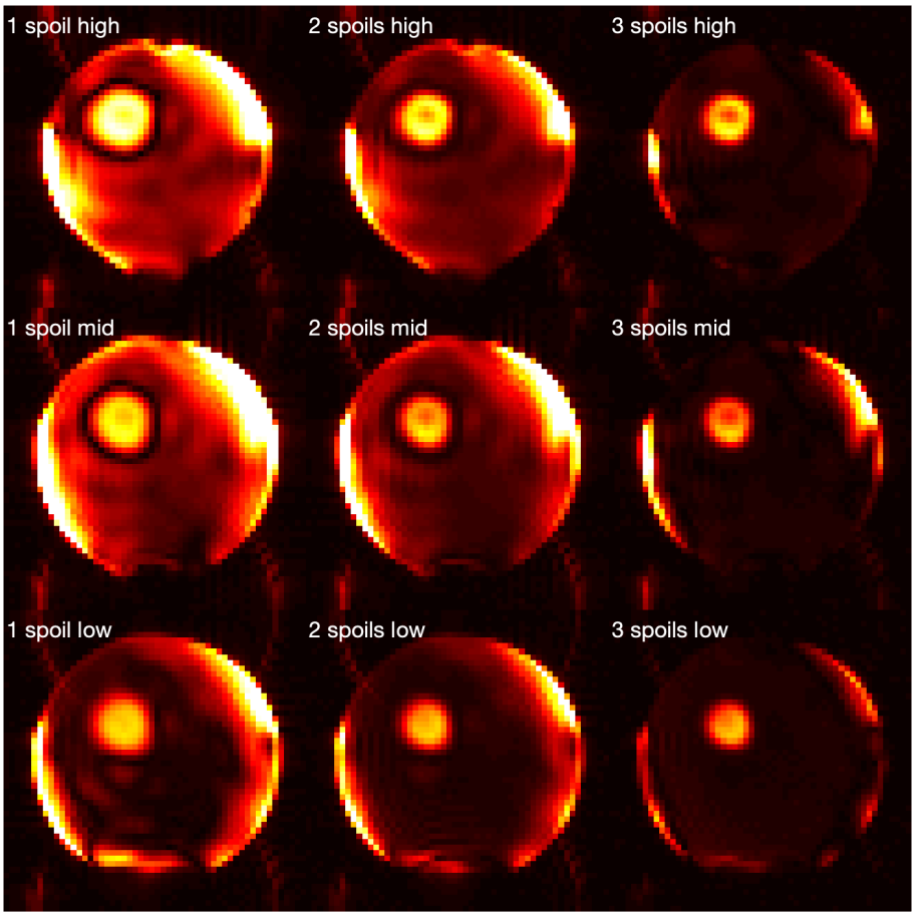


Figure 5.12: EPI images acquired on an oil phantom with a pulse voltage of 223V and different numbers of repetitions of the saturation module. The left, middle, and right columns show 1, 2, and 3 saturation module repetitions, respectively. The bottom, middle, top rows show images acquired at the bottom, in the middle, and at the top of the inversion slab, respectively.

During the experiment, it was observed that lowering the pulse voltage could improve the saturation performance. Therefore, the same experiments with a slightly lower pulse voltage of 180V were repeated (shown in Figure 5.13).

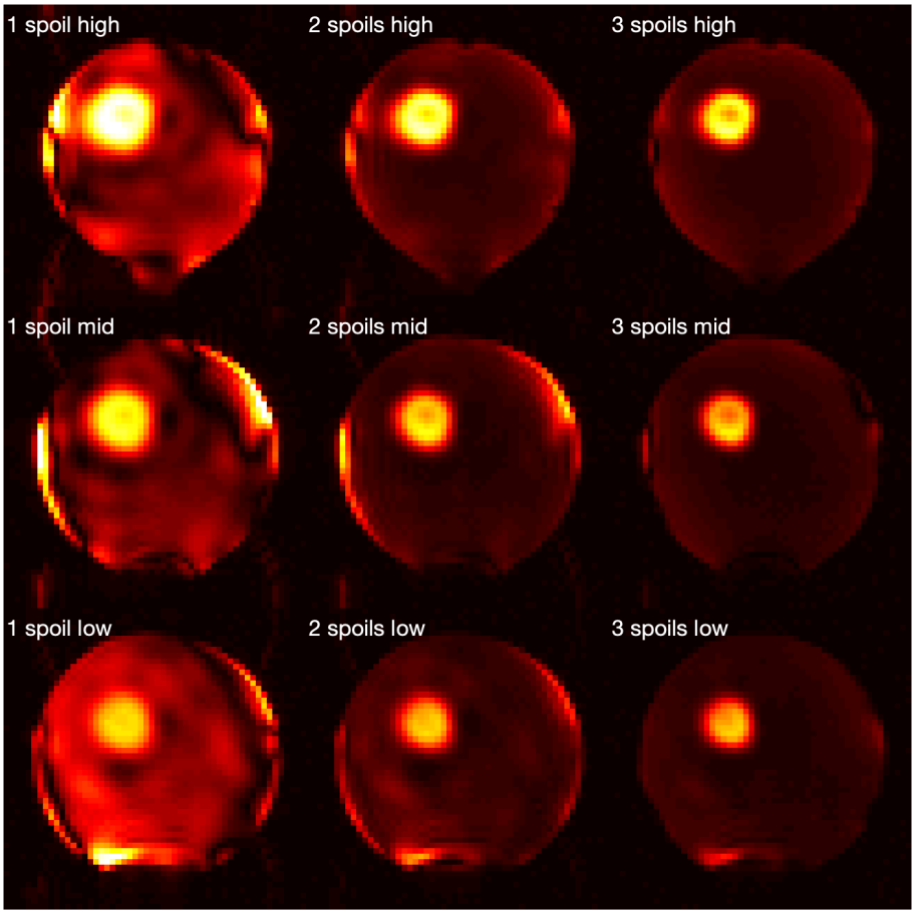


Figure 5.13: EPI images acquired on an oil phantom with a pulse voltage of 180V and different numbers of repetitions of the saturation module. The left, middle, and right columns show 1, 2, and 3 saturation module repetitions, respectively. The bottom, middle, top rows show images acquired at the bottom, in the middle, and at the top of the inversion slab, respectively.

To examine the saturation performance of the three-pulse strategy across the whole inversion slab, 10 slices were acquired covering the slab for both 180V and 223V pulses. These results are shown in Figures 5.14 (223V) and 5.15 (180V).

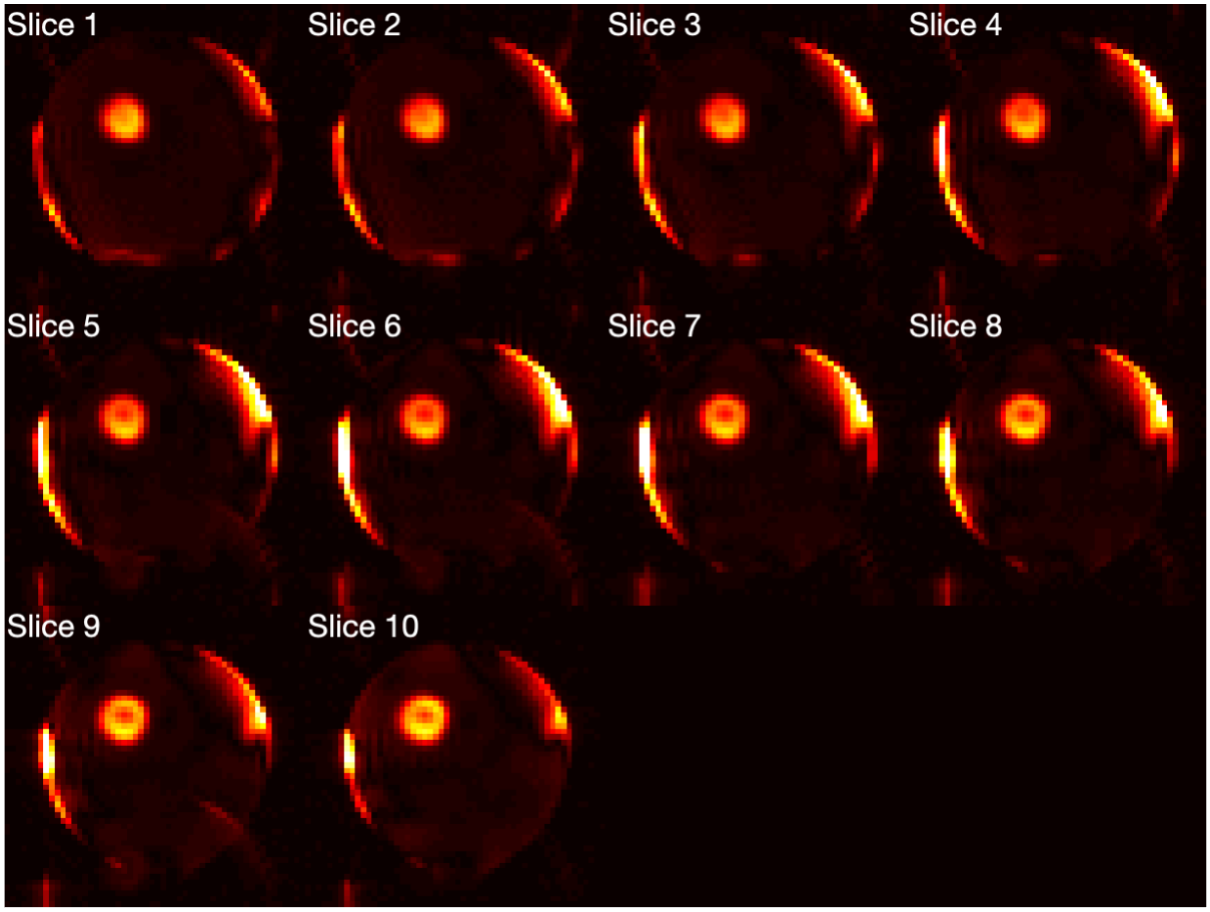


Figure 5.14: EPI images acquired on an oil phantom with a pulse voltage of 223V after three saturation modules covering the entire inversion slab. The slice gap was 3mm.

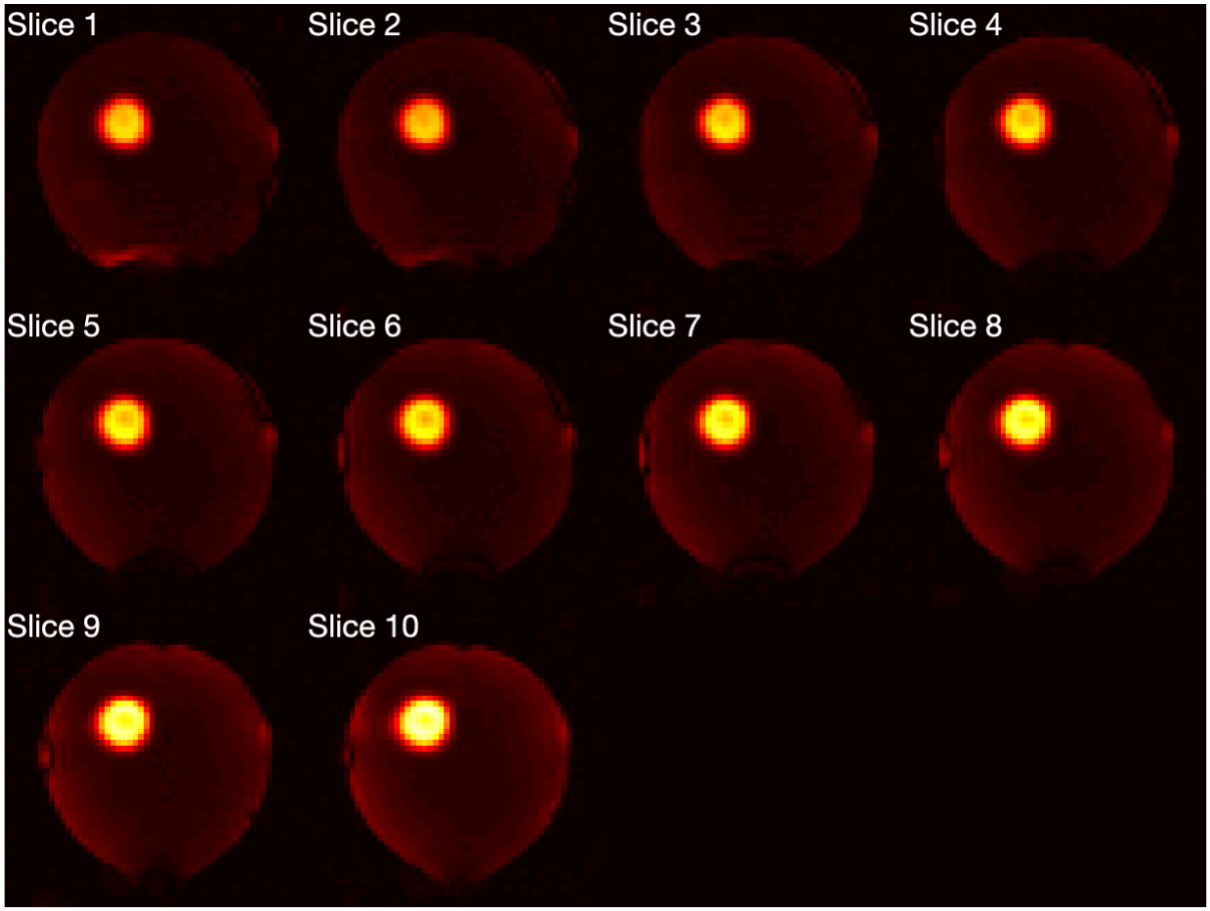


Figure 5.15: EPI images acquired on an oil phantom with a pulse voltage of 180V after three saturation modules covering the entire inversion slab. The slice gap was 3mm.

To investigate the relationship between the saturation accuracy and the pulse voltage, Bloch equation simulations were performed with different pulse voltages (100-250V). Simulated images (shown in Fig 5.16) for a slice through the middle of the inversion slab were generated by assuming that all transverse magnetisation was spoiled by the crusher gradient, and that the imaging pulse achieved a perfectly uniform 90° excitation immediately after the saturation.

Simulation results showed that decreasing the pulse voltage from the optimal value (223V) led to increasingly poor saturation outside the ROI, potentially due to under-flipping of the magnetisation. Increasing the pulse voltage beyond the optimal value similarly led to poorer saturation, likely due to over-flipping of the magnetisation. Inaccuracies in the B_1^+ mapping sequences could also be the source of the error.

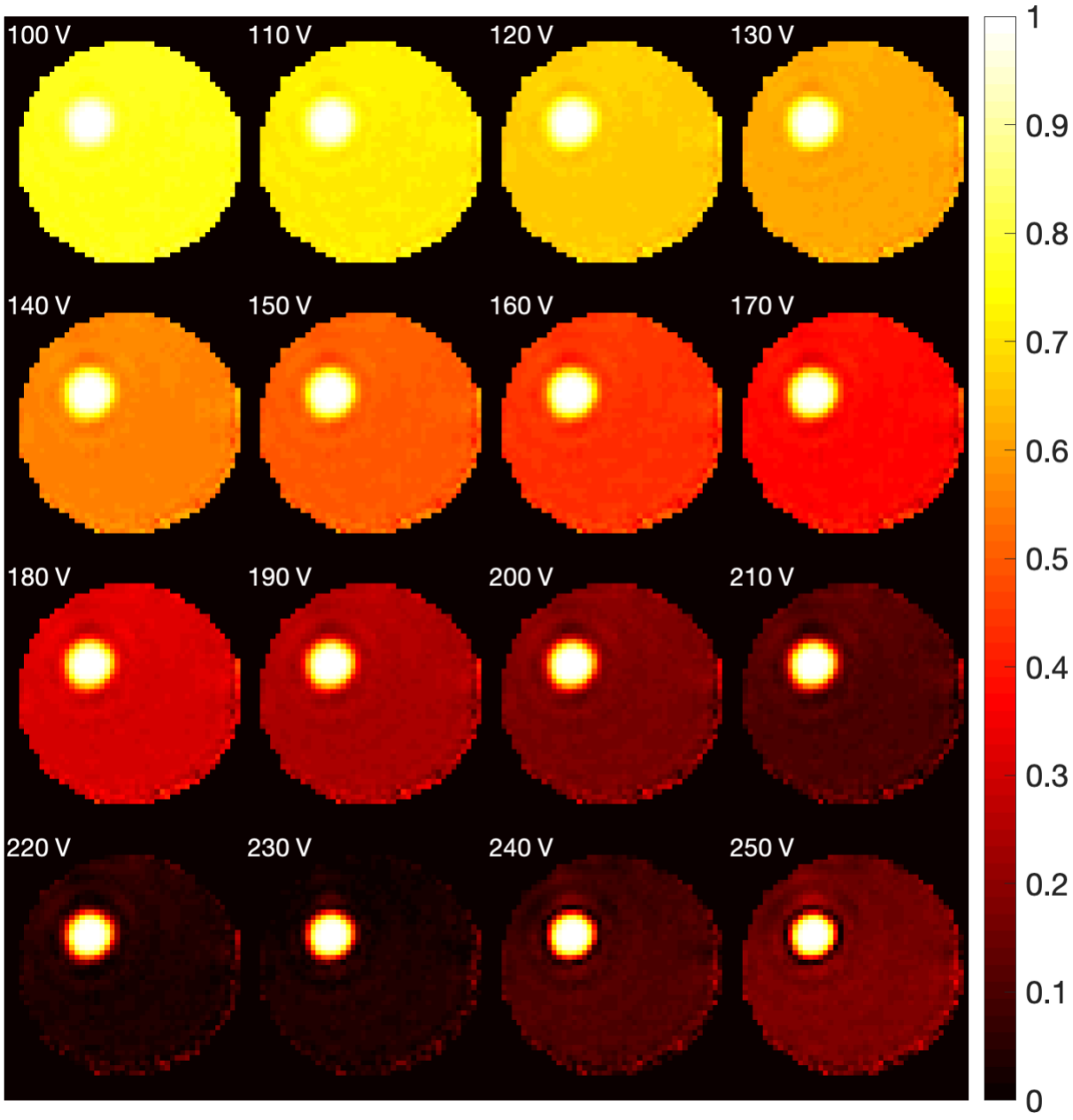


Figure 5.16: The expected images with different pulse voltages for a slice through the middle of the saturation slab generated from Bloch equation simulations. The scale of this figure represents the ratio of the expected signal to M_0.

The changes in the pulse voltage were then applied on the scanner. EPI images were acquired following saturation modules with different voltages (100-250V) settings were assessed. Images were acquired at the bottom, in the middle, and at the top of the saturation slab. Only the middle slice is shown in Figure 5.17 below for simplicity. The experimental results roughly matched with the simulation. However, the artefacts the appeared on the edges of the slice were not predicted by the simulation.

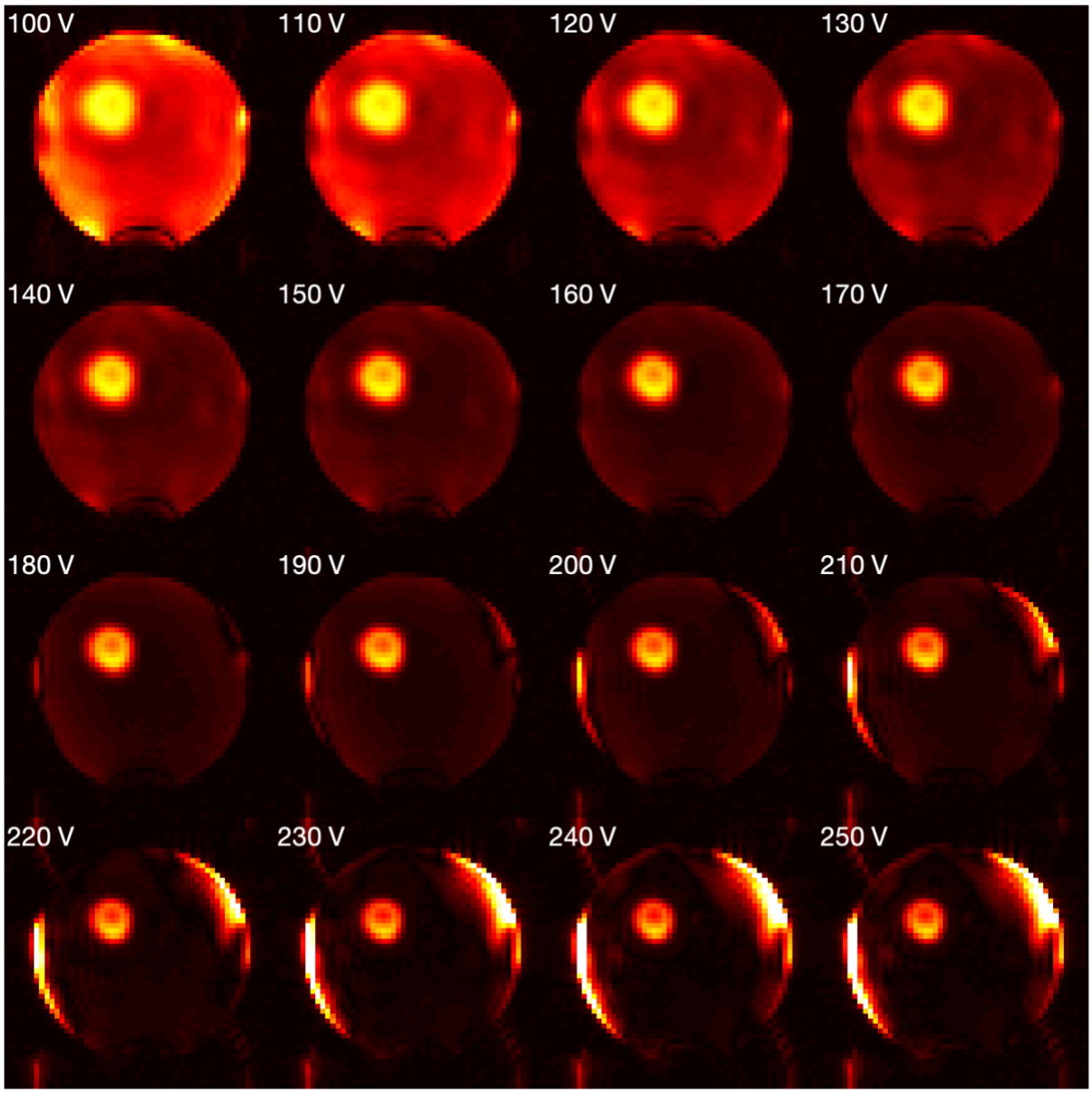


Figure 5.17: EPI images for a slice through the middle of the inversion slab acquired with different pulse voltages used for the saturation modules. The saturation module consists of three sets of spatially selective pulse followed by a spoiler gradient. The optimal voltage pTx pulse calculation should be 223V (according to the calibration procedure). Initially, increasing the pulse voltage improved the saturation of spins outside the ROI. However, further increases in pulse voltage produced worsened artefacts at the edges of the slice.

To investigate the relationship between the saturation accuracy and any potential asynchronisation between the RF and gradient channels, different time delays (relative time delays ranging from -10μs to +10μs) between the RF and gradient channels were simulated using Bloch equations for a slice through the middle of the inversion slab. As above, it was assumed that all transverse magnetisation was spoiled by the crusher gradient, and that the imaging pulse achieved a perfectly uniform 90° excitation immediately after the saturation.

Simulation results (shown in Figure 5.18) showed that increasing the time delay between the RF and gradient systems led to a deterioration in excitation accuracy. In addition, a slight rotation of excitation target was observed.

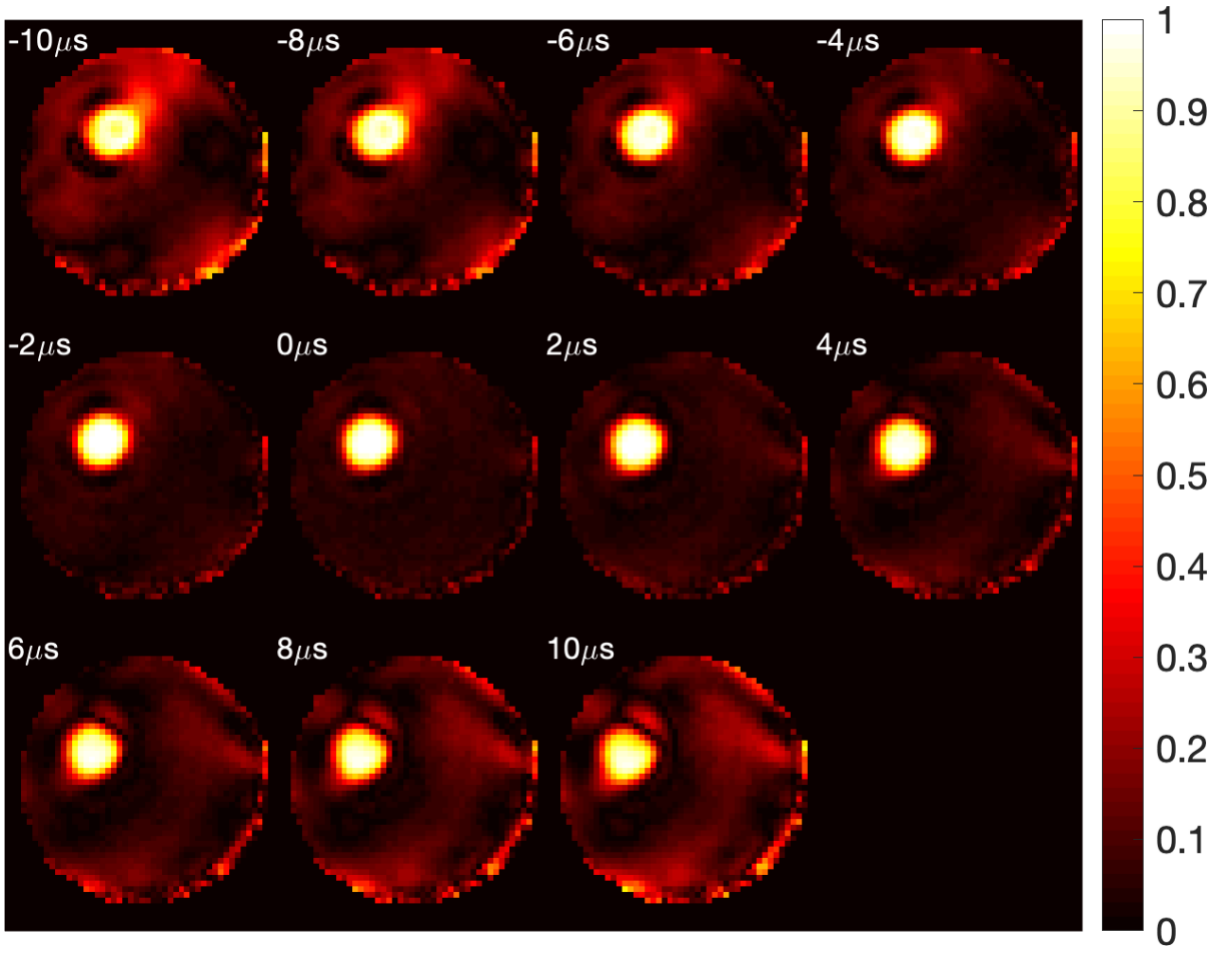


Figure 5.18: The expected images with different time delays in the middle of the saturation slab generated from the Bloch equation simulations. The scale of this figure represents the ratio of the expected signal to M_0.

Different time delays between the RF and gradient channels (relative time delays ranging from -10μs to +10μs) were then placed in the sequence. Images were acquired in the middle of the saturation slab, and with two pulse voltages were applied (223V shown in Figure 5.19 and 180V shown in Figure 5.20).

Experimental results broadly matched with the simulation. A slight rotation was observed similar to the simulation. However, the deterioration of saturation outside of the ROI was not as pronounced as expected. Moreover, having negative offsets (the gradient waveform played out the RF waveform) led to poorer preservation of longitudinal magnetisation in the ROI.

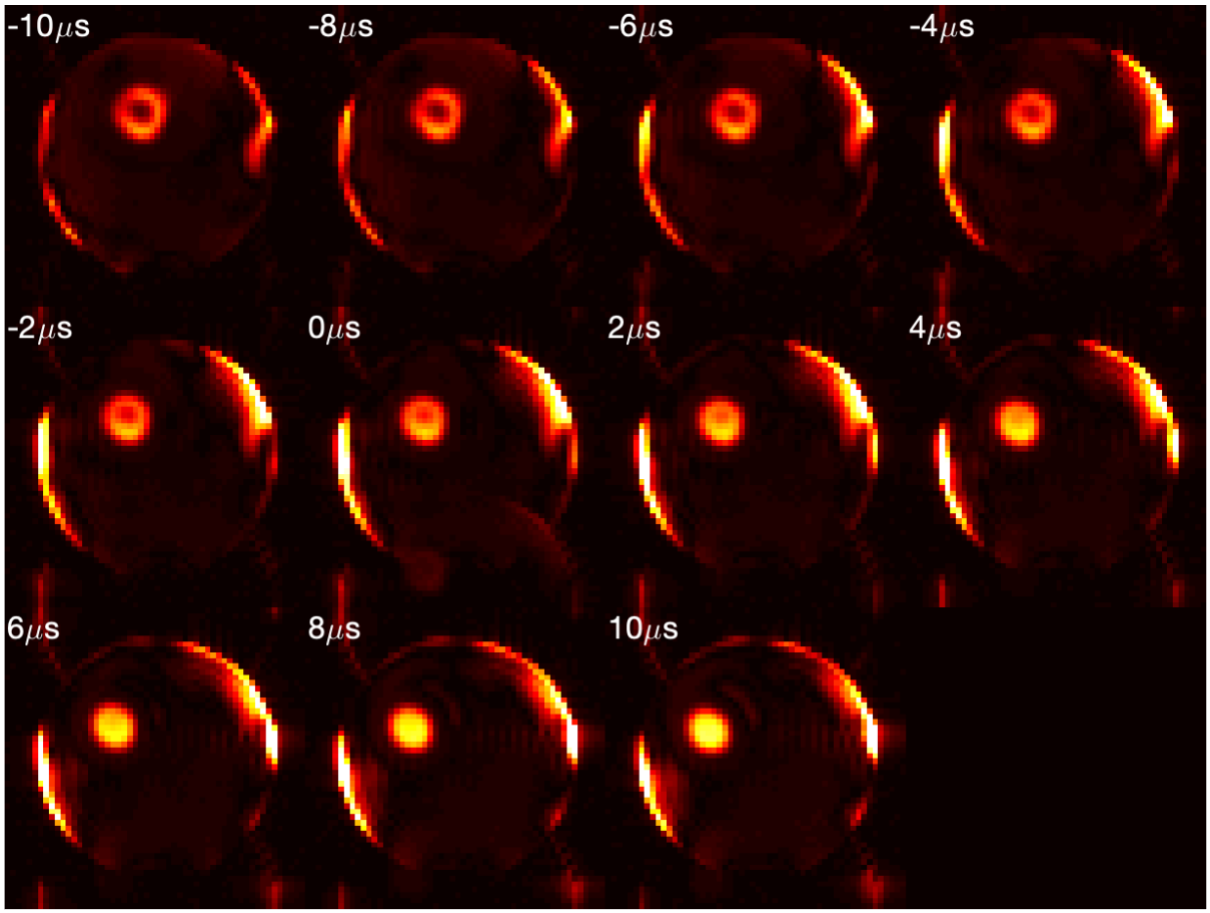


Figure 5.19: EPI images acquired with different time delays between the RF and gradient channels with a pulse voltage of 223V in the slice through the middle of the inversion slab. The saturation modules were repeated three times. Changing the time delay caused a rotation of the excitation target.

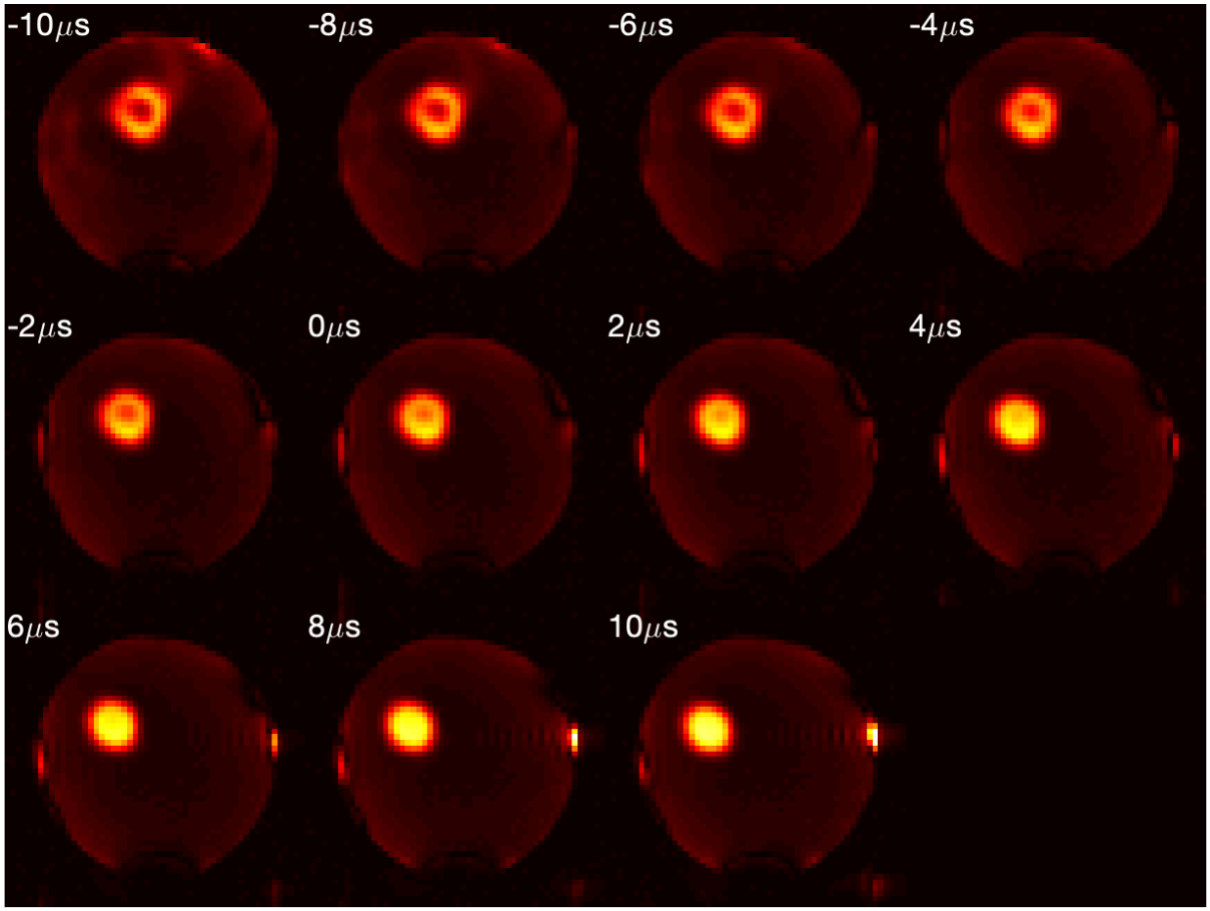


Figure 5.20: EPI images acquired with different time delays between the RF and gradient channels with a pulse voltage of 180V in slice through the middle of the inversion slab. The saturation modules were repeated three times.

5.2.4.2. Analysis of experimental results

The saturation errors could be evaluated by averaging the raw signal intensity of the voxels outside the ROI but within the phantom. Results (see Figure 5.21) show that the errors are significantly reduced when increasing the number of saturation pulses (for both 180V and 223V pulses).

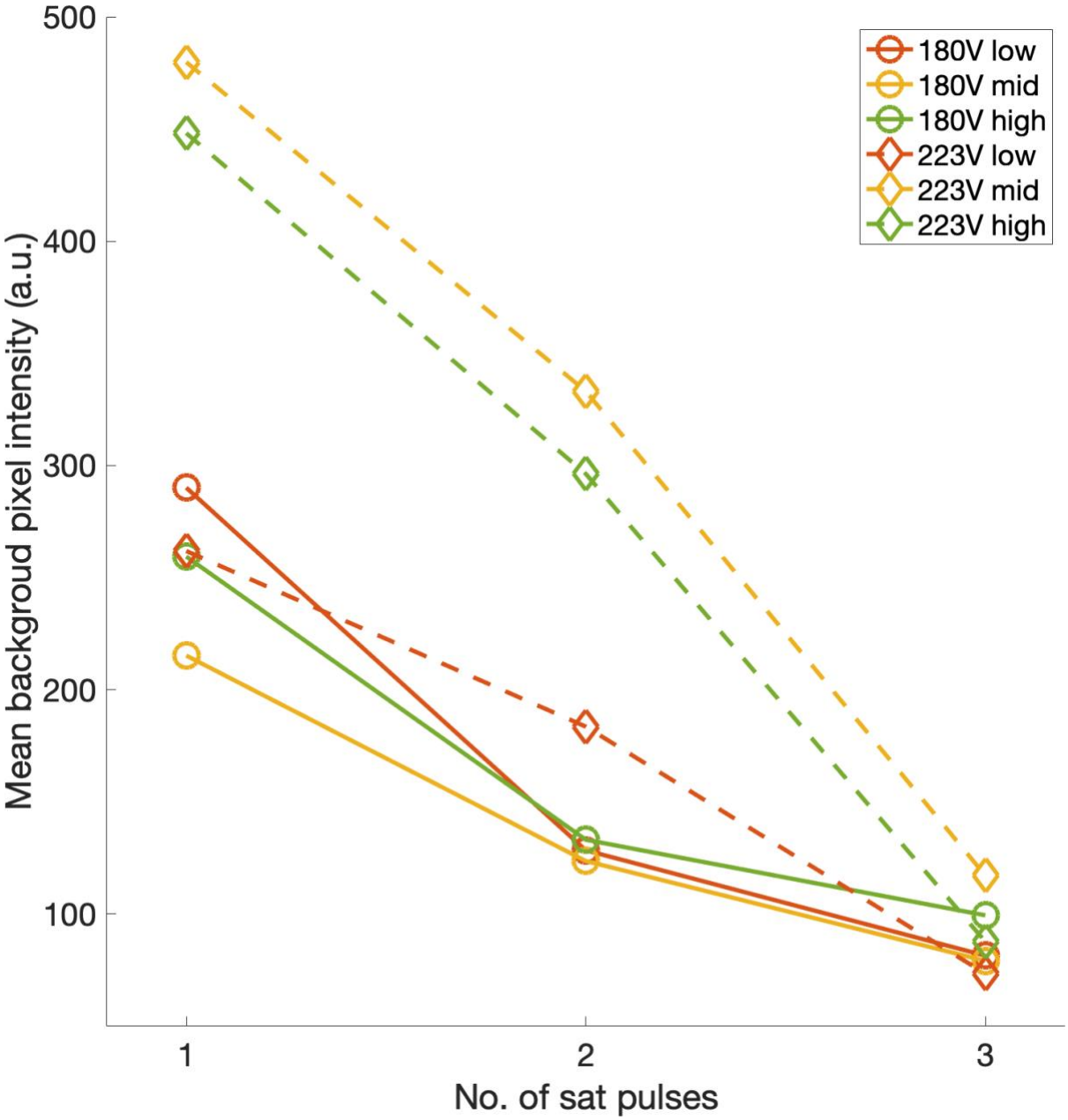


Figure 5.21: The mean background signal intensity vs. the number of saturation pulses applied. EPI images of three slices (low, mid and high of the inversion slab) were acquired. The correct pulse voltage should be 223V according to the calibration data and optimisation algorithm.

Similarly, the mean signal intensity in the ROI is also shown in Figure 5.22. The observed signal decreases with increasing number of pulses due to partial saturation of spins within the ROI, since the flip-angle profile of the designed pulse is not perfectly 0° throughout the ROI. However, this signal loss might be an acceptable trade-off for improved saturation accuracy outside the ROI. This is because it is more important to exclude signal from outside the ROI, since insufficient saturation will lead to signal contamination of the OEF measurement, particularly given the large volume fraction constituting the outer-ROI region.

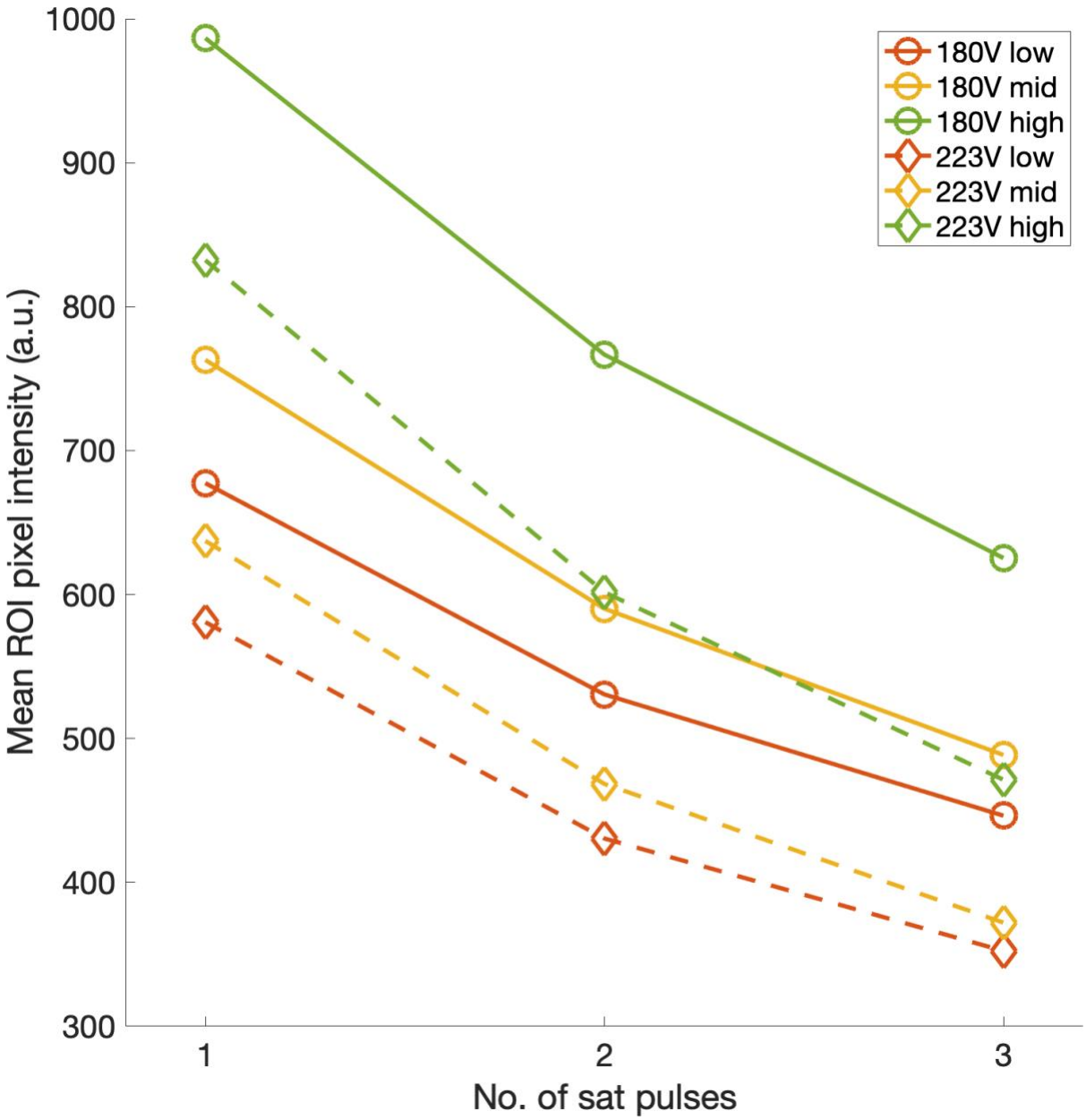


Figure 5.22: The mean background signal intensity vs. the number of saturation pulses applied. EPI images of three slices (bottom, middle and top of the inversion slab) were acquired. The correct pulse voltage should be 223V according to the calibration data and optimisation algorithm.

Example saturation profiles across the ROI are shown below. The saturation profiles were generated from images acquired with a pulse voltage of 180V in the middle of the inversion slab and with 1, 2, and 3 saturation modules applied, respectively. It can be observed that the mean signal intensity within the ROI decreases as the number of saturation modules increases. Moreover, additional pulses erode the saturation profile, leading to reduced values for the full-width half-maximum (see Figure 5.23).

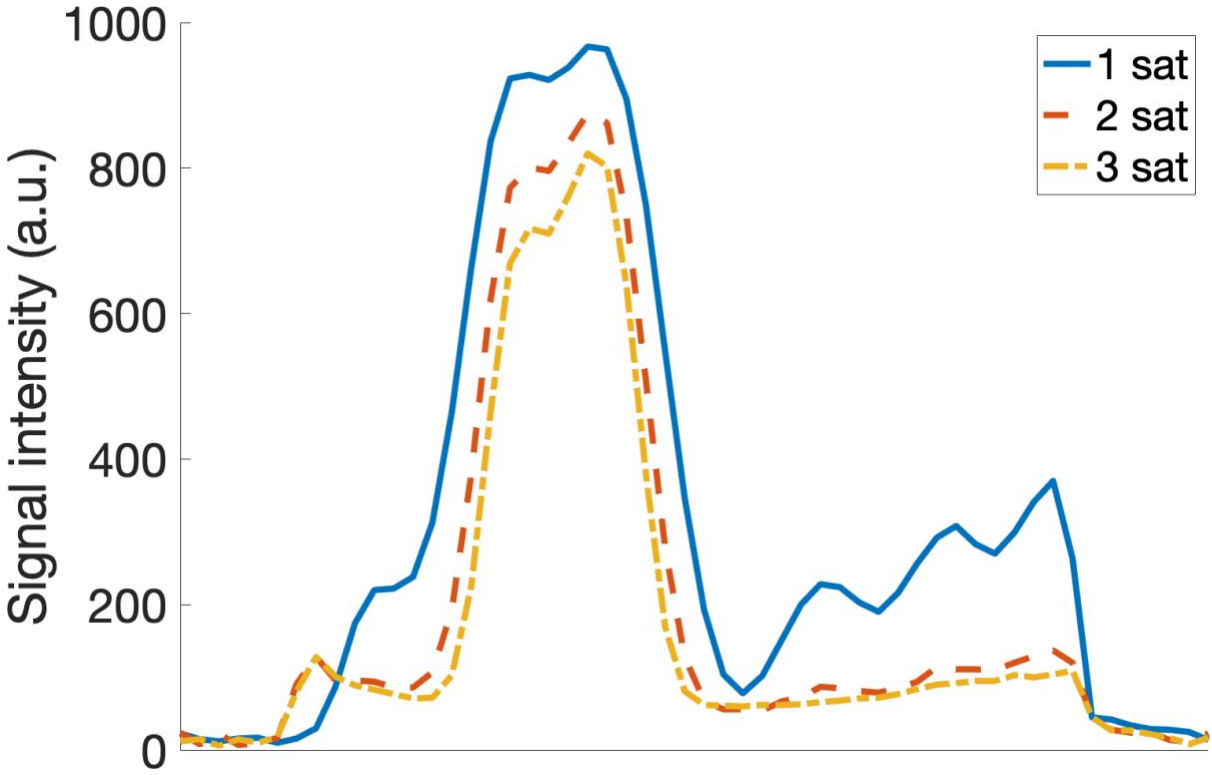


Figure 5.23: Example saturation profile through the ROI in the middle slice with 1, 2, and 3 inversion modules applied. The pulse voltage was 180V. The full-width-half maximum of the saturation profile was 11.2, 9.1 and 8.1 pixels for 1, 2, and 3 saturation modules, respectively.

Similarly, the mean signal intensity outside the ROI was also calculated for images acquired with different voltages. Results (see Figure 5.24) showed that the errors were reduced when slightly decreasing the pulse voltage, but further decreases led to higher saturation errors. The optimal voltage was between 170V to 190V.

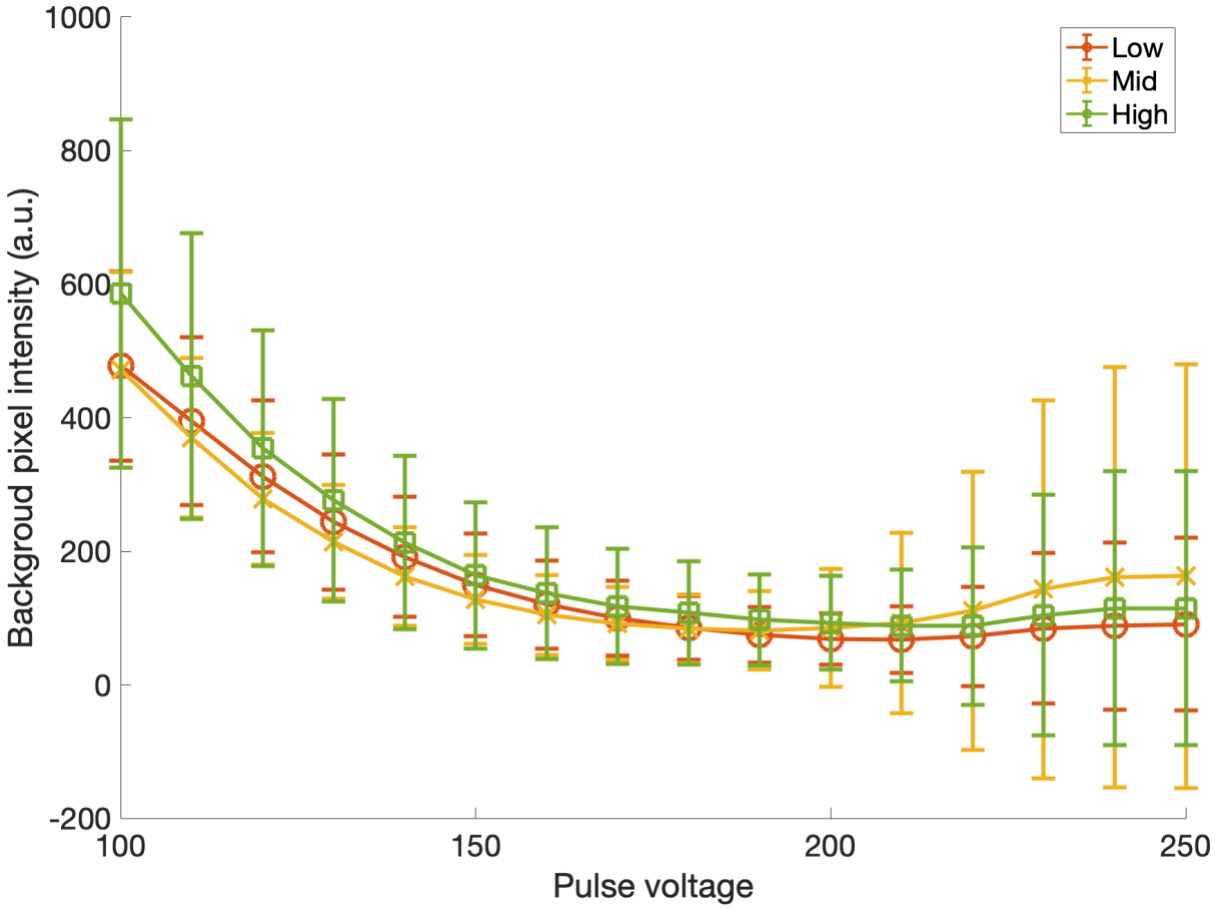


Figure 5.24: The mean and standard deviation of background signal intensity vs. the voltage of the pTx pulse applied. Three saturation pulses were applied, and EPI images of three slices (bottom, middle and top of the inversion slab) were acquired. The pulse voltage should be 223V according to the calibration data and optimisation algorithm.

Changing the time delay between the RF and gradient systems did not improve the saturation accuracy. Furthermore, such a change induced a rotation of the excited ROI, which was detrimental to the localisation needed for the goal of measuring local venous oxygenation in this study. This suggests that RF-gradient timing was not the main source of imperfections in the observed saturation.

5.2.4.3. Quantitative estimation of saturation errors

EPI images were acquired through the inversion slab to assess the accuracy of the saturation pulses. The minimal inversion time (TI) allowed in the TRUST sequence, defined as the time between the slab-selective inversion pulse and image acquisition, was 75 ms. The duration of the inversion pulse was 10.24 ms. Therefore, the duration between the end of the saturation module and beginning of image acquisition was the sum of TI and a half of the pulse duration, which was roughly 80 ms.

Thus, spins tipped into the transverse plane by the spatially-selective RF pulse would have experienced T_1 relaxation for 80 ms at the time of image acquisition. The T_1 value of the phantom was experimentally determined using an inversion-recovery sequence to be approximately 1370 ms.

The M_0 signal of the phantom was estimated by taking the maximum signal intensity in the ROI when only one saturation module was applied, which was 1229 arbitrary signal units (represented by S_0). However, this may be an under-estimate, since imperfections of the spatially-selective pulse may have excited a small amount of magnetisation within the ROI, and additional saturation pulses will decrease the signal intensity within the ROI further.

The expected longitudinal signal immediately after the saturation, denoted as $S_z(0)$, can be estimated by utilising the relationship between $S_z(0)$ and $S_z(t)$ (longitudinal signal at some later time t) based on the T_1 relaxation of the longitudinal magnetisation:

Equation 5.12

$$S_z(t) = S_0 - (S_0 - S_z(0))e^{-t/T_1}$$

$S_z(t)$ was defined as the mean signal intensity outside the ROI calculated over the whole inversion slab for images acquired at the earliest time (80 ms) for which imaging data could be acquired in the sequence after three saturation modules, which was 80.2 and 100.1 arbitrary signal units for pulse voltages of 180V and 223V, respectively.

$S_z(0)$ can be expressed in terms of $S_z(t)$ via the following rearrangements:

Equation 5.13

$$S_z(t) = S_0 - S_0 e^{-t/T_1} + S_z(0) e^{-t/T_1}$$

Equation 5.14

$$S_z(t) = S_0(1 - e^{-t/T_1}) + S_z(0) e^{-t/T_1}$$

Equation 5.15

$$S_z(0) e^{-t/T_1} = S_z(t) - S_0(1 - e^{-t/T_1})$$

Equation 5.16

$$S_z(0) = \frac{S_z(t) - S_0(1 - e^{-t/T_1})}{e^{-t/T_1}}$$

Substituting T_1 = 1370ms, t = 80ms, S_0 = 1229 signal units, $S_z(0)$ = 80.2 signal units (180V pulse), $S_z(0)$ for this voltage can be calculated as:

Equation 5.17

$$S_{z,180V}(0) = \frac{80.2 - 1229 \cdot (1 - e^{-80/1370})}{e^{-80/1370}} = 11.2$$

Similarly, for $S_z(0)$ = 100.1 signal units (223V pulse), $S_z(0)$ for this voltage can be calculated as:

Equation 5.18

$$S_{z,223V}(0) = \frac{100.1 - 1229 \cdot (1 - e^{-80/1370})}{e^{-80/1370}} = 32.2$$

For a perfect 90° excitation followed by a perfect spoiler, $S_z(0)$ should be zero. Therefore, the saturation error can then be estimated as:

Equation 5.19

$$e_{sat} = \frac{S_z(0)}{S_0}$$

Thus, the saturation error was 0.9% for a pulse voltage of 180V and 2.6% for a pulse voltage of 223V.

5.2.4.4. Estimation of signal contamination

Since an imperfect saturation would lead to a contaminating contribution of signal arising from outside the ROI in the T_2 measurement, it is important to assess the magnitude of such a contamination.

For each voxel at position **r** outside the ROI, the contribution to the T_2 measurement is $S_z(0)$, as it contributes to the signal difference between the control and label images in a TRUST experiment.

Therefore, the total contribution from regions outside the ROI can by calculated by summing $S_z(0)$ in all positions outside the ROI:

Equation 5.20

$$S_{background} = \sum S_z(0,\mathbf{r})$$

Similarly, the contribution from within the ROI can by calculated by summing the experimentally measured voxel intensities for all positions within it. This approach accounts for the signal loss due to partial saturation in the ROI when multiple saturation pulses are applied:

Equation 5.21

$$S_{ROI} = \sum S_{ROI}(\mathbf{r})$$

The contribution of contaminated signal can then be calculated as:

Equation 5.22

$$c_{background} = \frac{S_{background}}{S_{background} + S_{ROI}}$$

Based on the results of the previous subsection, the contribution from regions outside the ROI is estimated to be 21.2% and 53.7% for saturation pulse voltages of 180V and 223V, respectively. Note that this high level of contamination, despite low saturation error, is due primarily to the large ratio in volume fraction between the ROI and the regions outside it (6.9% and 93.1% of the volume of the inversion slab, respectively).

5.2.4.5. Estimation of T_2 quantification errors

Given the estimation of the signal contribution from regions outside the ROI, the estimation error in T_2 can be quantified by fitting T_2 decay curves generated by simulating MR signal from different signal contamination levels.

The first step is to identify the relationship between blood T_2 and oxygenation *Y.* Krishnamurthy *et al.* obtained the values of coefficients *A*, *B*, and *C* in equation 5.8 at 7 T with different Haematocrit levels (shown in Table 5-1) [191]. Note that these coefficients need to be calibrated for a particular field strength and a specific T_2 preparation module, which were kept the same as the those in the work by Krishnamurthy *et al*. [191] in this study.

Table 5-1: Coefficients for the equation describing the relationship between blood T_2 and oxygenation at different Haematocrit levels. This table is adapted from Table 1 of the work at 7 T by Krishnamurthy et al*. (doi: 10.1002/mrm.24868).*

Hct	*A*	*B*	*C*
34%	14.6	-31.2	223.5
42%	14.9	-17.6	264.0
54%	16.7	3.7	240.9

Based on these *A*, *B*, and *C* values, the relationship between T_2 and *Y* can be simulated (see Figure 5.25).

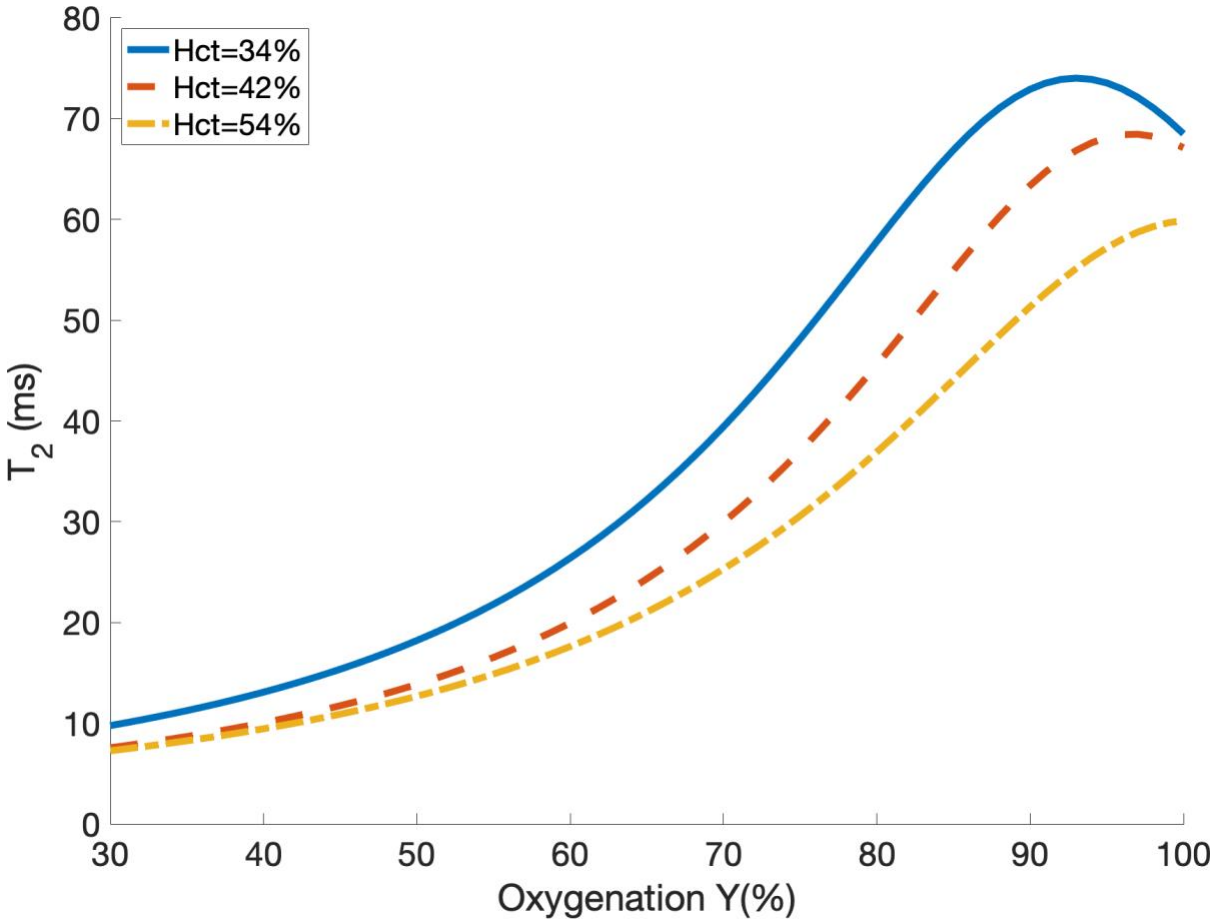


Figure 5.25: The relationship between T2 and Y for different Hct levels simulated from coefficients taken from the work by Krishnamurthy et al. *(doi: 10.1002/mrm.24868).*

Based on this relationship, an example scenario could be considered to evaluate the error in the OEF measurement using TRUST. If a pathological change within the ROI were to artificially lower the venous oxygenation in the ROI to 40%, whereas the rest of the brain was normal with a venous oxygenation of 65%, the corresponding T_2 values could be calculated to be 10.1 ms and 24.3 ms, respectively, for an Hct level of 42%.

Based on the signal equation described earlier, the difference signal in the sagittal sinus can be simulated for different eTEs (see Figure 5.26), assuming the blood T_1 to be 2100 ms [191].

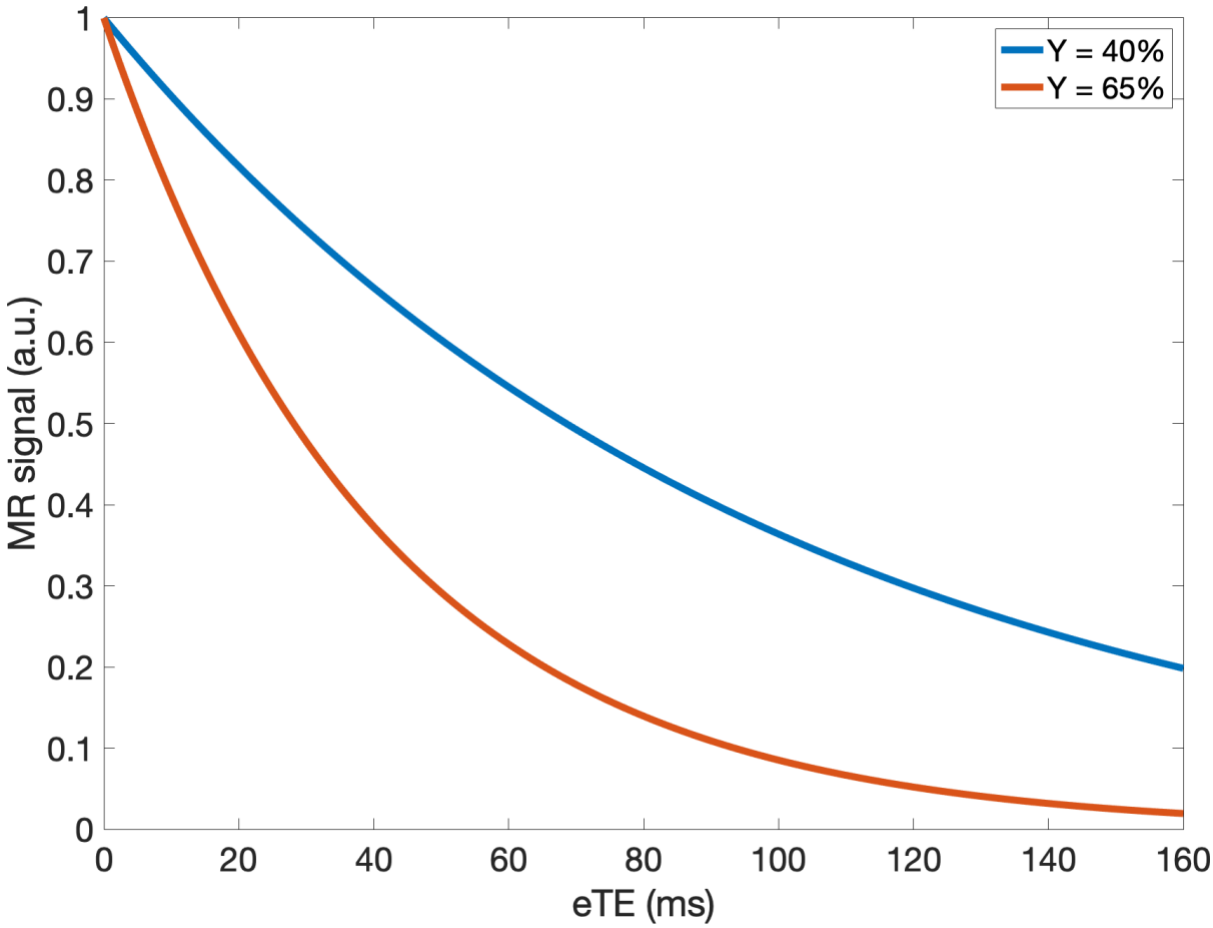


Figure 5.26: Simulated exponential decay curve of the observed signal in the difference image in a TRUST sequence with respect to eTE of two blood spin populations of different oxygenation levels (40% and 65%).

Similarly, the difference signal in the sagittal sinus can be simulated for different eTEs and signal contamination levels (see Figure 5.27), assuming the blood T_1 to be 2100 ms. The contamination level refers to the proportion blood spins with an oxygenation level of 65%.

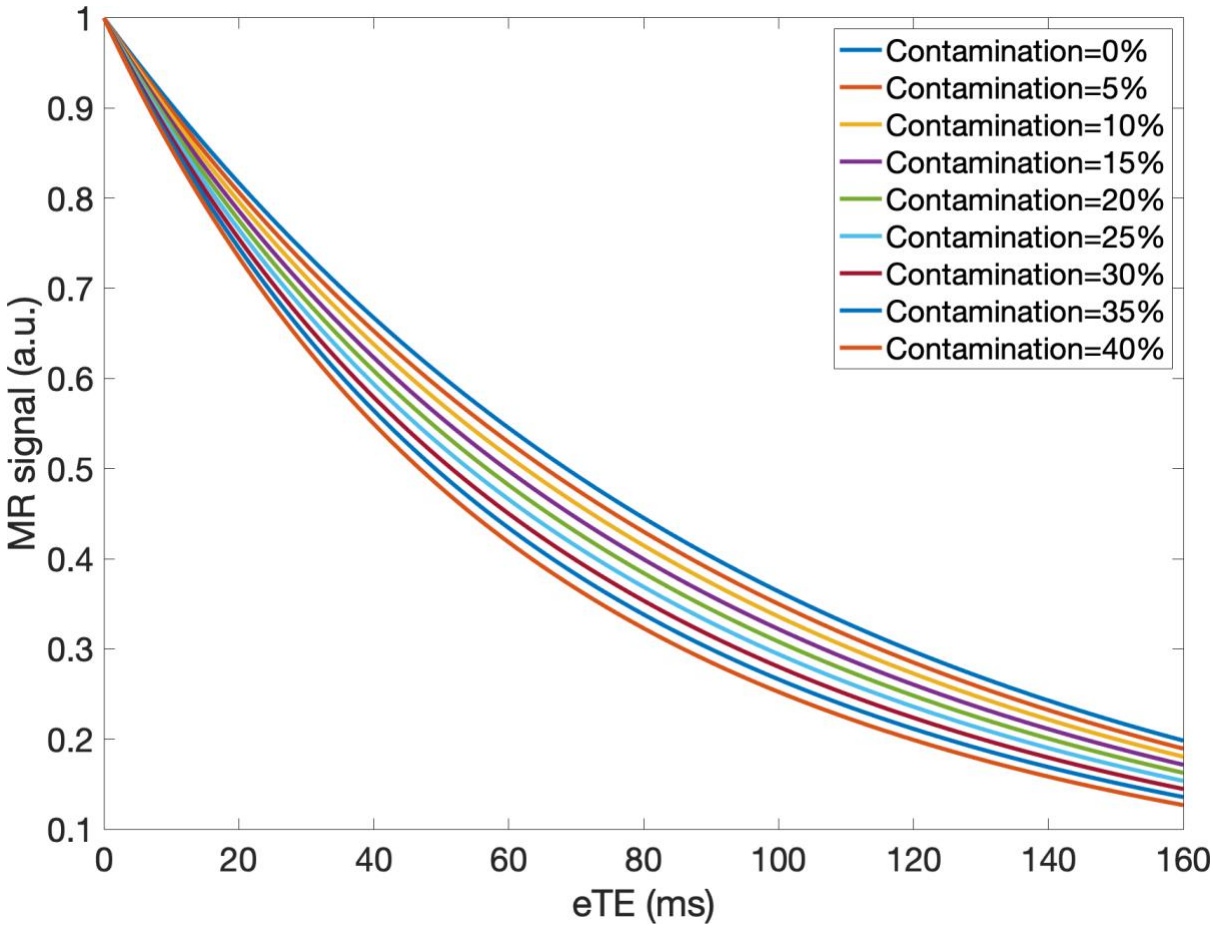


Figure 5.27: Simulated exponential decay curve of the observed signal in the difference image in a TRUST sequence with respect to eTE of different mixtures of two blood spin populations of different oxygenation levels (40% and 65%).The contamination level refers to the proportion blood spins with an oxygenation level of 65%.

A mono-exponential fit can be used to estimate the blood T_2 with different levels of signal contamination. The venous oxygenation Y can be then calculated by solving a quadratic equation. The relationship between T_2/Y and the contamination level is shown in Figure 5.28. It can be observed that the overestimation of the oxygenation level scales approximately linearly with the level of signal contamination.

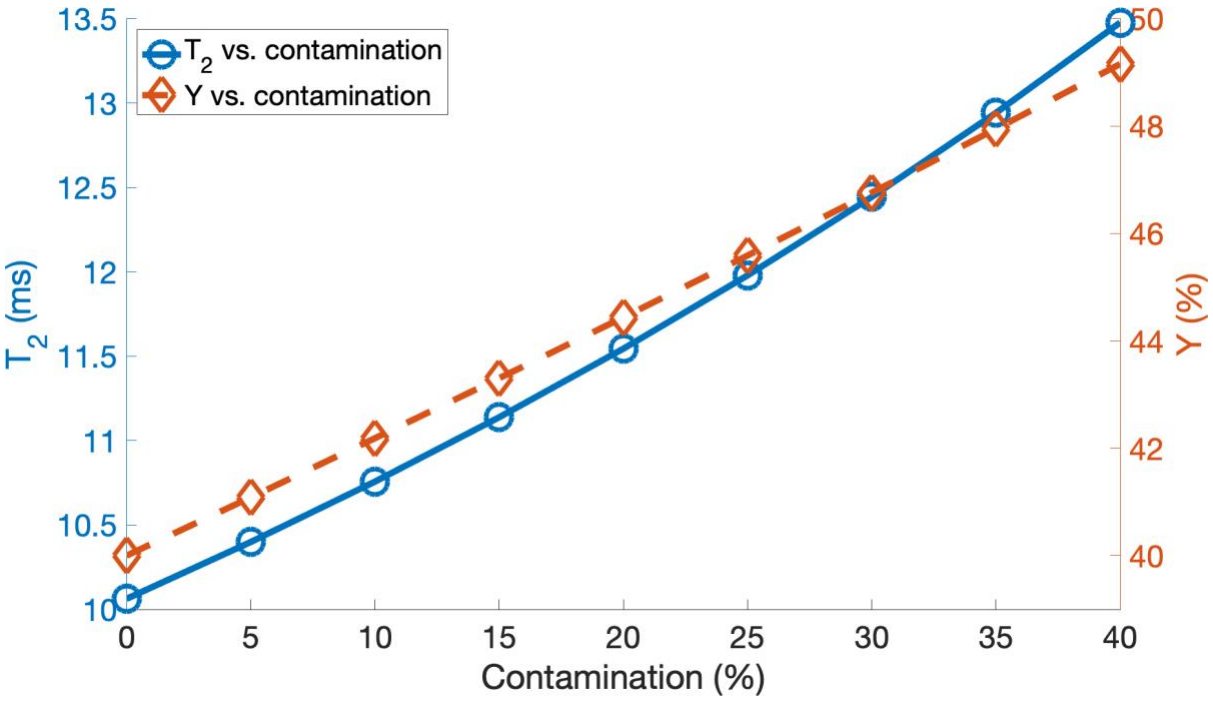


Figure 5.28: Estimated T_2 and Y values from a mono-exponential fit of simulated T_2 decay curve of different mixtures of two blood spin populations of different oxygenation levels (40% and 65%). The contamination level refers to the proportion blood spins with an oxygenation level of 65%.

The relationship between the volume ratio of spins inside and outside of the ROI, and the contamination level could also be estimated by assuming that the mean signal intensity remains unchanged for an ROI of a different size (see Figure 5.29).

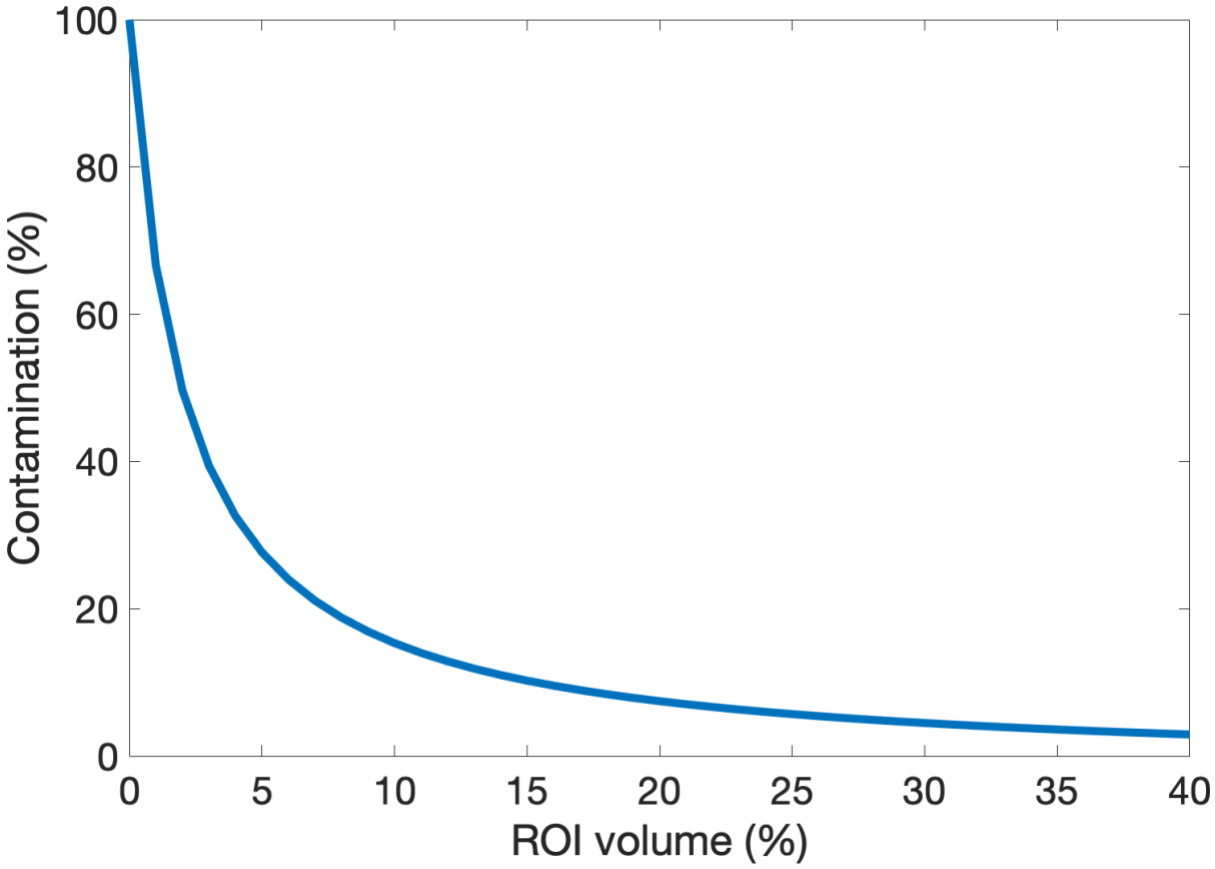


Figure 5.29: The relationship between signal contamination level and the percentage volume of the ROI in the inversion slab. The simulation was carried out by using signal intensities from whole-slab images acquired using a 180V pulse.

The relationship shown above indicates that a moderate increase in the ROI volume percentage would substantially decrease the level of signal contamination. For instance, an ROI volume ratio of 15% corresponds to a contamination level of 10%.

5.2.5. Considerations on excitation k-space trajectory

No gradient trajectory optimisation was used in the *in vivo* and phantom experiments detailed in the previous sections. There are several reasons for this. Firstly, jointly optimisation of the gradient trajectory and RF pulses is computationally challenging. In the work by Davids *et al.* [190], the full optimisation of the shape parameters could take

several hours, which is not practically feasible since the pulse calculation has to take place after the acquisition of B_0 and B_1^+ maps and before applying the TRUST sequence. Secondly, the location and shape of the ROI in an *in vivo* regional OEF measurement using TRUST may differ from patient to patient. Therefore, pre-calculated gradient trajectories based on existing B_0 and B_1^+ maps and a pre-defined ROI might not be suitable for a different subject or a different brain region.

Despite the difficulty of generating an optimised gradient trajectory for each use case, it might be worth investigating the relationship between the shape parameters and the performance of the RF pulses. As indicated in Section 5.1.2, the shape parameters φ_1, φ_2, φ_3, φ_4, φ_5, φ_6, and φ_7 represent k_x extent (in m^{-1}), k_y extent (in m^{-1}), k_z extent (in m^{-1}), the number of shells, the number of revolutions, the number of revolutions of the centremost shells, and the non-uniformity of the shell radii, respectively. The φ parameters in this chapter were heuristically chosen to be 40, 40, 20, 7, 6, 1, 1, and 1.

To assess alternative excitation trajectories, pulse calculations were carried out by varying parameters for k-space extent (φ_1, φ_2, and φ_3). Meanwhile, φ_4, φ_5, φ_6, and φ_7 were kept constant to isolate the effects of φ_1, φ_2, φ_3. The extent in k_x and k_y was varied from 5 m^{-1} to 60 m^{-1} with an increment of 5 m^{-1}, and the extent in k_z was varied from 5 m^{-1} to 20 m^{-1} with an increment of 5 m^{-1}. Results (shown in Figure 5.30) indicate that increasing the k_x and k_y extent from 5 m^{-1} to 20 m^{-1} produced large improvements in the excitation RMSE, whilst further increases in k_x and k_y extent only yielded moderate additional improvements.

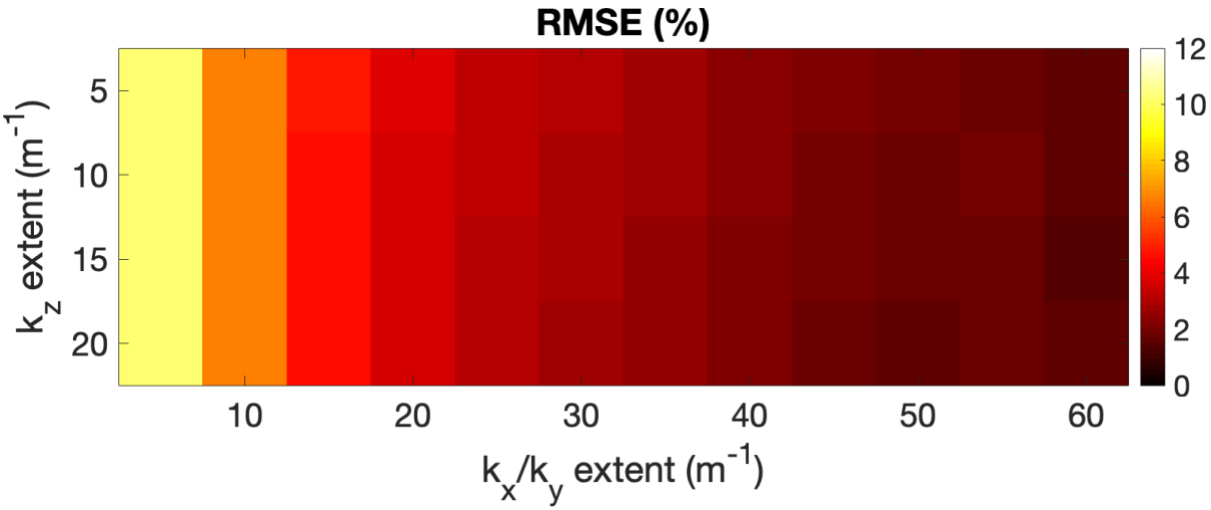


Figure 5.30: The relationship between the RMSE of the excitation profile in simulation and the excitation k-space extent.

Table 5-2: The pulse duration in ms when varying k_x/k_y and k_z extent.

		k_z extent (m^{-1})											
		5	10	15	20	25	30	35	40	45	50	55	60
$k_{x,y}$ extent (m^{-1})	5	3.01	4.12	4.96	5.68	6.30	6.87	7.40	7.88	8.35	8.78	9.21	9.60
	10	3.16	4.25	5.10	5.82	6.43	7.00	7.52	8.01	8.50	8.90	9.33	9.70
	15	3.27	4.36	5.20	5.92	6.55	7.10	7.62	8.14	8.57	9.00	9.41	9.79
	20	3.36	4.45	5.30	6.00	6.62	7.19	7.72	8.20	8.65	9.09	9.50	9.89

The simulations detailed above showed that there is a trade-off between the duration of the RF pulse, which is determined by the k-space extent and the complexity of the gradient trajectory, and the excitation accuracy. Once a sufficient k-space coverage is achieved, further increases in k-space extent bring only marginal additional reductions in RMSE. Furthermore, increasing the number of shells of trajectories always reduced the RMSE, but at a cost of a longer RF pulse duration. The relationship between pulse duration and excitation k-space extent is shown in Table 5-2.

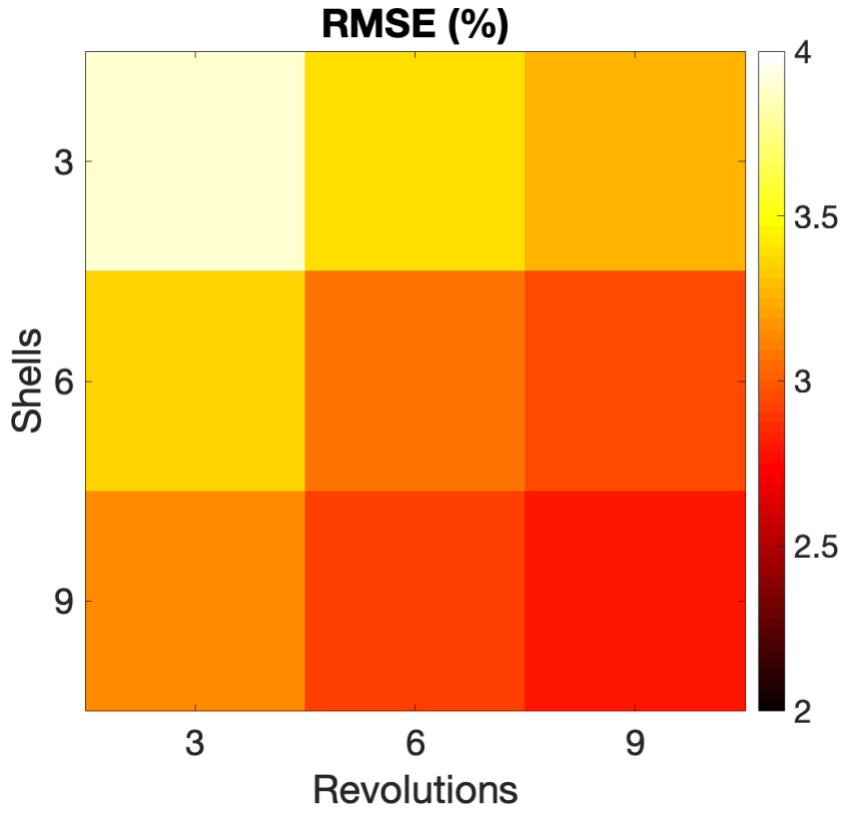


Figure 5.31: The relationship between the RMSE of the excitation profile in simulation and the number of shells and the number of revolutions of the excitation k-space trajectory.

Pulse calculations were also performed by varying the number of shells (φ_4) and the number of revolutions (φ_5) while keeping φ_1, φ_2, φ_3, φ_6, and φ_7 constant. φ_1, φ_2, φ_3, φ_6, and φ_7 were set to 30 (m^{-1}), 5 (m^{-1}), 5 (m^{-1}), 1, and 1, respectively. φ_3 and φ_4 were varied from 3 to 9 with an increment of 3. Results (shown in Figure 5.31) indicate that increasing the number of shells and increasing the number of revolutions both moderately improve the excitation RMSE. Similar to the excitation k-space extent, increasing φ_4 and φ_5 also increased the pulse duration, detailed in Table 5-3.

Table 5-3: The pulse duration in ms when varying the number of shells (φ_4) and the number of revolutions (φ_5).

	$\varphi_5 = 3$	$\varphi_5 = 6$	$\varphi_5 = 9$
$\varphi_4 = 3$	1.37	2.53	3.71
$\varphi_4 = 3$	2.78	5.11	7.46
$\varphi_4 = 3$	4.18	7.68	11.23

Similar simulations were carried out for φ_6, and φ_7 as well. φ_1, φ_2, φ_3, φ_4, and φ_5 were kept constant and set to 30 (m^{-1}), 5 (m^{-1}), 5 (m^{-1}), 6, and 6, respectively. Results (shown

in Figure 5.32) indicate that modifying φ_6, and φ_7 resulted in negligible improvements in excitation RMSE. Changing φ_6, and φ_7 has no impact on the duration of the RF pulse.

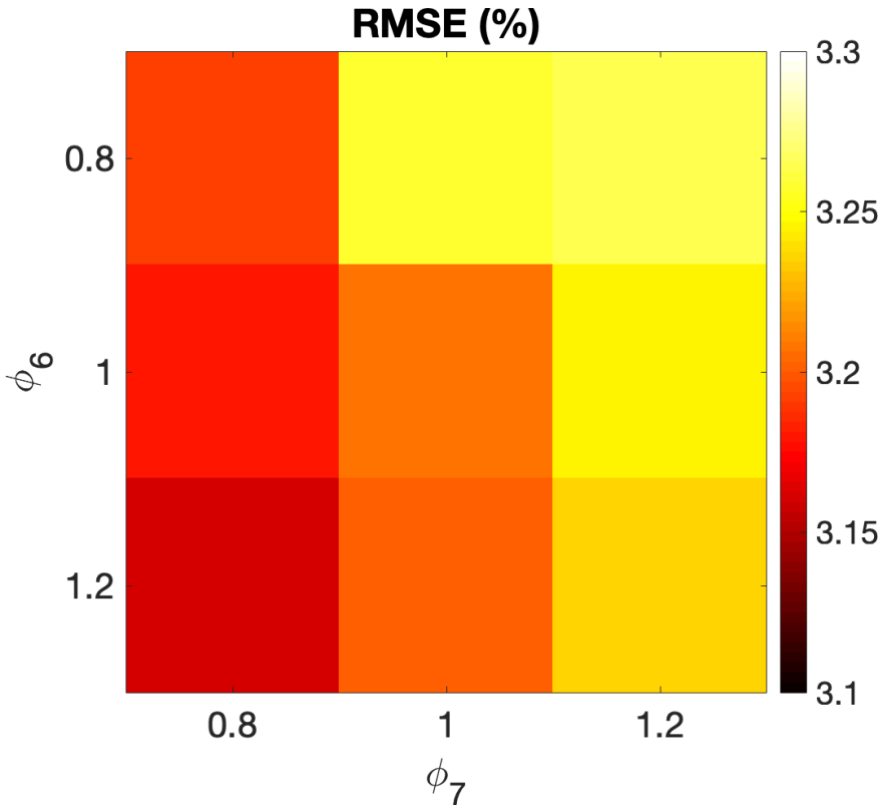


Figure 5.32: The relationship between the RMSE of the excitation profile and parameters φ_6, and φ_7. φ_6 controls the number of revolutions of the centermost shells, and φ_7 controls the relative distance between concentric shells.

Despite the relatively low RMSE in simulations, large excitation errors were present for *in-vivo* and phantom experiments. One of the possible causes for error is a mismatch between prescribed and achieved waveforms due to hardware imperfections of the gradient system. Simulations above showed that decreasing the k-space extent and the number of shells and revolutions slightly increased the RMSE, but could greatly reduce the pulse duration. Therefore, a shorter RF pulse is less susceptible to these hardware-induced errors and might be desirable despite a slightly higher RMSE in simulation. As a result, a shorter RF pulse may be more desirable also because of the reduced relaxation effects, which would be a more significant issue in a multi-pulse saturation module.

5.3. Discussion

5.3.1. Summary of the study

5.3.1.1. The saturation strategy

The main contribution of this study is the addition of a spatially-selective saturation module to the TRUST sequence, thereby allowing the OEF of a single arbitrary brain region to be measured. The saturation module consists of a spatially-selective pTx RF pulse and gradients, followed by saturation-crusher gradients. A shells trajectory [190] was used to design the spatially-selective pulse. To evaluate the pulse performance the EPI imaging readout module was orientated in the labelling slab to directly visualise the spatial saturation. Despite Bloch simulation of the designed pulse showing outer-volume saturation, the initial phantom study with a single saturation module showed poor saturation performance. A circular ROI was visible in the acquired image, but the signal outside the ROI was not sufficiently suppressed. The preliminary *in-vivo* study on one subject demonstrated disappointing results similar to the phantom.

The initial interpretation of the results was that the transverse magnetisation outside the ROI was not properly spoiled. However, changing the magnitude, polarity or axis of the spoiler gradient following the spatially-selective pTx pulse did not change the quality of the image. Therefore, it was hypothesised that the poor nulling of signal outside the ROI was not a result of inadequate spoiling due to low gradient amplitudes but, rather, it was a result of imperfections in the spatially-selective pTx pulse. In other words, rather than unspoiled transverse magnetisation, it was remaining longitudinal magnetisation outside the ROI that led to the poor saturation.

The ROI could be easily identified in the preliminary phantom and *in-vivo* images, and the signal intensity in the ROI was much higher than that in the rest of the slice. Therefore, it was reasonable to infer that the majority of the magnetisation within the ROI remained along the longitudinal axis after the spatially-selective pTx pulse, as intended. Consequently, reapplying the saturation module should further saturate the magnetisation outside the ROI while substantially preserving that within the ROI.

Indeed, later phantom studies confirmed the hypothesis that repeating the saturation module greatly improves the saturation performance. Moreover, the improvement of applying three saturation modules was larger than applying two modules, as expected.

5.3.1.2. Advantages of spatially-selective saturation

The proposed method achieves spatial localisation of the desired region by applying pTx pulses that selectively excite spins outside the ROI, followed by crusher gradients to spoil that magnetisation. As an alternative, a single pTx pulse could be designed to spatially invert spins in the ROI directly. However, the difficulty of the pulse design problem is further increased when the required flip-angle is higher as the small-tip-angle approximation no longer holds. Spatially-selective inversion using pTx can be achieved, but more sophisticated approaches are needed. For instance, Jang *et al.* achieved spatially-selective inversion by replacing each piece-wise constant element of a hyperbolic-secant pulse by a 2D selective pulse [192].

In our application a cylindrical pattern needs only to be enforced within a slab. There is no need to consider the magnetisation outside the slab since the TRUST sequence is a subtraction-based method. Therefore, the pulse design problem in this study is simpler compared to other previously proposed inner-volume excitation methods [190, 193]. For the application in this study, it is more important to saturate the magnetisation outside the ROI than it is to keep spins precisely aligned along the longitudinal plane within the ROI. This is because the main objective of the pTx pulse design is to isolate T_2-prepared signal from blood water, and then to measure its T_2. Imperfections of the spatially selective pulses should still result in a pure, albeit reduced, T_2-encoded signal from the target ROI. Moreover, such a decrease in blood signal can be predicted by the performance of the RF pulse. However, imperfections outside the ROI will lead to an imperfect subtraction between the label and control images, thus contaminating the spatial extent of the T_2 measurement, and consequently the oxygenation measurement of the desired ROI.

As a result, the absolute signal from the ROI derived in the difference image is of limited importance, as long as the signal contamination level is kept at an acceptable level.

However, the estimated signal contamination of the TRUST signal was large (21.2% and 53.7% for 180V and 223V pulses, respectively) despite the high accuracy of the saturation strategy (0.9% and 2.6% error for 180V and 223V pulses, respectively), primarily due to the low volume ratio of the target ROI (6.9%). An ROI volume ratio of 15% corresponds to a contamination level of 10%. The level of signal contamination will be discussed in more detail in section 5.3.3.

5.3.2. The discrepancy between experimental and simulation results in the phantom study

The experimental results broadly matched with Bloch equation simulations carried out in this study. For different time delays between the gradient and RF channels a deterioration of the saturation accuracy, and a rotation of the excitation target, were observed both in the simulations and in the experiments. Furthermore, adding time delays in the experiment did not visibly improve the results, which suggested that the RF and gradient channels were sufficiently synchronised using the default Siemens calibration. For different pulse voltages, a similar trend was observed both in simulation and in experiment: namely, that deviations from the optimal voltage led to a poorer saturation profile. The poorer saturation performance might be due to under-flipping of the magnetisation at a lower voltage, and over-flipping of the magnetisation at a higher voltage.

Despite the broad agreements, there were several key discrepancies between the simulations and the experiments. First, although simulation results showed that a sufficient saturation could be achieved using just one spatially-selective pulse, a good experimental saturation performance was achieved only after the repetition of the saturation module. Second, the Bloch equation simulation failed to predict the artefacts presented at the edges of the phantom. Third, whereas the optimal pulse voltage was 223V in simulation, a voltage of 170V-190V produced the best saturation performance in the experiments, as measured by the mean signal intensity outside the ROI.

However, these three observations might be connected. Although the artefacts were more pronounced at higher voltages on the edges of the phantom, the centre of the phantom had relatively low intensities. Therefore, the poor saturation performance at the designed voltage (223V) could be primarily attributed to the artefacts at the edges of the phantom that were not predicted by simulation.

One possible explanation for the poor performance of the one-pulse approach might be that there was a systematic bias in the B_1^+ maps that led to under-flipping of the magnetisation. Moreover, the complicated B_1^+ and B_0 patterns at the boundary between the phantom and surrounding air might not have been accurately captured by the B_1^+ and B_0 mapping sequences in this study, which would explain the artefacts that were not predicted by the simulation. However, such an effect might not occur on a human subject or phantoms with different dielectric properties. A comprehensive B_1^+ and B_0 mapping study on the oil phantom is needed to provide a more thorough explanation of the discrepancies between the simulation and the experiments.

5.3.3. The level of signal contamination

Despite the high accuracy of the saturation strategy (0.9% and 2.6% for 180V and 223V pulses, respectively), the estimated contamination of the TRUST signal (if *in-vivo* scans were to be carried out) was large (21.2% and 53.7% for 180V and 223V pulses, respectively). This can be explained by the small volume fraction of the target ROI relative to the entire inversion slab (<7%). Simulation results showed that a moderate increase in the volume ratio substantially decreased the level of signal contamination in the TRUST measurement, which then in turn could improve the accuracy of the OEF estimation. This finding suggested that a cylindrical ROI with larger relative volume might be needed for accurate local OEF measurement. However, in the proposed method, it is worth noting that the level of signal contamination is dictated by the in-plane area of the ROI, and it would not be affected by the thickness of the inversion slab. In other words, a shorter (in the z axis) cylindrical ROI with larger base area could allow an improved signal localisation with the same absolute volume.

The signal contribution from the ROI was estimated by multiplying the mean experimentally measured signal intensity within the ROI by its size. Therefore, the low mean signal intensity within the ROI led to a large fractional signal contamination estimation. The M_0 value was assumed to be the highest voxel intensity in the ROI, which was 1229. However, the mean signal intensity in the ROI was much less than that. This might largely be due to the following reasons:

- First, the excitation target was smoothed to avoid a rapid transition between 0° and 90°, as such a sharp excitation profile is hard to achieve. Therefore, the ideal excitation profile in the ROI contained a transition band, by design.

- Second, the mean signal intensity within the target ROI decreased when more saturation pulses were applied. The signal contamination calculation was done on images that used the strategy of three saturation pulses, that showed superior saturation outside the ROI. However, three saturation pulses also led to a lower signal within the ROI, compared to the case of one and two pulses. This was because the spatially-selective excitation was not perfect, and therefore spins within the ROI were partially saturated. In addition to a slight decrease in the peak signal within the ROI, additional saturation pulses also led to an eroded residual ROI profile. As a result, the effective size of the ROI in the experiment was smaller than the size that had been designed. A solution to this problem might be to prescribe an enlarged ROI during the pulse design stage, thus allowing the eroded residual ROI profile to match the intended boundary of the ROI. However, more in-depth characterisation and calibration of the saturation profile is needed for the implementation of this approach.

In addition, the saturation error in this study was complicated by the minimal timing delay (80ms) between the saturation module and the read-out in the modified TRUST sequence, which was to allow time for the inversion pulse (when present) to be played out. Such a difference introduced T_1 decay to the saturated spins outside the ROI. Therefore, this effect needed to be accounted for by extrapolating the signal at the end of saturation from the signal at the time of imaging based on the T_1 of the phantom. Alternatively, the designed pulses could be included in a simpler sequence where an

image can be acquired immediately after the saturation, thus eliminating the complication of T_1 decay.

The method proposed in this chapter provides an alternative approach to achieve spatial localisation in TRUST. Therefore, it might be useful to compare the effectiveness of saturation strategies using WET and pTx pulses. In the *in vivo* SL-TRUST experiments at 3 T, O'Brien *et al.* found that a hemispheric saturation resulted in a mean signal decrease of 64.5% [189]. A strictly hemispheric saturation would lead to a 50% signal reduction. The higher signal reduction could be partially explained by the placement of the saturation band, which covered the sagittal sinus. Therefore, blood signal could be contributed from the sagittal sinus itself and a small portion of the contralateral hemisphere.

However, O'Brien *et al.* did not acquire images in the saturation slab to evaluate the saturation profile in the *in vivo* experiments [189]. Since the signal reduction in the sagittal sinus is an indirect measurement of the saturation efficiency, it is difficult to directly compare the two saturation strategies (i.e. using WET versus pTx pulses). O'Brien did, however, show an example saturation profile acquired on a circular phantom using WET saturation [194]. From visual inspection, the example saturation profile shown in this chapter seemed to offer a superior saturation efficiency. Nevertheless, without a more comprehensive and quantitative characterisation of a saturation profile covering the slab-of-interest (as opposed to an example line of a slice), no firm conclusion on the saturation efficiency can be drawn. Furthermore, SL-TRUST experiments were only conducted at 3 T. If the same 3 T experiments were to be repeated at 7 T, the efficiency of the WET saturation scheme might be expected to decrease due to increased B_1^+ variations at 7 T, although pTx approaches could also be incorporated to improve the B_1^+ homogeneity of the individual sub-pulses.

5.3.4. Proposed human study

At the time of writing the 2020 coronavirus pandemic has halted development-focussed scanning at University of Oxford sites. This section describes the proposed next steps

when scanning is permitted, incorporating plans to overcome the additional steps of an *in vivo* implementation.

The first step of any human study would be to reproduce the results from phantom experiments using the strategy of three saturation modules described in this chapter. B_1^+ and B_0 maps would be acquired, from which the RF pulses could be designed. To test this, the imaging slice could be placed within the inversion slab, enabling the quality of the suppression of signals outside of the ROI to be assessed.

Once the accuracy of the spatial saturation is confirmed, the next step would be to measure OEF within an ROI using the proposed method. The sequence would be repeated with different eTEs, and the signal difference between the label and control images in the sagittal sinus could be recorded for each eTE. A mono-exponential curve could then be used to fit the relationship between the signal difference and eTE, and estimate the blood T_2. The OEF could then be calculated based on known relationships between blood T_2 and oxygenation (once the haematocrit level is accounted for).

A few additional steps (detailed in the following subsections) would further validate the proposed method in human subjects.

5.3.4.1. HCT measurement by T_1

First, the blood T_2 is not only related to OEF, but to the HCT level as well. Although some studies assume that HCT is constant across subjects, it is beneficial to assess subject-specific HCT non-invasively. Shimada *et al.* proposed calculation of HCT by measuring blood T_1 [195]. O'Brien *et al.* used a multi-TI inversion recovery sequence to estimate venous blood T_1 in the sagittal sinus in the SL-TRUST method [189]. The same approach can be used in a 7T *in-vivo* study to measure OEF using pTx pulses.

5.3.4.2. Validation against global measurements

To validate the proposed method in human subjects, a comparison can be made between global and regional OEF measurements. If the proposed sequence correctly estimates

regional OEF, it is expected for a healthy subject that the normalised T_2 decay curve in the regional measurement would match that in the global measurement. This is because the OEF would be uniform across different brain regions in healthy subjects at rest. Furthermore, the raw signal intensity should scale with the volume ratio of the ROI compared to the global measurement. The proposed method could also be compared against the SL-TRUST method that uses conventional saturation pulses. The raw T_2 decay curve should be similar for ROIs of similar location and sizes. Additional intra-session and inter-session comparison studies could be used to assess the stability, reliability and reproducibility of the proposed method.

5.3.4.3. Gas challenge and patient scans

Further studies in healthy subjects involving vasoactive challenges such as hypercapnia and caffeine challenges could determine the sensitivity of OEF measurement using pTx pulses. This is because gas challenge studies allow for the OEF of a subject to change within a session. OEF measurements in a region of the brain can be obtained with and without hypercapnia, and OEF changes that broadly agree with literature values would confirm the sensitivity of the proposed method. Finally, patient studies could be conducted if the robustness of the regional OEF measurement were to be established. It may even be possible to compare the values measured with another technique, such as PET OEF measurements, although PET has its own logistical challenges.

5.3.4.4. TI selection

A TI of 1200 ms was used in the study by O'Brien *et al.* [189]. Nevertheless, as discussed by O'Brien *et al.*, the SL-TRUST method is more sensitive to CBF changes than the original TRUST method, which could be more pronounced in the target clinical population [189]. As a result, it would be helpful to choose an optimised TI based on the location of the ROI and the particular population. An excessively long TI would lead to a significant signal contribution from the capillary or tissue water rather than the venous blood of interest [189].

5.3.4.5. T_2-encoding

In the phantom experiments detailed in this chapter, the T_2-encoding module was turned off to isolate the effects of the spatially-selective saturation. However, the T_2-encoding module is crucial to the signal formation of the TRUST sequence, and therefore must be turned on for *in vivo* experiments. The T_2-encoding module consists of a train of nonselective 180° pulses between two 90° pulses (see Section 5.1 for details), and the duration of the module determines the effective echo time (eTE). Nevertheless, achieving the desired T_2-encoding at UHF is challenging due to increased B_1^+ inhomogeneity. Accurately delivering large-flip-angle pulses is particularly challenging at 7 T. In addition, the 180° pulses are repeated multiple times. Therefore, the effect from any errors in the achieved flip-angle will be amplified, leading to large deviations from the desired amount of T_2-encoding. One way to mitigate this problem is to replace the hard 180° pulses with composite 180° pulses that are more robust to B_1^+ inhomogeneity. In the first 7 T TRUST study, Krishnamurthy *et al.* used composite refocusing pulses (90_x-180_y-90_x) to replace the original hard 180° pulses in order to mitigate B_1^+ inhomogeneity of the T_2-encoding [191]. Results from Bloch equation simulation (see Figure 5.33) showed that composite 180° pulses are more robust to both B_1^+ and B_0 inhomogeneities, and can be easily incorporated into the current implementation of the modified TRUST sequence.

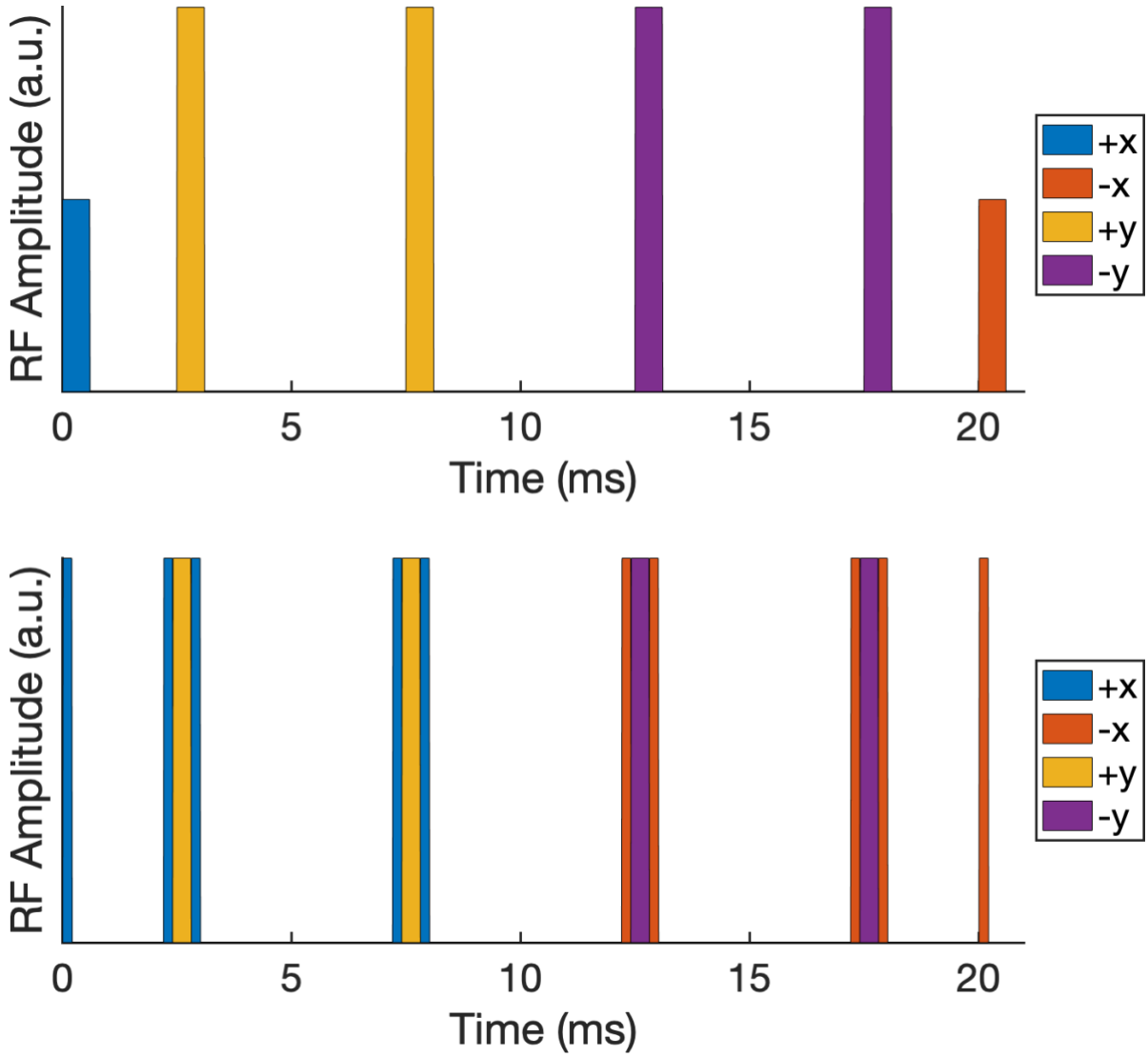


Figure 5.33: Two T_2-encoding schemes for an effective TE of 20 ms with τ_{CPMG} = 5 ms (the gap between the 180° pulses). The legends indicate the axis on which the RF pulses are played out. Shown on the top is the encoding scheme using hard 180° pulses, similar to the one used in the study by Lu et al. *(doi: 10.1002/mrm.21627). Note that the 180° pulse is achieved by doubling the RF amplitude compared to the 90° pulse. Shown on the bottom is the encoding scheme using complex 180° pulses, similar to the one used in the study by Krishnamurthy* et al. *(doi: 10.1002/mrm.24868). Note that the 180° pulse is achieved by doubling the duration compared to the 90° pulse.*

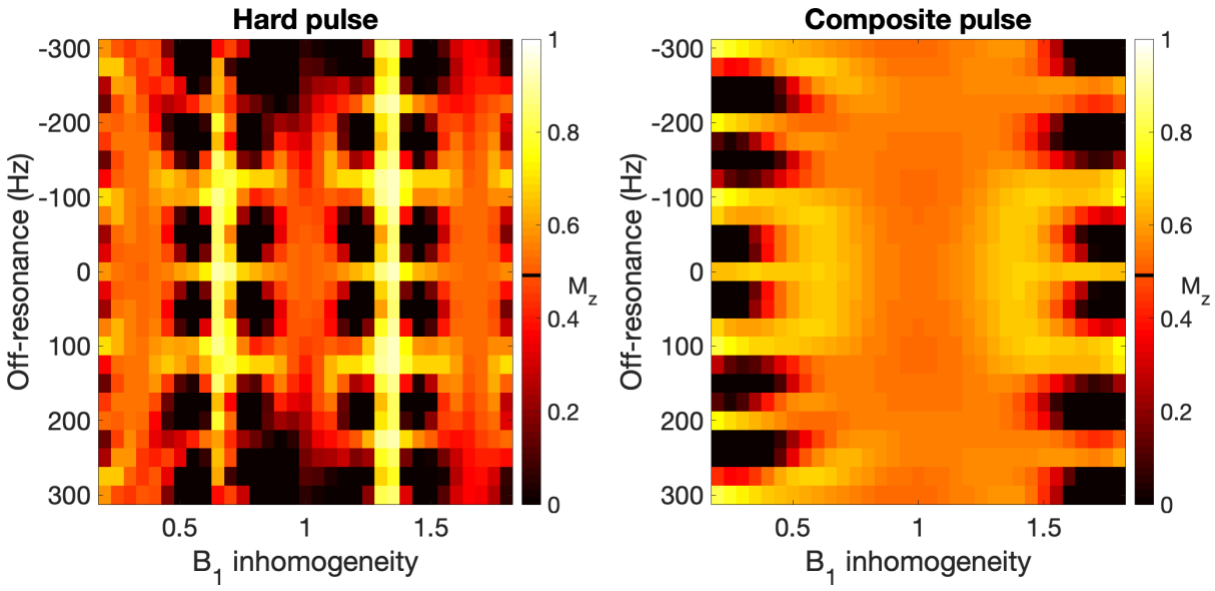


Figure 5.34: The magnetisation in the z axis (M_z) after T_2-encoding modules using hard 180° pulses and composite 180° pulses from Bloch equation simulation. The black line on the colour bar shows the expected M_z following a perfect T_2-encoding.

Furthermore, in the case of regional OEF measurement, since the signal from the ROI is isolated by the spatially-selective saturation module, only spins within the ROI need to be T_2-encoded. In other words, the achieved flip-angle of the T_2-encoding pulses only needs to be accurate within the ROI. Therefore, although more sophisticated pTx strategies are available, RF shimming might be a suitable approach due to the small size of the ROI.

5.3.4.6. SAR considerations

At present, the modified TRUST sequence (with the pTx saturation modules added) can be played out with a TR of 5 seconds for eTEs up to 40 ms. An eTE of 40 ms corresponds to eight 180° pulses (when τ_{CPMG}=5 ms). Additional inversion pulses needed for T_2 preparations at higher eTEs would cause the sequence to exceed the RF power limit placed on the 7 T pTx system. Therefore, using an eTE of 60 ms requires increasing the TR. However, choosing an eTE higher than 80 ms might not be realistic due to faster T_2 decay at 7 T. More discussion on this point can be found in the next section.

The background suppression module for the imaging slice, consisting of a pre-saturation pulse and a pair of inversion pulses, was turned off in the experiments in this chapter. Including background suppression would improve the SNR and enhance the reliability of

the OEF estimation, but at a cost of higher RF power/SAR. This challenge could be overcome by increasing the TR of the sequence at the cost of a longer scan time. However, a longer scan time restricts the clinical applicability of the proposed method. As mentioned in Chapter 5, the current challenges are primarily due to the conservative RF power limits that are used in "protected mode" defined by the scanner vendor Siemens on the pTx system. Validated EM simulations and VOP files for the transmit coil would allow for the use of "experimental mode", which has more relaxed RF power limits.

5.3.4.7. Benefits and challenges at 7 T

The primary motivation of applying the TRUST sequence at 7 T in this chapter is to utilise the flexibility to individually control the RF waveform in each transmit channel of the pTx system, which is more commonly found at 7 T compared to lower field strengths. However, it is less straightforward to assess the gain of moving to higher field strengths. In most conventional sequences, improving the image SNR or the temporal SNR is often the ultimate goal. In the TRUST sequence, only a single oxygenation measurement is produced based on signal in the sagittal sinus from the subtracted image. It is therefore the accuracy of the oxygenation estimation that is of the highest importance, rather than the raw image SNR. The following paragraphs attempt to address the implications of moving to UHF for TRUST. Since no complete *in vivo* data is available for this chapter, most of the discussion is based on the work on applying the TRUST sequence at 7 T by Krishnamurthy *et al.* [191].

There are several benefits of moving to UHF for the TRUST sequence apart from the ability for more flexible spatial selection using pTx pulses. First, the increase in intrinsic SNR at UHF increases the SNR of the control and label images, and therefore the subtraction image. Second, the blood T_2 is more sensitive to oxygenation changes at 7 T due to the increased susceptibility effects of deoxyhaemoglobin [191]. Moreover, with a longer T_2 at UHF, the label-control difference is preserved for longer, leading to an improved SNR.

Nevertheless, there are several key challenges for the TRUST sequence at 7 T as well. Due to the faster T_2 relaxation, Krishnamurthy *et al.* were unable to use eTEs longer than 80

ms [191], as too much signal would have decayed away after the T_2 encoding scheme. Although B_0 and B_1^+ inhomogeneities will also be present in the imaging slice, it is a comparatively less pressing issue in TRUST than other sequences. This is because only voxels containing the sagittal sinus are of interest. Therefore, it could be expected that B_0 and B_1^+ inhomogeneities could be resolved by simply adjusting the RF pulse voltage and the shim setting. B_1^+ inhomogeneity is a more severe issue for T_2 encoding, since a series of 180° pulses are required. Strategies for mitigating B_1^+ inhomogeneity for T_2 encoding are discussed in Section 5.3.4.5.

The paragraphs below aim to quantify the change to the TRUST signal when moving to UHF.

1) As shown in Chapter 2, intrinsic SNR scales with the main magnetic field strength. Therefore, moving from 3 T to 7 T should result in an imaging SNR improvement of 2.33 fold.

2) Zhang *et al.* measured venous blood T_1 at different field strengths by applying a non-selective inversion pulse before a Look-Locker EPI sequence, and found the venous blood T_1 to be 1592 ms at 3 T, and 2007 ms at 7 T [164]. When using a TI of 1200 ms, moving from 3 T to 7 T would result in an SNR improvement of 17% (or an SNR ratio of 1.17).

3) Shorter T_2^* at higher field strengths decreases the image SNR since more signal would have decayed away at the time of image acquisition. When assuming a T_2^* value of 55 ms at 3 T and 32 ms at 7 T based on a study van der Zwaag *et al.* [163], a TE of 20 ms would lead to an image SNR ratio of 0.78 (7 T vs. 3 T).

4) The effects of shorter T_2 at higher field strengths are more difficult to quantify, since dependence of T_2 on blood oxygenation is the source of contrast of the TRUST sequence. In addition, blood T_2 depends on haematocrit levels, as well. Figure 5.35 below shows the relationship between T_2 and Y at 3 T and 7 T when Hct is 42%. Table 5-4 shows the normalised signals at different eTEs at 7 T and 3 T when Hct is 42% and Y is 60%. A faster T_2 relaxation results in reduced signal at

higher eTEs, making additional measurements of the exponential decay curve (MR signal of the subtraction image vs. eTE) more challenging.

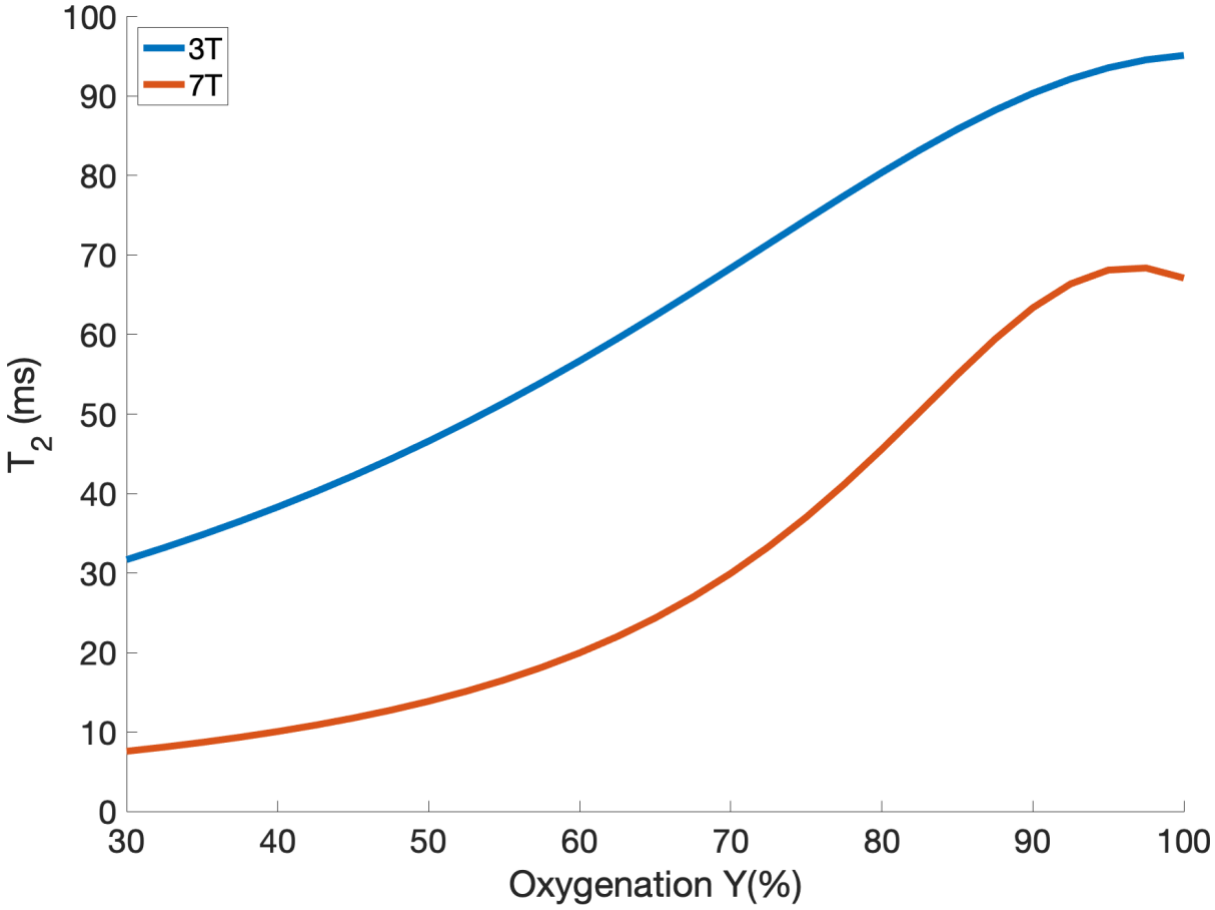


Figure 5.35: The relationship between T_2 and Y at 3 T and 7 T when Hct is 42%. The simulations were based on calibration studies by Lu et al. (*doi: 10.1002/mrm.22970*) *for 3 T and Krishnamurthy* et al. *(doi: 10.1002/mrm.24868) for 7 T.*

Table 5-4: Normalised signals at different eTEs at 7 T and 3 T when Hct is 42% and Y is 60%. The ratio between 7 T and 3 T is shown in the bottom row. The simulations were based on calibration studies by Lu et al. (*doi: 10.1002/mrm.22970*) *for 3 T and Krishnamurthy* et al. *(doi: 10.1002/mrm.24868) for 7 T.*

	eTE=0	eTE=20 ms	eTE=40 ms	eTE=60 ms	eTE=80 ms
7T signal	1	0.723	0.484	0.347	0.244
3T signal	1	0.367	0.135	0.049	0.018
Ratio	1	0.522	0.272	0.143	0.074

5.3.5. The pulse design approach

5.3.5.1. Limitations of the current approach

Since tailored pulses have to be produced within a scanning session, the pulse design time needs to be short. Such a time constraint limits the complexity of the pulse design approach. The variable-exchange (V-E) method was used in this study for pulse calculation [72]. The RF power was indirectly controlled by a Tikhonov regularisation parameter in the V-E method. The pulse design could be improved by applying more sophisticated optimisation algorithms with an explicit RF power constraint. However, running such a nonlinear pulse design optimisation is inherently more computationally demanding. It is particularly challenging for the pTx pulses used in this study, since the number of parameters to optimise is large. This is because the pulse amplitude and phase at each time point of the RF waveform are allowed to change, whereas there are only two variables (amplitude and phase) for each channel in the case of RF shimming. Similarly, there are only two variables per channel for each spoke in the case of spokes pulses, and only two variables per channel for each k_T-point in the case of k_T-points pulses. In simulation, pTx pulses produced an excitation RMSE of 2.1%, whereas pulses designed without pTx (CP-mode like) using the same trajectory produced an RMSE of 4.8%.

No gradient trajectory optimisation was carried out in this study. Jointly optimising the RF and gradient waveform will further improve the spatially selectivity. The simulation work detailed in Section 5.25 showed that the trajectory used in the experimental studies in this chapter could be simplified with only slight degradation in excitation accuracy. However, the optimal trajectory is likely to change with the subject being scanned, and the exact location of the ROI. For example, in the study by Davids *et al.*, the computation time for joint optimisation was a number of hours, which is far from practical within a single scanning session [190]. Davids *et al.* suggested that implementing multithreading using a graphic processing unit (GPU) might significantly reduce the computation time [190], but major changes in the optimisation code would be needed and additional hardware would be required. In the intended clinical application the exact location of the ROI would be determined by the clinician or radiographer on a case-by-case basis. Therefore, it is impractical to optimise for a gradient trajectory that is tailored to an unknown ROI of a patient prior to the scan.

A retrospective simulation study on the influence of the gradient trajectory on the RF pulse design performance was detailed in Section 5.2.5. The simulation results showed that the trajectory chosen for the experiments in this chapter might have been too complex for the intended excitation target. First, the excitation k-space coverage might have been too large. Once a sufficient coverage of is reached, extending the excitation k-space coverage only brings marginal improvements in excitation accuracy at the cost of a longer pulse duration. Second, the number of shells and revolutions might have been too large as well. Reducing the number of shells and revolutions leads to slightly larger excitation errors, but reduces the pulse duration significantly. Therefore a simpler, shorter pulse with a more limited excitation k-space coverage and a smaller number of shells and revolutions might be more suitable. A shorter duration allows the RF pulse to be repeated multiple times for better saturation efficiency. Furthermore, shorter RF pulses are less susceptible to off-resonance effects and gradient system imperfections.

The goal of the pulse design in this chapter is to minimise the RMSE between the excitation profile and the excitation target for a single pulse. Experimental data showed that a single spatially-selective pulse followed by crusher gradients was not able to achieve a satisfactory saturation profile. Therefore, the pTx pulses and crusher gradients were repeated for a better saturation efficiency. However, it might be necessary to aim for an optimal saturation profile after a train of pulses, instead of an optimal excitation after a single pulse. Ogg *el al.* designed the WET saturation pulses in order to provide T_1 and B_1^+ insensitivity [114]. For a four-pulse train, the optimal nominal flip-angles are 81.4°, 101.4°, 69.3°, and 161.0° [114]. Similar approaches could be adopted on the pTx saturation module in this chapter as well by modifying the RF voltage of each pTx arbitrary pulse. However, additional experimental studies are required to validate this approach.

5.3.5.2. The possibility of using universal pulses

Boulant *et al.* proposed the concept of universal pulses to first perform in-depth optimisation of pTx pulses off-line based on a series of B_1^+ maps acquired from a number of representative subjects, and then apply the pre-calculated pulses to new subjects

without any further calibration [99]. Despite the demonstrated improvement in B_1^+ inhomogeneity, the concept of universal pulses has been primarily applied on non-selective 3D pulses using the k_T-points trajectory approach. Geldschläger *et al.* applied the concept of universal pulses to the design of 3D inner volume excitation pulses using a stack-of-spiral-in trajectory [196]. Results showed that universal pulses achieved similar excitation patterns and errors compared to subject-specific tailored pulses [196]. Therefore, universal pulses could reasonably be expected to deliver a comparable excitation performance in the case of spatial saturation as well.

The study by Geldschläger *et al.* only looked into fixed excitation patterns (a cuboid and a cylinder) [196]. However, as mentioned above, regional mapping of oxygenation in the brain is inherently subject-specific. This challenge could be tackled by applying the concept of universal pulses in the following way: First, a fixed set of RF waveforms and a fixed gradient trajectory could be jointly optimised based on previously acquired B_1^+ and B_0 maps for each vascular territory. This would invariably lower the quality of the spatial saturation but would eliminate the need for subject-specific calibration completely. Second, if the accuracy of the universal pulses is insufficient, an optimal gradient trajectory could be calculated for each vascular territory ahead of time. It would then be possible to calculate the tailored RF pulse element of the calculation during the scan based on the optimal gradient trajectory. Moreover, the pre-calculated universal RF pulses could potentially be used for initialisations in the optimisation algorithm.

5.3.6. OEF maps vs. regional OEF measurement

O'Brien *et al.* recently proposed a new method called spatially-encoded T_2-Relaxation-Under-Spin-Tagging (SE-TRUST) based on the SL-TRUST method [197]. The SE-TRUST method encodes spatial information in the longitudinal magnetisation using cosine modulation, and decodes it in the draining venous blood to produce a low-resolution OEF map by applying an inverse Fourier transform. The spatial encoding in SE-TRUST is placed between the T_2 encoding module and the pre-saturation pulse, and is achieved by sinusoidal modulation which involves the following steps: First, a hard 90° pulse tips the magnetisation into the transverse plane. Second, phase encoding gradients are played out to induce a linear phase variation. Third, another hard 90° tips the magnetisation back to

the z-axis. The sinusoidal modulation is now stored in the longitudinal magnetisation. The encoding module is also phase-cycled to perform sine modulation as well, thus allowing for the acquisition of both real and imaginary components. Similar to SL-TRUST, both control and label images are then acquired for different eTEs, and a T_2 decay curve is produced to estimate the OEF based on the difference image. By varying the phase encoding gradients, a 2D matrix in k-space can be obtained. An inverse fast Fourier transform can then be applied to convert the k-space matrix to image space. The resulting image is a spatial map of OEF. Despite the proven sensitivity, SE-TRUST suffers from relatively long scan time. A 7x7 grid required a scan time of 37 minutes. This is because a label-control pair has to be acquired for each cosine modulation and each eTE. Compressed sensing could potentially accelerate the acquisition if random k-space encoding is applied.

In a clinical setting, given the availability of generating an OEF map and a regional OEF measurement, the clinician could make a decision according to the circumstance of the patient. If an OEF map is needed to identify a brain region of pathology, then SE-TRUST is more suitable. If there is a region with pathology that has been identified, then SL-TRUST using pTx pulses is more appropriate. Furthermore, the two methods could be combined to give much finer spatial resolution. SL TRUST using pTx can be used for reduced FOV imaging, and further subdivision can be achieved by the SE TRUST method.

Chapter 6 Summary and future work

6.1. Summary

This thesis applies pTx approaches to two spin labelling techniques: arterial spin labelling (ASL) in which spins in the arterial blood are labelled, and T_2-Relaxation-Under-Spin-Tagging (TRUST), in which spins in the venous blood are labelled.

ASL

RF shimming was applied to improve the labelling pulse train in a PCASL sequence. The four major feeding vessels in the labelling plane through the neck were selected from a time-of-flight image as the ROI. An optimisation algorithm was implemented to minimise difference between the flip-angle in the ROI and a target of 20° under an explicit power constraint.

Simulation results showed that the proposed method significantly increased the mean flip-angle in the ROI while decreasing the variance. *In-vivo* results showed that the temporal SNR in perfusion-weighted images improved considerably when adopting pTx strategies compared to images acquired in a standard CP mode under the same RF power limit.

Perfusion-weighted images were also acquired at 3 T for comparison. Results showed that the temporal SNR of perfusion-weighted images acquired at 7 T did not outperform those acquired at 3 T with the same sequence parameters. This could in part be due to increased physiological noise at higher field strength. Acquiring images with higher spatial resolution might better leverage the image SNR gain at 7 T, since temporal SNR plateaus when physiological noise dominates [159]. Currently, the stringent SAR/RF power limit for the pTx system at 7 T leads to a compromise between increasing the labelling duration, increasing the labelling pulse voltage, or applying background suppression.

TRUST

Despite being a robust method to measure tissue oxygen extraction fraction using MRI, the original TRUST sequence [171] lacks regional specificity. Chapter 5 introduced arbitrary pTx pulses based on a shells trajectory [190] to achieve spatially selective saturation in a modified TRUST sequence. The saturation module consists of an arbitrary pTx pulse that excites all the spins in the slab except for those in the ROI, followed by a crusher gradient. In the label case, a slab-selective inversion pulse is applied after the saturation module, thus inverting the spins in the ROI. In the control case, no inversion is applied, and the spins in the ROI are left intact. Therefore, the difference between the control and label images includes only signal from the ROI. Preliminary *in-vivo* experiments showed that although the ROI was clearly identified, saturation of signal outside of the ROI was not achieved with great accuracy. Later experiments demonstrated that repeating the spatial saturation module improved the quality of saturation.

Despite low saturation errors outside the ROI, the signal contamination was somewhat high (approximately 20%) due to the low volume ratio of the ROI in the inversion slab. This might suggest that the ROI chosen in Chapter 5 was too small for accurate spatial localisation in the OEF measurement. Simulations showed that moderate increase in the volume ratio of the ROI substantially decreased the level of signal contamination. Therefore, an ROI of a larger size might need to be selected for *in-vivo* study. In addition, adding additional pulses partially saturated the magnetisation within the ROI, and slightly eroded the saturation profile. However, the effect could be mitigated by prescribing an ROI that is larger than the desired region. Unfortunately, further *in-vivo* images from human subjects could not be acquired due to the ongoing COVID-19 pandemic.

6.2. Widening the adoption of pTx

The wider adoption of pTx has to be facilitated by the MRI scanner vendors. Currently, most research groups using pTx have developed in-house software pipelines to calculate

RF pulses and implant them into pulse sequences. Typically, groups also make use of tailored B_1^+ and B_0 mapping sequences, and custom image handling software. The great variety in approaches inhibits an easy distribution of pTx methods from the original development site to other potential users.

Although methods such as universal pulses [99] have shown enormous potential in recent years as a calibration-free pTx approach , applications mentioned in this thesis, namely improving labelling efficiency via RF shimming and measuring regional blood oxygenation levels, currently rely on subject-specific tailored RF pulses. In addition, although universal pulses have proven to be a robust method of applying non-selective pulses for 3D imaging, applying the concept of universal pulses on a slice-by-slice basis is challenging. This is because, although the overall variation in the B_1^+ distribution in the human head is relatively small across subjects, such variation within individual slices might be large because of the difference in head sizes and slice positions.

As demonstrated in Chapter 4, the RF power limit on the Siemens Magnetom 7 T scanner is prohibitively stringent. Although methods such as virtual observational points (VOPs) have been proposed to simply the calculation of local SAR, such methods are not commonly used in studies in *in-vivo* experiments. This is because the burden of guaranteeing safe operation under "experimental mode" on the Siemens pTx platform falls on the local institution and the scanner operator. Furthermore, the users need to generate their own VOP files to enable local SAR monitoring.

Apart from universal pulses, pTx strategies usually require a long time for calibration or preparation. Various approaches have been proposed to shorten the pulse calculation time. Despite these impressive accelerations, calculations are usually carried out on externally mounted computers instead of being properly integrated into the scanner console. Therefore, the time required to transfer, load, and sort B_1^+ and B_0 maps could not be omitted.

Knowledge of sequence programming, B_1^+ mapping, RF pulse design, SAR calculation, pTx-specific scanner operation, is often needed to start a pTx project. Basic knowledge of RF coil design might also be desirable. From the perspective of the scanner vendor,

although on-site scientists from vendors can certainly provide many aspects of the expertise mentioned above, implementing the following will greatly expand the applicability of pTx:

- Provide fast and robust standardised B_1^+ and B_0 mapping sequences.
- Handle and manage the B_1^+ and B_0 maps internally but output the maps for later analysis.
- Provide basic pTx pulses.
- Allow for flexible selection of ROIs.
- Allow easy modifications of basic pTx pulses in the user interface (e.g., number of k_T points, gradient blips between spokes).
- Record the RF pulses being played out and output them for later analysis.

Note that the discussions in this section are based on experience on the Siemens Magnetom scanner at the University of Oxford and experiences shared by colleagues from other institutions in previous meetings. Some of these challenges have been partially addressed by a newer generation of scanner, such as the Siemens Magnetom Terra.

6.3. Future work

6.3.1. Benefits and challenges of operating under "experimental mode"

The conservative SAR/RF power limit currently in place on the pTx system of the Siemens 7 T scanner at the Wellcome Centre of Integrative Neuroimaging presents a challenge to both the ASL and the TRUST studies. In the ASL study, a less stringent SAR/RF power limit would allow the following possibilities. First, the maximum RF power of the labelling pulse could be increased, thus allowing the achieved mean flip-angle in the feeding vessels to more closely approach the target of 20°. However, simulations showed that such an improvement in the mean flip-angle would only lead to marginal improvements in the labelling efficiency, as the mean flip-angle achieved in Chapter 4 was approximately 18°. Second, the labelling duration could be increased. The resulting perfusion signal should scale with the labelling duration, since increasing the labelling duration directly increases the amount of labelled arterial blood. In the experiments carried out in Chapter 4, the labelling duration was 1s, which was much shorter than 1.8s, the recommended

value in the ASL white paper [129]. Third, suppression of the static tissue signal using a pre-saturation pulse and two inversion pulses can be applied. Since physiological noise dominated in the experiments conducted in this thesis, applying background suppression might greatly improve the temporal SNR of the perfusion-weighted images. Fourth, the TR could be reduced to shorten the scan time, thus improving SNR per-unit-time.

Similar to ASL, the TRUST sequence could benefit from a shorter TR and the use of background suppression. Although background suppression was not implemented in the original TRUST sequence [171], it was applied in the SL-TRUST study to minimise subtraction errors and mitigate partial volume effects [189]. Furthermore, since a longer eTE requires additional 180° pulses in the T_2 encoding module, Krishnamurthy *et al.* only used two eTE values (40ms and 80ms) due to SAR constraints [191]. Therefore, a relaxed SAR limit could allow for more points to be measured, enabling fitting of an exponential curve to the data for more accurate blood T_2 estimation.

Operating under the "experimental mode" on the Siemens Magnetom 7 T scanner, as opposed to the "protected mode", would allow for a less conservative RF limit. However, additional work is needed before local approval of scanner operation under the "experimental mode" is permitted. Validation studies need to be conducted to make sure that the coil vendor-supplied EM simulations match experimental thermal measurements and other appropriate tests. From these, VOP models must be created, and scanning restricted to appropriate populations, which are unlikely to include patient groups in the first instance.

6.3.2. Adopting pTx approaches in the read-out module of blood labelling sequences

pTx approaches were used to improve the performance of the labelling pulse train in the ASL study, and to achieve spatially selective saturation in the TRUST study. However, pTx pulses (RF shimming or spokes pulses) could also be used to reduce the flip-angle inhomogeneity of the slice-selective imaging excitation pulses. Such an approach would be more beneficial to the ASL study than the TRUST study. This is because whereas all the imaging slices are of interest in an ASL sequence, only the sagittal sinus in the single

imaging slice is of interest in the TRUST sequence. Therefore, simple RF shimming would be sufficient to improve the B_1^+ in the sagittal sinus for the TRUST sequence, while spokes pulses might be needed to achieve a homogeneous excitation in whole slices for the ASL sequence. In practice, a hybrid approach would be used for both sequences, whereby the labelling portion (the focus of this thesis) and the imaging portion would have separately optimized pTx schemes, with dynamic alternation between them during the pulse sequence playout.

6.3.3. Applying RF shimming more widely in ASL

In the PCASL study described in Chapter 4, VERSE shimming was only applied to the PCASL labelling module. The same approach could also be applied to other recent advances in PCASL sequence design. VERSE shimming could be easily incorporated into vessel-encoded ASL [141, 167] at UHF to improve the efficiency of the labelling pulses. Recent developments in PCASL-based MR angiography (MRA) techniques could also leverage the improved labelling efficiency and perfusion SNR for their application at UHF. Such developments locally include the work by Okell *et al.* that acquires both angiography and perfusion images by a continuous radial sampling after the PCASL labelling module [198]; the work by Suzuki *et al.* that reduces the acquisition time of dynamic MRA by roughly half by only acquiring a single control image [199, 200]; and the work by Schauman *et al.* that highly accelerates MR angiography by using compressed sensing and by exploiting the additional sparsity of angiograms [201].

6.3.4. Spatially-selective inversion

In the TRUST study described in Chapter 5, a sophisticated saturation strategy involving three saturation pulses was adopted. An additional inversion pulse was applied in the label case to invert the spins in the ROI (which was not applied in the control case), so that the difference image would only contain signal from the ROI. Experimental results showed that three spatially-selective pulses were needed to achieve a saturation of sufficient accuracy.

Achieving 3D spatially-selective inversion using a single RF pulse would avoid the complexity of the method proposed in Chapter 5. Furthermore, no additional inversion pulses would be needed. However, there are a few challenges. First, a full Bloch equation simulation would be required during pulse optimisation, as opposed to relying on the small tip-angle approximation used in Chapter 5. This change would considerably increase the computation time of the pulse design. Second, a spatially-selective inversion pulse might be particularly difficult to achieve for a small ROI, since the flip-angle needs to change from 0° to 180° over a very small distance.

6.3.5. Optimising the workflow

The work in this thesis aims at demonstrating the benefits of pTx applications without focusing on optimising the workflow. One way to assess the difficulty of scan operation is by measuring the number of mouse clicks during a session. In this regard, both applications of pTx methods in this thesis are currently very challenging to operate. Although future vendor updates would potentially make operation of the pTx system easier, certain steps could facilitate easier operation of the current pTx system.

In the PCASL study, the position of the labelling slice was selected manually after the operator visually inspected the time-of-flight images. Similarly, the four feeding arteries were drawn manually as ROIs for RF shimming calculation. Both procedures are time-consuming and complicate operation. A fully automatic selection of the labelling plane and the feeding arteries would increase the practicality of the proposed RF shimming method considerably. An algorithm could be designed to first segment the vessels from the TOF angiography. Recent work by Fan *et al.* using deep neural networks would allow for a fast TOF segmentation [202]. Then, a cost function could be established to determine the optimal labelling slice position based on the B_1^+, B_0 and the tortuosity of the feed vessels in a particular slice. The tortuosity of the vessels is important because the labelling plane should be chosen so that it is perpendicular to the flowing vessels. Such an automatic algorithm could be easily used in vessel-selective PCASL sequences as well, since the location of the vessels are needed to calculate the amplitude of gradient pulse blips between two adjacent RF pulses in the PCASL labelling train.

Compared to the ASL study, automatic selection of the ROI in the TRUST experiment is less straightforward since the ROI needs to be identified on a case-by-case basis depending on the patient physiology/pathology in a clinical setting. However, running the RF pulse calibration on the console would benefit both sequences.

6.4. Final remarks

This thesis investigates various pulse design approaches and explores the applications of parallel transmission on ASL and TRUST sequences. RF shimming was applied to the labelling pulse train to improve the labelling efficiency of ASL scans, and an arbitrary spatially localised pulse was used for regional oxygenation measurement in the TRUST sequence.

Despite the success of the proposed methods, there are two major obstacles for their application to routine research scans or clinical practice. The first obstacle is prohibitively conservative RF power/SAR constraints currently implemented in the Siemens Magnetom scanner. However, such a challenge might be alleviated by developments of the pTx system on newer models of UHF scanners. The second challenge is the difficulty of programming and operating on the pTx system. This consists of the additional calibration scans (primarily B_1^+ and B_0 maps), calibration data transfer, loading and processing, RF pulse design, and the switching from the single channel system to the pTx system. Further development from both the UHF research community and the scanner and coil vendors is needed to make image acquisition on the pTx system easier and more robust.

Nevertheless, pTx remains an exciting field of research in the MR community. An increasing array of pTx pulses have been incorporated into commonly used sequences for routine scans. More sophisticated RF pulse design approaches are being proposed. Some include direct SAR or temperature control. Others aim to reduce the calculation time of the optimisation algorithm. Like many other fields of MR, machine learning has been adopted in pTx RF pulse design. Furthermore, unlike the conventional goals of improving excitation uniformity and spatial selection, pTx has more recently been used for completely new purposes such as motion correction [113], and RF power reduction

for patients with deep brain stimulation [203]. These and other applications indicate that pTx has a valuable future in the armoury of MRI techniques, once the challenges outlined above are overcome.

References:

1. Hoult, D.I. and R.E. Richards, *The signal-to-noise ratio of the nuclear magnetic resonance experiment.* Journal of Magnetic Resonance (1969), 1976. **24**(1): p. 71-85.
2. de Graaf, R.A., et al., *On the magnetic field dependence of deuterium metabolic imaging.* NMR Biomed, 2020. **33**(3): p. e4235.
3. Padormo, F., et al., *Parallel transmission for ultrahigh-field imaging.* NMR Biomed, 2016. **29**(9): p. 1145-61.
4. Moser, E., et al., *7-T MR--from research to clinical applications?* NMR Biomed, 2012. **25**(5): p. 695-716.
5. He, X., et al., *First in-vivo human imaging at 10.5T: Imaging the body at 447 MHz.* Magn Reson Med, 2019.
6. Budinger, T.F. and M.D. Bird, *MRI and MRS of the human brain at magnetic fields of 14T to 20T: Technical feasibility, safety, and neuroscience horizons.* Neuroimage, 2018. **168**: p. 509-531.
7. Pruessmann, K.P., et al., *SENSE: sensitivity encoding for fast MRI.* Magn Reson Med, 1999. **42**(5): p. 952-62.
8. Griswold, M.A., et al., *Generalized autocalibrating partially parallel acquisitions (GRAPPA).* Magn Reson Med, 2002. **47**(6): p. 1202-10.
9. Wiesinger, F., et al., *Parallel imaging performance as a function of field strength--an experimental investigation using electrodynamic scaling.* Magn Reson Med, 2004. **52**(5): p. 953-64.
10. Ugurbil, K., *Magnetic resonance imaging at ultrahigh fields.* IEEE Trans Biomed Eng, 2014. **61**(5): p. 1364-79.
11. Ogawa, S., et al., *Intrinsic signal changes accompanying sensory stimulation: functional brain mapping with magnetic resonance imaging.* Proc Natl Acad Sci U S A, 1992. **89**(13): p. 5951-5.
12. Hangel, G., et al., *Ultra-high resolution brain metabolite mapping at 7 T by short-TR Hadamard-encoded FID-MRSI.* Neuroimage, 2018. **168**: p. 199-210.
13. Vaidya, M.V., et al., *Dependence of B-1(+) and B-1(-) Field Patterns of Surface Coils on the Electrical Properties of the Sample and the MR Operating Frequency.* Concepts in Magnetic Resonance Part B-Magnetic Resonance Engineering, 2016. **46**(1): p. 25-40.
14. Vaughan, J.T., et al., *7T vs. 4T: RF power, homogeneity, and signal-to-noise comparison in head images.* Magnetic Resonance in Medicine, 2001. **46**(1): p. 24-30.
15. Juchem, C., et al., *Dynamic Shimming of the Human Brain at 7 Tesla.* Concepts Magn Reson Part B Magn Reson Eng, 2010. **37B**(3): p. 116-128.
16. Blamire, A.M., D.L. Rothman, and T. Nixon, *Dynamic shim updating: a new approach towards optimized whole brain shimming.* Magn Reson Med, 1996. **36**(1): p. 159-65.
17. Shellock, F.G. and J.V. Crues, *MR procedures: Biologic effects, safety, and patient care.* Radiology, 2004. **232**(3): p. 635-652.
18. Yarnykh, V.L., *Actual flip-angle imaging in the pulsed steady state: a method for rapid three-dimensional mapping of the transmitted radiofrequency field.* Magn Reson Med, 2007. **57**(1): p. 192-200.

19. Nehrke, K. and P. Bornert, *DREAM--a novel approach for robust, ultrafast, multislice B(1) mapping.* Magn Reson Med, 2012. **68**(5): p. 1517-26.
20. Sacolick, L.I., et al., *B1 mapping by Bloch-Siegert shift.* Magn Reson Med, 2010. **63**(5): p. 1315-22.
21. Bloch, F. and A. Siegert, *Magnetic Resonance for Nonrotating Fields.* Physical Review, 1940. **57**(6): p. 522-527.
22. Tse, D.H., et al., *Encoding methods for B1(+) mapping in parallel transmit systems at ultra high field.* J Magn Reson, 2014. **245**: p. 125-32.
23. Brunner, D.O. and K.P. Pruessmann, *B1(+) interferometry for the calibration of RF transmitter arrays.* Magn Reson Med, 2009. **61**(6): p. 1480-8.
24. Malik, S.J., D.J. Larkman, and J.V. Hajnal, *Optimal linear combinations of array elements for B1 mapping.* Magn Reson Med, 2009. **62**(4): p. 902-9.
25. Nehrke, K. and P. Bornert, *Eigenmode analysis of transmit coil array for tailored B1 mapping.* Magn Reson Med, 2010. **63**(3): p. 754-64.
26. Malik, S.J., G.D. Kenny, and J.V. Hajnal, *Slice profile correction for transmit sensitivity mapping using actual flip angle imaging.* Magn Reson Med, 2011. **65**(5): p. 1393-9.
27. Teeuwisse, W.M., W.M. Brink, and A.G. Webb, *Quantitative assessment of the effects of high-permittivity pads in 7 Tesla MRI of the brain.* Magn Reson Med, 2012. **67**(5): p. 1285-93.
28. O'Brien, K.R., et al., *Dielectric pads and low- B1+ adiabatic pulses: complementary techniques to optimize structural T1 w whole-brain MP2RAGE scans at 7 tesla.* J Magn Reson Imaging, 2014. **40**(4): p. 804-12.
29. Vu, A.T., et al., *High resolution whole brain diffusion imaging at 7T for the Human Connectome Project.* Neuroimage, 2015. **122**: p. 318-31.
30. Vu, A.T., et al., *Tradeoffs in pushing the spatial resolution of fMRI for the 7T Human Connectome Project.* Neuroimage, 2017. **154**: p. 23-32.
31. Metzger, G.J., et al., *Local B1+ shimming for prostate imaging with transceiver arrays at 7T based on subject-dependent transmit phase measurements.* Magn Reson Med, 2008. **59**(2): p. 396-409.
32. Lattanzi, R. and D.K. Sodickson, *Ideal current patterns yielding optimal signal-to-noise ratio and specific absorption rate in magnetic resonance imaging: computational methods and physical insights.* Magn Reson Med, 2012. **68**(1): p. 286-304.
33. Raaijmakers, A.J., et al., *Design of a radiative surface coil array element at 7 T: the single-side adapted dipole antenna.* Magn Reson Med, 2011. **66**(5): p. 1488-97.
34. Oezerdem, C., et al., *16-channel bow tie antenna transceiver array for cardiac MR at 7.0 tesla.* Magn Reson Med, 2016. **75**(6): p. 2553-65.
35. Clement, J.D., R. Gruetter, and O. Ipek, *A human cerebral and cerebellar 8-channel transceive RF dipole coil array at 7T.* Magn Reson Med, 2019. **81**(2): p. 1447-1458.
36. Erturk, M.A., et al., *A 16-channel combined loop-dipole transceiver array for 7 Tesla body MRI.* Magn Reson Med, 2017. **77**(2): p. 884-894.
37. Grissom, W.A., et al., *Small-tip-angle spokes pulse design using interleaved greedy and local optimization methods.* Magn Reson Med, 2012. **68**(5): p. 1553-62.
38. Sharma, A., et al., *Low peak power multiband spokes pulses for B1 (+) inhomogeneity-compensated simultaneous multislice excitation in high field MRI.* Magn Reson Med, 2015. **74**(3): p. 747-55.

39. Eggenschwiler, F., et al., *Improving T-2-Weighted Imaging at High Field Through the Use of k(T)-Points.* Magnetic Resonance in Medicine, 2014. **71**(4): p. 1478-1488.
40. Eggenschwiler, F., et al., *3D T 2-weighted imaging at 7T using dynamic kT-points on single-transmit MRI systems.* MAGMA, 2016. **29**(3): p. 347-58.
41. Tannus, A. and M. Garwood, *Adiabatic pulses.* NMR Biomed, 1997. **10**(8): p. 423-34.
42. Balchandani, P., J. Pauly, and D. Spielman, *Slice-selective tunable-flip adiabatic low peak-power excitation pulse.* Magn Reson Med, 2008. **59**(5): p. 1072-8.
43. Balchandani, P., et al., *Self-refocused adiabatic pulse for spin echo imaging at 7 T.* Magn Reson Med, 2012. **67**(4): p. 1077-85.
44. Balchandani, P. and D. Spielman, *Fat suppression for 1H MRSI at 7T using spectrally selective adiabatic inversion recovery.* Magn Reson Med, 2008. **59**(5): p. 980-8.
45. Balchandani, P., J. Pauly, and D. Spielman, *Interleaved narrow-band PRESS sequence with adiabatic spatial-spectral refocusing pulses for 1H MRSI at 7T.* Magn Reson Med, 2008. **59**(5): p. 973-9.
46. Scheenen, T.W., A. Heerschap, and D.W. Klomp, *Towards 1H-MRSI of the human brain at 7T with slice-selective adiabatic refocusing pulses.* MAGMA, 2008. **21**(1-2): p. 95-101.
47. Katscher, U., et al., *Transmit SENSE.* Magn Reson Med, 2003. **49**(1): p. 144-50.
48. Zhu, Y., *Parallel excitation with an array of transmit coils.* Magn Reson Med, 2004. **51**(4): p. 775-84.
49. Childs, A.S., et al., *Impact of number of channels on RF shimming at 3T.* Magma, 2013. **26**(4): p. 401-10.
50. Curtis, A.T., et al., *Slice-by-slice B1+ shimming at 7 T.* Magn Reson Med, 2012. **68**(4): p. 1109-16.
51. Schmitter, S., et al., *Cerebral TOF angiography at 7T: Impact of B1 (+) shimming with a 16-channel transceiver array.* Magn Reson Med, 2014. **71**(3): p. 966-77.
52. Pauly, J., D. Nishimura, and A. Macovski, *A k-space analysis of small-tip-angle excitation. 1989.* J Magn Reson, 2011. **213**(2): p. 544-57.
53. Setsompop, K., et al., *Slice-Selective RF Pulses for In Vivo B(1)(+) Inhomogeneity Mitigation at 7 Tesla Using Parallel RF Excitation With a 16-Element Coil.* Magnetic Resonance in Medicine, 2008. **60**(6): p. 1422-1432.
54. Malik, S.J., et al., *Tailored excitation in 3D with spiral nonselective (SPINS) RF pulses.* Magn Reson Med, 2012. **67**(5): p. 1303-15.
55. Cloos, M.A., et al., *kT -points: short three-dimensional tailored RF pulses for flip-angle homogenization over an extended volume.* Magn Reson Med, 2012. **67**(1): p. 72-80.
56. Saekho, S., et al., *Fast-kz three-dimensional tailored radiofrequency pulse for reduced B1 inhomogeneity.* Magn Reson Med, 2006. **55**(4): p. 719-24.
57. Setsompop, K., et al., *Slice-selective RF pulses for in vivo B1+ inhomogeneity mitigation at 7 tesla using parallel RF excitation with a 16-element coil.* Magn Reson Med, 2008. **60**(6): p. 1422-32.
58. Bloch, F., *Nuclear Induction.* Physical Review, 1946. **70**(7-8): p. 460-474.
59. Grissom, W., et al., *Spatial domain method for the design of RF pulses in multicoil parallel excitation.* Magn Reson Med, 2006. **56**(3): p. 620-9.

60. IEC, *Medical electrical equipment - Part 2-33: Particular requirements for the basic safety and essential performance of magnetic resonance equipment for medical diagnosis*, in *60601-2-33:2010*. 2010.
61. AG, Z.M. *Sim4Life*. 2020; Available from: https://zmt.swiss/sim4life/.
62. Inc., R. *Remcom: Electromagnetic Simulation Software & EM Modeling*. 2020; Available from: https://www.remcom.com/.
63. Ansys, I. *Electromagnetic, Electronics, Thermal and Electromechanical Simulation*. 2020; Available from: https://www.ansys.com/en-gb/products/electronics.
64. Systèmes, D. *CST Studio Suite 3D EM simulation and analysis software*. 2020; Available from: https://www.3ds.com/products-services/simulia/products/cst-studio-suite/.
65. Villena, J.F., et al. *MARIE–a MATLAB-based open source software for the fast electromagnetic analysis of MRI systems*. in *Proceedings of the 23rd Annual Meeting of ISMRM, Toronto, Canada*. 2015.
66. Guerin, B., et al., *The 'virtual DBS population': five realistic computational models of deep brain stimulation patients for electromagnetic MR safety studies.* Physics in Medicine and Biology, 2019. **64**(3).
67. Barber, B.J., et al., *Thermal effects of MR imaging: worst-case studies on sheep.* AJR Am J Roentgenol, 1990. **155**(5): p. 1105-10.
68. Massire, A., et al., *Thermal simulations in the human head for high field MRI using parallel transmission.* J Magn Reson Imaging, 2012. **35**(6): p. 1312-21.
69. Rieke, V. and K. Butts Pauly, *MR thermometry.* J Magn Reson Imaging, 2008. **27**(2): p. 376-90.
70. Eichfelder, G. and M. Gebhardt, *Local specific absorption rate control for parallel transmission by virtual observation points.* Magnetic resonance in medicine, 2011. **66**(5): p. 1468-1476.
71. Brunner, D.O. and K.P. Pruessmann, *Optimal design of multiple-channel RF pulses under strict power and SAR constraints.* Magn Reson Med, 2010. **63**(5): p. 1280-91.
72. Hoyos-Idrobo, A., et al., *On variant strategies to solve the magnitude least squares optimization problem in parallel transmission pulse design and under strict SAR and power constraints.* IEEE Trans Med Imaging, 2014. **33**(3): p. 739-48.
73. Dupas, L., et al., *Two-spoke placement optimization under explicit specific absorption rate and power constraints in parallel transmission at ultra-high field.* Journal of Magnetic Resonance, 2015. **255**: p. 59-67.
74. Eryaman, Y., et al., *Parallel transmit pulse design for patients with deep brain stimulation implants.* Magn Reson Med, 2015. **73**(5): p. 1896-903.
75. Gras, V., et al., *Joint design of k T-points trajectories and RF pulses under explicit SAR and power constraints in the large flip angle regime.* Journal of Magnetic Resonance, 2015. **261**: p. 181-189.
76. Pendse, M. and B. Rutt. *IMPULSE: a generalized and scalable algorithm for joint design of minimum SAR parallel transmit RF pulses*. in *Proceedings of the 23rd Scientific Meeting, International Society for Magnetic Resonance in Medicine, Toronto, Canada*. 2015.
77. Vinding, M.S., et al., *Local SAR, global SAR, and power-constrained large-flip-angle pulses with optimal control and virtual observation points.* Magn Reson Med, 2015.

78. Deniz, C.M., et al., *Subject- and resource-specific monitoring and proactive management of parallel radiofrequency transmission.* Magn Reson Med, 2016. **76**(1): p. 20-31.
79. Martin, A., et al., *Parallel transmission pulse design with explicit control for the specific absorption rate in the presence of radiofrequency errors.* Magn Reson Med, 2016. **75**(6): p. 2493-504.
80. Pendse, M. and B. Rutt. *IMPULSE-SMS: local SAR and peak power optimized pTx pulse design for simultaneous multislice imaging at high*. in *Proceedings of the 24th Scientific Meeting, International Society for Magnetic Resonance in Medicine, Singapore*. 2016.
81. Boulant, N., et al., *Radiofrequency pulse design in parallel transmission under strict temperature constraints.* Magn Reson Med, 2014. **72**(3): p. 679-88.
82. Deniz, C.M., G. Carluccio, and C. Collins, *Parallel transmission RF pulse design with strict temperature constraints.* NMR Biomed, 2017.
83. Setsompop, K., et al., *High-flip-angle slice-selective parallel RF transmission with 8 channels at 7 T.* J Magn Reson, 2008. **195**(1): p. 76-84.
84. Setsompop, K., et al., *Magnitude least squares optimization for parallel radio frequency excitation design demonstrated at 7 Tesla with eight channels.* Magn Reson Med, 2008. **59**(4): p. 908-15.
85. Ma, C., et al., *Joint Design of Spoke Trajectories and RF Pulses for Parallel Excitation.* Magnetic Resonance in Medicine, 2011. **65**(4): p. 973-985.
86. Cloos, M.A., et al., *Multiparametric imaging with heterogeneous radiofrequency fields.* Nat Commun, 2016. **7**: p. 12445.
87. Wu, X., et al., *High-resolution whole-brain diffusion MRI at 7T using radiofrequency parallel transmission.* Magn Reson Med, 2018.
88. Wu, X., et al. *High resolution resting-state functional MRI at 7 Tesla using RF parallel transmission*. in *Proceedings of the 25th Scientific Meeting, International Society for Magnetic Resonance in Medicine*. 2017. Honolulu.
89. Tse, D.H., et al., *B1+ inhomogeneity mitigation in CEST using parallel transmission.* Magn Reson Med, 2017.
90. Poser, B.A., et al., *Simultaneous multislice excitation by parallel transmission.* Magn Reson Med, 2014. **71**(4): p. 1416-27.
91. Wu, X., et al., *Simultaneous multislice multiband parallel radiofrequency excitation with independent slice-specific transmit B1 homogenization.* Magn Reson Med, 2013. **70**(3): p. 630-8.
92. Guerin, B., et al., *Design of parallel transmission pulses for simultaneous multislice with explicit control for peak power and local specific absorption rate.* Magn Reson Med, 2015. **73**(5): p. 1946-53.
93. Schmitter, S., et al., *Simultaneous multislice imaging in dynamic cardiac MRI at 7T using parallel transmission.* Magn Reson Med, 2017. **77**(3): p. 1010-1020.
94. Tse, D.H.Y., C.J. Wiggins, and B.A. Poser, *High-resolution gradient-recalled echo imaging at 9.4T using 16-channel parallel transmit simultaneous multislice spokes excitations with slice-by-slice flip angle homogenization.* Magn Reson Med, 2017. **78**(3): p. 1050-1058.
95. Ma, D., et al., *Magnetic resonance fingerprinting.* Nature, 2013. **495**(7440): p. 187-92.
96. Schmitter, S., et al., *Seven-tesla time-of-flight angiography using a 16-channel parallel transmit system with power-constrained 3-dimensional spoke radiofrequency pulse design.* Invest Radiol, 2014. **49**(5): p. 314-25.

97. Saib, G., et al., *Time-of-flight angiography at 7T using TONE double spokes with parallel transmission.* Magn Reson Imaging, 2019. **61**: p. 104-115.
98. Malik, S.J., et al., *Spatially resolved extended phase graphs: modeling and design of multipulse sequences with parallel transmission.* Magn Reson Med, 2012. **68**(5): p. 1481-94.
99. Gras, V., et al., *Universal pulses: A new concept for calibration-free parallel transmission.* Magn Reson Med, 2017. **77**(2): p. 635-643.
100. Gras, V., et al., *Homogeneous non-selective and slice-selective parallel-transmit excitations at 7 Tesla with universal pulses: A validation study on two commercial RF coils.* PLoS One, 2017. **12**(8): p. e0183562.
101. Gras, V., et al., *Robust nonadiabatic T2 preparation using universal parallel-transmit kT -point pulses for 3D FLAIR imaging at 7 T.* Magn Reson Med, 2019. **81**(5): p. 3202-3208.
102. Gras, V., et al., *Optimizing BOLD sensitivity in the 7T Human Connectome Project resting-state fMRI protocol using plug-and-play parallel transmission.* Neuroimage, 2019. **195**: p. 1-10.
103. Ianni, J.D., Z. Cao, and W.A. Grissom, *Machine learning RF shimming: Prediction by iteratively projected ridge regression.* Magn Reson Med, 2018.
104. Tomi-Tricot, R., et al., *SmartPulse, a machine learning approach for calibration-free dynamic RF shimming: Preliminary study in a clinical environment.* Magn Reson Med, 2019.
105. Cavusoglu, M., et al., *Correction of parallel transmission using concurrent RF and gradient field monitoring.* MAGMA, 2017.
106. Boesch, C., R. Gruetter, and E. Martin, *Temporal and Spatial-Analysis of Fields Generated by Eddy Currents in Superconducting Magnets - Optimization of Corrections and Quantitative Characterization of Magnet Gradient Systems.* Magnetic Resonance in Medicine, 1991. **20**(2): p. 268-284.
107. Liu, Q., D.G. Hughes, and P.S. Allen, *Quantitative Characterization of the Eddy-Current Fields in a 40-Cm Bore Superconducting Magnet.* Magnetic Resonance in Medicine, 1994. **31**(1): p. 73-76.
108. Wu, Y.H., et al., *Gradient-induced acoustic and magnetic field fluctuations in a 4T whole-body MR imager.* Magnetic Resonance in Medicine, 2000. **44**(4): p. 532-536.
109. Foerster, B.U., D. Tomasi, and E.C. Caparelli, *Magnetic field shift due to mechanical vibration in functional magnetic resonance imaging.* Magnetic Resonance in Medicine, 2005. **54**(5): p. 1261-1267.
110. Keupp, J., et al. *Parallel RF transmission based MRI technique for highly sensitive detection of amide proton transfer in the human brain at 3T*. in *Proc Int Soc Magn Reson Med*. 2011. Montréal.
111. Hess, A.T., et al., *Diaphragm position can be accurately estimated from the scattering of a parallel transmit RF coil at 7 T.* Magn Reson Med, 2018. **79**(4): p. 2164-2169.
112. Jaeschke, S.H.F., M.D. Robson, and A.T. Hess, *Cardiac gating using scattering of an 8-channel parallel transmit coil at 7T.* Magn Reson Med, 2018. **80**(2): p. 633-640.
113. Jaeschke, S.H.F., M.D. Robson, and A.T. Hess, *Scattering matrix imaging pulse design for real-time respiration and cardiac motion monitoring.* Magn Reson Med, 2019.

114. Ogg, R.J., P.B. Kingsley, and J.S. Taylor, *WET, a T1- and B1-insensitive water-suppression method for in vivo localized 1H NMR spectroscopy.* J Magn Reson B, 1994. **104**(1): p. 1-10.
115. Luo, Y., et al., *BISTRO: an outer-volume suppression method that tolerates RF field inhomogeneity.* Magn Reson Med, 2001. **45**(6): p. 1095-102.
116. Sung, K. and K.S. Nayak, *Design and use of tailored hard-pulse trains for uniformed saturation of myocardium at 3 Tesla.* Magn Reson Med, 2008. **60**(4): p. 997-1002.
117. Kim, D., N. Oesingmann, and K. McGorty, *Hybrid adiabatic-rectangular pulse train for effective saturation of magnetization within the whole heart at 3 T.* Magn Reson Med, 2009. **62**(6): p. 1368-78.
118. Tao, Y., et al., *Optimized saturation pulse train for human first-pass myocardial perfusion imaging at 7T.* Magn Reson Med, 2015. **73**(4): p. 1450-6.
119. Pauly, J., D. Nishimura, and A. Macovski, *A k-space analysis of small-tip-angle excitation.* Journal of Magnetic Resonance (1969), 1989. **81**(1): p. 43-56.
120. Brenner, D., et al. *3DREAM—a Three-Dimensional Variant of the DREAM Sequence*. in *Proceedings of the 22nd scientific meeting, International Society for Magnetic Resonance in Medicine, Milan*. 2014.
121. Grissom, W.A., et al., *Minimum envelope roughness pulse design for reduced amplifier distortion in parallel excitation.* Magn Reson Med, 2010. **64**(5): p. 1432-9.
122. Detre, J.A., et al., *Perfusion imaging.* Magn Reson Med, 1992. **23**(1): p. 37-45.
123. Williams, D.S., et al., *Magnetic resonance imaging of perfusion using spin inversion of arterial water.* Proc Natl Acad Sci U S A, 1992. **89**(1): p. 212-6.
124. Buxton, R.B., et al., *A general kinetic model for quantitative perfusion imaging with arterial spin labeling.* Magn Reson Med, 1998. **40**(3): p. 383-96.
125. Kim, S.G., *Quantification of relative cerebral blood flow change by flow-sensitive alternating inversion recovery (FAIR) technique: application to functional mapping.* Magn Reson Med, 1995. **34**(3): p. 293-301.
126. Wong, E.C., R.B. Buxton, and L.R. Frank, *Implementation of quantitative perfusion imaging techniques for functional brain mapping using pulsed arterial spin labeling.* NMR Biomed, 1997. **10**(4-5): p. 237-49.
127. Wong, E.C., R.B. Buxton, and L.R. Frank, *Quantitative imaging of perfusion using a single subtraction (QUIPSS and QUIPSS II).* Magnetic Resonance in Medicine, 1998. **39**(5): p. 702-708.
128. Andersson, J.L., S. Skare, and J. Ashburner, *How to correct susceptibility distortions in spin-echo echo-planar images: application to diffusion tensor imaging.* Neuroimage, 2003. **20**(2): p. 870-88.
129. Alsop, D.C., et al., *Recommended implementation of arterial spin-labeled perfusion MRI for clinical applications: A consensus of the ISMRM perfusion study group and the European consortium for ASL in dementia.* Magn Reson Med, 2015. **73**(1): p. 102-16.
130. Teeuwisse, W.M., A.G. Webb, and M.J.P. van Osch, *Arterial spin labeling at ultra-high field: All that glitters is not gold.* International Journal of Imaging Systems and Technology, 2010. **20**(1): p. 62-70.
131. Gardener, A.G. and P. Jezzard, *Investigating white matter perfusion using optimal sampling strategy arterial spin labeling at 7 Tesla.* Magn Reson Med, 2015. **73**(6): p. 2243-8.

132. Haast, R.A.M., et al., *Anatomic & metabolic brain markers of the m.3243A>G mutation: A multi-parametric 7T MRI study.* Neuroimage Clin, 2018. **18**: p. 231-244.
133. Zuo, Z., et al., *Turbo-FLASH based arterial spin labeled perfusion MRI at 7 T.* PLoS One, 2013. **8**(6): p. e66612.
134. Wang, Y., et al., *Simultaneous multi-slice Turbo-FLASH imaging with CAIPIRINHA for whole brain distortion-free pseudo-continuous arterial spin labeling at 3 and 7 T.* Neuroimage, 2015. **113**: p. 279-288.
135. Stafford, R.B., et al., *An Actively Decoupled Dual Transceiver Coil System for Continuous ASL at 7 T.* Int J Imaging Syst Technol, 2016. **26**(2): p. 106-115.
136. Zimmer, F., et al., *Pulsed arterial spin labelling at ultra-high field with a B-1(+)-optimised adiabatic labelling pulse.* Magnetic Resonance Materials in Physics Biology and Medicine, 2016. **29**(3): p. 463-473.
137. Jezzard, P., M.A. Chappell, and T.W. Okell, *Arterial spin labeling for the measurement of cerebral perfusion and angiography.* J Cereb Blood Flow Metab, 2018. **38**(4): p. 603-626.
138. Conolly, S., et al., *Variable-Rate Selective Excitation.* Journal of Magnetic Resonance, 1988. **78**(3): p. 440-458.
139. Cavusoglu, M., et al., *VERSE-guided parallel RF excitations using dynamic field correction.* NMR Biomed, 2017. **30**(6).
140. Tong, Y., et al. *Improving arterial spin labeling at ultra-high field using parallel transmission: a simulation study*. in *Proceedings of the 27th Scientific Meeting, ISMRM*. 2018. Paris.
141. Okell, T.W., et al., *Cerebral blood flow quantification using vessel-encoded arterial spin labeling.* J Cereb Blood Flow Metab, 2013. **33**(11): p. 1716-24.
142. Ye, F.Q., et al., *Noise reduction in 3D perfusion imaging by attenuating the static signal in arterial spin tagging (ASSIST).* Magnetic Resonance in Medicine, 2000. **44**(1): p. 92-100.
143. Hargreaves, B.A., et al., *Variable-rate selective excitation for rapid MRI sequences.* Magn Reson Med, 2004. **52**(3): p. 590-7.
144. Dupas, L., et al., *Two-spoke placement optimization under explicit specific absorption rate and power constraints in parallel transmission at ultra-high field.* J Magn Reson, 2015. **255**: p. 59-67.
145. *IEC 60601-2-33:2010 Medical electrical equipment - Part 2-33: Particular requirements for the basic safety and essential performance of magnetic resonance equipment for medical diagnosis*. 2010.
146. *Constrained Nonlinear Optimization Algorithms*. [cited 2017; Available from: https://uk.mathworks.com/help/optim/ug/constrained-nonlinear-optimization-algorithms.html#brnox01.
147. Jenkinson, M., et al., *Fsl.* Neuroimage, 2012. **62**(2): p. 782-90.
148. Smith, S.M., *Fast robust automated brain extraction.* Hum Brain Mapp, 2002. **17**(3): p. 143-55.
149. Jenkinson, M., et al., *Improved optimization for the robust and accurate linear registration and motion correction of brain images.* Neuroimage, 2002. **17**(2): p. 825-41.
150. Jenkinson, M. and S. Smith, *A global optimisation method for robust affine registration of brain images.* Med Image Anal, 2001. **5**(2): p. 143-56.
151. Chappell, M.A., et al., *Variational Bayesian Inference for a Nonlinear Forward Model.* IEEE Transactions on Signal Processing, 2009. **57**(1): p. 223-236.

152. Brant-Zawadzki, M., G.D. Gillan, and W.R. Nitz, *MP RAGE: a three-dimensional, T1-weighted, gradient-echo sequence--initial experience in the brain.* Radiology, 1992. **182**(3): p. 769-75.
153. Lu, H., et al., *Determining the longitudinal relaxation time (T1) of blood at 3.0 Tesla.* Magn Reson Med, 2004. **52**(3): p. 679-82.
154. Rooney, W.D., et al., *Magnetic field and tissue dependencies of human brain longitudinal 1H2O relaxation in vivo.* Magn Reson Med, 2007. **57**(2): p. 308-18.
155. Berry, E.S.K., P. Jezzard, and T.W. Okell, *Off-resonance correction for pseudo-continuous arterial spin labeling using the optimized encoding scheme.* Neuroimage, 2019. **199**: p. 304-312.
156. Li, X., et al. *Improve PCASL Brain Imaging at 7T Using Dynamically Applied B1+ Shimming Solutions*. in *Proceedings of the 27th Scientific Meeting, ISMRM*. 2018. Paris.
157. Boland, M., et al. *Robust and SAR-efficient whole-brain pseudo-continuous ASL at 7T*. in *Proceedings of the 26th Scientific Meeting, ISMRM*. 2019. Montreal.
158. Serrai, H., et al., *Using variable-rate selective excitation (VERSE) radiofrequency pulses to reduce power deposition in pulsed arterial spin labeling sequence at 7 Tesla.* Magn Reson Med, 2019.
159. Triantafyllou, C., et al., *Comparison of physiological noise at 1.5 T, 3 T and 7 T and optimization of fMRI acquisition parameters.* Neuroimage, 2005. **26**(1): p. 243-50.
160. Zaharchuk, G., et al., *Multislice perfusion and perfusion territory imaging in humans with separate label and image coils.* Magn Reson Med, 1999. **41**(6): p. 1093-8.
161. Amukotuwa, S.A., C. Yu, and G. Zaharchuk, *3D Pseudocontinuous arterial spin labeling in routine clinical practice: A review of clinically significant artifacts.* J Magn Reson Imaging, 2016. **43**(1): p. 11-27.
162. Setsompop, K., et al., *Parallel RF transmission with eight channels at 3 Tesla.* Magn Reson Med, 2006. **56**(5): p. 1163-71.
163. van der Zwaag, W., et al., *fMRI at 1.5, 3 and 7 T: characterising BOLD signal changes.* Neuroimage, 2009. **47**(4): p. 1425-34.
164. Zhang, X., et al., *In vivo blood T(1) measurements at 1.5 T, 3 T, and 7 T.* Magn Reson Med, 2013. **70**(4): p. 1082-6.
165. Ordidge, R.J., et al., *Frequency offset corrected inversion (FOCI) pulses for use in localized spectroscopy.* Magn Reson Med, 1996. **36**(4): p. 562-6.
166. Davies, N.P. and P. Jezzard, *Selective arterial spin labeling (SASL): perfusion territory mapping of selected feeding arteries tagged using two-dimensional radiofrequency pulses.* Magn Reson Med, 2003. **49**(6): p. 1133-42.
167. Wong, E.C., *Vessel-encoded arterial spin-labeling using pseudocontinuous tagging.* Magn Reson Med, 2007. **58**(6): p. 1086-91.
168. Chappell, M.A., et al., *A general framework for the analysis of vessel encoded arterial spin labeling for vascular territory mapping.* Magn Reson Med, 2010. **64**(5): p. 1529-39.
169. Fox, P.T. and M.E. Raichle, *Focal physiological uncoupling of cerebral blood flow and oxidative metabolism during somatosensory stimulation in human subjects.* Proc Natl Acad Sci U S A, 1986. **83**(4): p. 1140-4.
170. Powers, W.J., et al., *Cerebral blood flow and cerebral metabolic rate of oxygen requirements for cerebral function and viability in humans.* J Cereb Blood Flow Metab, 1985. **5**(4): p. 600-8.

171. Lu, H. and Y. Ge, *Quantitative evaluation of oxygenation in venous vessels using T2-Relaxation-Under-Spin-Tagging MRI.* Magn Reson Med, 2008. **60**(2): p. 357-63.
172. Levitt, M.H., R. Freeman, and T. Frenkiel, *Broadband heteronuclear decoupling.* Journal of Magnetic Resonance (1969), 1982. **47**(2): p. 328-330.
173. Shaka, A.J., S.P. Rucker, and A. Pines, *Iterative carr-purcell trains.* Journal of Magnetic Resonance (1969), 1988. **77**(3): p. 606-611.
174. Xu, F., Y. Ge, and H. Lu, *Noninvasive quantification of whole-brain cerebral metabolic rate of oxygen (CMRO2) by MRI.* Magn Reson Med, 2009. **62**(1): p. 141-8.
175. Xu, F., et al., *On improving the speed and reliability of T2-relaxation-under-spin-tagging (TRUST) MRI.* Magn Reson Med, 2012. **68**(1): p. 198-204.
176. Lu, H., et al., *Calibration and validation of TRUST MRI for the estimation of cerebral blood oxygenation.* Magn Reson Med, 2012. **67**(1): p. 42-9.
177. Wright, G.A., B.S. Hu, and A. Macovski, *1991 I.I. Rabi Award. Estimating oxygen saturation of blood in vivo with MR imaging at 1.5 T.* J Magn Reson Imaging, 1991. **1**(3): p. 275-83.
178. Golay, X., et al., *Measurement of tissue oxygen extraction ratios from venous blood T(2): increased precision and validation of principle.* Magn Reson Med, 2001. **46**(2): p. 282-91.
179. Liu, P., F. Xu, and H. Lu, *Test-retest reproducibility of a rapid method to measure brain oxygen metabolism.* Magn Reson Med, 2013. **69**(3): p. 675-81.
180. Liu, P., et al., *Multisite evaluations of a T2 -relaxation-under-spin-tagging (TRUST) MRI technique to measure brain oxygenation.* Magn Reson Med, 2016. **75**(2): p. 680-7.
181. Stout, J.N., et al., *Assessing the effects of subject motion on T2 relaxation under spin tagging (TRUST) cerebral oxygenation measurements using volume navigators.* Magn Reson Med, 2017. **78**(6): p. 2283-2289.
182. Peng, S.L., et al., *Age-related increase of resting metabolic rate in the human brain.* Neuroimage, 2014. **98**: p. 176-83.
183. Jordan, L.C., et al., *Non-invasive imaging of oxygen extraction fraction in adults with sickle cell anaemia.* Brain, 2016. **139**(Pt 3): p. 738-50.
184. Thomas, B.P., et al., *Reduced global brain metabolism but maintained vascular function in amnestic mild cognitive impairment.* J Cereb Blood Flow Metab, 2017. **37**(4): p. 1508-1516.
185. Hokari, M., et al., *Impact of oxygen extraction fraction on long-term prognosis in patients with reduced blood flow and vasoreactivity because of occlusive carotid artery disease.* Surg Neurol, 2009. **71**(5): p. 532-8; discussion 538, 538-9.
186. Brown, J.M. and A.J. Giaccia, *The unique physiology of solid tumors: opportunities (and problems) for cancer therapy.* Cancer Res, 1998. **58**(7): p. 1408-16.
187. Langen, K.J. and S.M. Eschmann, *Correlative imaging of hypoxia and angiogenesis in oncology.* J Nucl Med, 2008. **49**(4): p. 515-6.
188. Blanchet, L., et al., *Discrimination between metastasis and glioblastoma multiforme based on morphometric analysis of MR images.* AJNR Am J Neuroradiol, 2011. **32**(1): p. 67-73.
189. O'Brien, C., et al., *Volume-localized measurement of oxygen extraction fraction in the brain using MRI.* Magn Reson Med, 2019. **82**(4): p. 1412-1423.
190. Davids, M., et al., *Fast three-dimensional inner volume excitations using parallel transmission and optimized k-space trajectories.* Magn Reson Med, 2016. **76**(4): p. 1170-82.

191. Krishnamurthy, L.C., et al., *Dependence of blood T(2) on oxygenation at 7 T: in vitro calibration and in vivo application.* Magn Reson Med, 2014. **71**(6): p. 2035-42.
192. Jang, A., et al., *Designing 3D selective adiabatic radiofrequency pulses with single and parallel transmission.* Magn Reson Med, 2018. **79**(2): p. 701-710.
193. Schneider, J.T., et al., *Inner-volume imaging in vivo using three-dimensional parallel spatially selective excitation.* Magn Reson Med, 2013. **69**(5): p. 1367-78.
194. O'Brien, C.F., *Measurement of localized oxygen extraction fraction in brain using magnetic resonance imaging*. 2019, University of Oxford.
195. Shimada, K., et al., *In vivo measurement of longitudinal relaxation time of human blood by inversion-recovery fast gradient-echo MR imaging at 3T.* Magn Reson Med Sci, 2012. **11**(4): p. 265-71.
196. Geldschläger, O., T. Shao, and A. Henning. *Universal Parallel Transmit Pulse Design for 3-Dimensional Local-Excitation: A 9.4 T Simulation Study*. in *27th Annual Meeting and Exhibition of the International Society for Magnetic Resonance in Medicine (ISMRM 2019)*. 2019.
197. O'Brien, C., et al. *Oxygen Extraction Fraction Mapping using Remote Sensing: Spatially Encoded T2-Relaxation-Under-Spin-Tagging (SE-TRUST)*. in *Proceedings of the 28th Scientific Meeting, International Society for Magnetic Resonance in Medicine*. 2020.
198. Okell, T.W., *Combined angiography and perfusion using radial imaging and arterial spin labeling.* Magn Reson Med, 2019. **81**(1): p. 182-194.
199. Suzuki, Y., et al., *Acceleration of ASL-based time-resolved MR angiography by acquisition of control and labeled images in the same shot (ACTRESS).* Magn Reson Med, 2018. **79**(1): p. 224-233.
200. Suzuki, Y., et al., *Acceleration of vessel-selective dynamic MR Angiography by pseudocontinuous arterial spin labeling in combination with Acquisition of ConTRol and labEled images in the Same Shot (ACTRESS).* Magn Reson Med, 2019. **81**(5): p. 2995-3006.
201. Schauman, S.S., M. Chiew, and T.W. Okell, *Highly accelerated vessel-selective arterial spin labeling angiography using sparsity and smoothness constraints.* Magn Reson Med, 2020. **83**(3): p. 892-905.
202. Fan, S., et al., *Unsupervised Cerebrovascular Segmentation of TOF-MRA Images Based on Deep Neural Network and Hidden Markov Random Field Model.* Front Neuroinform, 2019. **13**: p. 77.
203. Guerin, B., et al., *Parallel transmission to reduce absorbed power around deep brain stimulation devices in MRI: Impact of number and arrangement of transmit channels.* Magn Reson Med, 2020. **83**(1): p. 299-311.